Numerical Simulation of Resistivity and Investigation of Porosity Exponent in Carbonates

Haitao Wang

Submitted for the degree of Doctor of Philosophy

Heriot-Watt University

Institute of Petroleum Engineering

School of Energy, Geoscience, Infrastructure and Society

June 2015

ABSTRACT

In carbonates, the petrophysical interpretation is strongly controlled by the porosity exponent used in Archie's Law due to the variety of the pore types, the complexity of the pore geometry and the topology. Traditionally, the petrophysical model modifies the porosity exponent with consideration of the porosity based on experimental resistivity. Additionally, the porosity models can be used to predict porosity exponent based on the equivalent resistance network, in series or parallel or both.

However, these models do not consider the intrinsic factors, affecting the porosity exponent, such as pore geometry and topology and simplify the arrangement of pore types. In order to further build the formulation between porosity exponent and these intrinsic factors for accurately predicting porosity exponent, non-destructive pore scale measurement-CT imaging is used to extract pore geometry and topology, and to determine the main pore types. At the same time measurements of porosity exponent in the lab can be used to calibrate the pore scale modelling and used to investigate the influence of the pore geometry, topology and pore type on the porosity exponent.

It is found that the key factors affecting porosity exponent are the ratio of pore cross section area ratio to the pore throat cross sectional area ratio (PTAR) and Euler number representing the connectivity. With the increase of the PTAR and Euler number, the porosity exponent increases. Both of them are related to the pore types. Fracture-like (FT) pores can reduce the PTAR and Euler number resulting in the decrease of the formation factor, porosity exponent and the anisotropy while vuggy-like (VG) pores increase PTAR and Euler number resulting in the increase of porosity exponent with less influence on anisotropy. The effect on formation factor is related to the type of VG, whether connected or non-connected. In coquinas from the Morro do Chaves Formation (Lower Cretaceous, NE Brazil) there are many combinations of pore, pore shape and pore connectivity that make numerical modelling of resistivity in these rocks such a useful addition to help explain the laboratory measurements and add an understanding of the dominant pore structure which was found to vary from sample to sample. Some interesting concavo-convex pore systems have been identified.

ACKNOWLEDGEMENT:

I would like to sincerely express my deepest gratitude to my supervisor Professor Patrick Corbett for his constant support, guidance, patience and encouragement during the study. Without his assistance and encouragement, the work would never have been done. Meanwhile, I thank him for his financial support in the tuition fees for three years.

I would like to thank Dr. Jingsheng Ma and Dr. Kejian Wu. Dr. Jingsheng Ma gives me a lot of help and suggestions in building up a reasonable outline for the research and offering useful information in mathematics and software for imaging. Dr. Kejian Wu introduced me to Heriot-Watt University as a PhD candidate.

I also would like to thank Professor Jianmeng Sun in China University of Petroleum (East China) for introducing numerical simulation to me and supporting me as a PhD candidate in Heriot-Watt University.

Meanwhile I would like to thank China Scholarship Council (CSC) for financial supporting the living fees for three years.

My gratitude is also expressed to Dr. Tim Pritchard, Head of Petrophysics at BG Group and Dr. Florian Doster from Heriot-Watt University for serving on my examination committee.

I also thank Dr. Zeyun Jiang, Dr. Rink van Dijke for attending the dry run of my thesis presentation which is helpful for my viva defence.

Finally I would like to thank my parents. Thanks for their unconditional love and immense support!

ACADEMIC REGISTRY
Research Thesis Submission

Name*:*	Haitao Wang		
School/PGI:	EGIS/IPE		
Version: *(i.e. First, Resubmission, Final)*	Final	Degree Sought (Award **and** Subject area)	Degree of Doctor of Philosophy in Petroleum Engineering

Declaration

In accordance with the appropriate regulations I hereby submit my thesis and I declare that:

1) the thesis embodies the results of my own work and has been composed by myself
2) where appropriate, I have made acknowledgement of the work of others and have made reference to work carried out in collaboration with other persons
3) the thesis is the correct version of the thesis for submission and is the same version as any electronic versions submitted*.
4) my thesis for the award referred to, deposited in the Heriot-Watt University Library, should be made available for loan or photocopying and be available via the Institutional Repository, subject to such conditions as the Librarian may require
5) I understand that as a student of the University I am required to abide by the Regulations of the University and to conform to its discipline.

* *Please note that it is the responsibility of the candidate to ensure that the correct version of the thesis is submitted.*

Signature of Candidate*:*		Date:	

Submission

Submitted By *(name in capitals):*	HAITAO WANG
Signature of Individual Submitting:	
Date Submitted:	

For Completion in the Student Service Centre (SSC)

Received in the SSC by *(name in capitals):*			
Method of Submission *(Handed in to SSC; posted through internal/external mail):*			
*E-thesis Submitted (**mandatory for final theses)***			
Signature:		Date:	

TABLE OF CONTENTS

Chapter 1 Introduction---------- 1

1.1 Background ---------- 2

1.2 Challenges ---------- 10

1.3 Motivation and Objective ---------- 11

1.4 Outline of This Thesis ---------- 13

Chapter 2 Background of Pore Scale Technologies and Resistivity Models in Numerical and Empirical ---------- 15

2.1 $x-CT$ Images ---------- 19

2.1.1 Principle and History of $x-CT$ ---------- 20

2.1.2 $\mu-CT$ Application ---------- 21

2.1.3 Acquisition of 3D $\mu-CT$ Images ---------- 22

2.1.4 Image Processing ---------- 23

2.2 Pore Network Extraction ---------- 24

2.3 Pore Geometry (GM) and Topology (TP) Calculation ---------- 26

2.3.1 Minkowski Functions ---------- 27

2.3.2 Pore Geometry and Topology from PNW ---------- 30

2.4 Numerical Solutions ---------- 32

2.4.1 Electrostatic Equations ---------- 33

2.4.1 Finite Difference (FD) ---------- 33

2.4.2 Random Walk Simulation (RW) ---------- 36

2.4.3 Renormalisation ---------- 39

2.4.4 Comparison of Numerical Methods ---------- 40

2.5 Empirical Equations for Electricity ---------- 41

2.5.1 Porosity Exponent Development ---------- 42

2.5.2 Archie First Equation Development ---------- 43

2.5.3 Ranges for Porosity Exponent ---------- 47

2.6 Factors Affecting Porosity Exponent ---------- 49

2.6.1 Grains and Pores ---------- 49

2.6.2 Specific Surface Area ---------- 50

2.6.3 Tortuosity ---------- 50

2.6.4 Anisotropy ---------- 50

2.6.5 Overburden Pressure (Compaction) ---------- 51

2.6.6 Temperature ---------- 52
2.7 Porosity Exponent in Carbonates ---------- 52
2.7.1 Influence of Interparticle Pores ---------- 53
2.7.2 Influence of Moldic Pores ---------- 55
2.7.3 Influence of Matrix Pores ---------- 56
2.7.4 Influence of Vuggy Pores ---------- 56
2.7.5 Influence of Fracture and Fissure Pores ---------- 57
2.7.6 Influence of Micro Pores ---------- 57
2.8 Porosity Models ---------- 60
2.8.1 Dual Porosity Models ---------- 61
2.8.2 Triple Porosity Model ---------- 64
2.9 Pore Scale Modelling ---------- 67
2.10 Discussions ---------- 69
2.10.1 CT Imaging ---------- 69
2.10.2 Pore Network Extraction ---------- 69
2.10.3 Geometry and Topology Calculation ---------- 70
2.10.4 Numerical Resistivity Calculation ---------- 70
2.10.5 Empirical Equations ---------- 71
2.10.6 Porosity Exponent in Carbonates ---------- 71
2.10.7 Porosity Models ---------- 71
2.10.8 Pore Scale Modelling ---------- 71
2.11 Conclusions ---------- 72
Chapter 3 Resistivity Calculation and Interpretation of Three Carbonate Samples 73
3.1 $x-CT$ Images ---------- 75
3.1.1 Sample Description ---------- 75
3.1.2 Pore Space Images ---------- 78
3.2 Representative Elementary Volume (REV) Analysis ---------- 78
3.3 Comparison Resistivity Simulation with Experimental Result ---------- 84
3.3.1 Experiment Results ---------- 84
3.3.2 Simulation Results ---------- 86
3.3.3 Heterogeneity and Anisotropy of Carbonates ---------- 92
3.4 Topology and Geometry of the Pore Space ---------- 96
3.4.1 Minkowski Functions Application ---------- 96
3.4.2 Pore Geometrical Properties ---------- 104

3.4.3 Pore Topology---------- 108
3.4.4 Explain Porosity Exponent by Geometry and Topology---------- 112
3.5 Component Labelling---------- 116
3.5.1 Component Labelling Algorithm---------- 116
3.5.2 Topology and Geometry of the Predominant Pore Cluster ---------- 126
3.5.3 The Effect of Pore Clusters on the Porosity Exponent ---------- 128
3.5.4 Prediction Porosity Exponent Considering the Influence of Different Pore Clusters---------- 131
3.5.5 Main Pore Type for Three Carbonates ---------- 134
3.6 Discussion---------- 136
3.6.1 Variation of Porosity Exponents in REV Analysis ---------- 136
3.6.2 Resistivity Simulation---------- 137
3.6.3 Pore Types Influence on the Geometry and Topology ---------- 137
3.6.4 Explanation the Porosity Exponent by Pore-Throat Conjunction -- 138
3.6.5 Length and Size of the Pore Space effect on Porosity Exponent --- 138
3.6.6 Relation between Pore Types and Porosity Exponent---------- 140
3.6.7 Explanation the Large Simulation Result in Pet1 ---------- 141
3.7 Conclusion ---------- 141
Chapter 4 Model Investigation of the Impact of Pore Types on the Porosity Exponent ---------- 144
4.1 Theoretically Electrical Models for Pore-Throat Conjunction ---------- 146
4.1.1 Size and Length of the Pore System Effect on the Porosity Exponent 148
4.1.2 Relative Cross Sectional Area Ratio Effect on the Porosity Exponent 148
4.2 Effect of Pore Types on Porosity Exponent by Pore Scale Modelling -- 152
4.3 Effect of Pore Types on Porosity Exponent by Simple Tubes---------- 153
4.3.1 Representation of the IG, FT and VG by Simple Tubes ---------- 154
4.3.2 Generation the Models of IG+FT and IG+VG ---------- 156
4.3.3 Effect of the Pore Type on the Porosity Exponent and Formation Factor 157
4.4 Effect of Pore Types on Porosity Exponent Based on Rock Models ---- 160
4.4.1 Representation of the IG, FT and VG ---------- 161
4.4.2 Generation the Models for IG+FT and IG+VG ---------- 163

4.4.3 Pore Type Effect on the Porosity Exponent ---------- 165
4.4.4 Pore Type Effect on the Formation Factor (FF) ---------- 168
4.4.5 Contribution of the FT, IVG and CVG to Electrical Current ------- 170
4.4.6 Pore Type Effect on the Anisotropy of the Porosity Exponent ----- 172
4.5 Pore Type Effect on GM and TP ---------- 176
4.5.1 GM and TP of the IG+FT Model ---------- 176
4.5.2 GM and TP of the IG + Tiny CVG Models ---------- 178
4.5.3 GM and TP of the IG + Large CVG Models ---------- 180
4.5.4 GM and TP of the IG + Tiny IVG Models ---------- 183
4.5.5 GM and TP of the IG + Large IVG Models ---------- 186
4.6 Discussion ---------- 189
4.6.1 Effect of the IVG on the Porosity Exponent ---------- 189
4.6.2 Coordination Number Increase for IG+FT and IG+CVG models -- 190
4.6.3 Effect of the FT on the GM, TP, FF and Porosity Exponent -------- 191
4.6.4 Effect of the CVG on the GM, TP, FF and Porosity Exponent ----- 192
4.6.5 Effect of the IVG on the GM, TP, FF and Porosity Exponent ------ 193
4.7 Conclusion ---------- 195
Chapter 5 Discussion, Conclusion and Future Research ---------- 196
5.1 Discussion ---------- 197
5.2 Conclusion ---------- 199
5.3 Future Research ---------- 202
Appendices ---------- 205
Appendix A A Random Walk Resolution for Direct Current Resistivity -------- 206
A.1 Relationships between Tortuosity and Formation Factor and Resistivity Index 207
A.2 Feasibility of Random Walk Simulation for DC Resistivity ---------- 209
A.3 Calculation of Tortuosity ---------- 210
Appendix B Micro-CT Image Processing and Visualization ---------- 212
B.1 Importing and Saving Images ---------- 213
B.2 Processing Images ---------- 214
B.2.1 Cropping ---------- 214
B.2.2 Filtering ---------- 215
B.2.3 Segmentation ---------- 216
Appendix C Pore Network Extraction ---------- 217

C.1 Basic concepts ---------- 218
C.1.1 Maximal Balls (MBs) ---------- 219
C.1.2 Cluster ---------- 220
C.2 Pore Network Extraction ---------- 222
C.2.1 Maximal Balls Generation ---------- 222
C.2.2 Identification of the Maximal Ball Clusters ---------- 223
C.2.3 Pore Space Segmentation ---------- 223
Appendix D Basic Definitions and Notations ---------- 225
Appendix E Relationships between Pore (Throat) Radius, Shape Factor, Specific Surface and Cross Sectional Area ---------- 231
Appendix F Porosity Exponent for A Pore-Throat Conjunction in The Mix Electrical Combination ---------- 235
F.1 Porosity Exponent for A Simple Channel ---------- 237
F.1.1 Effect of The Tortuosity on The Porosity Exponent ---------- 237
F.1.2 Effect of The Size of The Pore Channel on The Porosity Exponent 238
F.2 Porosity Exponent for A Pore-Throat Conjunction ---------- 238
F.2.1 Effect of The Tortuosity on The Porosity Exponent ---------- 239
F.2.2 Effect of The Size of The Pore and Throat on The Porosity Exponent 240
References ---------- 243

LISTS OF FIGURES *(optional)*

Figure 1.1: Main methods and work flow in this thesis. 12
Figure 2.1: Lab-based μ-CT. Sample is in the range of X-ray resource and detector and its position determines magnification (Cnudde and Boone, 2013[50]). 21
Figure 2.2: Synchrotron μ-CT. The X-ray beam is parallel to offer a high X-ray flux and the geometrical magnification is controlled by optical lens (Cnudde and Boone, 2013[50]). 21
Figure2.3: X-ray μ-CT Skyscan 1173 which is a high-energy spiral μ-CT (from http://www.bruker.com/products/x-ray-diffraction-and-elemental-analysis/x-ray-micro-ct/skyscan-1173/overview.html). 22
Figure 2.4: The planar plates in 13 different directions. Three orthogonal directions are in (a)-(c). Four corner scanning plates are in the middle from (d)-(g); the rest six plates (h)-(m) are in the diagonal direction (Jiang, 2008[92]). 25
Figure 2.5: The effect of cleaning up for medial axis algorithm. The medial axis is sensitively affected by the irregularity in the transition surface area from pore to solids and the disconnection of the pore clusters misidentified in segmentation. The left picture is the medial axis from a sub-volume of a Berea Sandstone image with resolution about 4.93 μm; the right is the result after trimming all dead ends. The colours are in rainbow scale reflecting the distance from pore voxels to its nearest grain volxels (http://www.ams.sunysb.edu/~lindquis/3dma/3dma_rock/3dma_rock.html). 25
Figure 2.6: Example of a voxel configuration in basic 2x2x2 voxels. Pore voxels are in the grey hatch area (a) and the related numbering scheme is illustrated in (b). The sequence in the scheme is based on bit positions (Vogel *et al.*, 2010[212]). 29
Figure 2.7: The definition of the shape factor which is the dimensionless parameter for pore network elements (Mason and Morrow, 1991[130]). 30
Figure 2.8: Schematic picture of the length definition for pores (nodes) and throats (bonds) based on their radii and relative locations in the pore space (Dong, 2007[63]). 31
Figure 2.9: The geometry of a cube inclusion (phase 1) in a cubic host (phase 2). 34
Figure 2.10: Cross plot of σ second term versus σ_2 when σ_2 differs only slightly from σ_1. The straight line is Brown's exact expansion to second order in contrast to $(\sigma_2 - \sigma_1)$. 35
Figure 2.11: Porosity exponent simulation results compared with experiment data. 35
Figure 2.12: Example of a 2-D trajectory of a single random walker trial through the pore space in 2D slice. The red square is the starting point and the purple circle is the termination. 36

Figure 2.13: Mean square displacement versus time (b) simulated in a 2D slice for the free space whose porosity is 100% and the porous space of a tube (a), black is pore while white is solid. 37
Figure 2.14: Comparison the porosity exponents calculated by finite difference (FD) and random walk (RW) in eight sub samples of Fb22 sandstones. 38
Figure 2.15: The error of the porosity exponents in three directions for the eight samples of Fb22 sandstone. 38
Figure 2.16: Illustration of the renormalisation approach (Khalili *et al.*, 2012[103]). ... 39
Figure 2.17: Comparison the porosity exponents of Fb22 (480^3) respectively calculated by renormalisation GP and KK methods to finite difference (FD). 40
Figure 2.18: Comparison of Humble and Archie equations. Source: Courtesy of Core Laboratories (Tiab and Donaldson, 1996[195]). 44
Figure 2.19: Genetic classification of porosity type correlated (porosity is black) (Focke and Munn, 1987[74]). 53
Figure 2.20:FF and *m* (a=1) vs.ϕ for intergranular porosity and intercrystalline porosity (Focke and Munn, 1987[74]). 54
Figure 2.21: General downward trend in *m* values with increasing interparticle porosity (Ragland, 2002[161]). 54
Figure 2.22: *m* (a=1) vs. ϕ for moldic limestones with four permeability classes. Perm1<*0.1md*, *0.1md*<Perm2<*1md*, Perm3 is from *1md* to *100md*, Perm4>*100md* (Focke and Munn, 1987[74]). 55
Figure 2.23: FF and *m* (a=1) vs.ϕ for moldic dolomites. Symbols refer to different permeability classes (Focke and Munn, 1987[74]). 55
Figure 2.24: General upward trend in *m* values with increasing moldic porosity. Note that two of the three fractured samples have significantly lower *m* values (Ragland, 2002[161]). 56
Figure 2.25: FF and *m* (a=1) vs.ϕ for rock types with matrix or chalky porosity only. Symbols refer to different wells (Focke and Munn, 1987[74]). 56
Figure 2.26: A downtrend in average *m* as micro porosity increases (from Ragland, 2002[161]). 57
Figure 2.27: Measured values of porosity exponent vs. vug porosity ratio (after Lucia, 1983[121]). 59

Figure 2.28: Measured values of *m* versus vug porosity ratio. Dash lines are regarded as speculative by Focke and Munn (1987[74]). Black continuous solid line is Lucia's best-measured average from Figure 2.27. Black dots represent moldic limestone. 60
Figure 2.29: Serra's (1989[182]) chart for determining porosity exponent as a function of fracture porosity (left, solid line) and as a function of the porosity of non-connected vugs (right, dash line). It assumed m_b was equal to 2.0 and m_f was 1.0.....62
Figure 2.30:Aguilera and Aguilera's (2003[5]) chart for determining porosity exponent as a function of fracture porosity (left, solid line) and as a function of the porosity of non-connected vug (right, dash line). It assumed m_b was equal to 2.0 and m_f was 1.0...63
Figure 2.31: Schematic showing (a) reservoir rock with matrix, fractures (lineaments) and non-connected vugs (black spots), (b) volumetric distribution of matrix, fractured, and non-connected vug porosities, and (c) matrix and fractures in parallel, and the combination of matrix and fractures in series with the non-connected vugs (after Aguilera and Aguilera, 2004[9]) 64
Figure 2.32: A cross plot of the porosity exponent versus total porosity based on triple porosity model assuming the matrix porosity exponent is 2.0 (after Al-Ghamdi *et al.*, 2011b[12]). The definition of the porosity of ϕ_2 and ϕ_{nc} refers to Figure 2.31.....66
Figure 2.33: Capillary tube models. (a) Ideal porous material of n straight cylindrical capillaries. (b) Inclined capillary tube model. (c) Two-size capillary tube model of porous media (Tiab and Donaldson, 1996[195]). 68
Figure 2.34: Pore network model. (a) Pore geometrical model of a porous medium composed of spherical pore nodes connected via cylindrical pore bonds. (b) Cross-section through a unit cube with spherical node and cylindrical bonds for the derivation of the resistance (Abousrafa *et al.*, 2009[1]).....68
Figure 2.35: pore type models from grain packs. (a) Intergranular pore by small-grained packing. (b) Intergranular pore with fracture. (c) Intergranular pore with vuggy porosity. (d) Intergranular pore with moldic porosity. Gray is pore space; white is grain; light gray is moldic porosity; yellow is cement(Mousavi *et al.* (2012[139]).....68
Figure 3.1: Location Map of the São Sebastião Quarry in S. Miguel dos Campos, near Maceio (Alagoas, NE Brasil) (from Câmara *et al.*, 2014[42]).....76
Figure 3.2: Bivalve coquinas from the Morro de Chaves Formation (Sergipe-Alagoas Basin, NE Brazil) in thin section photomicrographs – showing corrosion (a) and moldic porosity (b, same scale as a) in blue (from Corbett *et al.*, 2013a[57]); thin sections cut

vertically (c) and horizontally (d) showing pore scale anisotropy. Views are 2.5 – 5 *mm* across. (Corbett and Borghi, 2013[55]). 76
Figure 3.3: The μ-CT cross sections for Pet1 (a), Pet4 (b) and Pet6 (c). Their resolution is 19.04 μm, 20.44 μm and 19.27 μm respectively. The sizes of the CT images for these three samples are 2240x2240x1411, 1440x1440x1261 and 1968x1968x1975 pixels respectively. 76
Figure 3.4: Function of median filter shown by comparing the original CT image cross section (a) with the filtered CT images (b) and their related binary image in (c) and (d) respectively. 77
Figure 3.5: The segmentation results of Pet1 (a, d, g), Pet4 (b, e, h) and Pet6 (c, f, i) are shown in cross section (a, b, c), 3D cube (d, e, f) and pore space visualization (g, h, i). The 3D cubes (800^3) for these three samples are chosen from their CT images. 77
Figure 3.6: REV analysis by porosity calculation over different centred volumes. 78
Figure 3.7: REV analysis results based on porosity (%) for three carbonate samples, Pet1 (b), Pet4 (c), Pet6 (d) taken sandstone Fb22 (a) as comparison.....79
Figure 3.8: The absolute permeability of 20 sub-samples calculated in three directions and their average permeability versus the size of the sub-samples united by voxels in primary x-axis. The secondary x-axis is the ratio of the image size to the first decay length. When the ratio exceeds three, the absolute permeability keeps stable (Dong, 2007[63]).....81
Figure 3.9: The two-point correlation function correlogram which is the average function in three directions for sandstone Fb22 and carbonates Pet1, Pet4, Pet6. The first decay length for sandstone Fb22 (a) with 5.68 μm resolution is 21 voxels; The first decay length for Pet1 is 192 voxels, the resolution of Pet1 is 19.04037μm (b); The first decay length of Pet4 is 200 voxels, its resolution is 20.44 μm (c) and this length for Pet6 (d) is 155 voxels with 19.27 μm as the resolution. 81
Figure 3.10: The porosity exponents of 15 sub-samples calculated in three directions (x, y, z) and their average (ave) values versus their size united by voxels are in (a) and versus the length of the samples united by the first decay length are in (b). When the ratio reaches about two, the porosity exponents are gradually convergent.....83
Figure 3.11: The relationship between the types of the representative elementary volume (REV) and their size for Pet6. 83
Figure 3.12: The experiment results for Pet1, Pet4 and Pet6. The figure (a) is the cross plot for porosity exponent versus porosity; the relationship between porosity exponent

and permeability is in (b) and the porosity exponents for these three samples from two labs in (c), the black line is 1:1. 85
Figure 3.13: The simulation result from (FD) can match the experimental result for Pet6.....87
Figure 3.14: The simulation results based on random walk for Pet1, Pet4 and Pet6 (SC800) are compared with the experiments (RW-Random Walk). 88
Figure 3.15: The eight Sub REV samples (SC400) distribution in the whole Sup REV sample (SC800) for Pet6. 88
Figure 3.16: The distribution of the three directional porosity exponents for the eight Sub REV samples. The results for these samples (SC300) are shown in blue diamond, the data for the samples (SC400) are expressed by red rectangles and data for SC600 are shown in green symbol. 89
Figure 3.17: The estimation porosity exponents based on a renormalisation method with two calculation algorithms denoted by GP and KK. In (a) the estimation results from eight Sub REV samples (SC300) for each carbonate samples are shown as red triangle and rectangle while the data from the Sub REV samples (SC400) for these carbonates are shown in (b), (C) shows the estimation based on REV samples (SC600). 91
Figure 3.18: The current flow density distribution from a Sub REV sample (SC300) of Pet6. The binary image (a) consists of pore in blue and matrix in red. In the current density distribution, the legend is magnitude of the current density based on logarithm10 scale, the direction of the current flow is in X,Y,Z from (b), (c), (d) respectively, the 2D slice (e, f, g) is a XY plane extracted from Z=150. 92
Figure 3.19: The distribution of the average porosity exponents for sandstone Fb22 (SC240) and carbonates Pet1, Pet4 and Pet6 (SC400).....93
Figure 3.20: The heterogeneity of the porosity and porosity exponent for the sandstone Fb22 (SC240) and carbonates Pet1, Pet4 and Pet6 (SC400). 94
Figure 3.21: The distribution of the porosity exponents in three directions for the eight Sub REV samples (SC400) in Pet1 (b), Pet4 (c) and Pet6 (d). The results of Fb22 (SC240) are used as a comparison in (a). The x, y, z in the legend denotes the porosity exponents in three directions and the x-axis denotes the eight Sub REV samples (SC400) from 1 to 8. 94
Figure 3.22: The distribution of the anisotropic coefficients for the eight Sub REV samples of Fb22 (SC240) and carbonates Pet1, Pet4 and Pet6 (SC400). The x-axis denotes the eight Sub REV samples from 1 to 8.....95

Figure 3.23: The Euler number (in primary axis) and Porosity (%) (secondary axis) versus Min pore radius which is the minimum of the pore sizes (a). The pore space related to the pore size including the Euler number and porosity is shown in the bottom from b to i. 97
Figure 3.24: The porosity versus threshold is shown in (a) and the pore spaces for different thresholds of grey scale are presented from (b) to (g). 98
Figure 3.25: A cross section of Pet6 in grey scale is shown in a colourful image with its colour map on the right. There are three symbols (located by black arrows) in this image. One circular is in a big pore centre which is blue and the rest are located in a green area by triangle showing the irregular pore corners and edges in green colour. ... 99
Figure 3.26: The relationship between the porosity exponents and threshold is shown in (a). The exponents include the exponents in three directions and their average exponent. The Euler number is in (b). The percolation is expressed by a dash segment in orange and the related threshold is 29 in grey scale. When the threshold value is less 29, the pore space generated is firstly not percolated in x direction and then in y direction. ... 100
Figure 3.27: The flow current density in 3D for different thresholds. (a), (e), and (i) are the pore space and its porosities; (b), (f) and (j) are the current density distribution for the current flow in x direction; (c), (g), and (k) are for the current flow in the y direction and the results of the current flow in z direction are in (d), (h) and (l); The legend is the magnitude of the current density on logarithm 10. 101
Figure 3.28: The porosity versus new threshold is shown in (a) and the pore spaces for different new threshold are presented from (b) to (f). 101
Figure 3.29: The relationship between the porosity exponents and new threshold *"NThreshold"* is shown in (a). The porosity exponents include the exponents in three directions and their average exponent. The Euler number is in (b). The percolation is expressed by a dash segment in orange and the related threshold is 76 in grey scale. When the new threshold value is less 76, the generated pore space is percolated until the new threshold *"NThreshold"* >76 103
Figure 3.30: The flow current density in 3D for different thresholds. (a), (e) and (i) are the pore space and the porosities; (b), (f) and (j) are the current density distribution in x direction; (c), (g) and (k) are in the y direction and the density in z direction are in (d), (h) and (l); The legend is the magnitude of the current density on logarithm 10. 104

Figure 3.31: The pore size distribution for Pet1, Pet4, Pet6 (SC800) and Fb22 (SC400). The x-axis is shown in logarithm and y-axis is the percentage (%) of each radius. Fb22 has a much smaller distribution. 106
Figure 3.32: The throat size distribution for Pet1, Pet4, Pet6 (SC800) and Fb22 (SC400). The x-axis is shown in logarithm. 106
Figure 3.33: The throat shape factor distribution for Pet1, Pet4, Pet6 (SC800) and Fb22 (SC400). 107
Figure 3.34: Pore shape factor distribution for Pet1, Pet4, Pet6 (SC800) and Fb22 (SC400). 107
Figure 3.35: The distribution of tortuosity for Pet1, Pet4, Pet6 (SC800) and Fb22 (SC400). 108
Figure 3.36: The coordination number for Pet1, Pet4, Pet6 (SC800) and Fb22 (SC400). 109
Figure 3.37: The coordination number of the pores increases from four to six when the two pores are merged together. 110
Figure 3.38: The binary cross section slice for Pet1 (a) (2240x2240), Pet4 (b) (1440x1440) and Pet6 (c) (1968x1968) from left to right (in Figure 3.3). The pore is black and the void is white. The size of the pore in the same cross section is close for Pet1 and Pet4 while the pore size is various in Pet6 with different size scales. 110
Figure 3.39: The Euler number considering with size of the pore system presented by “Min radius” for Pet1, Pet4, Pet6 (SC800) and Fb22 (SC400) is shown in the figure of (a) and the expanded image for Pet1, Pet4 and Pet6 is in (b). 111
Figure 3.40: The structure of the pore and throats in a pore-throat conjunction point (Chen and Zhang, 1987[46]). 113
Figure 3.41: The porosity exponent distribution for different pore-throat shapes (from Chen and Zhang, 1987[46]). 113
Figure 3.42: The distribution of the PTRR (a) and PTAR (b) for Pet1, Pet4, Pet6 (SC800) and Fb22 (SC400). PTRR is defined as the ratio of the pore radius to the throat radius and PTAR is the cross sectional area ratio of the pore to the throat. 114
Figure 3.43: The simple models for porosity close to 10% with various PTAR (pore–throat cross sectional area ratio) are shown from (c), (d), (e) to (f) as well as from (g), (h), (i) to (j), these models in two sereis respectively from (c), (d), (e) to (f) and from (g), (h), (i) to (j) are the same. The simulated Formation Factors and porosity exponents versus PTAR based on these models are shown in (a) and (b) respectively. 115

Figure 3.44: The workflow for the component labelling. 121
Figure 3.45: 2D illustration for 8- and 4- adjacent pore cluster labelling. The (a) is the original binary image, 1 is object pixel and 0 is the background. In the picture of (b), the sequential number of the objects is related to the scanning process. 122
Figure 3.46: Array LId for pore cluster labelling by 8-adjacent (a) and 4-adjacent (b) of object pixels. The column numbers present the entry of the array LId, which is also the current used labels and the row numbers are the scanned order for each object pixels. 122
Figure 3.47: The process of calculating the total number of the independent pore clusters is shown in this flow chart. *sum* records the total number and the array *Rindex* records the sequential label for each pore cluster in *LId*. 123
Figure 3.48: The labelled image can be renewed according to this process. *lbl* and *Nlbl* are two temporary variations to record the proper label of the pore clusters which are negative in array *LId*. 123
Figure 3.49: Initial labels for the pore cluster labelling 8- and 4- adjacent with 25 pixels in Figure 3.45 scanned. 124
Figure 3.50: The final labels for the pore cluster labelling which are related to the value of *LId*. 124
Figure 3.51: The images with the finally sequential labels for 8-adjacent and 4-adjacent object pixels. 124
Figure 3.52: The histograms of the pore cluster labels for Pet1 (a), Pet4 (b) and Pet6 (c) (SC800) after component labelling algorithm. The relative percentage (shown by logarithm scale) is calculated by the ratio of the number of the pore voxels in this pore cluster to the total number of the pore voxels. In two cases for Pet4 (b) and Pet6 (c), one main cluster has about 70% of the porosity. 125
Figure 3.53: The pore space distribution for the original samples in (b), (f) and (j) for Pet1, Pet4 and Pet6 (SC800), the results after the labelling algorithm are shown in (c), (g) and (k) and the right column including (d), (h) and (l) are the pore space of the remaining labels. (a), (e) and (i) are the binary images in 3D for Pet1, Pet4 and Pet6 from top to bottom, white is solid and the black is void. The relative percentage of the porosity for the main pore cluster from (c), (g) to (k) for Pet1, Pet4 and Pet6 (SC800) are 30%, 75% and 77% respectively. 125
Figure 3.54: The Euler number versus the minimal radius of the pore space for the largest clusters. 126

Figure 3.55: The geometry and topology extracted by pore network method for the largest pore cluster labelled as Pet1_cl2968 (SC800) and the second largest pore cluster labelled as Pet1_cl925 (SC800) in Pet1. 128
Figure 3.56: The simulated porosity exponents based on the Formation Factor (FF) of the largest pore cluster after component labelling algorithm and the total porosity of the whole sample. Now the simulated porosity exponents from random walk can compare well with the experimental data for Pet4 and Pet6 (SC800), not well for Pet1 which will be discussed further in the text. 129
Figure 3.57: The simulated porosity exponents based on the FF and porosity of the largest pore cluster (Pcl1, Pcl4 and Pcl6 (SC800)) for each carbonate sample. Then the simulated porosity exponents from random walk can compare better with the experimental data. 130
Figure 3.58: The random walk simulation based on different input pore spaces. The captions in the legend identify the pore space used for Formation Factor (FF) or the resistivity of the fully brine saturated sample. (a) is for the FF simulated on the whole pore space and the total porosity; (b) is for FF and porosity from the largest pore cluster; (c) is based on FF from the largest pore cluster and the total porosity assuming no contribution of the remaining pore clusters to the resistivity. 133
Figure 3.59: The best simulation of porosity exponent for Pet1, Pet4 and Pet6 (SC800). The porosity exponent for Pet1 is based on the largest pore clusters and the porosity exponent for Pet4 is based on the Formation Factor (FF) from the whole sample and its total porosity and the Pet6 is the same as for Pet4. 134
Figure 3.60: The distribution of the Pet1, Pet4and Pet6 in the dual porosity model (Aguilera and Aguilera, 2003[5]). 135
Figure 3.61: The schematic of the pore throat structure for the three carbonate samples Pet1 (a), Pet4 (b) and Pet6 (c). Red identifies pores and blue is pore throat. 138
Figure 3.62: The pore network for the three carbonate samples Pet1 (a), Pet4 (b) and Pet6 (c) (SC800) and their predominant pore clusters after component labelling process denoted as Pcl1 (d), Pcl4 (e) and Pcl6 (f) (SC800). 139
Figure 4.1: The theoretical model for tube model with consideration of the pore size and length (from Watfa and Nurmi, 1987[216]). 146
Figure 4.2: Pore-throat conjunctions in the pore network (a) and its pore-throat conjunction electrical model (b) considering the size and length of the pore system as well as its equivalent resistance circuit (c). 146

Figure 4.3: The schematic of a simple pore-throat conjunction model, its length is L and its cross section area is A. The length and cross sectional area of the pore space in this cell model are L_w and A_w respectively. 150
Figure 4.4: Porosity exponent versus tortuosity (TT) (a) and porosity exponent versus the logarithm of the cross sectional area ratio (CSAR) (b). 150
Figure 4.5: The equivalent resistance model (c), including two pore channels respecting throat and pore respectively, and circuit (d) for a pore-throat conjunction (a) and (b) with several throats in parallel connected to a pore in series. The cross sectional area of the equivalent throat is the weighted average of the cross sectional area, the weight of each throat is related to the reciprocal of its length. 151
Figure 4.6: Porosity exponent distribution in 2D slices and the axes of each picture respectively reflect the cross sectional area ratio (CSAR) of the two pore channels in the system. The porosity exponent distribution in the two dimensional slice is related to the TT of each channel (TT1 and TT2). 151
Figure 4.7: Porosity exponent versus the logarithm of the relative cross sectional area ratio (RCSAR) for different combinations of the TTs of the two channels in the pore-throat junction with one pore and one throat. 152
Figure 4.8: The schematics for IG, IG+FT, IG+VG including connected vug (CVG) and not connected or isolated vug (IVG) from the aspects of random grain pack (a), (b), (c) and (d), pore trap and channel (e), (f), (g) and (h) as well as simple pore network (PNW), the square is node and the line is bond in (i), (j), (k) and (l). In the random grain pack (top), the white is grain and the black is pore; for the pore trap and channel as well as the simple pore network, the white is void and the blue is the pore space. 153
Figure 4.9: The tubes are used for simulating pore types with different pore sizes and same length from (b) to (e). Their relative porosity exponents versus the logarithm of the pore throat area ratio (PTAR) are shown in (a). 155
Figure 4.10: The current density distribution of the four tubes with logarithm of the current density in the legend shown by a finer colour map. 155
Figure 4.11: The tubes are used for simulating pore types with different pore size and same length (b) to (e). Their relative porosity exponents versus the logarithm of the pore throat area ratio (PTAR) are shown in (a). 156
Figure 4.12: The current density distribution in the four tubes with logarithm of the current density in the legend. 156

Figure 4.13: The models for IG (a), IG+FT (b) and IG+VG (c), (d), (e) with consideration of their porosities and porosity exponents. 157
Figure 4.14: The porosity exponent versus the total porosity against the porosity of the FT and VG in the published work (Aguilera and Aguilera, 2003[5]). In their work, the porosity exponent of the IG is expressed by m_b and the porosity exponent of the FT is m_f. 158
Figure 4.15: Schematic for the models of IG (a), IG+FT (b) and IG+IVG (c). IG+IVG schematic responds to the model for the IG and not connected vug (IVG) in series resistance network in Aguilera and Aguilera (2003[5]). 159
Figure 4.16: The Formation Factor (FF) of the IG, IG+FT and IG+VG models in the published work (Aguilera and Aguilera, 2003[5]). In their work, the porosity exponent of the IG is expressed by m_b and the porosity exponent of the FT is m_f. (b) is the expanded image of (a). 160
Figure 4.17: IG pore space represented by the pore space of the Fontainebleau sandstone Fb13 (SC200) with the porosity as 13%. The pore type in this kind of sandstone is typically IG. 161
Figure 4.18: The process of the FT generation from the random grain pack. (a) is the small-grained packing and (b) is the FT generated by the same pack. Grey is pore space and white is grain (after Mousavi *et al.*, 2012[139]). 162
Figure 4.19: The process of the generation of the CVG (a) and IVG (b). The grains in black and grey are the chosen ones converted into VG with the white being the pore space. The black in the grain totally becomes pore space while the grey part is still as matrix. 162
Figure 4.20: The process of the IG (a), FT (b), CVG (c) and IVG (d) generation from the random grain pack. The black is pore space and white is grain 163
Figure 4.21: The models of IG+FT (c), (e) and (g) are built by combination of the IG (a) and FT (b), (d) and (f). 163
Figure 4.22: The IG+VG models including IG+CVG (c), (e) and IG+IVG (g), (i) are built by combination of the IG (a) and VG with (b), (d) for CVG and (f), (h) for IVG. For these IG+VG models, the VG is small size with numerous amounts. 164
Figure 4.23: The IG+VG models including IG+CVG for (c), (e) and IG+IVG for (g), (i) are built by combination of the IG (a) and VG consisting of CVG (b), (d) and IVG (f), (h). For these IG+VG models, the VG is large size with less numbers. 165

Figure 4.24: The porosity exponent for IG (filled blue diamond), IG+FT (purple cross), IG+CVG (filled makers with dotted maker line), IG+IVG (unfilled makers) for the VG model with small size and numerous numbers shown in (b). The porosity exponent of the IG is m_b=2.16 and the porosity exponent for FT is m_f=1.0 for Aguilera and Aguilera (2003[5]) theoretical model.....166
Figure 4.25: The porosity exponent for IG (filled blue diamond), IG+FT (purple cross), IG+CVG (filled makers with dotted maker line), IG+IVG (unfilled makers) for the VG model with large size and less numbers shown in the top right corner. The porosity exponent of the IG is m_b=2.16 and the porosity exponent for FT is m_f=1.0 for Aguilera and Aguilera (2003[5]) theoretical model.....167
Figure 4.26: Pore trap and channel schematic for IG (a), IG+FT (b), IG+CVG (c) and IG+IVG (d) models.....168
Figure 4.27: The Formation Factor (FF) for the IG (blue filled diamond), IG+FT (purple cross), IG+CVG (filled maker with dotted maker line) and IG+IVG (unfilled maker) models. The VG (b) in this figure is numerous with tiny size. (c) is the expanded of the (f) with consideration the theoretical FF from Aguilera and Aguilera (2003[5]) with m_b=2.16 for IG, m_f=1.0 for FT. The porosity exponent for the same porosity possibilities are in coloured line and dotted line.....169
Figure 4.28: The Formation Factor (FF) for the IG (blue filled diamond), IG+FT (purple cross), IG+CVG (filled maker with dotted maker line) and IG+IVG (unfilled maker) models. The VG (b) in this figure is large size with less number. The (c) is the expanded of the (f) with consideration of the theoretical FF from Aguilera and Aguilera (2003[5]), with m_b=2.16 for IG, m_f=1.0 for FT and the FF for the same porosity possibilities are in coloured line and dotted line.....170
Figure 4.29: The current density distribution for IG (a), (b) and IG+FT (c), (d) in FT percolating directions. The legend is the magnitude by the logarithm of the current density from -13 to -7.....171
Figure 4.30: The current density distribution for IG (a), (b), (c), IG+CVG (d), (e), (f) and IG+IVG (g), (h), (i) for the VG with tiny size and large numbers in three directions. The legend is the magnitude by the logarithm of the current density from -13 to -7. Green circle discussed in text.....171
Figure 4.31: The porosity exponent in three directions (a) and its anisotropy coefficient (b) for IG+FT compared with IG.....173

Figure 4.32: The porosity exponent in three directions (a) and (c), its average (red dotted line)as well as anisotropy(b) and (d) for IG+CVG (a), (b) and IG+IVG(c), (d) for the tiny VG with large numbers. 173
Figure 4.33: The porosity exponent in three directions (a) and (c), its average (red dotted line) as well as anisotropy (b) and (d) for IG+CVG (a),(b) and IG+IVG (c), (d) for the large VG with less numbers. 174
Figure 4.34: The current density distribution for IG (a), (b), (c) and IG+FT (d), (e), (f). 175
Figure 4.35: Pore radius (a) and throat radius (b) for the IG+FT models as well as IG. 177
Figure 4.36: The shape factor of the pore (a) and throat (b) for IG+FT models and IG model. 177
Figure 4.37: The pore throat cross sectional area ratio (PTAR) (a) and tortuosity (b) of the IG+FT models and IG model. 177
Figure 4.38: The coordination number (a) and Euler number (b) of the IG+FT models and IG model. 178
Figure 4.39: The pore network visualization for IG model (a), (e) and IG+FT models (b), (c), (d), (f), (g), (h). 178
Figure 4.40: The radius and shape factor of the pore (a), (c) and throat (b), (d) for IG+CVG models as well as IG model. 179
Figure 4.41: The pore throat cross sectional area ratio (PTAR) (a) and tortuosity (b) of the IG, IG+CVG models. 179
Figure 4.42: The coordination number (a) and Euler number (b) for IG and IG+CVG models with tiny and more numerous CVG. 180
Figure 4.43: The pore network 3D visualization for the IG (a), (d) and IG+CVG (b), (c), (e), (f) models for the tiny CVG with large numbers. 180
Figure 4.44: The radius and shape factor of the pore (a), (c) and throat (b), (d) for IG and IG+CVG models. The CVG is large and less numerous. 181
Figure 4.45: The pore throat cross sectional area ratio (PTAR) (a) and tortuosity (b) of the IG and IG+CVG models for the CVG with large size and less numbers. 182
Figure 4.46: The coordination number (a) and Euler number (b) for IG and IG+CVG models. The CVG is large and less numerous. 182
Figure 4.47: The pore network visualization in 3D for IG (a), (d) and IG+CVG models (b), (c), (e) and (f), the CVG is in large size and less numbers. 183

Figure 4.48: The radius of the pore (a) and throat (b) for the IG and IG+IVG models for the tiny numerous IVG. 184
Figure 4.49: The shape factor of the pore (a), (b) and throat (c) for the IG and IG+IVG models for the tiny numerous IVG. (b) is the expanded image of (a). 184
Figure 4.50: The pore throat cross sectional area ratio (PTAR) (a) and tortuosity (b) of the IG and IG+IVG models for the tiny numerous IVG. 185
Figure 4.51: The coordination number (a), (b) and Euler number (c) of the IG and IG+IVG models for the tiny numerous IVG. (b) is the expanded image of (a). 185
Figure 4.52: The pore network visualization in 3D for IG and IG+IVG models for the tiny numerous IVG. 186
Figure 4.53: The radius of the pore (a) and throat (b) for IG and IG+IVG models for the large less numerous IVG. 187
Figure 4.54: The shape factor of the pore (a) and throat (b) for IG and IG+IVG models for the IVG with large size and less numbers. 187
Figure 4.55: The pore throat cross sectional area ratio (PTAR) (a) and tortuosity (b) of the IG and IG+IVG models for the large IVG with less numbers. 188
Figure 4.56: Schematic pore network for IG (a), IG+IVG (b) and (c) to explain the pore and throat in the same size. 188
Figure 4.57: The coordination number (a), (b) and Euler number (c) of the IG and IG+IVG models for the large IVG with less numbers. The expanded picture for coordination number (a) is in (b). 188
Figure 4.58: The pore network visualization in 3D for IG and IG+IVG models for the IVG with large size and less numbers. 189
Figure 4.59: Schematic for the effect of the IVG on the connectivity of the pore system. 190
Figure 4.60: Schematic for the coordination number of IG+FT (a), (c) and (d) and IG+CVG models (b), (e) and (f). The bottom shows the coordination number of the FT (32) in (c) and (d) and CVG (12) in (e) and (f) with 9 pore bodies. 191
Figure 4.61: The effect of the FT on the GM and TP and then on the FF and porosity exponent. 192
Figure 4.62: The effect of the CVG on the GM and TP and then on the FF and porosity exponent. 193
Figure 4.63: The effect of the IVG on the GM and TP and then on the FF and porosity exponent. 193

Figure 4.64: Schematic distribution of the IG, IG+FT, IG+CVG and IG+IVG in the Formation Factor versus porosity cross plot, (b) is the expanded image of (a). 194
Figure 5.1: The porosity exponent and permeability for three carbonates increase from Pet4, Pet1 to Pet6. Porosity exponent is related to the PTAR and Euler number, the Permeability is related to the radius of the pore and throat. The first row shows the pore in red and throat in blue for them. 201
Figure 5.2: The porosity exponent is mainly affected by PTAR and Euler number as horizontal and vertical axis respectively. The porosity exponent increases along the diagonal direction. For FT+IG model, FT reduces the PTAR and Euler number reducing porosity exponent. For CVG+IG model, CVG mainly increases PTAR with less influence on Euler number resulting in the increase of the porosity exponent. For IVG+IG model, IVG increases the porosity exponent attributing to the increase of Euler number with less effect on PTAR. The increase of porosity exponent from IVG is larger than the increase from CVG. 203
Figure 5.3: The porosity exponent is mainly affected by PTAR and Euler number with less influence from pore size. (a) for FT+IG and CVG+IG, FT decreases the PTAR reducing porosity exponent while CVG introduces larger PTAR increasing porosity exponent. (b) for FT+IG and IVG+IG, FT decreases the Euler number improving the connectivity of the pore space reducing porosity exponent while IVG increases Euler number undermining the connectivity of the pore space and increasing the porosity exponent. 204
Figure A.1: Schematic of the electrical model. In the cylindrical rock sample model, its length is *L* and its cross section area is *A* with the voltage of the electrical circuit is *V*. 207
Figure A.2: Simple models (a), (b), (c), (d), (e) and the simulated tortuosity compared with the geometric results (f). In the top the red is pore and the dot line in the bottom images is 1:1. 211
Figure B.1: Dialogue box for importing 3D volumetric data. 213
Figure B.2: Dialogue box for importing a series of 2D cross section images. 213
Figure B.3: Dialogue box for saving images in the same format. 214
Figure B.4: The cropping area is set by the square with yellow boundary in (a) and (b) is the result after cropping. 214

Figure B.5: The cropped images can be filtered by the median filter just set the radius of the filter. The effect of median filter can be shown in this figure. The noise which is the small points in (a) can be smoothed in (b). 215
Figure B.6: The histogram of the images which can be used to offer threshold. If the threshold is difficult to extract from the histogram, the threshold can be chosen by comparing the difference of segmentation results with variable thresholds by the "Threshold" dialogue in (a) and (b). (c) is the binary image from auto threshold by the "Auto" function. 215
Figure C.1: Clusters are defined to merge the spheres with the same size in the pore space (Al-Khrausi and Blunt, 2007[13]). 218
Figure C.2: Example of a digital sphere with $R_2=6$ (a) and $R_2=8$ (b) voxel units (Dong, 2007[63]). 219
Figure C.3: The representation of digital balls with different radius by discrete voxels: (a) R=1;(b)R= $\sqrt{3}$;(c)R= $\sqrt{13}$ (Silin *et al.*, 2003[189]). 220
Figure C.4: This is a schematic figure of a single cluster. The white ball is the principal ball which is the parent and its children is the smaller balls surrounded in a range of $2R$, ($R>R_1>R_2>R_3>R_4$). The children are defined by the smaller pores overlapping or touching the parent ball and the generation number of the children will be 1 greater than their parent (Dong, 2007[63]). 220
Figure C.5: Single clusters extend their family trees by absorbing their related new generations for the ancestor, and its offspring to generate multi-clusters. Generation number, family name and parent's name are recorded to keep the connection of the family tree from top to bottom and converse. When throat is distinguished as a common child of different families, MB chains are formed in white arrows and two pore-throat structures are built (Dong, 2007[63]). 221
Figure C.6: Three kinds of directional lines based on central cell are used in inflating step to find the nearest solid surface. The left picture shows 6 lateral directions with 1 voxel length for each step. The middle figure is 12 diagonal lines and each step is $\sqrt{2}$ voxel length. The right one defines the 8 diametrical direction lines and the length of each step is $\sqrt{3}$ voxel (Dong, 2007[63]). 222
Figure C.7: Pore-throat chains merged in one channel (Dong, 2007[63]). 224
Figure D.1: The direct neighbourhoods $N(p)$ of a point p. (a) and (b) show different representations of the 2D direct (3×3) neighbourhoods, where

$N(p)=\{q_1,q_2,q_3,q_4,p,q_5,q_6,q_7,q_8\}$; (c) and (d) show two different representation of the 3D direct $(3\times3\times3)$ neighbourhood, where $N(p)=\{q_1,q_2,\cdots,q_{13},p,q_{14},q_{15},\cdots,q_{26},\}$ (Jiang, 2008[92]).....229
Figure D.2: Examples of paths, curves and components. (a) a path $\{1,2,\cdots,9,2,10\}$ intersect itself;(b) a path $\{1,2,\cdots,10\}$ touches itself; (c) the set of grey pixels can be organized as a closed 8-curve, but not as a 4-curve; (d) the set of grey voxels is a 26-path, but not a 26-curve because voxel p has three 26-adjacent grey voxels. The set of grey pixels in (c) is an 8-component but not 4-component, and the set of grey pixels in (d) is a 26-component but not a 18- or a 6-component. Note that in (a)~(d) all white (background) voxels are invisible for clarity. In (e) an example is shown of 4 26-components in 3D (Jiang, 2008[92]).....230
Figure E.1: The dimensionless shape factor for network pores and throats (Mason and Morrow, 1991[130]).....232
Figure E.2: The inscribed circle with radius r in an arbitrary triangle with three angles as 2α, 2β and 2γ.....233
Figure E.3: The inscribed circle with radius r in a rectangular cross section.....234
Figure F.1: Actual current flow path with its length L_w and cross sectional area A_w compared with the length L and the cross sectional area A of the pore-throat conjunction.....237
Figure F.2: The model for pore-throat conjunction with the throats in parallel and then connected to the pore in series. The size and the length of the throat are expressed by A_{twi} and L_{twi} and A_{pw}, L_{pw} are for pore with the length and the cross section area of this conjunction as L and A.....238

Lists of Table

Table 2.1: Coefficients and exponents used to calculate Formation Factor (FF) as a function of porosity(ϕ)(adopted after Mabrouk and Soliman, 2014[126]). 45
Table 2.2: Factors affecting the Formation Factor (FF) parameters (*a* and *m*) (adopted after Ransom, 1974[165]). 46
Table 2.3: Ranges for the porosity exponent *m* (Kadhim *et al.*, 2013[97]). 48
Table 2.4: Trends in porosity exponent *m* values for basic pore types and modified pore systems (Ragland, 2002[161]). 58
Table 3.1: The porosity of the three carbonates measured with different methods (Câmara *et al.*, 2014[42]). 84
Table 3.2: The geometrical properties for Pet1, Pet4 and Pet6 (SC800) before component labelling. 126
Table 3.3: The geometrical properties for Pcl1, Pcl4 and Pcl6 (SC800) after component labelling. 126
Table 3.4: Total porosity, the porosity of the largest pore cluster and the porosity of the rest pores for Pet1, Pet4 and Pet6 (SC800). 134
Table 5.1: The porosity exponent and permeability for three carbonates increase from Pet4, Pet1 to Pet6. Porosity exponent is related to the PTAR and Euler number, the Permeability is related to the radius of the pore and throat. The first row shows the pore in red and throat in blue for them. 201

NOMENCLATURE

a	Lithology factor or tortuosity factor;
a_v	Connectivity of the pore type;
A_w	Cross sectional area occupied by the wet phase;
b	Saturation factor;
D_{bulk}	Diffusion coefficient;
D_{free}	Diffusion coefficient in free space (Porosity=100%);
D_{porous}	Diffusion coefficient in porous medium;
E	Electric field;
$g2$	Two point correlation function;
g_e	Effective conductance;
G	Shape Factor;
I	Electrical current;
L	Segment length;
m	Porosity exponent
m_b	Porosity exponent for interparticle pore type;
m_f	Porosity exponent for fracture;
m_{ip}	Porosity exponent for Intergranular Pore;
n	Saturation exponent;
N_{node}	Number of nodes with at least one connected bond;
N_{bond}	Number of bonds;
P	Perimeter;
R_0	Resistivity of the brine fully saturated rock;
R_2	Resistivity of the fracture;
R_h	Resistivity parallel to the bedding planes;
R_{max}	Maximum of the porosity exponents in three directions;

R_{matrix} Resistivity of the matrix (interparticle pore);

$R_{\min}$ Minimum of the porosity exponents in three directions;

R_{nc} Resistivity of the not connected vug;

R_{par} Resistivity for the components in parallel;

R_t Resistivity of the partially brine saturated rock;

R_{tri} Resistivity for triple porosity model;

R_v Resistivity normal to the bedding planes;

R_w Resistivity of the brine;

S_w Saturation of the brine;

t Random walk time;

U Electrical potential;

V Volume;

Z Phase function;

GREEK SYMBOLS USED

ϕ Porosity;

ϕ_b Porosity of the bulk rock;

ϕ_m Porosity of matrix (interparticle pore)

ϕ_{nc} Porosity of the not connected vug;

τ Tortuosity;

σ Conductivity;

σ_w Conductivity of bulk water;

σ_{fluid} Conductivity of the brine;

σ_{rock} Conductivity of the rock fully saturated by brine;

φ Electrostatic potential;

$\mu\phi$ Micro pores;

λ_e Electric anisotropy coefficient;

χ Euler number;

ψ Cross sectional area ratio;

ψ_r Relative cross sectional area ratio;

δr Displacement length for each step;

δt Duration time for each step;

SUBSCRIPTS

0 Rock fully saturated by brine;

2 Fracture;

a Arithmetic average;

b Matrix (interparticle) pore;

eff Effective properties;

f Fracture

h Harmonic average;

i Sub sample numbers;

ip Intergranular pore;

nc Not connected vug;

par Parallel;

t Total;

tri Triple;

v Vug;

w Fluid;

x X direction;

y Y direction;

z Z direction;

ABBREVIATIONS

2D Two dimensions;

3D Three dimensions;

ave Average;

CSAR Cross sectional area ratio;

CT Computed/computerized tomography;

CVG Connected vug;

DC Direct current;

Fbϕ Fontainebleau sandstone sample porosity ϕ (eg. Fb22=22%).

FD Finite difference method;

FEM Finite element method;

FF Formation Factor;

FT Fracture;

GM	Geometry/Geometrical properties;
IC	Intercrystalline pore;
IG	Intergranular pore
IVG	Not connected vug /isolated vug;
PNW	Pore network;
PTRR	Pore throat cross sectional radius ratio;
PTAR	Pore throat cross sectional area ratio;
RCSAR	Relative cross sectional area ratio;
REV	Representative elementary volume;
RI	Resistivity index;
RW	Random walk simulation;
$SCnum$	Number of voxels in each direction of the cube sample is *num*;
TP	Topology/Topological properties;
TT	Tortuosity;
TTp	Ratio of the pore length to the length of the two pore centres;
TTt	Ratio of the throat length to the length of the two pore centres;
$\mu - CT$	Micro CT;
VG	Vug;
$x - CT$	X-ray computed/computerized tomography;

PUBLICATIONS:

Wang, H. and Corbett, P., 2015: "*Archie's Porosity Exponent: REV, Heterogeneity and Anisotropy in a Coquina Carbonate"*. presented at 77th EAGE Conference and Exhibition, Madrid, Spain, 1-4 June. EAGE. p. 1-5.

Chapter 1

Introduction

Fluid flows through porous media and the macroscopic properties such as thermal, electrical and acoustic are largely controlled by the structure of the pore system. The pore structure is described by its geometry and topology. Discovering accurate relationships between pore structure and these macroscopic properties of porous media is a fundamental problem of long-standing interest in range of disciplines and of significant commercial importance. The major theme in this study is to determine the key geometrical (GM) and topological (TP) parameters and pore types, which affect the pore geometry and topology, and then to investigate these parameters and pore types effect on electrical properties in carbonates due to their significant reserves in hydrocarbon. This in turn will enable researchers to develop accurate relationships to predict and correlate electrical properties for carbonates. In recent years, high resolution computed tomography (CT) imaging, pore scale measurement, can provide high quality 3D images for pore space reconstruction, the pore geometry (GM) and topology (TP) can be extracted from the binary images of the reconstructed pore space to determine the key geometrical and topological parameters and pore types. The resistivity can be simulated based on these same binary images, the simulation results compare with the experimental results to reflect the applicability of the existing electrical simulation methods for carbonates. The validated electrical simulation methods and pore scale modelling methods are used to investigate the effect of pore geometry (GM) and topology (TP) and pore types on the electrical properties in carbonates. The pore scale modelling methods are used to represent pore types in the carbonates such as intergranular (IG), fracture like (FT) and vug (VG) pore. These investigations involve the hydrocarbon calculation from resistivity, carbonates, pore space reconstruction, image processing, pore space characterization, resistivity simulation and pore scale modelling.

1.1 Background

Carbonate reservoirs distribute widely in the world and offer about half of the world oil and gas reserves. In carbonate reservoirs, resistivity measurements are fundamental to calculate hydrocarbon in place by determining fluid saturation. The correlation between resistivity measurements and the fluid saturation is log interpretation model.

The conventional log interpretation model is Archie's Law, it includes two Archie's equations (Archie, 1942[15]; Schlumberger, 1987[176]) which break down in

carbonates with complex pore structure (Dixon *et al.*, 1990[61]). These two equations are developed several decades ago for simple petrophysical case. Archie's equations assume that single rock type, homogeneous, isotropic, single pore size, compositionally clean, intergranular (IG) porosity, water wet and $S_w > 15\%$. They are written as:

$$FF = \frac{R_0}{R_w} = \frac{a}{\phi^m} \tag{1.1}$$

and

$$RI = \frac{R_t}{R_0} = \frac{b}{S_w^n} \tag{1.2}$$

The formation factor FF in Archie's First Equation (1.1) is defined as the ratio of the brine fully saturated rock resistivity R_0 to the resistivity of the brine R_w. The resistivity index RI is the ratio of the resistivity of partially brine saturated rock R_t to R_0. m and n are the porosity and saturation exponents and a and b are empirical constants. Conventionally, values are assumed to be $m = n = 2$ and $a = b = 1$. In carbonates, the "Archie constants" are not constant.

The impact of these four Archie parameters to the reservoir saturation has been measured. The impact of m and n to the reservoir saturation have been found to be stronger than the influence of a and b on the reservoir saturation (Gomez-Rivero, 1976[79]; Rasmus, 1983[166]; Sherman, 1983[186]; Borai, 1987[36]; Focke and Munn, 1987[74]; Yuan, 1991[227]; Salem, 1993[171]; Unalmiser and Bova, 1993[203]; Tabibi and Emadi, 2003[193]; Knackstedt *et al.*, 2007[105]; Kurniawan and Bassiouni, 2007[110]; Haghighi *et al.*, 2008[82]; Al-Ghamdi *et al.*, 2011a[11] and 2011b[12]). According to the physical meaning of m and n, they are two independent parameters and there is no connection between them. Based on the Archie equations, the effect of variables m and n on the reservoir saturation is analysed. With the same error in m and n, m has a great effect on the calculation of S_w especially in complex reservoirs including low porosity and low resistivity. Within each lithology, the distribution range and change amplitude of m are both greater than those of n, and the influence of m on the calculation of S_w is stronger than that of n. It is concluded that compared with n, m should be more accurately calculated and a high precision m model should be established (Li *et al.*, 2013[113]).

Porosity exponent m may be the first issue that comes into mind in reservoir evaluation. For well-sorted clean sandstones, the porosity exponent m is generally 2 in resistivity well logging interpretation (Archie, 1942[15]; Sen *et al.*, 1997[180]). For

carbonate rocks with complex texture and pore systems, this value varies widely (Archie, 1942[15]; Lucia, 1983[121]; Focke and Munn, 1987[74]). Focke and Munn (1987[74]) have measured values from 1.5 to 5.4 for carbonate samples from Middle Eastern reservoirs. They showed that hydrocarbon saturation decreased from 80% to zero when m changed from 2 to 3 and 4. However, Rajan and Delaney (1991[162]) reported reserve increase in carbonates of Fateh and Dubai (Thamama Formation) with improved estimation of porosity exponent m, saturation exponent n, and water resistivity. Walsh *et al.* (1994[213]) showed that a commercial hydrocarbon productive zone could be missed using $m = 2$. In brief, it is well understood that m values for carbonate samples are location dependent and these values are often representative for specific rock types. From one perspective the porosity exponent can be said to often represent the essence of carbonate petrophysics (Ballay, 2012[27]). The essence of carbonate petrophysics is pore system heterogeneity, as compared to clastics. It is necessary to first consider in carbonate rocks.

In carbonates, the prediction of accurate porosity exponent is rather challenging based on two aspects. One aspect is that discovery of the accurate relationship between pore structure and macroscopic properties of porous media is a long-standing problem (Arns, 2002[19]). The other aspect lies in the various pore structures and pore types, causing the difficulty in predicting accurate porosity exponent, due to the heterogeneity and anisotropy of the carbonates (Bakke *et al.*, 2007[26]). The pore types are described by the pore classification in the carbonates, Petrographers and petroleum geologists prefer to use the porosity classification of Choquette and Pray (1970[47]), which links sedimentological fabrics and pore types on the basis of depositional settings or diagenetic evolution. Petrophysicsts and reservoirs engineering prefer the classification of Archie (1952[17]) and Lucia (1983[121], 1995[122], 2007[124]) because they link pore classification to pore geometries and flow properties as does (Lønøy, 2006[119]).

The existing porosity exponent descriptions in carbonates are based on evaluating the source of resistivity behaviour-porosity (Sen *et al.*, 1997[180]; Kazatchenko and Mousatov, 2002[100]). These descriptions can be classified into two classes. The first class of methods are trying to modify the Archie's First Equation (1.1) to represent the porosity exponent as a function of total porosity (Kazatchenko and Mousatov, 2002[100]). In the alternative methods, the resistivity considering pore geometry and pore types are presented by porosity models (Watfa and Nurmi, 1987[216]; Serra, 1989[182]; Kazatchenko and Mousatov, 2002[100]; Aguilera and Aguilera, 2003[5]). In

the porosity models, the pore types are regarded as equivalent resistance networks. However, these models either ignore pore structure details or use simplified representation of pore structure to evaluate porosity exponent (Arns, 2002[19]). The accurate prediction of porosity exponent should be related to the pore structure in carbonates. The importance of the pore structure in transport properties has been pointed out by several researchers (Sheppard *et al.*, 1999[185]; Vogel, 2000[209]; Blunt, 2001[33]; Øren and Bakke, 2003[146]; Lindquist, 2006[116];).

In order to relate the porosity exponent to the pore structure, it is necessary to firstly determine the key geometrical and topological parameters and pore types affecting porosity exponent and secondly to investigate the effect of these parameters and pore types on the porosity exponent based on pore scale modelling in carbonates. Conversely, this enables researchers to develop accurate models to predict and correlate electrical properties for carbonates. The pore geometry is the spatial features including pore size, pore shape, area, volume and physical location and the pore topology is the reflection of the pore connectivity (Ohser *et al.*, 2002[143]; Vogel, 2002[210] Levitz, 2007[112]). Pore connectivity includes coordination number-the number of pore throat (bond) connected to a pore body (node), specific Euler number which is used as a characteristic describing the connectivity of the components of a composite material or of the pore space of a porous medium. Both of them can be calculated from the pore space representation in 3D (Lindquist and Venkatarangan, 1999 [115]; Ioannidis and Chatzis, 2000[89]; Lindquist *et al.*, 2000[118]; Sok *et al.*, 2002[190]; Prodanović *et al.*, 2007[158]; Jiang, 2008[92]; Vogel *et al.*, 2010[212]).

3D pore space can be represented by direct computed tomography (CT) imaging (Dunsmuir *et al.*, 1991[67]; Coles *et al.*, 1994[53]; Spanne *et al.*, 1994[192]; Hazlett, 1995[85]; Coker *et al.*, 1996[51]; Coles *et al.*, 1996[52]) of core samples or by numerical reconstructions from 2D thin sections (Joshi, 1974[96]; Quiblier, 1984[160]; Adler *et al.*, 1990[3], Adler, 1992[4]; Hazlett, 1997[86]; Roberts, 1997[169]; Yeong and Torquato, 1998a[225] and 1998b[226]; Manwart and Hilfer, 1999[128]; Okabe and Blunt, 2004[144]; Wu *et al.*, 2006[221]) or from process-based methods simulating particle sedimentation process (Bakke and Øren, 1997[25]; Øren and Bakke, 2002[145]; Thane, 2006[194]; Mousavi and Bryant, 2007[136]; Mousavi, 2010[135]; Mousavi and Bryant, 2012[137] and 2013[138]). However, recent quantitative comparisons of these models with tomographic images of sedimentary rocks have shown that numerical reconstructions may differ significantly from the original sample in their geometrical

connectivity (Hazlett, 1997[86]; Manwart *et al.*, 2000[129]; Øren and Bakke, 2003[146]).

The accurate geometrical and topological parameters and pore types can be determined from the 3D CT images, these CT images convert into binary images (Dong, 2007[63]; Jiang, 2008[92]) due to the requirement of calculating geometry and topology (Vogel, 2002[210]; Jiang, 2008[92]; Vogel *et al.*, 2010[212]) and simulating resistivity (Auzerais *et al.*, 1996[24]; Øren and Bakke, 2002[145]; Arns *et al.*, 2005a[18]; Øren *et al.*, 2007[148]; Han *et al.*, 2009[83]; Nakashima and Nakano, 2011[141]), which are discretized voxel representation of the pore system. However, the reconstruction, visualization, analysis and numerical simulation of such 3D binary images are limited in computer terms. Thus, it is not always possible to reconstruct the images with the total size of the tomography sample, the representative elementary volume (REV) should be determined, which has to be large enough to represent the characteristics of the sample and as small as possible compared with its total volume (Corbett *et al.*, 1999[54]; Vik *et al.*, 2013[206]; Corbett *et al.*, 2014[56]), this is REV analysis.

Based on the representative sample, the geometrical (GM) and topological (TP) characterization of the 3D pore space can be broadly categorised into two classes: image-based methods (Vogel, 2002[210]) and pore network (PNW) analysis (Lindquist and Venkatarangan, 1999 [115]; Ioannidis and Chatzis, 2000[89]; Lindquist *et al.*, 2000[118]; Sok *et al.*, 2002[190]; Prodanović *et al.*, 2007[158]; Jiang, 2008[92]). Minkowski Functions, which have been introduced by Mecke (2000[133]) and applied to porous media by Vogel (2002[210]), are basic geometric measures defined for binary images. In three dimensions (3D), Minkowski Functions provide volume, surface area, curvature and Euler number (Vogel, 2002[210]; Vogel *et al.*, 2010[212]). However, Minkowski Functions are not sufficient to characterize pore geometry (Jiang *et al.*, 2011[93]), these geometrical properties can be easily obtained from PNW which is a topologically and geometrically equivalent network of pore bodies interconnected by pore throats (Fatt, 1956[71]; Kantzas *et al.*, 1988[98]; Øren *et al.*, 1992[149] and 1994[150]; Blunt *et al.*, 1995[32]; McDougall and Sorbie, 1995[132]; van Dijke and Sorbie, 2002[204]).

The pore network can be extracted from the binary images of the pore space in 3D, the extraction methods include Voronoi methods (Bryant and Blunt, 1992[40]; Bryant *et al.*, 1993[41]; Øren *et al.*, 1998[147]; Øren and Bakke, 2002[145] and 2003[146]), medial axis methods (Lindquist *et al.*, 1996[117]; Lindquist and Venkatarangan,

1999[115]; Sheppard *et al.*, 2005[184]; Shin *et al.*, 2005[187]; Prodanović *et al.*, 2006[157]; Jiang, 2008[92]) and maximal ball (MB) methods (Silin *et al.*, 2003[189]; Silin and Patzek, 2006[188]; Al-Kharusi and Blunt, 2007[13]; Dong, 2007[63]). However, the application of the Voronoi methods is limited in complex pore systems and there are problems of identifying pores and throats for medial axis methods (Dong, 2007[63]; Blunt *et al*., 2013[34]), maximal ball based (MB) method (Dong, 2007[63]) extracts the pore network of the carbonates with priority in accurately predicting the location and size of the pore and throat. Based on PNW, many geometrical (GM) and topological (TP) properties such as coordination number, Euler number, size of pore and throat, shape factors of pore and throat are extracted (Lindquist and Venkatarangan, 1999 [115]; Ioannidis and Chatzis, 2000[89]; Lindquist *et al.*, 2000[118]; Sok *et al.*, 2002[190]; Dong, 2007[63]; Prodanović *et al.*, 2007[158]; Jiang, 2008[92]). The key geometrical parameter affecting porosity exponent is the difference between pore and throat investigated by Etris *et al.* (1989[70]), Ehrlich *et al.* (1991[68]) and Verwer *et al.* (2011[205]), its effect on the porosity exponent is illustrated by pore-throat conjunction model (Chen and Zhang, 1987[46]) consisting of a pore node and several pore bonds connecting to this pore node. The topological parameter affecting porosity exponent is Euler number with seldom investigation before.

Due to the non-destructive technique of the $x-CT$ imaging and resistivity measurements, the core plug scanned by CT can be used to implement resistivity measurements in the lab to calculate porosity exponents and vice versa. The experimental porosity exponents can be used to validate the existing resistivity simulation methods (Johnson *et al.*, 1986[95]; Schwartz and Banavar, 1989[177]; Garboczi and Day, 1995[76]; Arns *et al.*, 2002[21]; Bohn and Garboczi, 2003[35]; Øren *et al.*, 2007[148]; Toumelin and Torres-Verdín, 2008[199]; Han *et al.*, 2009[83]; Nakashima and Nakano, 2011[141]; Khalili *et al.* (2012[103]) by comparing to the simulated porosity exponents based on REV sample. These resistivity simulation methods include finite difference method (FD) (Garboczi and Day, 1995[76]; Arns *et al.*, 2002[21]; Bohn and Garboczi, 2003[35]), random walk simulation (RW) (Toumelin and Torres-Verdín, 2008[199]; Han *et al.*, 2009[83]) and a renormalization method (Nakashima and Nakano, 2011[141]; Khalili *et al.* (2012[103]). FD calculates the resistivity by directly solving Laplace equation. However, the time consumption is huge and the calculation for large sample is a challenge in terms of computer (Han *et al.*, 2009[83]; Nakashima and Nakano, 2011[141]), RW is an efficient method to estimate

the resistivity by calculating the average geometry tortuosity analogous to the electrical path with less consumption of time and memory in computer. For the large sample with calculation beyond the capacity of the computer, an upscale method can estimate the resistivity of this large sample based on the resistivity of its sub-samples while the resistivity of the sub-samples can be simulated by FD or RW (Nakashima and Nakano, 2011[141]; Khalili *et al.* (2012[103]), this method is a renormalisation method. The feasibility of these three methods can be proved by comparing the simulation results to the experimental data. With consideration of the size of the representative samples and consumption of time and memory, RW is used to estimate the porosity exponent for REV samples while FD is applied in calculating the porosity exponent for sub-REV samples, renormalisation is imporved feasible for further application without direct use in this thesis.

These simulation methods can be used to investigate the heterogeneity and anisotropy of carbonates and the effect of the REV on the porosity exponent by the simulated porosity exponents and REV samples. Meanwhile, the simulated porosity exponent can be used to investigate the effect of image segmentation and pore space on the porosity exponent with consideration of the topology of samples. These investigations offer better understanding of the contribution of the different parts of the pore space to current flow.

Additionally, the experimental porosity exponents can be used to determine the key pore type in each sample by their distribution in the cross plot of porosity exponent versus porosity from dual porosity model (Aguilera and Aguilera, 2003[5]), the key pore type can also be determined by investigating the effect of pore clusters on the resistivity (Nakashima and Kamiya, 2007[140]). Nakashima and Kamiya (2007[140]) presented that pore clusters affected the formation factor (FF) with the resistivity simulated by RW in their investigation. The pore clusters can be extracted from the binary images in 3D by different algorithms (Park and Rosenfeld, 1971[152]; Hoshen and Kopelman, 1976[88]; Jiang, 2008[92]).

The key parameters of pore geometry and topology as well as key pore types can be determined based on the pore scale measurement-CT imaging, their effect on the porosity exponent can be investigated by pore scale modelling (Fatt, 1956[71]; Watfa and Nurmi, 1987[216]; Etris *et al.*, 1989[70]; Ehrlich *et al.*, 1991[68]; Dullien, 1992[66]; Abousrafa *et al.*, 2009[1]; Mousavi *et al.*, 2012[139]). In the pore scale models, the pore space can be simulated by capillary tubes (Fatt, 1956[71]; Dullien,

1992[66]), pore network (Watfa and Nurmi, 1987[216]; Etris *et al.*, 1989[70]; Ehrlich *et al.*, 1991[68]; Abousrafa *et al*., 2009[1]) and grain packs from process-based methods (Mousavi and Bryant, 2007[136]; Mousavi, 2010[135]; Mousavi and Bryant, 2012[137]; Mousavi *et al.*, 2012[139]; Mousavi and Bryant, 2013[138]). Capillary tube models treat the pore space as a complex bundle of capillary tubes (Fatt, 1956[71]; Dullien, 1992[66]), the capillary tubes are easy to simulate pore types with various porosity exponents and to investigate various arrangements of pore types such as in parallel or in series or both. Thus pore scale models based on capillary tubes are used to validate the porosity exponents from dual porosity exponent (Aguilera and Aguilera, 2003[5]) and to investigate the pore types effect on the porosity exponent. Additionally, mathematical derivation of the electric flow equations is simple due to the simplicity of the pore structure.

However, capillary tubes are a restrictive simplification of the pore network and absence of the connectivity (Abousrafa *et al*., 2009[1]), a more realistic system is used to represent the pore space, in this system, the pore bodies are connected by pore throats (Watfa and Nurmi, 1987[216]; Etris *et al.*, 1989[70]; Ehrlich *et al.*, 1991[68]; Abousrafa *et al*., 2009[1]), this pore network model can be used to derive the theoretical resistivity equations considering the pore geometry and topology. Theoretical analysis of pore size and length effect on porosity exponent is based on pore-throat conjunction, which is simulated by pore network model. In this process, the resistance is calculated by Ohm's law and the assumption is that in the equivalent resistance model, the pore bonds are in parallel and are connected to the pore node in series. Compared with models of Watfa and Nurmi (1987[216]) and Abousrafa *et al*. (2009[1]), this model is improved in the aspects of the coordination number, the number of throats connected to the same node, and the length of the bond, both of them are various.

However, the capillary and pore network models are too simple to reflect the real characteristics of the intergranular pore (IG), fracture like pore (FT), vug pore (VG) and the connectivity of the pore space (Mousavi *et al.*, 2012[139]), the voxel representation of the pore space based on grain packs can represent the characteristics of the pore types and pore connectivity. The IG is simulated by the Fontainebleau sandstone with porosity close to 13%, which is a classic intergranular pore (IG) (Arns, 2002[19]), the FT and VG are based on the models of Mousavi *et al.*, 2012[139]. These models can be used to study the effect of pore types on porosity exponent. The effect of the pore types

on pore geometry and topology, formation factor as well as anisotropy is also investigated, which is less investigated before.

In the pore scale modelling, the voxel representation of the pore space by capillary tubes and models from grain packs can be used to simulate resistivity by the existing simulation methods. The resistivity is simulated by FD based on the voxel representation of the pore scale models, which is binary, pore space and solid. FD is efficient in sub-samples and offers the current density distribution (Garboczi and Day, 1995[76]; Garboczi, 1998[77]) which is helpful to explain the contribution of pore types to the electrical current flow. The pore scale models for intergranular and fracture (IG+FT) and intergranular and vug (IG+VG) are both built by taking IG as host medium inserted by FT or VG. This method is applied to the capillary tube models and models based on grain packs from process-based methods.

These investigations are the preliminary work, which is necessary and fundamental, to predict accurate porosity exponent. The aspects involved in these investigations and the main work flow are shown in Figure 1.1.

1.2 Challenges

The understanding of petrophysical and transport properties is essential for the assessment and exploitation of hydrocarbon reserves; these properties in turn depend on the 3D geometry and connectivity (topology) of the pore space. The determination of the pore size distribution in carbonate rocks remains challenging; extreme variability in carbonate depositional environments and susceptibility to a range of post-depositional process results in complex pore structures comprising length scales from tens of nanometres to several centimetres. To increase understanding of the role of pore structure on connectivity, resistivity, permeability, and hydrocarbon recoveries one to probe the pore scale structures in carbonates in a continuous range across over seven decades of length scales (from 10 nm to 10 cm) (Sok *et al.*, 2010[191]). These pore scale structures can reflect by 3D $\mu - CT$ at different resolutions and then the GM and TP of these structures can be obtained from pore space analysis. So CT images can be regarded as input data for resistivity simulation and the simulation results can be calibrated with the experimental data from the same rock sample, because CT imaging technique and resistivity measurements in laboratory are both non-destructive for rock cores. The only problem of the CT imaging is the trade-off between image resolution and image size. For this problem, the electrical experiments could be helpful.

The GM and TP as well as simulation results are from CT images. Hence, measurements and calculation require a complete three dimensional of the pore space or at least a representative elementary volume (REV). This can be achieved for simple isotropic media as sandstones where a few cubic millimetres may be sufficient to fully characterize the porous structure. In more heterogeneous porous media where the pore space is extremely anisotropic, a representative three dimensional sample is extremely expensive.

In this thesis, local porosity distribution and two-point correlation function in CT images for sandstones and carbonates have been applied to get a representative elementary volume (REV) respectively. Resistivity simulation and pore space analysis have been done on these representative elementary volumes.

1.3 Motivation and Objective

Carbonate reservoirs contain approximately half of the world's hydrocarbon resources. Accurate porosity exponent can improve the accuracy of the well logging interpretation, effectively distinguishing the oil reservoir and then raising profit for the oil company.

Hydrocarbon calculation depends on Archie's Equation (1.1) and Equation (1.2) relating resistivity to hydrocarbon saturation, the parameters in Archie's Equations (1.1) and (1.2) for carbonates are not constant. In order to get accurate hydrocarbon saturation, accurate Archie parameters for a specific carbonate rock based on numerical simulation and the properties of GM and TP are required.

The objective of this thesis is two-fold: (1) to improve the accuracy of porosity exponent prediction for carbonates considering simulation results and GM and TP of the pore space analysis from 3D images; (2) to describe the impact of anisotropy on porosity exponent simulation in three directions for carbonates, which is helpful for vertical and horizontal well logging interpretation. This objective is achieved through the following steps:

- Intensive study of the accuracy of resistivity numerical simulation methods by introducing error analysis, comparing each other's simulation results and comparing to theoretical and empirical results.
- Analysis of different pore types impact on GM and TP and then on the FF and porosity exponent (m) using pore scale modelling to reveal the pore types effect on the porosity exponent as well as its anisotropy.

- Extraction of pore geometrical and topological properties using pore network based method and Minkowski Functions.
- Validation of the correctness of the resistivity simulation methods by comparing the simulation results with experiment data based on 3D CT images.
- Interpretation of these results of the simulation and experiment porosity exponent considering pore geometry and topology properties.

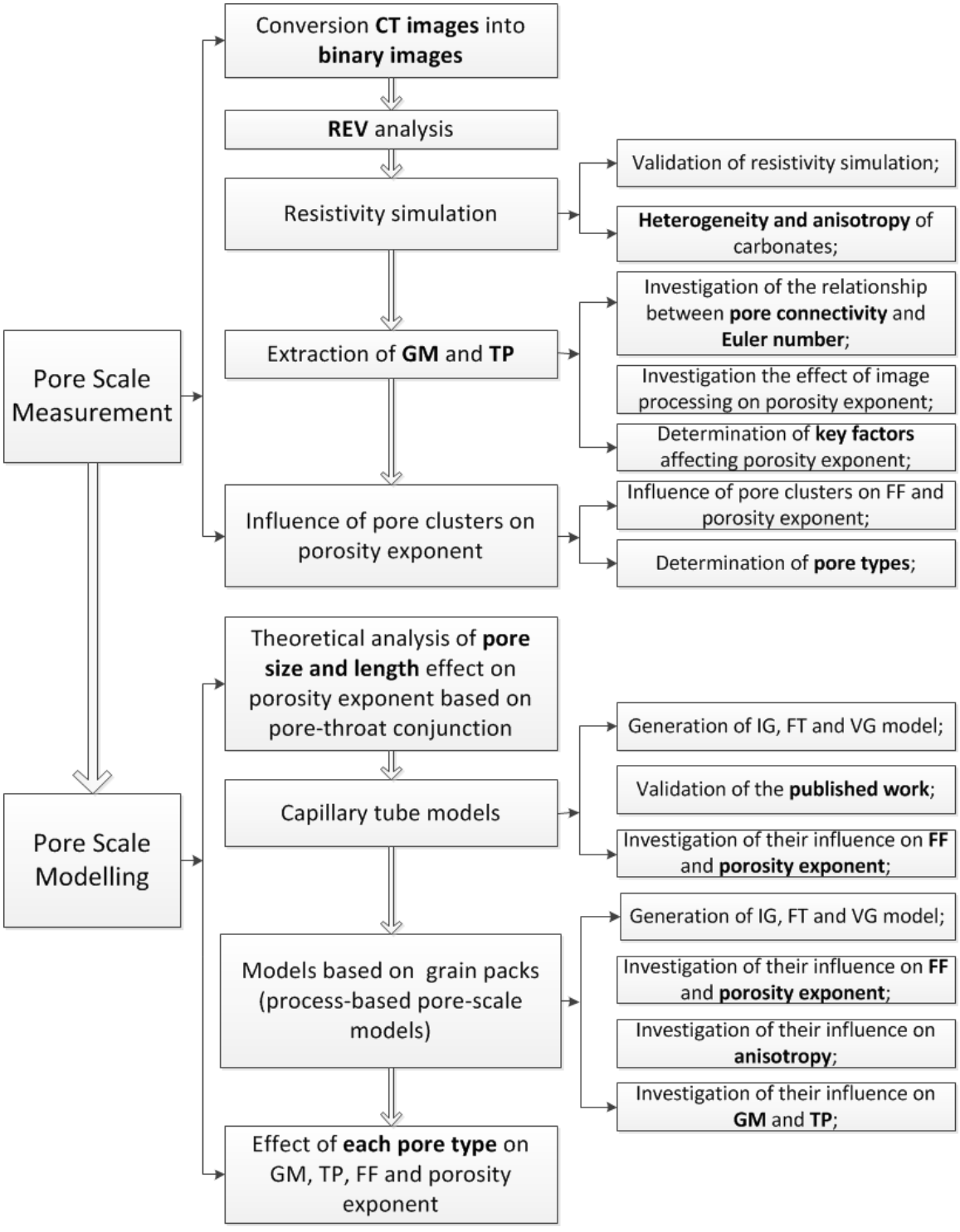

Figure 1.1: Main methods and work flow in this thesis.

1.4 Outline of This Thesis

This thesis is structured as follows.

Chapter 1 has given a brief introduction to the limitations of interpretation models, pore type complexity and heterogeneity for carbonates, the simulation methods to calculate resistivity and pore system's geometry and topology.

Chapter 2 reviews CT imaging, pore network extraction, pore geometry and topology calculation, resistivity calculation with emphasis on improving the accuracy of numerical simulation methods.

In Chapter 3, pore scale measurement is used to calculate the resistivity by simulation methods and extract their geometry and topology. This Chapter includes

- CT images ;
- REV analysis;
- Resistivity calculation based on the REV;
- Extraction of the geometry and topology of the REV;
- Explain the effect of the percolation and isolation pore clusters on the geometry and topology as well as porosity exponent from pore-throat conjunction (Chen and Zhang, 1987[46]);
- Explain the main pore type in each carbonate samples by their distribution in published work of Aguilera and Aguilera (2003[5]).

This chapter has determined the key geometrical and topological parameters and pore types affecting porosity exponent. In order to relate the porosity exponent to the pore structure, it is necessary to investigate the effect of these parameters and pore types on the porosity exponent based on pore scale modelling in carbonates.

In Chapter 4, pore scale modelling is used to investigate the GM effect on the porosity exponent and the pore types impact on the GM and TP as well as FF and then on the porosity exponent. It includes

- Theoretical analysis the GM effect on the porosity exponent;
- Pore type effect on the porosity exponent based on capillary tube models and the validation of the above published work by the simulation porosity exponent;
- Analysis of the fracture (FT), CVG (connected vug), IVG (not connected or isolated vug) effect on the Formation Factor (FF) and porosity exponent taken intergranular (IG) model as host medium from their effect on GM and TP;

The modelling can reflect the impact of the pore type on the GM and TP and then their effect on the FF, porosity exponent as well as its anisotropy.

A summary of the main finding and conclusions which have been achieved and some future research directions are given in Chapter 5.

Chapter 2

Background of Pore Scale Technologies and Resistivity Models in Numerical and Empirical

The electrical properties, especially for the porous media fully saturated by brine, are related to the pore structure. The successful correlation requires an ability to characterize the pore structure and the prediction of the electrical properties based on the characterization. This in turn will enable researchers to develop accurate relationships to predict and correlate electrical properties for porous media.

The accurate characterization of the pore structure depends on its accurate reconstruction. Due to the limitation of the reconstruction from 2D slices in preserving the connectivity of the pore space (Hazlett, 1997[86]; Manwart *et al.*, 2000[129]; Øren and Bakke, 2003[146]), a direct reconstruction of a 3D pore structure at resolutions down to a few microns is now available from X-ray computed tomography (*x-CT*). However, the characterization of the pore structure by pore geometry (GM) and topology (TP) requires the binary images. These CT images are firstly converted into binary images by imaging processes and then the pore geometrical and topological properties can be calculated based on binary images by Minkowski Functions (Vogel, 2002[210]) or pore network (PNW) analysis (Lindquist and Venkatarangan, 1999 [115]; Ioannidis and Chatzis, 2000[89]; Lindquist *et al.*, 2000[118]; Sok *et al.*, 2002[190]; Prodanović *et al.*, 2007[158]; Jiang, 2008[92]). Minkowski Functions offer volume, surface area, curvature and Euler number. However, Minkowski Functions are not sufficient to characterize pore geometrical properties and some of these Functions are sensitive to the resolution of the porous media (Jiang *et al.*, 2011[93]). The geometrical properties can be extracted from the pore network of the porous media. At present, network extraction methods can find networks that make reasonable estimates of the transport properties reflecting the accurate representation of the pore geometry and topology (Blunt *et al.*, 2013[34]). The network extraction methods mainly include Voronoi methods (Bryant and Blunt, 1992[40]; Bryant *et al.*, 1993[41]; Øren *et al.*, 1998[147]; Øren and Bakke, 2002[145] and 2003[146]), medial axis methods (Lindquist *et al.*, 1996[117]; Lindquist and Venkatarangan, 1999[115]; Sheppard *et al.*, 2005[184]; Shin *et al.*, 2005[187]; Prodanović *et al.*, 2006[157]; Jiang, 2008[92]) and maximal ball (MB) methods (Silin *et al.*, 2003[189]; Silin and Patzek, 2006[188]; Al-Kharusi and Blunt, 2007[13]; Dong, 2007[63]). With consideration of the complexity of the porous media and the importance of determining pore, maximal ball method is used to extract the pore network of carbonates due to its priority in determining pore size and location, the limited application of Voronoi methods in complex porous media and the

problems of identification of pores and throats based on medial axis methods (Blunt *et al.*, 2013[34]).

The characterization of the pore structure has been considered, the electrical property of the porous media and the relationship between pore structures and electrical properties become emergent. Due to the complexity of the pore structure in carbonates and the capacity of computers, directly theoretical attempts to relate resistivity to pore structure are intractable (Arns, 2002[19]), electrical properties have been empirically correlated to the porosity, the most famous correlation is Archie Law including porosity exponent, which relates the resistivity of the porous media fully saturated by brine to the porosity. The pore geometry and topology is ignored in the empirical models. Empirical relations therefore tend to be more useful for correlating data than for predicting properties (Arns, 2002[19]). However, the successful of the Archie Law lies in its wide application in Petroleum Engineering for different reservoirs from clastics to carbonates according to its development and modification (Archie, 1942[15]; Kadhim *et al.*, 2013[97]; Mabrouk and Soliman, 2014[126]). The modification considers the factors effect on the resistivity. With consideration of the Coquina samples in this thesis, the factors effect on the resistivity and the porosity exponents in carbonates, the Archie Equation for carbonates in this thesis is determined by taking $a=1$ and the specific characteristics of carbonates lies in the complex pore space due to the variety of the pore types. Porosity exponent is used to reflect the effect of pore structure on the resistivity, the effect of the pore types on resistivity are investigated by porosity models (Watfa and Nurmi, 1987[216]; Serra, 1989[182]; Kazatchenko and Mousatov, 2002[100]; Aguilera and Aguilera, 2003[5]) based on theoretical analysis using oversimplified representations of the pore structure to derive the porosity exponent. Although the porosity models oversimplify the pore structure, they are still used to determine the pore type for each coquina sample in this thesis.

Another approach is to computationally solve electrical properties from digital images of the porous media. The modern imaging techniques now allow researchers to observe the full complexity of real porous media in 3D. The computational techniques have progressed to calculate porous media properties such as diffusivity, elasticity and resistivity on large three dimensional digital images containing up to 1000^3 voxels (Arns, 2002[19]). With consideration of the efficiency and further application, three methods are introduced including finite difference method (FD) (Garboczi and Day, 1995[76]; Arns *et al.*, 2002[21]; Bohn and Garboczi, 2003[35]), random walk

simulation (RW) (Toumelin and Torres-Verdín, 2008[199]; Han *et al.*, 2009[83]) and a renormalization method (Nakashima and Nakano, 2011[141]; Khalili *et al.* (2012[103]). FD calculates resistivity by directly solving Laplace equation, its accuracy is validated by comparing the numerical results to the theoretical data based on simple model and to the experimental data. However, its time consumption is huge and it is a challenge in terms of computer (Han *et al.*, 2009[83]; Nakashima and Nakano, 2011[141]). A method, which can offer accurate estimation and consume less time and memory of the computer, is necessary, RW is such an efficient method to estimate the resistivity by simulating the average geometry tortuosity to represent the electrical path. The validation of this method is to compare the simulation results to the numerical data from FD with the error determined. FD and RW can be used to calculate the electrical properties of porous media in the capacity of computer. However, for the large porous media, its calculation by FD and RW is out of the capacity of computer, an upscale method becomes necessary which can estimate the resistivity of the large porous media based on the resistivity of its sub-samples (Nakashima and Nakano, 2011[141]; Khalili *et al.* (2012[103]). This method is a renormalisation technique. In this thesis, this method is not directly used to calculate resistivity for coquina samples while its feasibility is tested by the Fontainebleau sandstone and three coquina samples for further application.

The pore structure characterization and electrical properties have been obtained, the relationship between pore structures and electrical properties can be built based on various pore structures and their resistivity. Due to the high costs of CT imaging and resistivity measurements for various porous media, it is impracticable to obtain, scan and experiment porous media with various pore structures and pore types while pore scale modelling and resistivity numerical methods can be applied to investigate the effect of the pore structure on the electrical porosities due to their flexibility in modelling pore structures and pore types. The pore scale models mainly include capillary tubes (Fatt, 1956[71]; Dullien, 1992[66]), pore network (Watfa and Nurmi, 1987[216]; Etris *et al.*, 1989[70]; Ehrlich *et al.*, 1991[68]; Abousrafa *et al.*, 2009[1]) and grain packs from process-based methods (Mousavi and Bryant, 2007[136]; Mousavi, 2010[135]; Mousavi and Bryant, 2012[137]; Mousavi *et al.*, 2012[139]; Mousavi and Bryant, 2013[138]). With consideration of the three coquina samples in this thesis and the variety of the pore types in the carbonates, models based on capillary tubes and grain packs are used to investigate the effect of the pore type on the resistivity

while models based on pore network are used to theoretically investigate the effect of pore geometry on the resistivity. The advantage of the capillary tube lies in its simplification of the pore space, it is easy to build models considering various arrangements of the pore types and theoretically derive the electrical equation. However, the capillary tubes lose the pore connectivity (Abousrafa *et al*., 2009[1]), the pore network model can be much closer to the real porous media with consideration of the pore connectivity and can be easy to theoretically derive resistivity from the geometrical and topological properties of the pore space. However, models from capillary tubes and pore network can not directly characterize the vug and fracture (Mousavi *et al.*, 2012[139]), the models based on grain packs are used to simulate pore types such as intergranular (IG), fracture (FT) and vug (VG).

The chapter is organised as follows. Firstly, the CT imaging including principle, application and acquisition and the imaging processing converting CT images into binary images are introduced. Due to the requirement of pore network in calculation of pore geometry and topology, the pore network extraction methods are reviewed secondly and followed by the description of the pore geometry and topology from Minkowski Functions and pore network analysis in the third section. The resistivity numerical simulations are listed in the fourth section and the empirical equations are in the fifth section including its development and ranges. The sixth and seventh sections describe the factors affecting electrical properties and the porosity exponent in carbonates respectively. The effect of the pore types on the porosity exponent in carbonates is investigated by porosity models in the eighth section. The ninth section illustrates the pore scale modelling. The methods used in this thesis are discussed in the tenth section. The final section is the conclusion.

2.1 $x-CT$ Images

The accurate characterization of the pore space depends on its reconstruction. *x-CT* is a direct measurement of a 3D porous medium while the CT images should be converted into binary images due to the requriment of characterization and simulation. This section firstly introduces the principle and history of *x-CT*, and then presents the application of the high resolution CT (μ-CT) followed by the description of the CT acquisition and image processing for the samples used in this thesis.

2.1.1 Principle and History of $x-CT$

The emergency of $x-CT$ is based on the discovery of the X-ray by Wilhelm Röntgen, the specific feature of X-ray lies in its capability of penetrating materials in varying degrees causing the generation and development of the $x-CT$ images. Its capability of penetration is expressed by Beer's Law describing the transmitted intensity of a monochromatic X-ray passing an object in Equation (2.1).

$$In = In_0 e^{-\int \mu(s)\, ds} \tag{2.1}$$

Where In is the transmitted intensity of the X-ray, In_0 is the incident beam intensity and $\mu(s)$ is the local linear attenuation coefficient along the ray path s (Cnudde and Boone, 2013[54]).

The first application of the X-ray was radiograph imaging which referred to "projection" or "shadow" imaging, projecting 3D object on 2D detector plane with losing of depth information. This limitation was overcome by a new technology called "computerized transverse axial tomography" (CAT or CT) in 1970s. This technology acquired projection images from various directions and then these projection images were used to build a 3D volume by dedicated computer algorithms, which has been a commonplace in the earth sciences for imaging geological samples (Cnudde and Boone, 2013[54]).

Following technological advances, a new research field emerged in high resolution X-ray tomography, commonly named micro-CT ($\mu-CT$) which was firstly discussed in the 1980s. The priority of the $\mu-CT$ lied in its high resolution reaching 200 μm, this resolution is not achievable for standard $x-CT$.

There are two kinds of setup for $\mu-CT$. One is the standard cone-beam $\mu-CT$. In this setup, the conical X-ray beam makes geometrical magnification possible by positioning the object under investigation at any position between X-ray source and detector (Figure 2.1). The other one is a synchrotron sources, the X-ray beam is almost parallel, making geometrical magnification impossible without X-ray optics but has a high X-ray flux. This high flux can be detected by a thin scintillator screen, converting the X-rays to visible light (Figure 2.2).

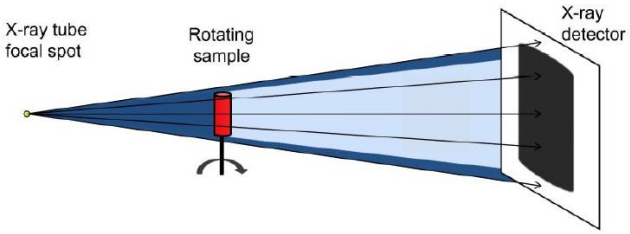

Figure 2.1: Lab-based µ-CT. Sample is in the range of X-ray resource and detector and its position determines magnification (Cnudde and Boone, 2013[50]).

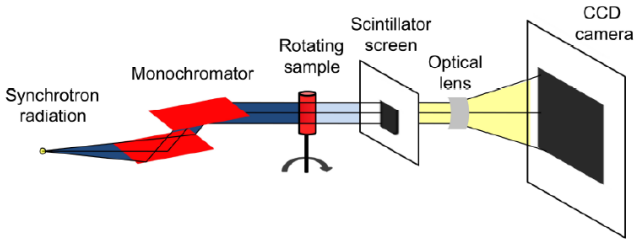

Figure 2.2: Synchrotron µ-CT. The X-ray beam is parallel to offer a high X-ray flux and the geometrical magnification is controlled by optical lens (Cnudde and Boone, 2013[50]).

2.1.2 $\mu-CT$ *Application*

The development of modern imaging methods lies in the reconstruction of $3D$ images from a series of $2D$ projections of these images at different angles. In the 1980s, these methods were firstly applied in soil science (Petrovic *et al.*, 1982[154]) and petroleum (Vinegar and Wellington, 1987[207]) to measure two and three phases saturation in laboratory with their resolution about $1\sim3mm$. Flannery and co-workers (1987[73]) at Exxon Research using laboratory and synchrotron sources scanned several rock samples with the resolution reaching about $3\mu m$ and then the $\mu-CT$ imaging was applied in the quantification of the topology (TP) of the pore space and transport in sandstones (Spanne *et al.*, 1994[192]; Coker *et al.*, 1996[51]). The first calculated transport property directly based on $\mu-CT$ images was relative permeability by Hazlett (1995[85]) using Lattice Boltzmann method.

One of pioneers of the continued work of this technology is the team at the Australian National University in collaboration with colleagues at the University of New South Wales. Their great achievement was in imaging a wide variety of rock samples in the laboratory and predicting transport properties (Turner *et al.*, 2004[202]; Arns *et al.*, 2005a[18], 2005b[20] and 2007[22]; Knackstedt *et al.*, 2010[106]). An excellent overview of the application of $x-CT$ imaging in geosciences is provide by Ketcham and Carlson (2001[102]) and Cnudde and Boone (2013[50]).

2.1.3 Acquisition of 3D $\mu - CT$ Images

In this thesis, $\mu - CT$ was acquired using an instrument SKYSCAN (model 1173 High Energy) (Figure2.3), owned by LAGESED from the Geology Department of Universidade Federal do Rio de Janeiro (UFRJ). This Skyscan 1173 High Energy equipment was with a microfocus X-Ray tube, tungsten anode, with a focal point less that 5 μm and potential of $8W$, its operational energies were between 40 to $130\,kV$ with a current of 0 to $120\,\mu A$ and its detector was a flat panel with matrix of 2240×2240 pixels, with pixel distribution varying between 50 μm and 12 bits of dynamic range, with object acquisition from approximately 140 mm diameter to 200 mm in length (Câmara *et al.*, 2015[44]). A brief summary of the processes undertaken to obtain raw $X-$ray attenuation profiles is given below.

Figure2.3: X-ray µ-CT Skyscan 1173 which is a high-energy spiral µ-CT (from http://www.bruker.com/products/x-ray-diffraction-and-elemental-analysis/x-ray-micro-ct/skyscan-1173/overview.html).

Sample Positioning

The sample must be located in the control panel of the system so that the sample is in the field of view as fully as possible while retaining a band of clear air to the left and right of the sample throughout the rotation. To obtain the highest possible resolution, the sample has to be regulated and aligned as well as well as possible (Dong, 2007[63]; Câmara, 2013[43]).

Sensor Calibration

First, the energy of X-ray reflected by the tuning the voltage has to be chosen sufficiently to make X-ray penetrate the minerals making good contrast between void and solid. The X-ray source of Skyscan 1173 is $110\,kV$, current $72\,\mu A$, aluminium filter ($1.0\,mm$) and external copper filter ($2.5\,mm$) with steps of 0.3^o, rotation of 180^o

and a resolution of $20\mu m$ (Câmara, 2013[43]; Câmara *et al.*, 2015[44]). Then the correction images have to be acquired to remove the effect of the surrounding, X-ray resource and detector with the help of the background images.

Operational Parameters

The scanning operation parameters include the average number of images for one projection, the metal thickness decreasing the effect of beam. The main parameter is the number of projections which should be similar or greater to the width of the object in pixel. This parameter determines the image quality.

Reconstruction

The software Avizo Fire software is used to reconstruct the pore model. The program allowed researchers to manipulate the images, subdividing the image to focus the different sub-regions identified. This program can identify, quantify and filter the pores depending on volume, as well as segment them from the rest of the rock, which is helpful for researchers to understand how each facies of coquinas shapes the pores as well as show how the connectivity of the pores developed for varying diagenetic cases (Corbett and Borghi, 2013[55]; Câmara *et al.*, 2015[44]).

2.1.4 Image Processing

Post-Processing

$\mu - CT$ 3D images are a 3D array where element is integrity from $0-255$ known as grey scale data. In order to extract the pore space to quantitatively determine its TP and GM and to calculate electrical properties, the 3D images should be segmented into binary images composed of the void (pore space) and solid. All the following work can be implemented by software "ImageJ" (Appendix B).

Median Filter

During the image scanning process, noise exists in the $\mu - CT$ images. This noise can be removed by filter. The median filter is the best choice which can not only remove the noise but also preserve the structure details of the images. The idea of a median filter is to get a new value of a voxel by the average value of its nearest several surrounding voxels depending on the radius of the filter.

Imaging Segmentation

In order to obtain binary images, a segmentation process is required to distinguish the pore space from the matrix by classifying the grey scale (0-255) into binary scale (0-1), pore and solid, based on the grey scale histogram.

Two peaks in the histogram reflect the void and solid respectively. A threshold value in the range of the two peaks should be chosen to segment the image into pore space and matrix. If the valley is flat, it is not easy for user to determine the threshold while an auto-threshold can be used in the software or visual inspection can be implemented by the dialogue box in "ImageJ" to show the results of segmentation with different thresholds.

2.2 Pore Network Extraction

The geometrical and toplogical characterization of the pore space is described by the pore network. Additionally, network extraction methods can extract networks that make reasonable estimates of transport properties reflecting the accurate representation of the pore geometry (GM) and topology (TP) (Blunt *et al*., 2013[34]). This section lists the methods to extract the pore network. The major algorithms to extract pore network include the medial axis (skeleton) based methods, the maximal ball methods and the Voronoi diagram based methods.

Pore Network Extraction Methods

Multi-orientation scanning method is proposed by Zhao *et al.* (1994[228]) to detect pore and throat using multi-orientated plates in 13 directions (Figure 2.4). These plates in different orientations can indicate the local minima to determine throats. However, the problem of this method lies in the difficulty of locating pore body. The idea of scanning in multiple directions are used in medial axis based method to find hydraulic radius of the pore space (Liang *et al.*, 2000[114]).

Medial axis based method is used to convert the pore space into a medial axis (skeleton) which is a simple representation of the pore space by a centrally located skeleton in the pore space with preservation of the topology. The segmentation of the pore space can be operated along the skeleton by determining the pore throats based on the local minima, which is calculated in multi-orientation, along bonds and pore bodies at the nodes (Lindquist *et al.*, 1996[117]; Lindquist and Venkatarangan, 1999[115]; Sheppard *et al.*, 2005[184]; Shin *et al.*, 2005[187]; Prodanović *et al.*, 2006[157]; Jiang,

2008[92]). The medial axis can determined by a thinning algorithm (Liang *et al.*, 2000[114]), pore space burning algorithm (Lindquist *et al.*, 1996[117]), or distance map based algorithm (Jiang, 2008[92]). The topological properties of the pore space can be preserved by this medial axis. However, the uncertainty of this method is the unambiguous identification of the pores caused by two facts. One is the clean-up process which is used to remove the trifling details on the skeleton, because the medial axis method is intrinsically sensitive to the noise in the images. The other is the reasonable requirement of trimming the skeleton and fusing the junctions together by various merging algorithms to keep coordination number in an acceptable number instead of unrealistically high number. Figure 2.5 gives an example of medal axis of Berea Sandstone and compares the difference between before and after the process of cleaning up showing the sensitivity of this method to the irregularity.

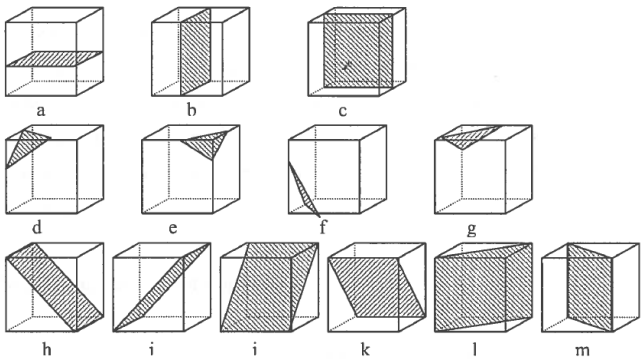

Figure 2.4: The planar plates in 13 different directions. Three orthogonal directions are in (a)-(c). Four corner scanning plates are in the middle from (d)-(g); the rest six plates (h)-(m) are in the diagonal direction (Jiang, 2008[92]).

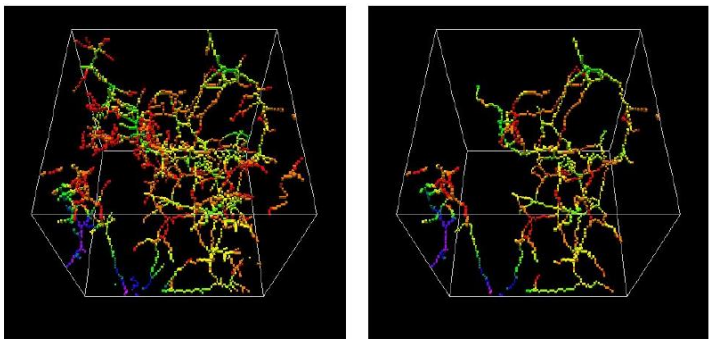

Figure 2.5: The effect of cleaning up for medial axis algorithm. The medial axis is sensitively affected by the irregularity in the transition surface area from pore to solids and the disconnection of the pore clusters misidentified in segmentation. The left picture is the medial axis from a sub-volume of a Berea Sandstone image with resolution about 4.93 μm; the right is the result after trimming all dead ends. The colours are in rainbow scale reflecting the distance from pore voxels to its nearest grain volxels (http://www.ams.sunysb.edu/~lindquis/3dma/3dma_rock/3dma_rock.html).

These problems of identification of pore and throats based on medial axis methods are illustrated by Silin and Patzek (Silin and Patzek, 2006[188]). To improve the accuracy of bond distinguish, some pore merging algorithms are developed (Sheppard *et al.*, 2005[184]; Jiang, 2008[92]). In conclusion, medial axis algorithms readily capture the interconnectivity of the pore space but encounter problems in identification of pores.

Voronoi diagram based algorithms are used to extract pore networks especially for the porous media knowing the coordination of the grain centres and these media are usually built by process-based method considering the geological information (Bryant and Blunt, 1992[40]; Bryant *et al.*, 1993[41]; Øren *et al.*, 1998[147]; Øren and Bakke, 2002[145] and 2003[146]). The pore network can be extracted by segmenting the pore space into Voronoi polyhedra. The pore bodies are defined by the vertices of the polyhedra which connect to the voxel from four or more different grains and the pore throats can be viewed by its edges whose voxels link to these voxels from three different grains. The pore networks extracted by Voronoi based methods have been proved successfully in pore-scale simulation (Delerue and Perrier, 2002[60]).

The maximal ball (MB) algorithm (Silin *et al.*, 2003[189]; Silin and Patzek, 2006[188]) firstly determines the inscribed spheres in each pore voxels which are defined by just touching the grain or the boundary and then those inscribed spheres which fully overlapped by other spheres can be regarded as inclusions and removed. The remaining spheres are named “maximal balls” which are used to describe the pore space without abundance. The description of the pore space is based on the largest balls standing for pore bodies and the smallest balls between pore bodies representing pore throats. The extended application of this method is to research the pore space of the sandstones and carbonates by Al-Kharusi and Blunt (2007[13]). This method clearly identifies the larger pores, but tends to identify a cascade of smaller and smaller elements down to the image resolution (Blunt *et al*., 2013[34]).

2.3 Pore Geometry (GM) and Topology (TP) Calculation

The electrical porperties of the porous media are related to the structure of the pore space which is characterized by GM and TP. This section illustrates the calculation of the GM and TP by Minkowski Functions based on image and PNW analysis.

2.3.1 Minkowski Functions

Minkowski Functions are basic geometric measures defined for binary porous media. For a binary porous media, Ω, in d dimension with its pore space $X \subset \Omega$, a limited set of d+1 Minkowski Functions can be provided by its integral geometry. In 3D, four functions can be provided by Minkowski Functions in Equation 2.2.

$$\begin{aligned} &M_0(X)=V_\Omega(X); \\ &M_1(X)=\int_{\delta X} ds = S(X) \\ &M_2(X) = \int_{\delta X}\left[\frac{1}{r_1}+\frac{1}{r_2}\right]ds = C(X) \\ &M_3(X) = \int_{\delta X}\frac{1}{r_1 r_2}ds = K(X) \end{aligned} \qquad (2.2)$$

Where δX denotes the surface of the pores; ds is a surface element, r_1 and r_2 are respectively the minimum and maximum radius of curvature for the surface element ds. This radius is positive for convex curvatures and negative for concave curvatures.

The first function M_0 is the total mass of the structural unit corresponding to porosity; M_1 corresponds to surface density relating to the interaction of solutes at pore-solid interfaces; the mean curvature M_2 correlates to pore shape affecting the energy density of wetting fluid or capillary pressure between different fluid phases; and M_3 is related to the connectivity of the pores usually presented by Euler number χ. The Euler number χ is defined by Equation 2.3.

$$\chi(X) = N - L + O = \frac{1}{4\pi}M_3(X) \qquad (2.3)$$

Where N is the number of isolated objects (closed convex); L is the number of redundant connections or loops (closed saddle surface); O is the number of cavities (closed concave);

M_3 is a dimensionless, topological measure that quantifies the connectivity of the pattern while M_0, M_1 and M_2 are metric with units $[L^3]$, $[L^2]$, $[L]$, respectively.

In order to compare results from different images, the effect of image size can be removed by the Minkowski density $m_K(X)$, which is the normalization of the functional results by the volume of the image, V_Ω.

$$m_K(X) = \frac{M_K(X)}{V_\Omega} \qquad (2.4)$$

Algorithms

For a binary image, each pixel or voxel x is classified as pore $x=1$ or solid $x=0$. The Minkowski Functions can be calculated by the open source C/C++ library Quantim (www.quantim.ufz.de). The algorithms of these functions are straightforward by evaluating of the voxel configurations of a basic 2x2x2 cube in each point of the image (Ohser and Mücklich, 2000[142]). The total number of the configurations q in the cube is $2^8=256$ and its frequency $f(q)$ can be obtained by recording the number of each configuration. Thus, firstly, the binary image is converted into 256 numbers with the frequencies of each configuration q irrespective the shape and size of the image. And then the Minkowski Functions are calculated by these configuration frequencies with their specific weight factor $I_K(q)$. Hence, the density of the Minkowski Functions can be calculated based on the frequency and contribution of each configuration in Equation 2.5:

$$\mathrm{m_k} = \omega_\mathrm{k} \sum_{q=0}^{255} I_k(\mathrm{q})\,\mathrm{f(q)}, \mathrm{k} = 0,1,2,3. \qquad (2.5)$$

Where $I_K(q)$ is the weight factor for each configuration q with frequency $f(q)$. ω_k are specific factors for different Minkowski densities. The calculation turns to determine the specific contribution $I_K(q)$ and related factor ω_k.

Porosity m_0: m_0 is related to the fraction of pore voxels in the image which can be obtained by setting $I_0(q)=1$ for any configuration located in a pore voxel and $I_0(q)=0$ for solid. The specific factor ω_0 to calculate porosity is 1 divided by the total number of voxel.

Surface density m_1: this parameter is linked to the number of transitions, $1 \leftrightarrow 0$ in binary image, from pore to solid along a line through the image. The transition along different directions can be easily examined and the number of all this transitions in a 2x2x2 basic cube can be calculated. An example of a basic cube is shown in Figure 2.6 with consideration of the numbering scheme and the directions evaluated. There are 13 evaluation directions in a basic cube are (1,2), (1,3), (1,4), (2,4), (1,5), (1,6), (2,5), (1,7), (3,5), (1,8), (3,6), (2,7) and (4,5). The rest within this cube can be scanned by the cube at other location in this image. The contribution $I_1(q)$ of each configuration to the surface density is the total number of transitions along these 13 directions of this cube.

The example cube with $I_1(37)=7$ is in Figure 2.6. The related factor ω_1 is related to the total length of the 13 different directions in the cube which is expressed in Equation 2.6,

$$\omega_1 = \frac{2}{\lambda\left(3+6\sqrt{2}+4\sqrt{3}\right)\sum_q f(q)} \qquad (2.6)$$

Where λ is the side length of a voxel.

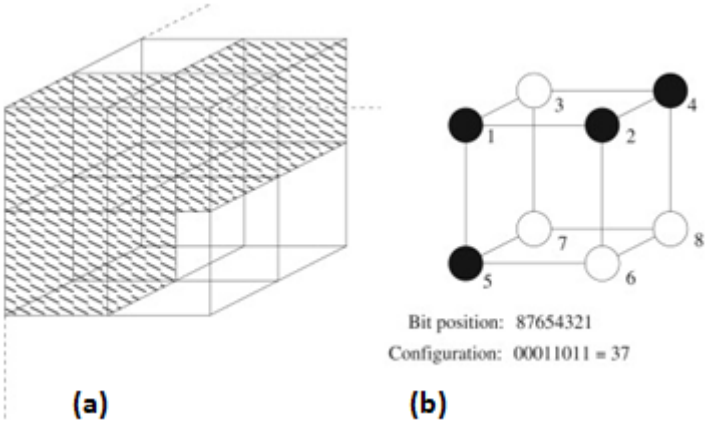

Figure 2.6: Example of a voxel configuration in basic 2x2x2 voxels. Pore voxels are in the grey hatch area (a) and the related numbering scheme is illustrated in (b). The sequence in the scheme is based on bit positions (Vogel *et al.*, 2010[212]).

Mean curvature m_2: the mean curvature of 3D surface is estimated by the expectation value of the two dimensional Euler number of a two dimensional section through it (Weibel, 1979[218]). The Euler number m_2 in two dimensions based on the basic cube can be expressed by the number of vertices, edges and faces within the various two-dimensional planes for different directions of section. The two dimensional Euler-number per total area of the evaluated section relates to the mean curvature m_2. The algorithm and specific factors are given by Lang *et al.* (2001[111]).

Euler number m_3: the Euler number of a pore space which consists of a series of compact convex voxels in a digital image can be calculated by the classical Euler formula in Equation 2.7:

$$\chi = \#\text{vertices-}\#\text{edges+}\#\text{faces-}\#\text{volumes} \qquad (2.7)$$

Where # denotes 'number of'. For a single pore voxel, this would be expressed by the Euler number of one convex body χ=8-12+6-1=1. The contribution $I_3(q)$ of each configuration is the Euler number easily obtained by counting the number of vertices, edges, faces and volumes. The specific factor is in Equation 2.8,

$$\omega_3 = \frac{4\pi}{\lambda^3\sum_q f(q)} \qquad (2.8)$$

Where 4π is due to the relation between total curvature and the Euler number and the denominator is just the total volume of the image. The Euler number is a parameter for pore topology property called connectivity.

2.3.2 Pore Geometry and Topology from PNW

This section lists the calculation of pore geometry and topology. The pore geometry describes in four aspects.

Firstly, the volumes of the pore and throat are defined by the percentage of the pore and throat voxles in the pore space. Secondly, the pore size is defined by the inscribed radius of the MB taken as pore body and the size of throat is determined by the maximum size of MBs in the pore-throat chains between two pores. Thirdly, in the pore network, the pore space is simplification by the nodes and bonds which replace the complexity and irregularity of the pore space by a series of cylindrical capillary tubes with constant but arbitrary cross sections. These cross sections are described by a dimensionless shape factor G in Equation 2.9.

$$G = \frac{VL}{A_s^2} \qquad (2.9)$$

Where A_s is the surface area of pore or throat volumes. This parameter is calculated by counting the number of surface voxels between void and solid in pore or throat cells. V is the volume of the pore or throat unit and L is the length of the unit.

The Equation 2.9 is equal to Equation 2.10

$$G = \frac{A}{p^2} \qquad (2.10)$$

Where A is the area of the cross section and p is the perimeter (Mason and Morrow, 1991[130]). These are illustrated in Figure 2.7.

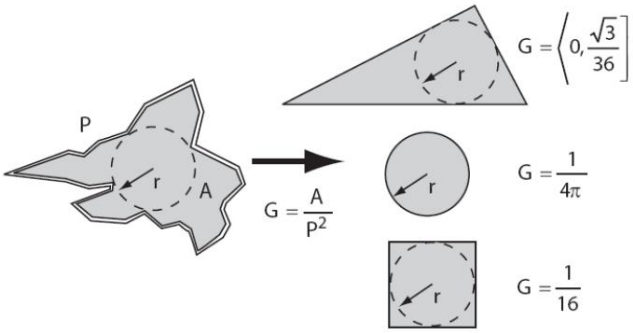

Figure 2.7: The definition of the shape factor which is the dimensionless parameter for pore network elements (Mason and Morrow, 1991[130]).

Fourthly, the length of the pores and throats are defined based on the method of Øren and Bakke (2003[146]) in Figure 2.8 and then can be used to define the tortuosity.

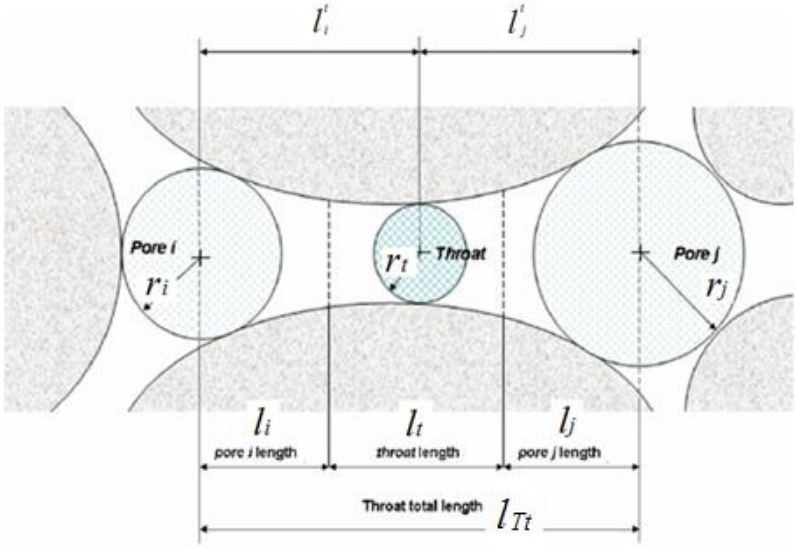

Figure 2.8: Schematic picture of the length definition for pores (nodes) and throats (bonds) based on their radii and relative locations in the pore space (Dong, 2007[63]).

The throat (bond) length l_t between the pore *i* and *j* is defined by throat total length, l_{Tt}, subtracted the two nodes' lengths in Equation 2.11.

$$l_t = l_{Tt} - l_i - l_j \qquad (2.11)$$

The length of the pore (node) is determined by Equation 2.12 and Equation 2.13,

$$l_i = l_i^t(1-0.6\frac{r_t}{r_i}) \qquad (2.12)$$

$$l_j = l_j^t(1-0.6\frac{r_t}{r_j}) \qquad (2.13)$$

Where r_i, r_j and r_t are the radii of the pore (node) *i*, pore (node) *j* and throat (bond) respectively; l_i^t and l_j^t are the distances between the centre of pore (node) *i* and the centre of pore (node) *j* to the throat (bond) centre.

The tortuosity is defined based on the Euclidean distance between two pore (node) centres, l_{ij}, l_i^t and l_j^t which are the distances between the centre of pore (node) *i* and the centre of pore (node) *j* to the throat (bond) centre in Equation 2.14.

$$\tau = \frac{l_i^t + l^t_j}{l_{ij}} \qquad (2.14)$$

The topological properties of the pore network are reflected by connection number (*Z*) and Euler characteristic (Euler number). The network of the pore space consists of nodes and bonds and the nodes are connected by bonds. So the connectivity of such

pore network can be described by the coordination number (connection number) which is the number of the bonds connected to the nodes.

The Euler number reflects the number N of isolated objects, i.e. pores, the number of redundant connections C within the pore space and the number of totally enclosed cavities H (Vogel, 2002[210]). The Euler characteristic (Euler number) χ is defined by Equation 2.15.

$$\chi = N - C + H \qquad (2.15)$$

The positive Euler number illustrates the pore structure with poor connection for $N > C$ while negative number responds to pore space with much better connection where $N < C$. For a pore network for natural porous media, the quantity H is close to 0 since it is nearly impossible for a grain cluster to float in the pore space. The priority of the Euler characteristic χ lies in its unbiased estimation from a 3D cutout of the pore space. This advantage makes Euler characteristic deduced from the local structure without explicit number of N, C and H demonstrated by Ohser *et al.* (2002[143]) for the application to the digital images.

The Euler characteristic is simply obtained by the number of nodes (pores) and bonds (throats) in the pore network from Equation 2.16.

$$\chi = N_{node} - N_{bond} \qquad (2.16)$$

Where N_{node} is the number of nodes with at least one connected bond and N_{bond} is the total number of bonds. This Euler number links to the pore size distribution by calculating the number of nodes and bonds with their size larger than this related size. So the connectivity function can be defined as the relationship between the Euler number of the pore space consisting of the pore and throats larger than a pore size and this pore size (Vogel and Roth, 2001[211]).

2.4 Numerical Solutions

In order to predict the electrical properties of porous media and investigate the relationship between resistivity and pore structures by pore scale modelling, the resistivity of the porous media should be directly solved due to the impractice of obtaining the porous media with various pore structrues and implementing resistivity measurement for all the porous media. However, the analytical solution of the porous media is intractable due to the complexity of the pore structure (Arns, 2002[19]). The resistivity should be numerically sovled. This section firstly introduces the physical background and then presents numerical approaches to calculate the effective electrical

properties and validation for each method. Finally, the characteristics of each numerical method are discussed.

2.4.1 Electrostatic Equations

In this section, the derivation of the effective direct current conductivity of the porous media in steady state is presented. The charge conservation Equation 2.17

$$\vec{\nabla} \cdot \vec{j} + \frac{\partial \rho}{\partial t} = 0 \qquad (2.17)$$

reduces to Equation 2.18

$$\vec{\nabla} \cdot \vec{j} = \vec{\nabla} \cdot \left(\rho \vec{\mathrm{E}} \right) = \vec{\nabla}^2 \varphi = 0 \qquad (2.18)$$

Where E is electric field and φ is electrostatic potential. With the internal boundary conditions at regions of phases i, j in contact having conductivities σ_i and σ_j in Equation 2.19,

$$\varphi_i = \varphi_j, \quad \sigma_i \vec{\nabla} \varphi_i \cdot \vec{n} = \sigma_j \vec{\nabla} \varphi_j \cdot \vec{n} \qquad (2.19)$$

The effective conductivity is then given by a macroscopic form of Ohm's law in Equation 2.20.

$$\sigma_{eff} \left\langle \vec{\nabla} \varphi \right\rangle = \left\langle \sigma \vec{\nabla} \varphi \right\rangle \qquad (2.20)$$

The DC conductivity of a material can be predicted by the volume, conductivities of each element of this material and their arrangement. For the complex internal boundaries of porous media an analytical solution to this problem becomes intractable while an alternative method, which incorporates full structural information, is to derive the solution to the problem of effective electrical properties for porous media numerically. With consideration of the efficiency and further application, the numerical simulation methods include finite difference (FD), random walk simulation (RW) and a renormalisation method. The principle and validation of each method are listed in their each section.

2.4.1 Finite Difference (FD)

FD derives the solution to the problem of effective conductivity for porous medium numerically. This method is to choose a finite mesh of points and solve a discretised version of the Laplace equation boundary conditions. To solve the Laplace equation with given boundary conditions (Equation 2.17-Equation 2.18), an industry standard finite difference (FD) code developed at NIST(National Institute of Standards and

Technology) is employed (Garboczi, 1998[77]; Arns, 2002[19]). The FD uses a conjugate gradient solver and a 6-neighbour finite difference scheme. The dimensional voxel microstructure is first converted into a network of resistors by connecting each pair of adjacent voxels of resistance and by a bond resistor of resistance. A potential gradient is applied across the sample and the system is relaxed using a conjugate gradient technique to evaluate the field. A detailed description of the original program is given in Garboczi (1998[77]).

To validate the finite difference (FD), FD is applied to a simple geometry and the numerical resistivity compares to the analytical solution. The geometry used is a $22\times22\times22$ cube inclusion centred in a $30\times30\times30$ unit cube as shown in Figure 2.9. The centred cube inclusion is defined to be phase 1 and cube host is defined to be phase 2. The analytical solution for two phase isotropic microstructure has been derived by Brown (1955[39]) and extended by Torquato (1991[197]). The effective conductivity (reciprocal of resistivity), to second order in the difference, is given by Equation 2.21:

$$\sigma=\sigma_1+c_2(\sigma_2-\sigma_1)-\frac{1}{d}c_1c_2\frac{(\sigma_2-\sigma_1)^2}{\sigma_1}+\mathrm{O}(\sigma_2-\sigma_1)^3+\cdots \qquad (2.21)$$

Where d is the dimensionality and c_i is the volume fraction of phase i, the coefficient for the $\mathrm{O}(\sigma_2-\sigma_1)^3$ and higher order terms involve details of the microstructure, and are given in terms of various correlation functions over the phase geometry (Brown, 1955[39]; Torquato, 1991[197]).

Taking $\sigma_1=1$ always, σ_2 is varied between 1 and 1.3. Figure 2.10 shows the result, plotted against σ_2, where the quantity $\sigma_1+c_2(\sigma_2-\sigma_1)$ had been subtracted from both the numerical and theoretical results. This has been done to show how the numerical results compare to the theoretical results in the quadratic term. The numerical data follows the theoretical line very closely.

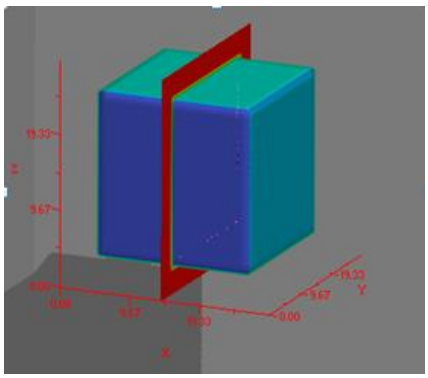

Figure 2.9: The geometry of a cube inclusion (phase 1) in a cubic host (phase 2).

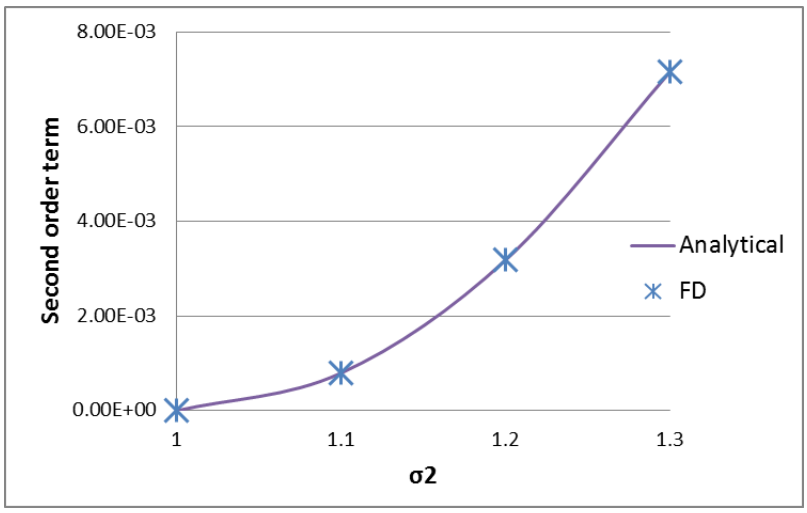

Figure 2.10: Cross plot of σ second term versus σ_2 when σ_2 differs only slightly from σ_1. The straight line is Brown's exact expansion to second order in contrast to (σ_2- σ_1).

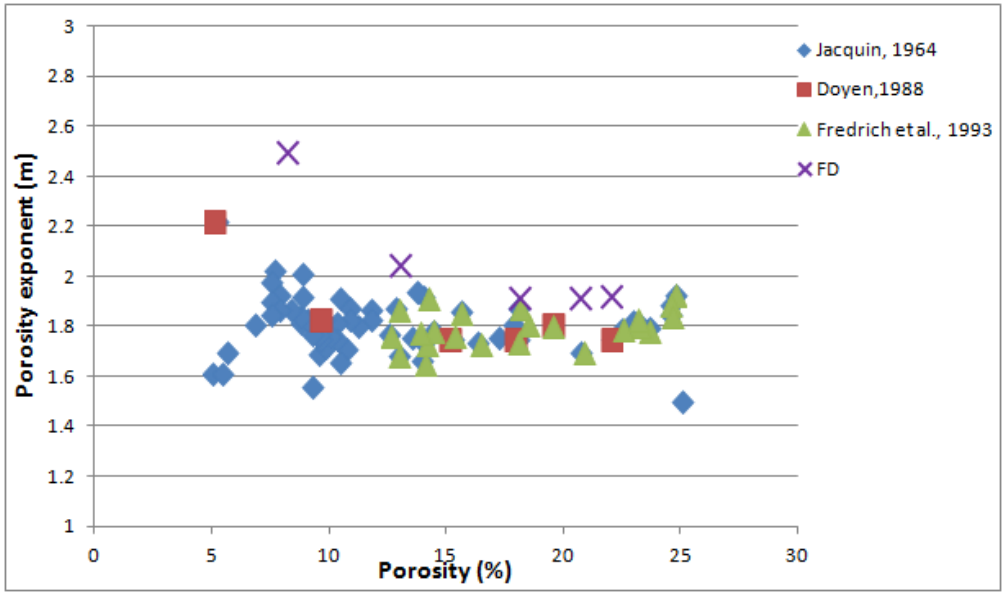

Figure 2.11: Porosity exponent simulation results compared with experiment data.

Comparison the calculation results from Fontainebleau sandstones with their experimental data is to further show the accuracy of the code in Figure 2.11. The porosity of these four Fontainebleau sandstones (from Australian National University by Arns, 2002[19]) is 7%, 13%, 17% and 22% with the same resolution of 5.68 μm. In the following text they are sometimes named $Fb\phi$, i.e. Fb13 for the 13% sample of Fontainebleau sandstone. The porosity exponent is calculated by FD by purple cross in Figure 2.11. The filled diamond, square and triangle symbols stand for the experimental results (Jacquin, 1964[91]; Doyen, 1988[64]; Fredrich *et al.*, 1993[75]). It is shown that the simulation results match well the experimental data, while the simulation result is

much bigger than the lab data for low porosity samples. This is due to the limitation of the resolution of the computed tomography (CT) image resulting into inability to distinguish the micro-pores whose contribution to the electricity is obvious (Arns, 2002[19]).

However, it takes a great deal of time and memory to solve a larger-scale Laplace equation even with a high-performance computing system (Han *et al.*, 2009[83]; Nakashima and Nakano, 2011[141]). An efficient mehod which consumes less time and memory and offers accurate resistivity or conductivty of the porous media is needed.

2.4.2 Random Walk Simulation (RW)

Diffusive random walk (RW) meets the requirement of less consumption in time and memory and estimates the corresponding values of electrical FF by calculating the average geometrical path to simulate the electrical path. Its feasibility lies in the common Laplace equation at steady state for diffusion and conduction transport processes (Toumelin and Torres-Verdín, 2005[198]).

Its usage in modelling steady state petrophysical transport properties governed by Laplace equation is not new (Johnson *et al.*, 1986[95]; Schwartz *et al.*, 1989[178]; Nakashima and Kamiya, 2007[140]). This method was successfully used to simulate single phase petrophysical measurements for rock geometries as varied as disordered grain packs or fractal rocks (Schwartz and Banavar, 1989[177]; Kostek *et al.*, 1992[108]) and micro porous carbonate rocks (Ramakrishnan *et al.*, 1998[163]; Toumelin *et al.*, 2002[200]).

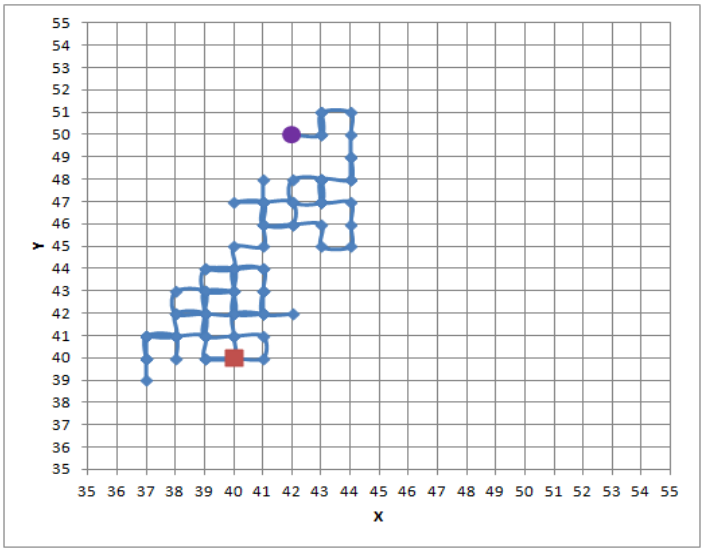

Figure 2.12: Example of a 2-D trajectory of a single random walker trial through the pore space in 2D slice. The red square is the starting point and the purple circle is the termination.

An example of a random walk trajectory in 2D slice is shown in Figure 2.12. The walker migrates on discrete pixel with time increasing by a unit time in pore space. A pore pixel is chosen randomly from among the whole image system as the start position and then the walker executes a random jump to one of the nearest pore pixels. If the randomly selected pixel is solid, the jump is not performed but the time still increases by a unit time. In this process, the mean-square displacement $\langle r^2 \rangle$ of the walkers is a function of time (t) and diffusion coefficient (D). This diffusion coefficient, D, can be expressed by the mean-square displacement divided by diffusion time t, $D = d\langle r^2 \rangle / dt$; The tortuosity of the pore structure is defined as the limiting value of the ratio of diffusion coefficient D in the free space to that in the porous media.

$$\tau^2 = \frac{D_{free}}{D_{porous}} \qquad (2.22)$$

$$FF = \frac{\tau^2}{\phi} \qquad (2.23)$$

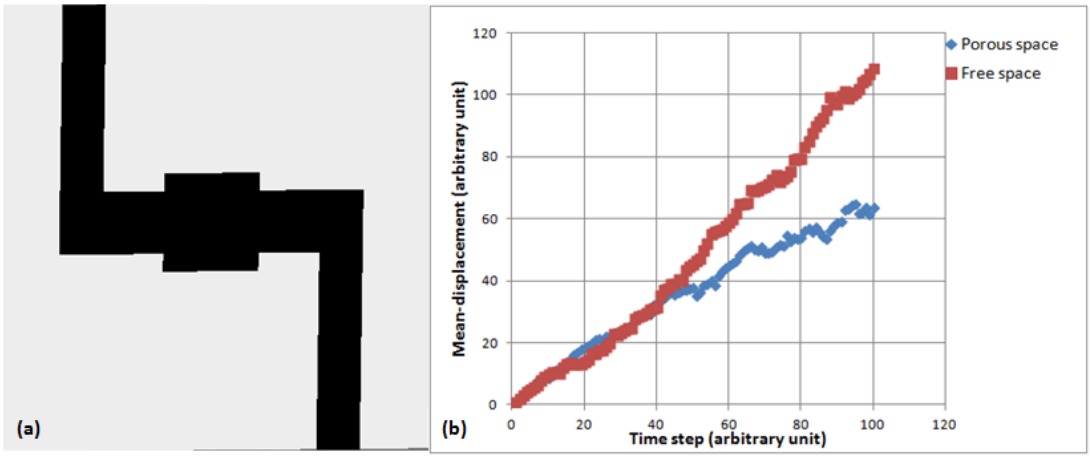

Figure 2.13: Mean square displacement versus time (b) simulated in a 2D slice for the free space whose porosity is 100% and the porous space of a tube (a), black is pore while white is solid.

Based on the Equations 2.22 and 2.23 (referred to Appendix A), the estimation of Formation Factor (FF) converts into the calculation of the slope of the curve which is the reflection of the mean-square displacement and time.

In the validation of the RW, the simulated porosity exponents are used to compare to the porosity exponents by FD. In this process, eight sub-samples (240^3 voxels) of Fb22 are used to calculate the porosity exponents in three directions shown in the Figure 2.14 and the errors in three directions are 5% (Figure 2.15). The resulting

porosity exponent for simulation time is long enough to reach asymptotic convergence with 5% error or less.

For calculation of the porous media in the capacity of the computer, FD and RW can be used according to the requirement of time and memory. However, for the large porous media which is beyond the capacity of the computer, FD and RW are not directly applied in this codition. An upscale estimation method is needed to estimate the electrical porperteis of the large porous media based on the electrical properties of its sub-samples.

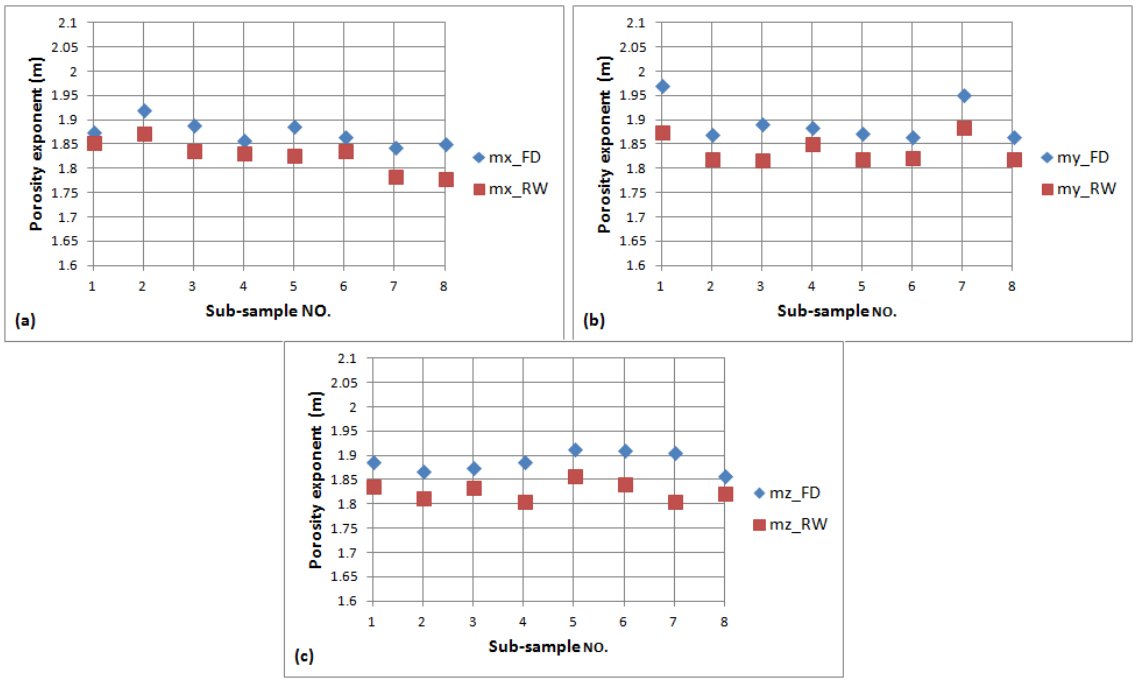

Figure 2.14: Comparison the porosity exponents calculated by finite difference (FD) and random walk (RW) in eight sub samples of Fb22 sandstones.

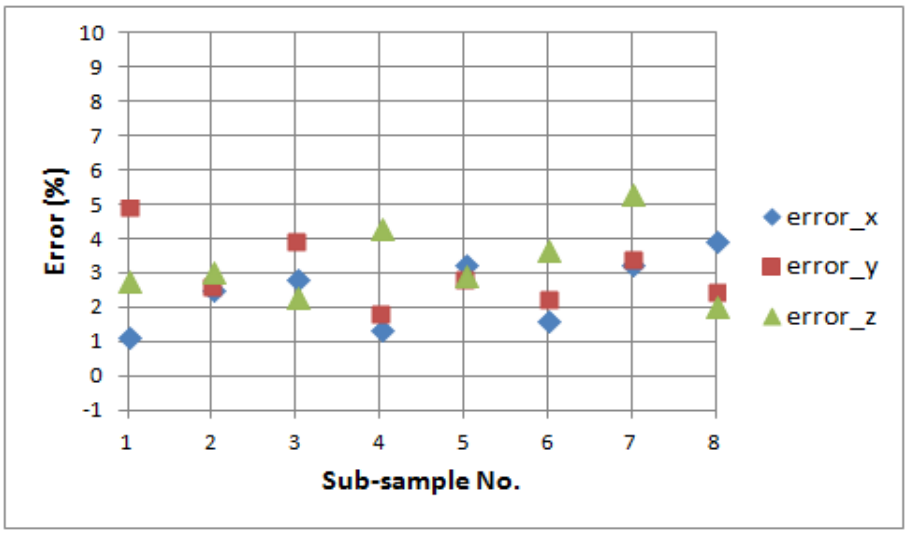

Figure 2.15: The error of the porosity exponents in three directions for the eight samples of Fb22 sandstone.

2.4.3 Renormalisation

Renormalization technique (King, 1989[104]; Renard and de Marsily, 1997[168]; Lunati *et al.*, 2001[125]; Daïan *et al.*, 2004[59]; Lu and Mai, 2007[120]; Pancaldi *et al.*, 2007[151]) is such a promising approximation method to estimate the FF of the large sample. This technique is based on repeatedly calculating the effective of a small-scale electrical network system and gradually upscaling to the original large-scale system according to Figure 2.16 (Nakashima and Nakano, 2011[141]).

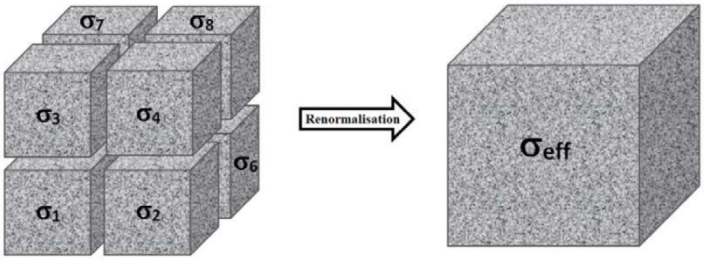

Figure 2.16: Illustration of the renormalisation approach (Khalili *et al.*, 2012[103]).

Renormalisation is significantly simplified by Green and Paterson (2007[80]), (GP method), where the exact block arrangement of block conductivity $\sigma_i, i=1,2,\cdots,8$ with i being the block number. In each iteration the effective conductivity at a larger scale is calculated as:

$$\begin{aligned}\sigma_{eff,3D} = \big[&\sigma_{eff,2D}(\sigma_1,\sigma_2,\sigma_3,\sigma_4)+\sigma_{eff,2D}(\sigma_5,\sigma_6,\sigma_7,\sigma_8)\\ &+\sigma_{eff,2D}(\sigma_5,\sigma_6,\sigma_1,\sigma_2)+\sigma_{eff,2D}(\sigma_7,\sigma_8,\sigma_3,\sigma_4)\big]/4\end{aligned} \quad (2.24)$$

Where

$$\begin{aligned}&\sigma_{eff,2D}(\sigma_1,\sigma_2,\sigma_3,\sigma_4) = 4(\sigma_1+\sigma_3)(\sigma_2+\sigma_4)\big[\sigma_1\sigma_3(\sigma_2+\sigma_4)+\sigma_2\sigma_4(\sigma_1+\sigma_3)\big]\\ &*\big\{(\sigma_1+\sigma_2+\sigma_3+\sigma_4)\big[\sigma_1\sigma_3(\sigma_2+\sigma_4)+\sigma_2\sigma_4(\sigma_1+\sigma_3)\big]\\ &+3(\sigma_1+\sigma_2)(\sigma_3+\sigma_4)(\sigma_1+\sigma_3)(\sigma_2+\sigma_4)\big\}^{-1}\end{aligned} \quad (2.25)$$

Karim and Krabbenhoft (2010[99]), (KK method), improved on the previous method by using an approximation inspired by the structure of the exact 2D solution.

$$\sigma_{eff,x} = \sqrt{\frac{\left(\frac{1}{\sigma_1}+\frac{1}{\sigma_2}\right)^{-1}+\left(\frac{1}{\sigma_3}+\frac{1}{\sigma_4}\right)^{-1}+\left(\frac{1}{\sigma_5}+\frac{1}{\sigma_6}\right)^{-1}+\left(\frac{1}{\sigma_7}+\frac{1}{\sigma_8}\right)^{-1}}{(\sigma_1+\sigma_3+\sigma_5+\sigma_7)^{-1}+(\sigma_2+\sigma_4+\sigma_6+\sigma_8)^{-1}}}\Big/2 \quad (2.26)$$

There are several other methods based on electrical analogy to show the equivalent conductivity (Renard and de Marsily, 1997[168]; Khalili *et al.*, 2012[103]).

$\mu - CT$ images have been used to calculate numerically the FF of a heterogeneous carbonate rock sample (Khalili *et al.*, 2012[103]). FF in this large scale can be estimated by renormalisation methods based on the FF in small REV block samples of that carbonate rock.

The accuracy of renormalisation method can be validated by comparison the estimation porosity exponents with porosity exponents calculated from FD. In this comparison, porosity exponents are derived from the conductivity based on the Equation 2.24, GP, and Equation 2.26, KK, in Figure 2.17. According to Figure 2.16, the FFs on the eight sub-samples (240^3) are simulated by FD and then these FFs are used to estimate the FF of large sample Fb22 (480^3) by GP and KK respectively. The porosity exponent can be calculated based on Archie First Equation in Equation (1.1 with a=1. The size of the REV for Fontainebleau sandstones is about 120 voxel in the resolution of 5.68 μm according to Arns (2002[19]). In this figure, the renormalisation method can give a good porosity exponent estimation for large scale samples.

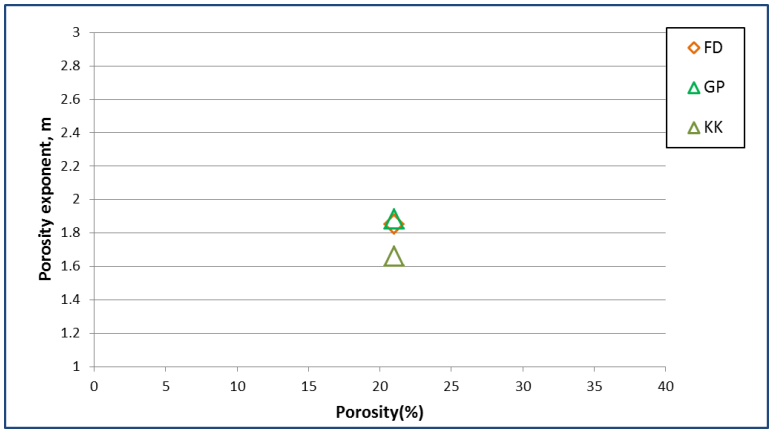

Figure 2.17: Comparison the porosity exponents of Fb22 (480^3) respectively calculated by renormalisation GP and KK methods to finite difference (FD).

2.4.4 Comparison of Numerical Methods

The principle and validation of each numerical method have been introduced. Their application depends on their advantages and weakness, this section lists the characteristics of each numerical method.

FD directly solves the Laplace equation to calculate porosity exponent.

Its advantage:

- Matching analytical and experimental data well (Garboczi, 1998[77]; Arns, 2002[19]).
- Offering current density distribution (Garboczi, 1998[77]).

- Suitable for the pore space reconstructed by CT images. The pore space itself is discretised (Arns, 2002[19]).

Disadvantage:

- Great time consumption (Han *et al.*, 2009[83]; Nakashima and Nakano, 2011[141]).
- Challenge in terms of computer, when the length of the cube is larger than 300 voxels, the simulation is beyond the calculation capacity of personal computer (CPU 3.20 GHz, RAM 8.00 GB and 64-bit operating system).

RW calculates the tortuosity of the pore space to estimate the resistivity and porosity exponent.

Advantage

- Less consumption of time and computer memory (Han *et al.*, 2009[83]; Nakashima and Nakano, 2011[141]).
- Error determined between the simulation results and experimental data (Toumelin and Torres-Verdín, 2008[199]; Nakashima and Nakano, 2011[141]).

Disadvantage

- Influence by the existence of isolated pore clusters (Nakashima and Kamiya, 2007[140]).
- Analogy to the current path instead of its real path (Clennell,1997[49]).

Renormalisation method estimates the porosity exponent of the samples based on the porosity exponents from its sub-samples.

Advantage

- Upscale method to estimate porosity exponent of large sample which is out of the calculation capacity of the computer (Nakashima and Nakano, 2011[141]; Khalili *et al.* (2012[103]).

Disadvantage

- Brief estimation of the porosity exponent;
- Dependence on the representativity of the sub samples (Nakashima and Nakano, 2011[141]; Khalili *et al.* (2012[103]).

2.5 Empirical Equations for Electricity

Electrical properties have been empirically correlated to the porosity, the famous one is Archie Law widely used from sandstones to carbonates. The Archie quations for

sandstones and carboantes are different with modification for specific condition. The Archie Equation used for carbonates in this thesis is determined according to review the existed equations. This section introduces porosity exponent development to emphasize the importance of the pore structure on the electrical properties and then presents the history of the Archie Equations to determine the equation used for coquina carbonates in this thesis. Finally the ranges of the porosity exponent are described.

As we are discussing porous media for sandstones and carbonates, the most common empirical equations are Archie's First Equation (Archie, 1942[15]) in Equation (1.1) and Archie's Second Equation in Equation (1.2), Archie's First Equation states the conductivity of the fluid saturated rock is proportional to the fluid conductivity $\sigma_0 \propto \sigma_w$. Introducing the Formation Factor (FF) in the first equation as Equation 2.27,

$$FF = \frac{\sigma_w}{\sigma_0} = \frac{R_0}{R_w} = \frac{a}{\phi^m} \qquad (2.27)$$

Based on empirical measurement of Gulf coast sandstones, Archie (1942[15]) found the porosity exponent "m" is related to lithology and the degree of cementation with $a = 1$ in his original paper. These two equations play an important role in well logging analysis with the porosity from various logging devices such as sonic log, formation density log, neutron log or electrical log in clean formation. The fluid saturation of the formation can be predicted by electrical log due to the variation of the water and oil in resistivity or conductivity. In the calculation of fluid saturation, Archie parameters a and m have to be known both of which are routinely derived from core measurement as fitting parameters.

2.5.1 Porosity Exponent Development

The first definition for the porosity exponent m was given by Archie in 1942([15]). He did not actually call it "porosity exponent", but found that this exponent helped in the description of the empirical relationship between porosity (ϕ), and Formation Factor (FF). He also found that this relationship could have a valuable application to quantitative studies of electrical logs, he was the first one who established the relationship between the resistivity (R_0) of the sand entirely filled with brine ($S_w = 1$) and the resistivity of the brine (R_w), for a large number of brine saturated cores as Equation 2.28:

$$R_0 = FF\, R_w \qquad (2.28)$$

Archie then stated that the FF is a function of formation type and porosity. This basic relationship works as a method to classify sand formations in Equation 2.29,

$$FF = \frac{1}{\phi^m} \qquad (2.29)$$

where m is a formation dependent parameter (porosity exponent). Archie explained that this exponent m takes a value of 1.3 in clean unconsolidated sand packs and falls in the range of 1.8 to 2.0 in consolidated sandstones.

Guyod (1944[81]), named the term "cementation factor" for the exponent (m). He defined it as a measure of the degree of cementation and consolidation of the rock. The greater degree of cement means the greater value of the cementation factor. Ransom (1974[165]) and Ransom (1984[164]) proposed that the exponent m is related to the geometry imposed upon the bulk volume of interstitial water by both solid and fluid insulating materials and this exponent m is more correct termed "porosity exponent". This new term was increasingly accepted due to its more accurate description of the processes affecting the porosity exponent. These processes include not only cementation but also other diagenetic processes. All of these eventually affect the pore structure (Jackson *et al.*, 1978[90]; Sen *et al.*, 1981[179]; Mendelson and Cohen, 1982[134]; Perez-Rosales, 1982[153]; Etris *et al.*, 1989[70]; Ehrlich *et al.*, 1991[68]). According to Pulido *et al.* (2007[159]), the porosity exponent of the carbonate reservoir is the most important parameter for applying the petrophysical characterization.

2.5.2 Archie First Equation Development

Porosity exponent firstly was defined as a measure of the degree of cementation and consolidation of the rock. The greater degree of cement means the greater value of the porosity exponent. Lately, the porosity exponent had been accepted as a measurement of the tortuosity of the pore geometry to current flow. Winsauer *et al.* (1952[219]) concerned with the effect of the pore geometry and tortuosity on the resistivity of the rock. Considering that the resistivity is the response to the existed fluids in rock pore throats, they introduced the tortuosity factor- a (Etris *et al.*, 1989[70]), to the Archie formula. The Archie relationship is given in the general form in Equation 2.30:

$$FF = \frac{a}{\phi^m} \qquad (2.30)$$

The form of Archie's Formation Factor (FF) relationship developed by Winsauer *et al.* (1952[219]) became known as the Humble Equation with *a* and *m* solved empirically.

$$FF = \frac{0.62}{\phi^{2.15}} \qquad (2.31)$$

Figure 2.18 compares graphically the Humble (Equation 2.31) and Archie Law for various values of the porosity exponent m and constant a. Table 2.1 represents a general equations for computing FF as a function of porosity with references to the values of "a" and "m" used in such calculation, and illustrates the effect of the lithology on FF.

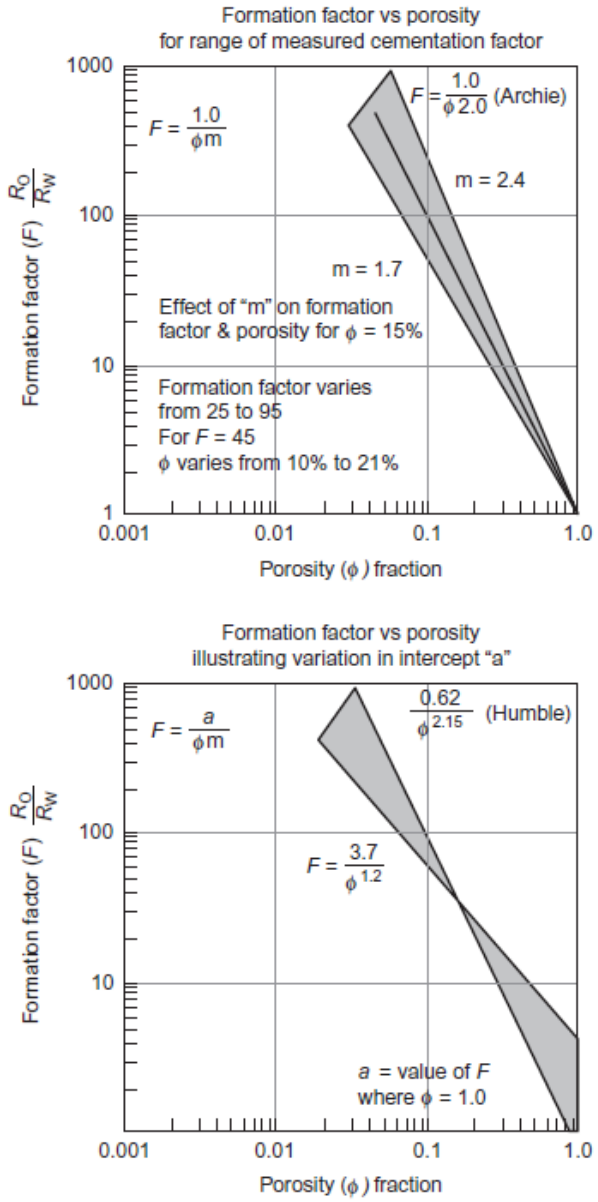

Figure 2.18: Comparison of Humble and Archie equations. Source: Courtesy of Core Laboratories (Tiab and Donaldson, 1996[195]).

"General Equations"	$FF = a/\phi^m$	General relationship (Archie 1942[15]) where: a =tortuosity factor m =porosity exponent ϕ =porosity
	$FF = 1/\phi^2$	General equation for Chalky Rocks
	$FF = 0.81/\phi^2$	For consolidated sandstones
	$FF = 0.62/\phi^{2.15}$	Humble formula for unconsolidated sands (Winsauer *et al.*, 1952[219]; Wyllie and Gregory, 1953[223])
"Philips Equations"	$FF = 1.45/\phi^{1.54}$	For average sands, 793 sandstone data points gathered by Carothers (1968[45]).
	$FF = 1.65/\phi^{1.33}$	For shaly-sands (after Carothers, 1968[45]).
	$FF = 1.45/\phi^{1.70}$	For calcareous sands (after Carothers, 1968[45]).
	$FF = 0.85/\phi^{2.14}$	For carbonates (after Carothers, 1968[45]).
	$FF = 1/\phi^{2.04}$	For 188 carbonate data points (Carothers, 1968[45]).
	$FF = 1/\phi^{2.2to2.5}$	Recommended for compacted carbonate rocks (Schlumberger, 1979[175]; Worthington, 1985[220])
"Shell Equations"	$FF = 1.0/\phi^{1.87+0.019/\phi}$	Recommended for low-porosity, non-fractured carbonates. (Schlumberger, 1979[175]; Worthington, 1985[220]).
	$FF = 2.45/\phi^{1.08}$	For Pliocene sands, Southern California; 1575 data points was gathered from 11 offshore wells. (after Porter and Carothers, 1970[156])
	$FF = 1.97/\phi^{1.29}$	For Miocene sands, Texas Louisiana, Gulf Coast; 720 data points was collected from 4 offshore wells. (after Porter and Carothers, 1970[156])
	$FF = 1.0/\phi^{(2.05-\phi)}$	For clean granular formations (after Sethi, 1979[183]).
"Chevron Formula"	$FF = 1.13/\phi^{1.73}$	Timur *et al.* (1972[196]) gathered an extensive collection of $FF-\phi$ data. The data consists of 1,833 sandstone samples.

Table 2.1: Coefficients and exponents used to calculate Formation Factor (FF) as a function of porosity(ϕ)(adopted after Mabrouk and Soliman, 2014[126]).

Table 2.2 shows the complexities of interplaying factors affecting such parameters which have always been preventing a precise estimation of FF, especially when indirect methods are used. Archie's Formation Factor relationship, in its general form (Equation 2.30), is applied broadly in the analysis of the full spectrum of reservoir lithology and textures in detection and evaluation of subsurface hydrocarbon accumulation.

Tortuosity factor "*a*"	**Porosity exponent "*m*"**
1. Surface conductance and ionic mobility occurring in water films absorbed to solid surface. i. The cation exchange capacity of particular solid materials. ii. The quantity of water absorbed to clay particles in the rock framework or within the interstices.	For the rock-water interface: 1. Pore geometry: i. Surface area to volume ratio of the rock particle, angularity, and sphericity. ii. Cementation; iii. Compaction iv. Uniformity of mineral mixture
2. Salinity of formation water	2. Anisotropy
3. Wettability relations between particular solid surface and hydrocarbons, as it influences cation exchange capacity.	3. Degree of electrical isolation by cementation
4. Presence and distribution of electrically conductive solid materials	4. Occurrence of an open fracture.

Table 2.2: Factors affecting the Formation Factor (FF) parameters (*a* and *m*) (adopted after Ransom, 1974[165]).

However, the true fundamental physical nature of these two elements "*a*" and "*m*" and consequent natural constraints on their values in Equation 2.30 has not been developed in the same breadth as its application (Adisoemarta *et al.*, 2000[2]). Hilchie (1982[87]) emphasized the importance of Archie's initial recognition that the structure of the rock system is a fundamental control of true formation resistivity. Many researchers (Borai, 1987[36]; Lucia, 1999[123]; Ragland, 2002[161]) have corroborated that porosity exponent *m* was altered by changing the amount of porosity and could be considered to be a function of it. These authors posited that the tortuosity factor a=1. This is agreed by other researchers whose consideration lies in that parameter "*a*" is a fitting parameter. Maute *et al.* (1992[131]) concluded that *a* was a weak fitting parameter without physical significance from core measurements and they recommended that *a* should be fixed to unity. Otherwise, it is mindless application of

curve-fitting programs without carful thinking (Glover, 2009[78]). Additionally, this condition (assumption) is much more suitable for carbonates according to the equations in Table 2.1, most equations for carbonates are the same with $a=1$ which are different from equations for sandstones with variable a caused by additional electricity from shale in sandstone which is a minor element in carbonates. Besides, a straight-line trend on a log plot of FF versus porosity (ϕ) with a constant for m and a ($a \neq 1$) has the same effect as applying a variable m value (at $a=1$) at different porosity values (Focke and Munn, 1987[74]).

In this thesis, Archie First Equation is taken as $a=1$, $FF=1/\phi^m$. So factors affecting on rock resistivity can be only reflected by porosity exponent (m). Now it is much more convenient to investigate factors influencing on porosity exponent which is the only considered parameter in Archie Equation 2.32.

$$FF=1/\phi^m \ (a=1) \qquad (2.32)$$

For carbonates, due to complexity and heterogeneity in pore geometry and also owing to the existence of fractures and vugs, m may vary over a wider range related to the properties of the rock. So next section, factors affecting porosity exponent would be introduced with $a=1$ after presenting the ranges of porosity exponent.

2.5.3 Ranges for Porosity Exponent

Mathematically, porosity exponent ranges from 1.0 to infinity (Wyllie and Rose, 1950[224]). Practically, it ranges from 1.0 to 3.0 (Archie, 1942[15]; Guyod, 1944[81]). When $m=1.0$, this responds to fractures aligned favourably in the direction of current flow and saturated fully by brine (Ransom, 1984[164]). The value of $m=3.0$ is found in non-connected moldic porosity (Hartmann and Beaumont, 1999[84]). There are two critical values for porosity exponent between 1.0 to 3.0: $m=1.3$ and $m=1.8$. The value $m=1.3$ corresponds theoretically to spherical grains (Pirson, 1947[155]). When the values is less than 1.3, the case is for the fractures or non-uniform features in the pore space extending along the direction of the current flow; when the value is larger than 1.3, it reflects the existence of the inefficient current paths, the irregularity of the grain in shapes, crystals and discontinuities until the value m=1.8 corresponds to the consolidated sandstones and intergranular pore, the irregularity and dead-end pore space derived from vug causes the increase of porosity exponent. A wide range of values for different sediments and rocks, including dolomites, limestones, sandstones, clays, was

exhibited by Salem and Chilingarian (1999[173]). Table 2.3 is a compilation of values for the porosity exponent (m) together with a bibliographic reference.

Author	Restrictions	m -range
Archie (1942[15])	Consolidated sandstone	1.8-2.0
	Clean unconsolidated sands packed in laboratory.	>1.3
Pirson (1947[155])	Theoretically and corresponds to grains that have a spherical shape	1.3
Wyllie and Rose (1950[224])	Mathematically	1.0-∞
	In practice	1.3-3.0
Winsauer *et al.* (1952[219])	Measurements in many sandstones	2.15
Keller (1953[101])	Oil-wet core sands	1.5-11.7
Waxman and Thomas(1974[217])	Non-clay	1.4
Clavier *et al.* (1977[48])	Clay-corrected	1.4
Ransom (1984[164])	m is independent of shaliness	1.8-2.1
	Fractures, 100% fracture porosity	1.89-2.13
Maute and Sprunt (1992[131])	Irregular grain shapes, crystals and discontinuities	1.3
	Carbonate reservoir using logs assuming $a=1$	>1.3
	Sandstone African cores: clean, high porosity. Conventional method	<1.3
	Core Archie-parameter estimation (CAPE) method	1.81-2.00
Hartmann and Beaumont (1999[84])	Shaly sandstones	1.79-1.81
AL-Awad (2001[10])	Clean sandstone	2.0

Table 2.3: Ranges for the porosity exponent *m* (Kadhim *et al.*, 2013[97]).

2.6 Factors Affecting Porosity Exponent

Porosity exponent relates the resistivity of the porous media to their pore structures. While the pore structures are affected by various cases, it is necessary to know about the factors effect on the porosity exponent. This section generally lists the factors effect on the porosity exponent.

Researchers have shown that the value of the porosity exponent is largely affected by secondary porosity, pore throat size, conductivity of water and minerals, surface area per unit volume and cement (Wardlaw, 1980[215]; Ransom, 1984[164]; Rasmus, 1986[167]). The porosity exponent strongly depends on shape and surface area of composite particles and tortuosity. It has been given considerable attention by researchers, because of its relation to sediments' behaviour (Salem, 1993[171]). Elias and Steagall (1996[69]) had shown that the values of the porosity exponent (m) and saturation exponent (n) were largely affected by reservoir pressure and temperature conditions, mineralogy, pore throat size distribution, pore geometry and the wettability condition of the reservoir rock. This fact reveals the need to carry out laboratory resistivity measurements in order to obtain representative values of such parameters for a particular reservoir system.

2.6.1 Grains and Pores

The higher angularity in the shape of the grains and pores results in higher value of porosity exponent, the angularity is caused by diagenesis, catagenesis, and epigenesist (consolidation, compaction, cementation and so on) (Salem and Chilingarian, 1999[173]).

In terms of type of grains, the existence of shaliness or clay minerals and the presence of heterogeneous mixtures in the grains lead to increase the porosity exponent. While the increase of sands, sandstones, porous dolomites, and fractured limestone generally results in lower value of porosity exponent (Salem and Chilingarian, 1999[173]).

The size of the grains has less effect on the porosity exponent compared with the effect of the grains' type (Salem and Chilingarian, 1999[173]).

In terms of the type of pores, based on petrographic analysis, porosity exponent can be defined as the logarithm of throat area divided by the logarithm of pore area (Ehrlich *et al.*, 1991[68]). This indicates that the closer the value of throat radius to pore radius, the closer is the value of m to unity. The porosity exponent is affected by the pore

system of the carbonates (intergranular, intercrystalline, fractured, or vuggy), and then the porosity exponent can indicate the type of porosity (total "absolute" porosity, open "saturation" porosity, or effective "dynamic" porosity) (Salem and Chilingarian, 1999[173]). Aguilera (1976[6]) showed that the increase of fractures decreases the value of m, and Lucia (1983[121]) exhibited that the increase of vug proportion increases the value of m. In low porous media (where porosity is less than 5%), the grains are pressed closer to each other and the pores become smaller resulting in the increase of porosity exponent (m).

2.6.2 Specific Surface Area

The specific surface area is variously defined as the interstitial surface area of the pores and pore channels per unit of bulk volume, grain volume, pore volume or per unit of weight. Its minimum corresponds to the spherical grains. It is the reflection of the irregularity of the grains, the more irregular of the grains, the larger of the specific surface area and then the larger of the porosity exponent (Salem and Chilingarian, 1999[173]).

2.6.3 Tortuosity

Tortuosity is defined as the ratio of the actual or effective length of a flow path to the length of a porous medium, parallel to the overall direction of flow. Its effect on porosity exponent m is significant. The dead-end pores and the grains with irregular shapes exert more resistance to the electrical current flow causing high tortuosity (Salem and Chilingarian, 1999[173]).

2.6.4 Anisotropy

Anisotropy is a measure of the variations of physical properties in the horizontal and vertical directions, which contributes to the variations of porosity exponent m. It is expressed in terms of the electric anisotropy coefficient $\lambda_e = \sqrt{R_v / R_h}$, where R_v and R_h are, respectively, normal and parallel to the bedding planes. Anisotropy is attributed to many reasons, including orientation of grains, variations in the properties of the grain and pore, tortuosity and so on (Salem, 1994[172]). Kunetz (1966[109]), Salem (1990[170]) and Tiab and Donaldson (1996[195]) pointed out that electric anisotropy coefficient λ_e normally ranged from 1 to 2. For shaly sandstones, Salem (1994[172])

obtained value ranging from 1 to 1.7. In this study, the average anisotropy coefficients for three carbonates are about 1.33, 2.02 and 1.53 respectively compared with 1.08 for the Fontainebleau sandstone (Fb22) where porosity is 22%. The average anisotropy coefficient for each rock sample is based on these anisotropy coefficients of the eight representative sub samples which comprise the whole rock sample. For each sub sample, the porosity exponent in three directions can be obtained and then set the maximal porosity exponent as m_v and the minimum as m_h.The anisotropy coefficient can be expressed in Equation 2.33:

$$\lambda_e = \sqrt{m_{\max} / m_{\min}} \qquad (2.33)$$

2.6.5 Overburden Pressure (Compaction)

The effect of overburden pressure on the porosity exponent m is not clearly known. While the overwhelming majority of the previous findings support the conclusion that as the pressure increases, the increase in porosity exponent is much greater than the corresponding decrease in porosity indicating that porosity exponent is a function of pressure even after porosity correction. It attributed to the change in pore structure caused by pressure such as the closure of crack-like pore space, increase of the pore constriction in low and medium porosity sandstones (Mahmood *et al.*, 1991[127]).

Its effect on porosity exponent (m), porosity (ϕ) and Formation Factor (FF), due to compaction, were investigated by Fatt (1957[72]) and Wyble (1958[222]) from experiment. Compression of rocks results in radical changes in pore structure and shape of grains. As the degree of compaction increases, grains are flattened (become more deformed), which results in higher degrees of angularity, pore constriction, cementation, and higher resistivity (and higher porosity exponent and FF). Meanwhile Fatt (1957[72]) found that the increase in porosity exponent by compression for rocks with conducting solids, shale, was smaller, after correcting for shale, the increase in porosity exponent became higher and the porosity exponent was only a function of the net pressure, which is the difference between the external and internal pressures.

However, an opposite behaviour (decrease) in porosity exponent with the increase of pressure was observed in high porosity sandstones. In carbonates, porosity exponent seemed to vary less with pressure (Mahmood *et al.*, 1991[127]).

2.6.6 Temperature

The effect of temperature on porosity exponent is related to the change in rock-fluid interaction and the change in the pore structure for sandstones and carbonates, its effect is observed by experimental results. For sandstones and shaly sandstones, the porosity exponent generally increases with the increase of temperature (Sanyal *et al.*, 1972[174]; Brannan and Von Gonten, 1973[38]; Jing and Archer, 1991[94]; Mahmood *et al.*, 1991[127]). There are two factors influencing porosity exponent, one is the most important component in sandstones, shale, offering excess conductivity which is related to the temperature and the other one is the thermal effect including thermal expansion of grains and perhaps some thermal induced pore collapses changing the pore structure by introduction of the pore constriction and surface area. For carbonates, Sanyal *et al.*, (1972[174]) observed that their porosity exponents increased with the increase of temperature attributing to the change of the pore constriction and surface area due to the thermal effect. However, Dolka (1981[62]) in his experiment for Saudi reservoir lime stones found that the effect of temperature on porosity exponent was nil which was the same as the result of Elias and Steagall (1996[69]) measuring the carbonates from Macaé formation of the Bonito Field, Campos Basin, Brazil.

2.7 Porosity Exponent in Carbonates

The characteristics of carbonates lie in its complexity of the pore structures due to the variety of the pore types. The effect of various pore types on the porosity exponent is listed in this section according to the existing experimental data.

Focke and Munn (1987[74]) presented the results of a study of the relationship between variable porosity exponent m values measured on core plugs and detailed carbonate rock types. They found that the high porosity exponent values are often representative for specific rock types and that these values should not be rejected but applied selectively in log analysis. A simplified schematic of the major genetic porosity types used in their study is presented in Figure 2.19. Various plugs, from reservoirs offshore Qatar, with a size up to 4 inch ($10cm$) in diameter were used. Most data refer to clean carbonate rocks. In clean carbonates, Formation Factor (FF) does not appear to be affected by brine salinity, that is, porosity exponent m is not influenced by this factor. Trends in porosity exponents (m) for carbonate pore systems were investigated by Ragland (2002[161]) according to the m values calculated from laboratory resistivity measurement, porosity data and section analysis of pore systems.

The pore types in their study in Figure 2.19 were classified as (a) intergranular (IG) (lime and dolomite grainstones); (b) intercrystalline (IC) (sucrosic dolomites); (c) moldic (moldic oolitic limestone and dolomite grainstones); (d) matrix or chalky (mudstones, chalks); (e) moldic or vuggy in addition to matrix (vuggy packstones and wackstones); (f) fracture (FT) or fissure porosity.

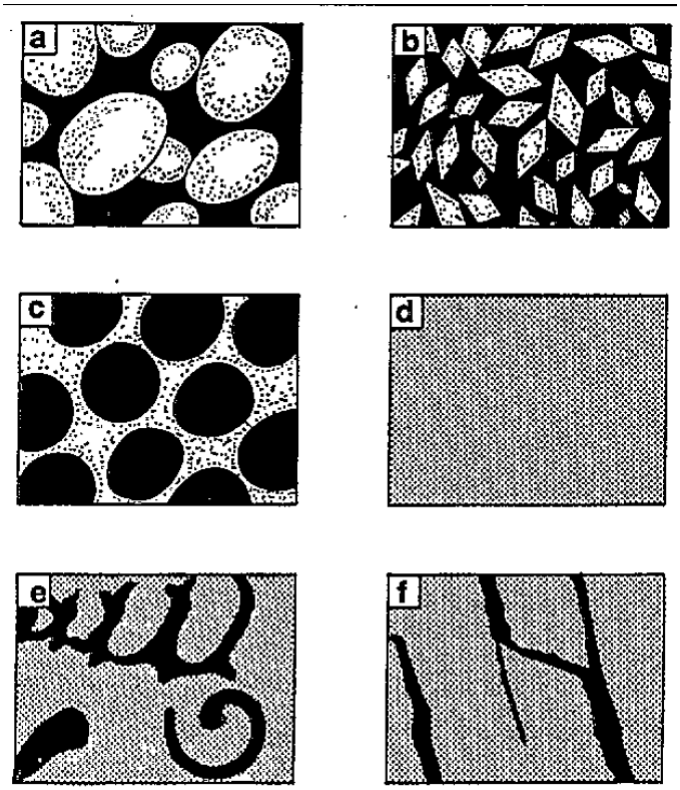

Figure 2.19: Genetic classification of porosity type correlated (porosity is black) (Focke and Munn, 1987[74]).

2.7.1 Influence of Interparticle Pores

In the Focke and Munn's study (Focke and Munn, 1987[74]), IG and IC show a very similar resistivity response in Figure 2.20 due to both of them belonging to interparticle pore type.

In the interparticle pore type, the relationship between FF and porosity is a straight line with the porosity exponent equal to 2 (Focke and Munn, 1987[74]). However, in their study, porosity exponent is less than 2 at porosity <5% possibly which is contrary to the expectation that low porosity samples should have more tortuous porosity systems and the value of m should be greater than 2. They pointed out that micro fractures (either induced or natural) were responsible for the low values of the porosity exponent. They have not found evidence supporting such fractures. But low porosity

exponent from low-porosity carbonates have also been reported elsewhere in the Arabian Gulf (Borai, 1985[37]).

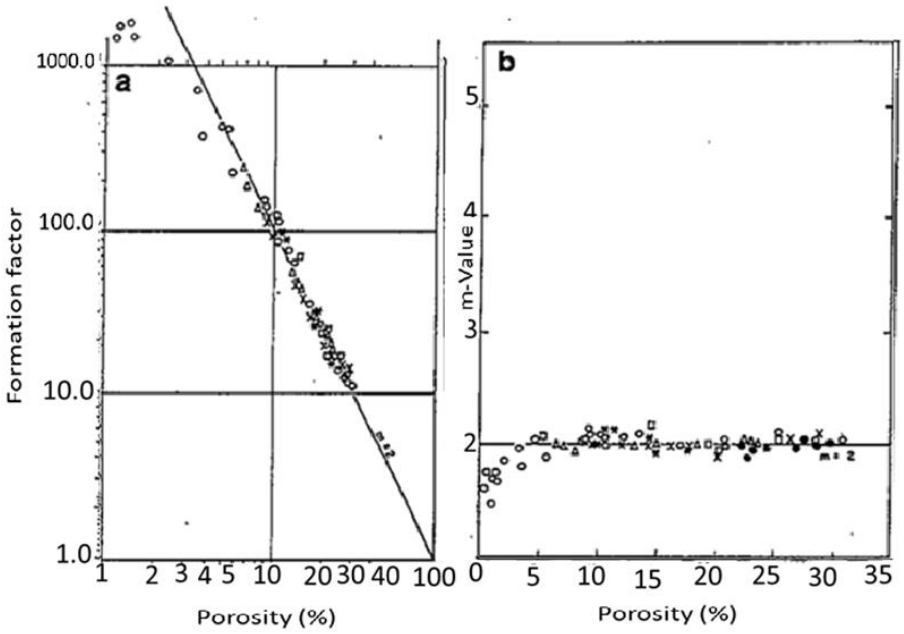

Figure 2.20:FF and *m* (a=1) vs.ϕ for intergranular porosity and intercrystalline porosity (Focke and Munn, 1987[74]).

The relationship between amount of interparticle pore and porosity exponent m was proposed by Ragland (2002[161]) that m decreased as the amount of interparticle porosity increased seen in the cross plot (Figure 2.21). In the interparticle porosity dominated carbonates, m values range from 1.38 to 2.48, with an average of 1.90.

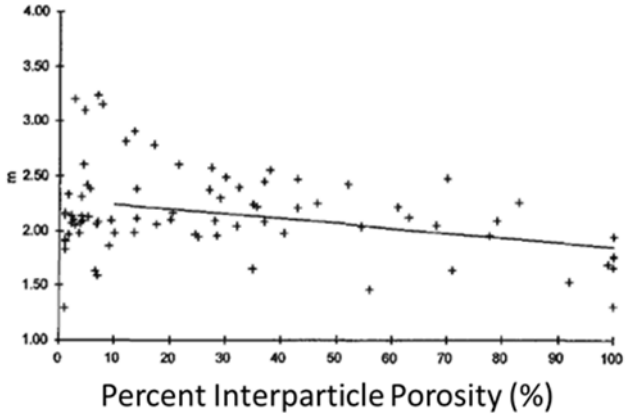

Figure 2.21: General downward trend in *m* values with increasing interparticle porosity (Ragland, 2002[161]).

2.7.2 Influence of Moldic Pores

The moldic pore type effect on the porosity exponent generally lies in the increase of porosity exponent with increasing porosity as well as some differentiation with permeability. The samples with lower permeability usually shows higher porosity exponent than the samples with higher permeability shown in Figure 2.22 and Figure 2.23 for moldic lime grainstones and dolomites respectively. A trend toward increasing m with increasing amounts of moldic porosity is apparent when m values are plotted against the percentage of moldic porosity (Figure 2.24).

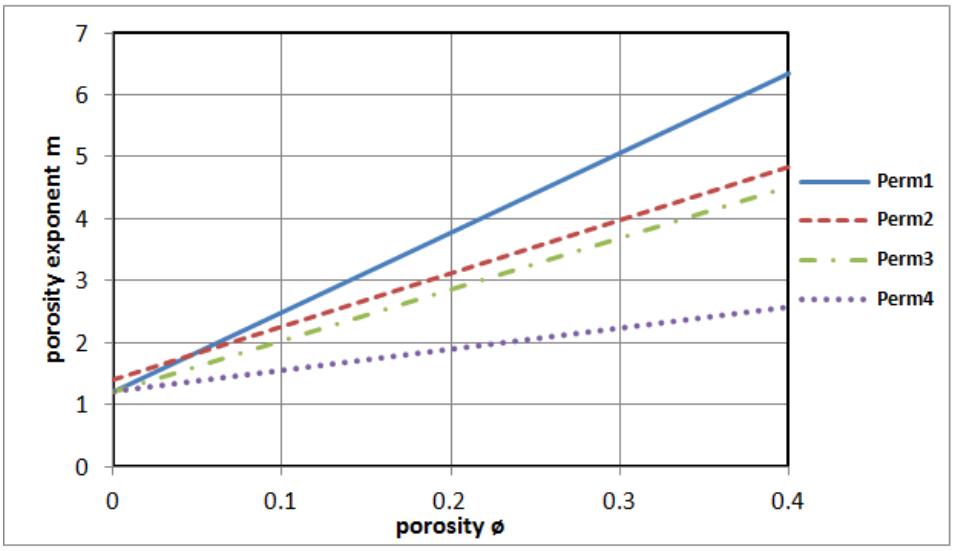

Figure 2.22: m (a=1) vs. ϕ for moldic limestones with four permeability classes. Perm1<*0.1md*, *0.1md*<Perm2<*1md*, Perm3 is from *1md* to *100md*, Perm4>*100md* (Focke and Munn, 1987[74]).

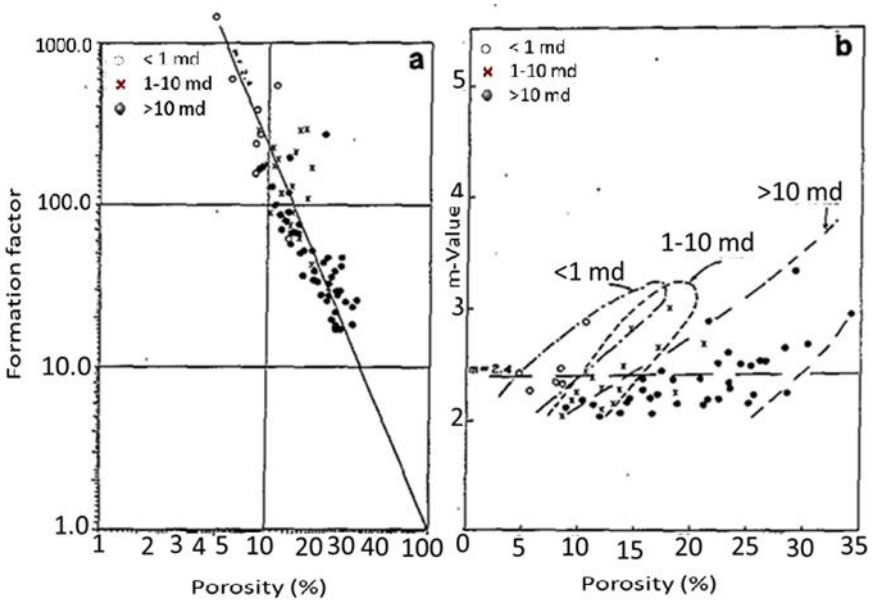

Figure 2.23: FF and m (a=1) vs.ϕ for moldic dolomites. Symbols refer to different permeability classes (Focke and Munn, 1987[74]).

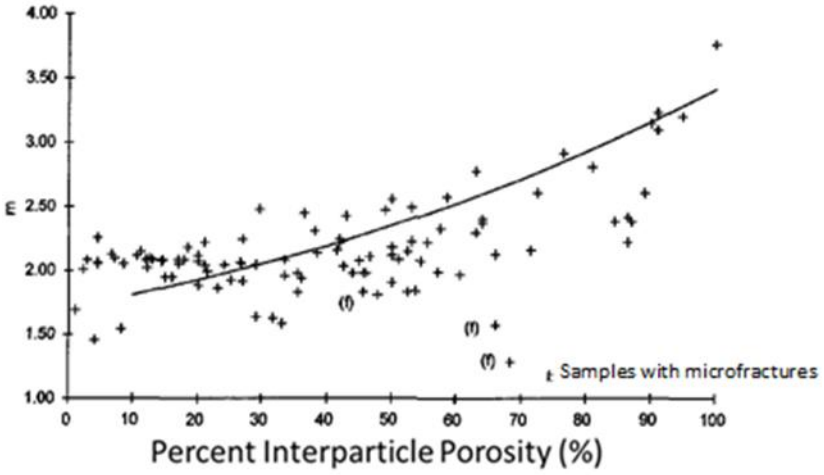

Figure 2.24: General upward trend in *m* values with increasing moldic porosity. Note that two of the three fractured samples have significantly lower *m* values (Ragland, 2002[161]).

2.7.3 Influence of Matrix Pores

Matrix pore type exists in mudstone and chalks with the character that there are not significant moldic, vuggy, fracture or fissure porosity. The porosity exponent is constant at around 2.0 in Figure 2.25.

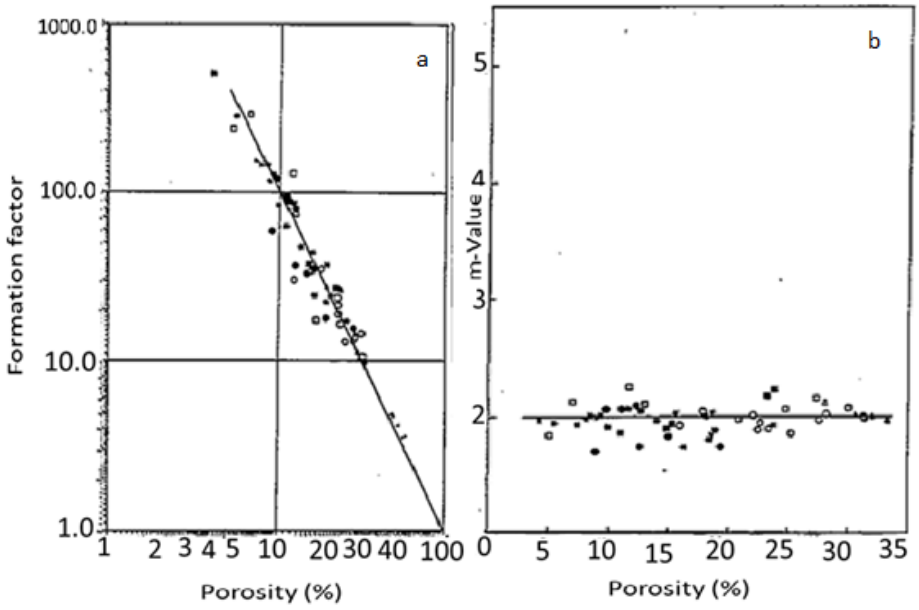

Figure 2.25: FF and *m* (a=1) vs.ϕ for rock types with matrix or chalky porosity only. Symbols refer to different wells (Focke and Munn, 1987[74]).

2.7.4 Influence of Vuggy Pores

Vuggy pores consist of the unconnected or poorly connected porosity in addition to matrix (chalky porosity) (Figure 2.19e). The effect of the vug (VG) lies in the increase

of the porosity exponent, the increase depends on the amount and degree of the interconnected vug in the rock (Focke and Munn, 1987[74]).

2.7.5 Influence of Fracture and Fissure Pores

Rocks with fracture and fissure porosity are shown in Figure 2.19f. Very few consistent laboratory data are available for this rock type. Porosity exponent values decrease (toward a theoretical value of unity) by straight pathways present in rock that also depend on orientation (Wyllie and Rose, 1950[224]; Sen *et al.*, 1981[179]; Rasmus, 1983[166]).

2.7.6 Influence of Micro Pores

Water-filled micro pores($\mu\phi$) (pore size<0.3/0.5 μm) can facilitate the flow of electricity through a rock, lithology with moderate to abundant $\mu\phi$ may have actual m values that are lower than expected based on the larger pores of the system. Electrical flow may not necessarily be confined to more tortuous paths through the larger pore system, but may follow a shorter course through the connected $\mu\phi$ (Asquith, 1985[23]). Consequently, trapped irreducible water with moderately to highly micro porous carbonates could lead to anomalously low resistivity measurements. When the estimated amounts of micro porosity in the study of Ragland (2002[161]) were plotted against porosity exponent, a slightly downward trend in porosity exponent was noted as micro porosity increased (Figure 2.26).

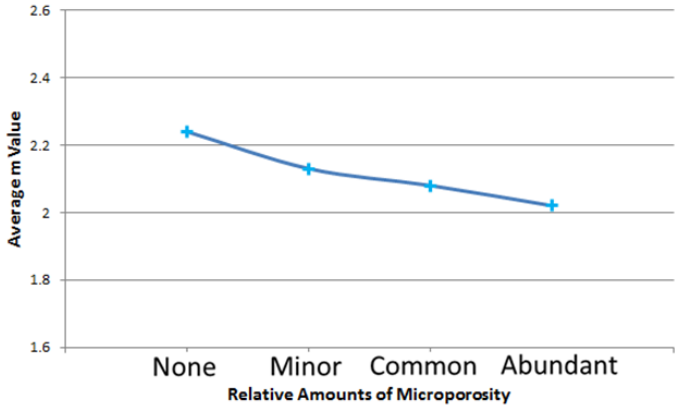

Figure 2.26: A downtrend in average *m* as micro porosity increases (from Ragland, 2002[161]).

From influences of pore types, it is clear that in carbonates, porosity exponent for interparticle or matrix porosity is about 2.0; Exponent m for fracture and fissure is close to unity which is related to their orientation; Variations of m happens in moldic or

vuggy pore type as well as this pore type connecting with other pore types. Trends in m values for basic pore types and modified pore systems are shown in Table 2.4. In this table, the rank of the relative abundances of pore types in a hierarchical system is devised by Ragland (2002[161]). In his manner, X is the predominant pore type and the rest pore types are $Y_1, Y_2, \cdots, Y_n$ with less amount. $X:Y$ means they are almost equal with the amount ratio of Y to X about 71 percent to 100 percent; $X>Y$ indicates that this ratio is about 30 to 70 percent; and $X(Y)$ indicates that Y is 10 to 29 percent as the same as X in that sample.

Pore Type	**Average *m* value**
Moldic>90	3.29
Moldic>50	2.46
Moldic (interparticle)	2.70
Moldic>interparticle	2.33
Moldic:interparticle	2.26
Moldic(connected dissolution pore)	2.18
Moldic>connected dissolution pore	2.20
Moldic: connected dissolution pore	2.06
Interparticle>90	1.67
Interparticle>50	1.90
Interparticle (moldic)	2.03
Interparticle>moldic	2.13
Interparticle:moldic	2.36
Intercrystalline>50	1.93
Intercrystalline>90	1.97

Table 2.4: Trends in porosity exponent m values for basic pore types and modified pore systems (Ragland, 2002[161]).

In the sample dominated by moldic pore, the inclusion of the dissolution pore lowers the porosity exponent slightly more than the presence of the interparticle pores. With the increase of the dissolution pore in the pore system dominated by moldic pore, porosity exponent decreases from 3.29 to 2.06 when the amount of dissolution pore

reaches 70% to 100% of the amount of the moldic pores. The porosity exponent drops to 2.26 for the same amount of the inclusion by interparticle pore.

For the sample dominated by interparticle pore, porosity exponent ranges from 1.6 to 2.4 with average porosity exponent of 1.90. With the increasing inclusion of moldic pore into the interparticle host medium, the porosity exponent increases to the value between 2.0 to 2.4. Therefore, the porosity exponent for the interparticle pore type is reasonable from 1.7 to 1.9. With the inclusion of isolated pore such as molds, it may shift above 2.0.

The effect of vuggy pores on porosity exponent in carbonates is also important. A relationship between porosity exponent, m, and a ratio called the vug porosity ratio, which is the percentage of separate vug porosity (not connected porosity) in the total porosity, is proposed by Lucia (1983[121]), the ratio is normalised to 1.0. This relationship is shown in Figure 2.27. The vug porosity ratio was measured visually at that time on a number of samples where porosity exponents had been measured. Figure 2.27 then can be used to estimate porosity exponent for carbonate rocks with no touching vugs. The effect of touching vugs on the porosity exponent is an unknown which would be investigated in this thesis from its effect on the geometry (GM) and topology (TP), Formation Factor (FF) as well as porosity exponent by pore scale modelling in Chapter 4.

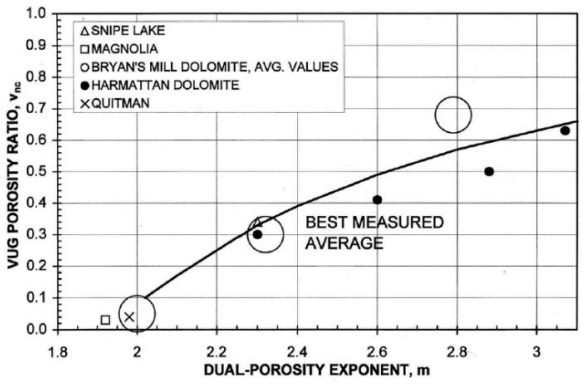

Figure 2.27: Measured values of porosity exponent vs. vug porosity ratio (after Lucia, 1983[121]).

Focke and Munn (1987[74]) correctly stated that in addition to the vug porosity ratio, the value of porosity exponent should also be a function of total porosity. On the basis of their laboratory data, they extended Lucia's plot (Figure 2.27) to incorporate results of vuggy carbonates as shown in Figure 2.28. Assuming their moldic limestone have a vug porosity ratio of approximately 100%, they postulated the dashed lines shown on Figure 2.28 for a series of porosities from 10% to 35%.

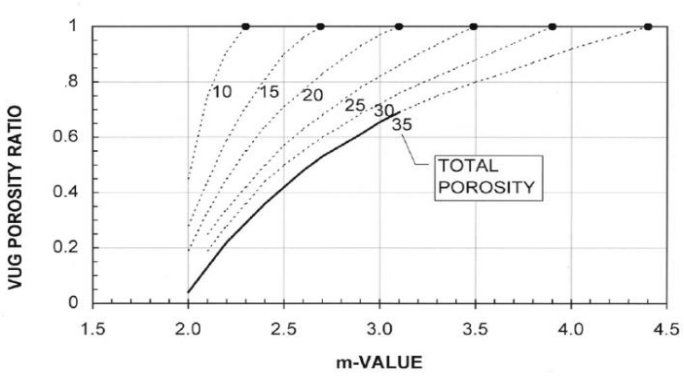

Figure 2.28: Measured values of *m* versus vug porosity ratio. Dash lines are regarded as speculative by Focke and Munn (1987[74]). Black continuous solid line is Lucia's best-measured average from Figure 2.27. Black dots represent moldic limestone.

In order to solve the effects of different pore types, especially vug (VG) and fracture (FT), on porosity exponent, theoretical models (porosity models) firstly from dual porosity model and then to triple porosity model are developed with assumption of the electrical arrangement of the pore types in series or parallel.

2.8 Porosity Models

In carbonates, the pore types dramatically affect the porosity exponent. The porosity exponent can be theoretically derived from the simplified arrangements of the pore types by porosity models to investigate the effect of pore types on the porosity exponent. This section illustrates the porosity models for carbonates.

The petrophysical characteristics of the porosity exponent (Archie, 1942[15]) in fractured and vuggy reservoirs have been investigated by many researchers for several decades. In these investigations, three different values of porosity exponent should be considered: one for the matrix representing interparticle pore (m_b), one for fractures (touching vug) (m_f), and one for the composite system (m).

Towle (1962[201]) in a classic paper used a theoretical model to present the porosity exponent of vuggy and fractured reservoirs. The porosity exponent of the vuggy reservoir was from 2.67 to more than 2.73, larger than usual, while the porosity exponent of the fractured reservoir from 1.07 to 1.25 was much smaller than usual. This was due to the ignorance of the matrix pore (Aguilera, 1976[6]). Aguilera then extended Towle's fractured model with consideration of matrix pore and his model indicated that with the increase of the fracture, the value of the porosity exponent became smaller. This latter effect is something that has been observed in practice over the ensuing year.

The effect of the tortuosity and porosity exponent of the fracture on the porosity exponent of the fracture model were investigated by Rasmus (1983[166]) and Draxler and Edwards (1986[65]). Their models were useful while they must be treated carefully as these models resulted in incorrect porosity exponents in values of $m > m_b$ as the total porosity increased (Aguilera, 1995[7]). Serra (1989[182]) and Aguilera and Aguilera (2003[5]) developed graphs of the porosity exponent m versus total porosity for dual-porosity systems representing (1) reservoirs with matrix pore and fractures and (2) reservoirs with matrix pore and non-connected vugs.

2.8.1 Dual Porosity Models

In dual porosity models, a reservoir with both matrix porosity and non-connected vug porosity can be modelled as a series resistance network. A reservoir with both matrix and fracture (connected vugs) porosities can be modelled as a parallel resistance network. Serra (1989[182]) presented a graph of the porosity exponent versus total porosity for both fractured reservoirs and reservoirs with non-connected vug (Figure 2.29). The graph was developed with the use of following equations:

$$m = \log\left[\left(\phi - \phi_2\right)^{m_b} + \phi_2^{m_f}\right] \Big/ \log\phi \qquad (2.34)$$

for the case of natural fractures or connected (touching) vugs, and

$$m = m_b \log\left(\phi - \phi_{nc}\right) \Big/ \log\phi \qquad (2.35)$$

for the case of non-connected vugs.

In the above equations, m_b is the porosity exponent for matrix porosity ϕ_m, (interparticle porosity, $\phi - \phi_2$ in Equation 2.34 and $\phi - \phi_{nc}$ in Equation 2.35 which is expressed by the volume of matrix interparticle pores divided by the rock sample bulk volume) and m_f is the porosity exponent for fractures or connected vugs whose porosity (ϕ_2) is the ratio of the volume of fractures or connected vugs to sample bulk volume. ϕ_{nc} is the non-connected vug porosity.

Wang and Lucia (1993[214]) developed a dual porosity model in Equation 2.36 with the two components (intergranular and vuggy porosity) in parallel resistance network. Each component satisfies Archie's relation between resistivity and Formation Factor (FF).

$$m = \log\left(\phi_{ip}^{m_{ip}} + \phi_v \Big/ a_v\right) \Big/ \log\left(\phi_t\right) \qquad (2.36)$$

where m_{ip} is the porosity exponent for IG with porosity of ϕ_{ip}, ϕ_v is the porosity of VG and its type is determined by a_v, ϕ_t is total porosity $\phi_t = \phi_{ip} + \phi_v$.

So the porosity exponent is a function of the total porosity, the porosity partition, the porosity exponent of the interparticle fraction (m_{ip}) and the connectivity of the vuggy fraction (a_v). The accuracy of the porosity partition is the key point for the determination of the porosity exponent (Ballay, 2012[27]).

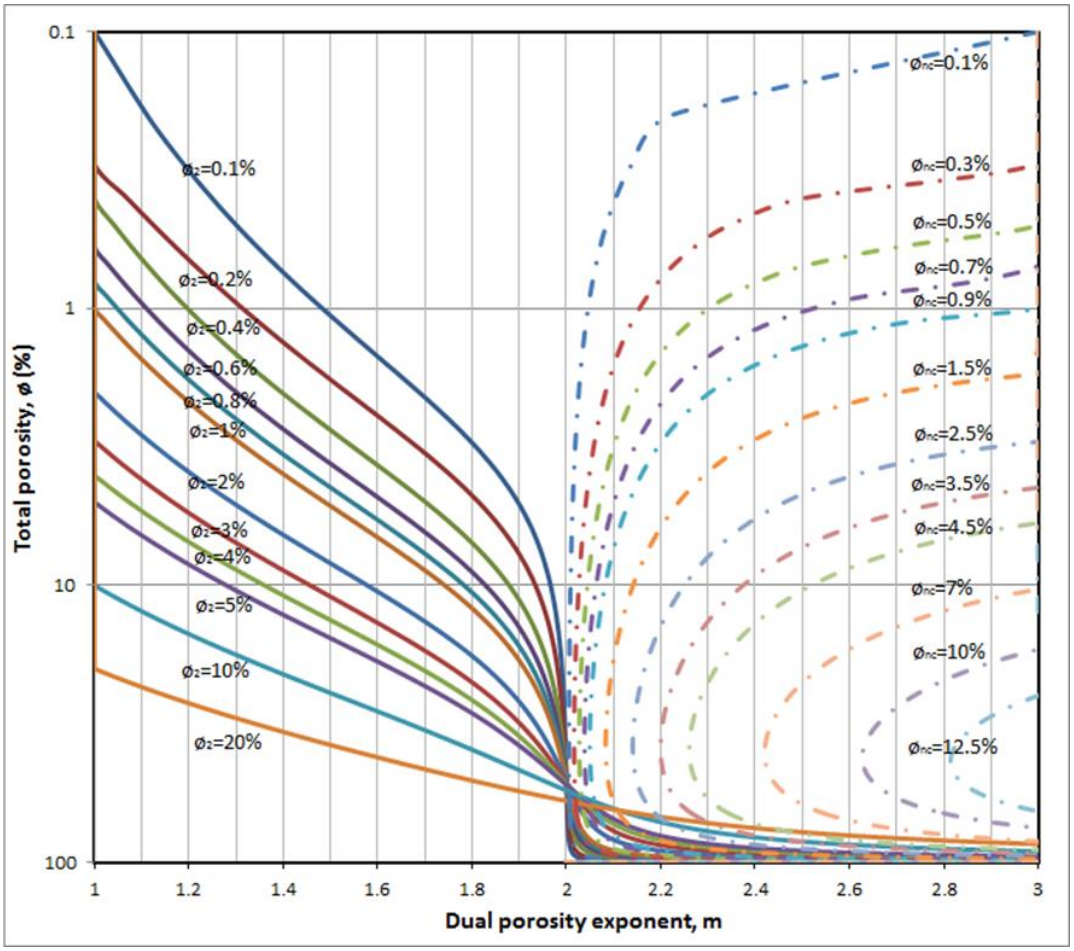

Figure 2.29: Serra's (1989[182]) chart for determining porosity exponent as a function of fracture porosity (left, solid line) and as a function of the porosity of non-connected vugs (right, dash line). It assumed m_b was equal to 2.0 and m_f was 1.0.

Serra's model provides reasonable results at low porosities but breaks down at about 0.4 (40%) porosity when the values of porosity exponent change direction and start to increase again. Aguilera (1995[7]) pointed out that Serra's model provided values of the porosity exponent larger than 2.0 for the composite system ($m_b = 2.0$) and could fail for m_f if different 1.0. The reason for the failure is an improper scaling of the matrix porosity (Aguilera and Aguilera, 2003[5]).

Improved dual porosity models with the same resistance network assumption are proposed by Aguilera and Aguilera (2003[5]). Its change lies in the value of porosity related to m_b, this porosity (ϕ_b) should be defined as the percent of the volume of interparticle pore in the matrix to the total volume of matrix system (without including any vugs or fractures) instead of the porosity of matrix (interparticle pore), ϕ_m, which is the volume of interparticle pore in the matrix divided by the sample bulk volume, which includes matrix system, vugs and fractures. The relationship between different pore types keeps constant.

$$\phi = \phi_m + \phi_2, \phi_b = \phi_m / (1 - \phi_2) \quad (2.37)$$

for the case of natural fractures or connected (touching) vugs, and

$$\phi = \phi_m + \phi_{nc}, \phi_b = \phi_m / (1 - \phi_{nc}) \quad (2.38)$$

for the case of non-connected vugs.

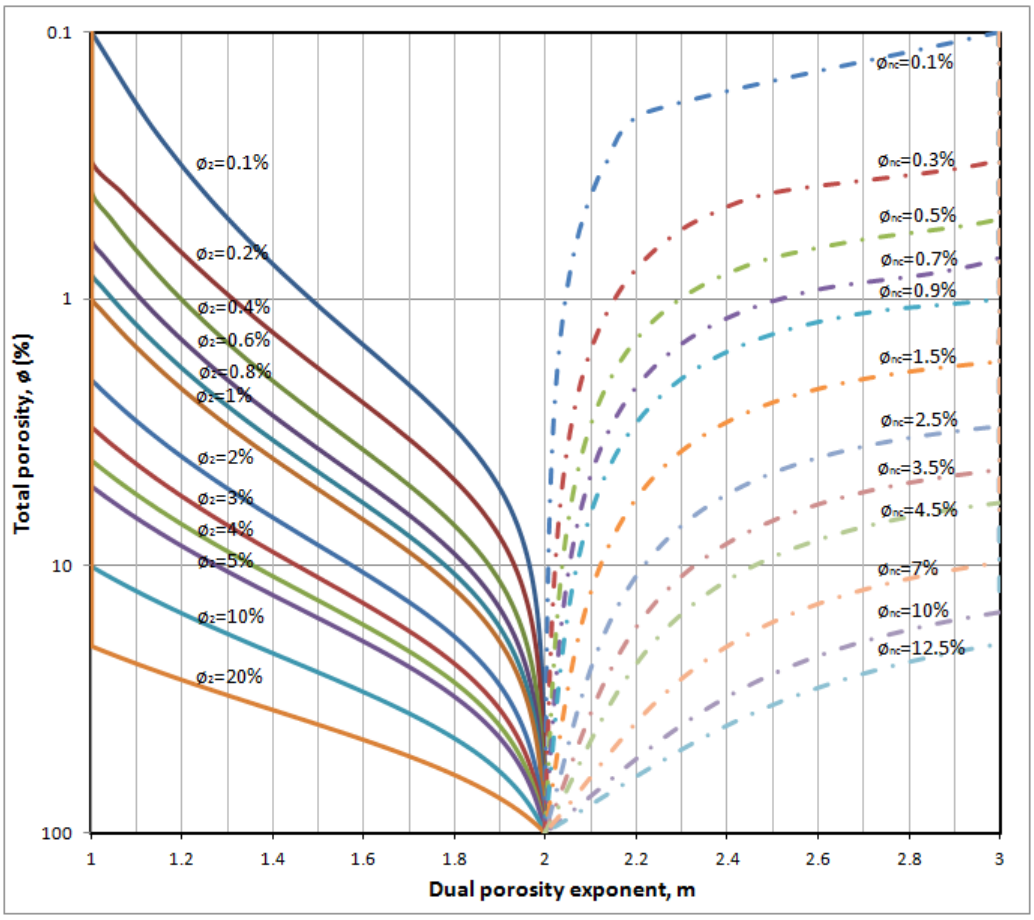

Figure 2.30:Aguilera and Aguilera's (2003[5]) chart for determining porosity exponent as a function of fracture porosity (left, solid line) and as a function of the porosity of non-connected vug (right, dash line). It assumed m_b was equal to 2.0 and m_f was 1.0.

The improved result is shown in Figure 2.30 following Equations 2.39 and 2.40.

$$m = \frac{\log\left(\phi_2 + \frac{1-\phi_2}{\phi_b^{-m_b}}\right)}{\log\phi} \qquad (2.39)$$

where ϕ is the total porosity, ϕ_b is the porosity of the bulk rock, m_b is the porosity exponent of the bulk rock, and ϕ_2 is the fracture porosity in relation to the total volume. The value of fracture (m_f) is not used and is implicitly assumed to be 1.0.

$$m = \frac{\log\left[\phi_{nc} + (1-\phi_{nc})\cdot\phi_b^{-m_b}\right]}{-\log\phi} \qquad (2.40)$$

The non-connected vugs and matrix equation (Equation 2.40) was validated using core data published by Lucia (1983[121]). The fractures and matrix equation was validated originally with data from Altamont trend in Utah and the Big Horn Basin in Wyoming (Aguilera, 1976[6]).

There are instances where the reservoir is composed mainly by matrix, fractures and non-connected vugs. In these cases, a triple porosity model is more suitable for petrophysical evaluation of the reservoir (Aguilera and Aguilera, 2004[9]).

2.8.2 Triple Porosity Model

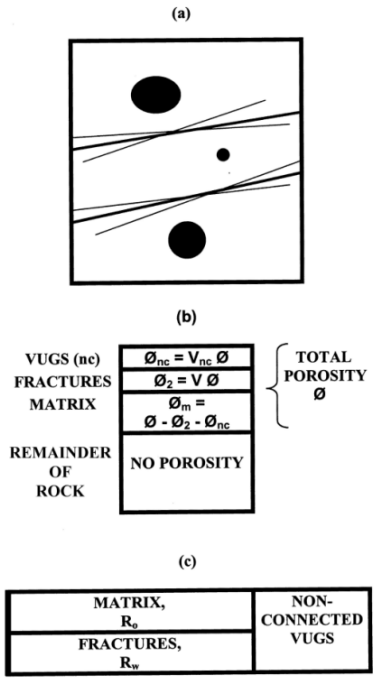

Figure 2.31: Schematic showing (a) reservoir rock with matrix, fractures (lineaments) and non-connected vugs (black spots), (b) volumetric distribution of matrix, fractured, and non-connected vug porosities, and (c) matrix and fractures in parallel, and the combination of matrix and fractures in series with the non-connected vugs (after Aguilera and Aguilera, 2004[9]) .

A triple porosity reservoir can be modelled as a parallel resistance network of matrix and fractures and a series resistance network for the non-connected vugs and the combination of matrix and fracture (Aguilera and Aguilera, 2004[9]), which is shown in Figure 2.31. The total porosity is ϕ, the porosity of the fractures and vugs are ϕ_2 and ϕ_{nc} respectively and the matrix porosity (interparticle porosity) is ϕ_m.

The Equation 2.41 representing the triple porosity model can be written as:

$$R_{tri} = \left(1-\phi_{nc}\right) R_{par} + \phi_{nc} R_{nc} \qquad (2.41)$$

Aguilera and Aguilera (2004[9]) gave the parallel resistivity (R_{par}) of the combination of matrix (R_{matrix}) and fractures (R_2) according to dual porosity model in Equation 2.42.

$$\frac{1}{R_{par}} = \frac{\phi_2}{R_2} + \frac{1-\phi_2}{R_{matrix}} \qquad (2.42)$$

The coefficients in fracture and matrix are the percentage of each volume to the composite bulk volume. However, these weight factors should be related to the volume of the matrix and fractures system instead of composite bulk volume according to Al-Ghamdi *et al.*(2011b[12]). The parallel resistivity of the matrix and fractures is in Equation 2.43,

$$\frac{1-\phi_{nc}}{R_{par}} = \frac{\phi_2}{R_2} + \frac{1-\phi_2-\phi_{nc}}{R_{matrix}} \qquad (2.43)$$

The improved Equations 2.44 and 2.45 are given

$$m = \frac{\log\left[\phi_{nc} + \dfrac{\left(1-\phi_{nc}\right)^2}{\phi_2 + \left(1-\phi_2-\phi_{nc}\right)/\phi_b^{-m_b}}\right]}{-\log\phi} \qquad (2.44)$$

$$\phi = \phi_m + \phi_2 + \phi_{nc} = \phi_b\left(1-\phi_2-\phi_{nc}\right) + \phi_{nc} \qquad (2.45)$$

Figure 2.32 shows a cross plot of the porosity exponent versus total porosity generated by triple porosity model (Equation 2.44) assuming that the porosity exponent of the matrix m_b is equal 2.0. The dashed lines and solid lines correspond to variation in fracture (FT) porosity and non- connected vug (IVG) respectively. It is clear that with increase of fracture, porosity exponent decreases and porosity exponent increases to 2.0 (m_b) with total porosity increases. While non-connected vugs result in higher porosity exponent (>2.0) and the porosity exponent firstly reaches a peak and then gradually

decreases to porosity exponent of the matrix when total porosity increases from 1% to 100%.

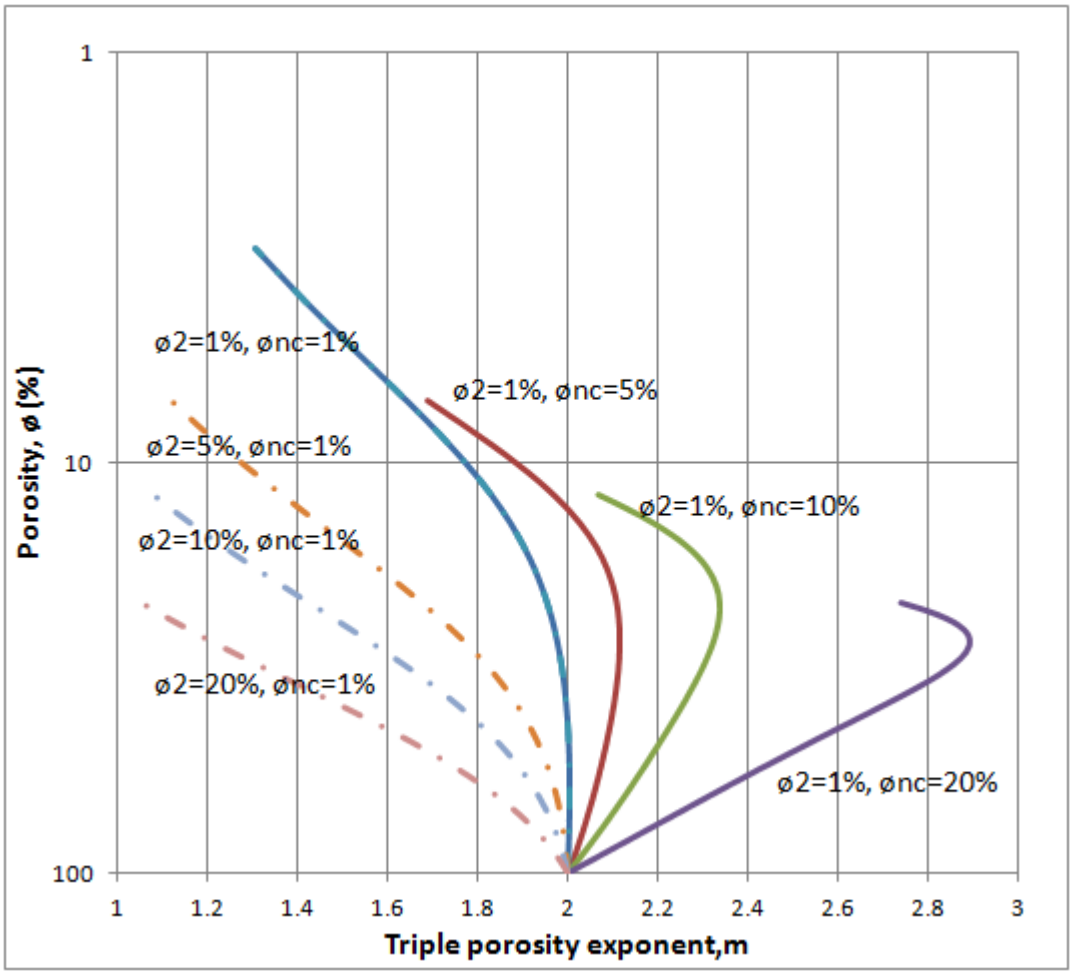

Figure 2.32: A cross plot of the porosity exponent versus total porosity based on triple porosity model assuming the matrix porosity exponent is 2.0 (after Al-Ghamdi *et al.*, 2011b[12]). The definition of the porosity of ϕ_2 and ϕ_{nc} refers to Figure 2.31.

In the above cases, it has been assumed that the flow of current is parallel to the fractures. The effect on porosity exponent of current flow that is not parallel to the fractures has been researched (Berg, 2004[30] and 2006[31]; Aguilera, 2010[8]). Berg (2004[30] and 2006[31]) has presented methods for evaluating the effect of fracture dip on dual and triple porosity models from effective medium theory. The exponent was calculated by iteration method.

In the porosity model, the prediction of porosity exponent, *m*, may match well with existed measured data. One problem is that porosity of each pore type is distributed randomly instead of a more structured realistic distribution. However the pore type can be simulated by pore scale models.

2.9 Pore Scale Modelling

In order to investigate the relationship between porosity exponent and the pore structure, the models with different pore structures caused by pore types should be built. This section describes the common models for pore scale modelling.

The pore space can be simulated by the pore scale models including capillary tubes (Fatt, 1956[71]; Dullien, 1992[66]), pore network (Watfa and Nurmi, 1987[216]; Etris *et al.*, 1989[70]; Ehrlich *et al.*, 1991[68]; Abousrafa *et al.*, 2009[1]) and grain packs simulated by process-based methods (Mousavi and Bryant, 2007[136]; Mousavi, 2010[135]; Mousavi and Bryant, 2012[137]; Mousavi *et al.*, 2012[139]; Mousavi and Bryant, 2013[138]).

Capillary tube models treat the pore space as a complex bundle of capillary tubes (Fatt, 1956[71]; Dullien, 1992[66]) which are shown in Figure 2.33. In their investigations, pore space with various geometries can be built with the resistivity simulated by numerical methods. Meanwhile these models can be used to derive the relationship between transport properties and the pore structure (Fatt, 1956[71]; Watfa and Nurmi, 1987[216]; Tiab and Donaldson, 1996[195]). Based on these models, the effect of the pore geometry on the resistivity is investigated.

Pore network models regard the pore space as geometrically and topologically equivalent pore network consisting of pore nodes and pore bonds. These models are used to theoretically investigate transport properties (Bryant and Blunt, 1992[40]; Bryant *et al.*, 1993[41]; Bakke and Øren, 1997[25]; Mousavi and Bryant, 2007[136]; Abousrafa *et al*., 2009[1]; Mousavi, 2010[135]; Mousavi and Bryant, 2012[137]). Based on pore network models, Etris *et al.* (1989[70]) and Ehrlich *et al.* (1991[68]) pointed out that the porosity exponent was related to the difference between the pore and throat in the pore system. Abousrafa *et al*. (2009[1]) developed a theoretical pore geometrical model to mimic a porous medium fully saturated by brine and derived the analytical equations for porosity and formation factor. The geometrical model and its basic cube unit consisting of pore node and several bonds are shown in Figure 2.34. The results indicated that radii of bond and node were the most important elements in the model.

Models based on grain packs from process-base methods are used to investigate the pore types and the diagentic processes effect on the porosity and permeability (Mousavi, 2010[135]; Mousavi and Bryant, 2012[137]). Mousavi *et al.* (2012[139]) proposed a new description of in the carbonate rocks for the purpose of pore-space modelling of these complicated rocks. They defined six pore types: interparticle, intercrystalline,

intraparticle, moldic (and vuggy), touching vug (fractures), and microporosity and three rock types: muddy, grainy and mixed rocks. The pore types of intergranular pore (IG) Fractrue (FT) and vug (VG) are simulated shown in Figure 2.35.

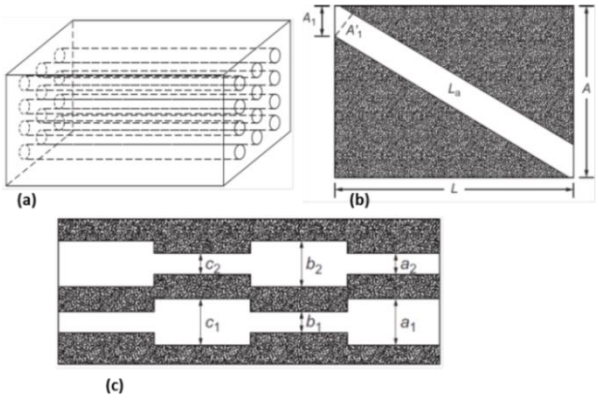

Figure 2.33: Capillary tube models. (a) Ideal porous material of n straight cylindrical capillaries. (b) Inclined capillary tube model. (c) Two-size capillary tube model of porous media (Tiab and Donaldson, 1996[195]).

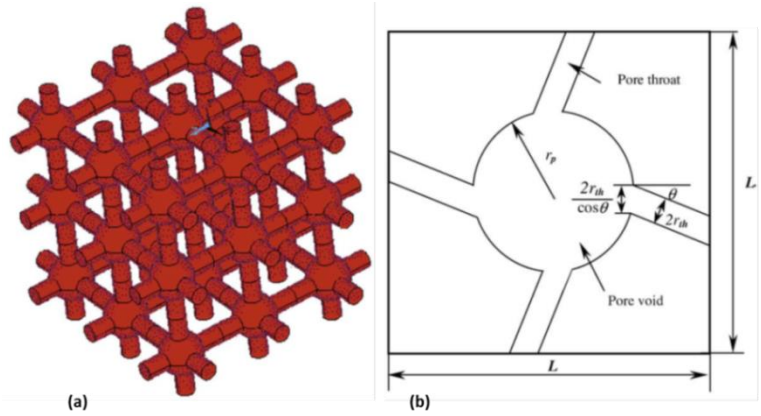

Figure 2.34: Pore network model. (a) Pore geometrical model of a porous medium composed of spherical pore nodes connected via cylindrical pore bonds. (b) Cross-section through a unit cube with spherical node and cylindrical bonds for the derivation of the resistance (Abousrafa *et al*., 2009[1]).

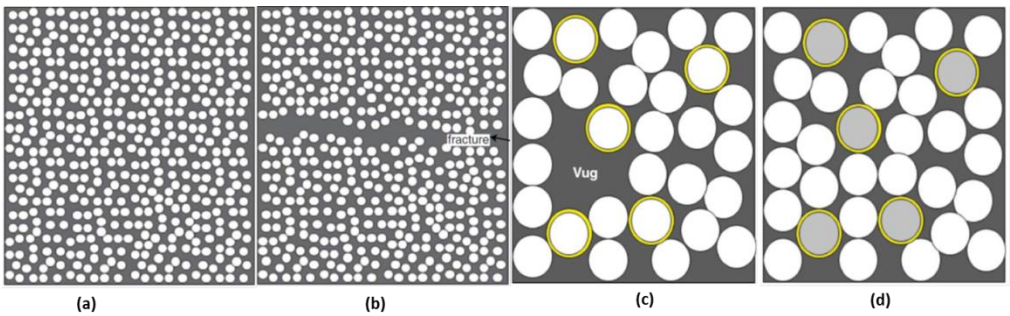

Figure 2.35: pore type models from grain packs. (a) Intergranular pore by small-grained packing. (b) Intergranular pore with fracture. (c) Intergranular pore with vuggy porosity. (d) Intergranular pore with moldic porosity. Gray is pore space; white is grain; light gray is moldic porosity; yellow is cement(Mousavi *et al.* (2012[139]).

2.10 Discussions

In this thesis, the CT images are used to determine the key pore geometrical and topological and key pore types affecting porosity exponent and then the pore scale modelling methods are used to investigate the effect of these elements on the porosity exponent, these are the preliminary investigation to accurately predict porosity exponent based on the pore structures. Based on the presented literature review, the methods employed in this work are summarized and discussed.

2.10.1 CT Imaging

3D imaging and analysing of the pore scale structure within core material allows one to directly measure the pore structure, tortuosity and degree of interconnections of the pore systems. This can give insight into the behaviour of *m* in realistic pore geometries (Knackstedt *et al.*, 2007[105]). Three coquina samples are scanned by $\mu - CT$ imaging in this thesis.

2.10.2 Pore Network Extraction

Voronoi diagram based methods (Bryant and Blunt, 1992[40]; Bryant *et al.*, 1993[41]; Øren *et al.*, 1998[147]; Øren and Bakke, 2002[145] and 2003[146]) work well for clearly granular media and are well suited for pore space representations derived not from images, but from the simulation of grain packing. These methods work less well for complex systems such as many carbonates (Blunt et al., 2013).

Medial axis methods (Lindquist *et al.*, 1996[117]; Lindquist and Venkatarangan, 1999[115]; Sheppard *et al.*, 2005[184]; Shin *et al.*, 2005[187]; Prodanović *et al.*, 2006[157]; Jiang, 2008[92]) find the skeleton of the pore space and define the topology however, these methods suffer from ambiguities given images of finite resolution and have difficulty uniquely identifying pores and their connections (Blunt et al., 2013).

Maximal ball methods (MB) (Silin *et al.*, 2003[189]; Silin and Patzek, 2006[188]; Al-Kharusi and Blunt, 2007[13]; Dong, 2007[63]) clearly identify the larger pores including its location and size, but tends to identify smaller elements down to the image resolution (Blunt et al., 2013).

Considering the complexity of the pore space in carbonates and the requirement of accurately identifying pores, the maximal ball (MB) method is used to extract pore

network, which is available from PERM of Imperial College on the website (http://www3.imperial.ac.uk/earthscienceandengineering/research/perm) based on the work of Dong (2007[63]). The principle and main work flow are introduced and the details can be referred to (Appendix C or Dong, 2007[63]).

2.10.3 Geometry and Topology Calculation

Minkowski Functions (Vogel *et al.*, 2010[212]) offer volume, surface area, curvature and Euler number, they are average quantification of the pore structure without considering the pore size distribution. The Euler number from Minkowski Functions is applied to investigate the effect of segmentation and pore space on the pore topology and porosity exponent.

However, these functions are not sufficient to characterize pore geometrical properties and some of these functions are sensitive to the resolution of the porous media (Jiang *et al.*, 2011[93]). So the geometrical properties including radius, volume and shape factor and the Euler number considering the pore size distribution can be extracted from the pore network of the porous media.

2.10.4 Numerical Resistivity Calculation

These three resistivity simulation methods can be validated by comparison the simulation results to the analytical results, experimental data and numerical results in the review. All of these methods are based on the voxel representation of the pore space. Meanwhile the advantage and disadvantage of each simulation method have been summarized.

Based on the characteristics of each method, in this thesis, with consideration of the consumption of time and memory of computer, RW is an efficient method to simulate porosity exponent for the sample larger than 300 voxels in length with determination of the error. FD is used in sample less than 300 voxels and offers current density. Renormalisation is just used to investigate the effect of the size of the sub-samples on the simulation results. All these simulation methods can compare with the experimental results to reflect their applicability in carbonates.

2.10.5 Empirical Equations

According to the development of Archie First Equation (1.1), the tortuosity factor, $a=1$, is used in this thesis, this is helpful to investigate the effects on the porosity exponent and relate the porosity exponent to pore system in carbonates.

2.10.6 Porosity Exponent in Carbonates

According to the literature review, the pore system of the carbonates is heterogeneity and anisotropy reflected by various pore types existing in carbonates, these pore types include interparticle pore, moldic pore, vugs, fractures and fissure. Pore types significantly affect porosity exponent. Key pore types should be determined and the effect of pore types on the porosity exponent is investigated by pore scale modelling in this thesis.

2.10.7 Porosity Models

Porosity models theoretically investigate the effect of pore types on the porosity exponent considering the pore types as their equivalent resistance network. In this thesis, the dual porosity model is used to determine the key pore type in each sample, which depends on the distribution of the experimental porosity exponents in the cross plot of porosity exponent versus porosity by dual porosity model.

2.10.8 Pore Scale Modelling

In order to study the effect of pore types on the porosity exponents, FD is used to calculate the porosity exponent of the pore scale models considering various pore types due to the requirement of the current density and the size of model less than 300 voxels.

Capillary tubes are simple and easy to simulate different pore types. Meanwhile they are convenient to consider the arrangement of pore types in parallel or in series or both. Thus in this thesis pore scale models based on capillary tubes are used to validate dual porosity model (Aguilera and Aguilera, 2003[5]) and to investigate the pore types effect on the porosity exponent. Intergranular pore (IG) is modelled by the capillary tube with porosity exponent close to 2, fracture like pore (FT) is simulated by the capillary tube with porosity exponent less than 2 and vug pore (VG) is presented by the capillary tube with porosity exponent close to 3. The capillary tubes present the voxel representation of the pore space.

Additionally, theoretical resistivity equation considering the pore geometry can be easily derived from capillary tubes. However, capillary tubes are a restrictive simplification of the pore network and absence of the connectivity (Abousrafa *et al*., 2009[1]), pore network model can be used to theoretical investigate the effect of pore size and length on porosity exponent based on a pore-throat conjunction.

However, the capillary and pore network models are too simple to reflect the real characteristics of the intergranular pore (IG), fracture like pore (FT), vug pore (VG) and the connectivity of the pore space (Mousavi *et al.*, 2012[139]), the models based on grain packs can model the real characteristics of the FT and VG and pore connectivity. the IG is simulated by the Fontainebleau sandstone with porosity close to 13%, which is a intergranular pore (IG) (Arns, 2002[19]), the FT and VG are based on the models of Mousavi *et al.* (2012[139]).

2.11 Conclusions

In this thesis, $a = 1$ $FF = 1/\phi^m$;

CT imaging is used to reconstruct pore space for three carbonate samples;

The maximal ball (MB) method is used to extract pore network;

Pore types significantly affect porosity exponent;

Dual porosity model is used to determine key pore type in each sample;

Models based on capillary tubes and grain packs are used to investigate the pore type effect on porosity exponent with the resistivity simulated by FD.

Model based on pore network is used to theoretically derive porosity exponent and investigate the effect of pore size and length on the porosity exponent.

The applicability of three resistivity simulation methods including FD, RW and a renormalisation is tested in carbonate.

Chapter 3

Resistivity Calculation and Interpretation of Three Carbonate Samples

X-ray Computed Tomography ($x-CT$) is a frequently used non-destructive 3D imaging and analysis technique for the investigation of internal structures of a large variety of objects. The sample scanned by $x-CT$ can be still used after $x-CT$ scanning to carry out experiments to compare the lab results with the simulation results.

In order to determine the key geometrical and topological parameters and pore types affecting porosity exponent, CT images are used to directly reconstruct pore space and then these images are converted into binary images for the pore geometry and topology calculation (Vogel, 2002[210]; Jiang, 2008[92]; Vogel *et al.*, 2010[212]) and resistivity simulation (Auzerais *et al.*, 1996[24]; Øren and Bakke, 2002[145]; Arns *et al.*, 2005a[18]; Øren *et al.*, 2007[148]; Han *et al.*, 2009[83]; Nakashima and Nakano, 2011[141]). However these binary images are too large to calculate in terms of computer, a representative volume, which should be large enough to represent the petrophysical properties of the original porous media and also should be as small as possible for the computer calculation (Corbett *et al.*, 1999[54]; Vik *et al.*, 2013[206]; Corbett *et al.*, 2014[56]), is determined by REV analysis. Due to the porosity exponent related to the pore structure, based on the REV sample the pore geometry and topology can be extracted to interpret the porosity exponents from experiment and then to determine the key geometrical and topological factor effect on porosity exponent. The experimental porosity exponents can be used to validate the accuracy of the resistivity numerical calculations based on REV by comparing the calculated data to the experimental data. These validated numerical methods can be further used in the pore scale modelling. Meanwhile in carbonates the pore types affect the pore structure, the key pore type for each sample is determined by two aspects. One aspect is to investigate the effect of the pore clusters on the porosity exponents and the other aspect is to determine the pore types according to the distribution of the experimental data in the cross plot of porosity exponent versus porosity from dual porosity models (Aguilera and Aguilera, 2003[5]).

This chapter firstly presents the CT images used in this thesis including the introduction of the three coquina samples and the image processing converting CT images into binary images, secondly describes the REV analysis to determine the representative volume for coquina samples. In the third section, the experimental data are presented and used to validate the accuracy of the numerical calculations of porosity exponents by comparing the numerical data based on REV samples to the experimental data. In this process, the numerical data can be used to calculate the anisotropy and

heterogeneity of the carbonates by their coefficient compared with a sample of Fontainebleau sandstone to reflect their difference. In order to explain the simulated and experimental results, the topology (TP) and geometry (GM) of three REV samples are used to determine the key geometrical and topological factors with consideration of the image processing and pore space effect on the porosity exponent in the fourth section. However, the abnormally large Euler number reflects the worse pore space connectivity. In order to improve the accuracy of the TP measurement of the pore system and investigate the pore clusters effect on the pore types, in the fifth section the pore clusters are extracted to investigate the pore clusters effect on the porosity exponent and the key pore types are determined with consideration of the porosity exponent from porosity model. The last two sections are discussion and conclusion respectively.

3.1 $x-CT$ Images

3.1.1 Sample Description

In this thesis, three carbonate samples (denoted as Pet1, Pet4 and Pet6) are coquinas, which are defined as concentrations of shells or shelly fragments deposited from the actions of some agent transport. The samples were acquired from the Morro do Chaves Formation in Sergipe-Alagoas Basin and described by Câmara (2013[43]).

The Sergipe-Alagoas Basin is known in Brazil as a "Teaching Basin" because of the exceptionally good outcrops that include all the sections of the Brazilian Margin evolution. The Morro do Chaves Formation of Aptian (local Jiquiá) Age marked by a lacustrine carbonate sequence with preferential development on relative structural highs, with a strong tectonic and climatic control and the coquinas are formed from non-marine bivalves and ostracods with a variable percentage of siliciclastic material (Câmara *et al.*, 2015[44]). The Morro do Chaves Formation is exposed in excellent outcrops in the São Sebastião Quarry (former Atol Quarry) (Figure 3.1) and this formation was chosen as a suitable analogue for potential offshore coquina reservoirs, and a series of rock samples were collected for the different rock types present. Nine samples (Pet 1-9) were analysed (Câmara *et al.*, 2014[42]), and three samples (Pet1, Pet4 and Pet6) were selected for this thesis.

Coquinas of the Morro do Chaves Formation have become the laboratory material of choice for much of the academic petrophysical community in Brazil. However, unlike the classic sandstones (such as the Berea and Bentheimer/Clashach/Lochabriggs sandstones used for studies in the USA and Europe) these carbonate samples show a

high-level of variability in pore type, size, geometry, distribution and connectivity due to the moldic and corroded pore structures which gives rise to a variety of rock types in outcrops onshore (in Figure 3.2). This will produce challenges in assessing petrophysical representativity and when comparing and applying the work of several different research groups (Corbett *et al.*, 2013b[58]).

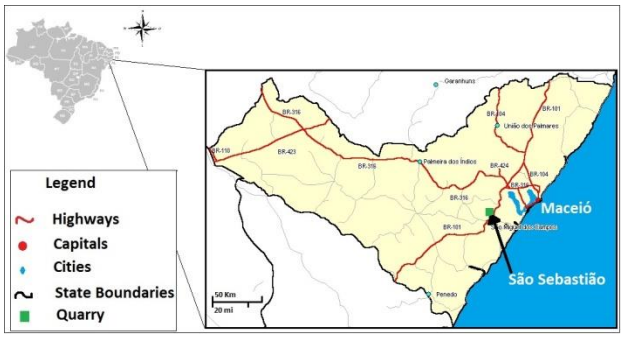

Figure 3.1: Location Map of the São Sebastião Quarry in S. Miguel dos Campos, near Maceio (Alagoas, NE Brasil) (from Câmara *et al.*, 2014[42]).

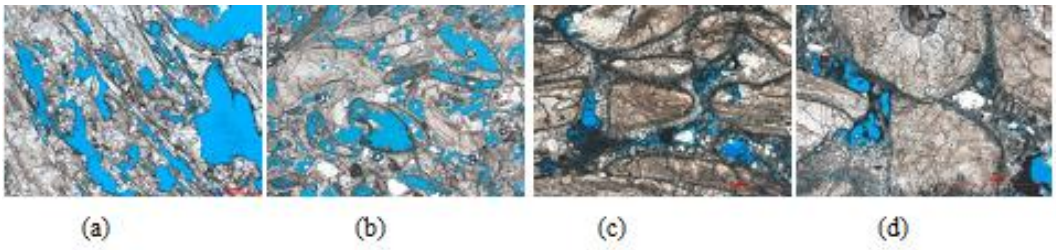

Figure 3.2: Bivalve coquinas from the Morro de Chaves Formation (Sergipe-Alagoas Basin, NE Brazil) in thin section photomicrographs – showing corrosion (a) and moldic porosity (b, same scale as a) in blue (from Corbett *et al.*, 2013a[57]); thin sections cut vertically (c) and horizontally (d) showing pore scale anisotropy. Views are 2.5 – 5 *mm* across. (Corbett and Borghi, 2013[55]).

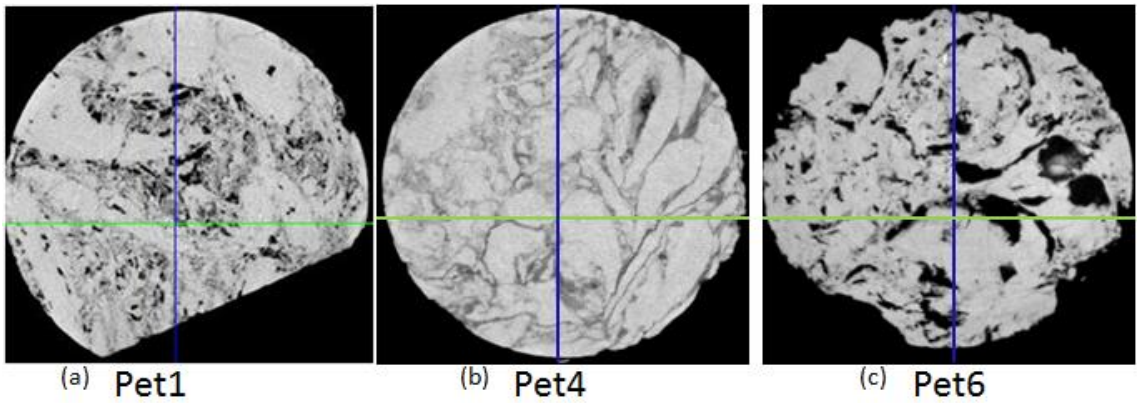

Figure 3.3: The μ-CT cross sections for Pet1 (a), Pet4 (b) and Pet6 (c). Their resolution is 19.04 µm, 20.44 µm and 19.27 µm respectively. The sizes of the CT images for these three samples are 2240x2240x1411, 1440x1440x1261 and 1968x1968x1975 pixels respectively.

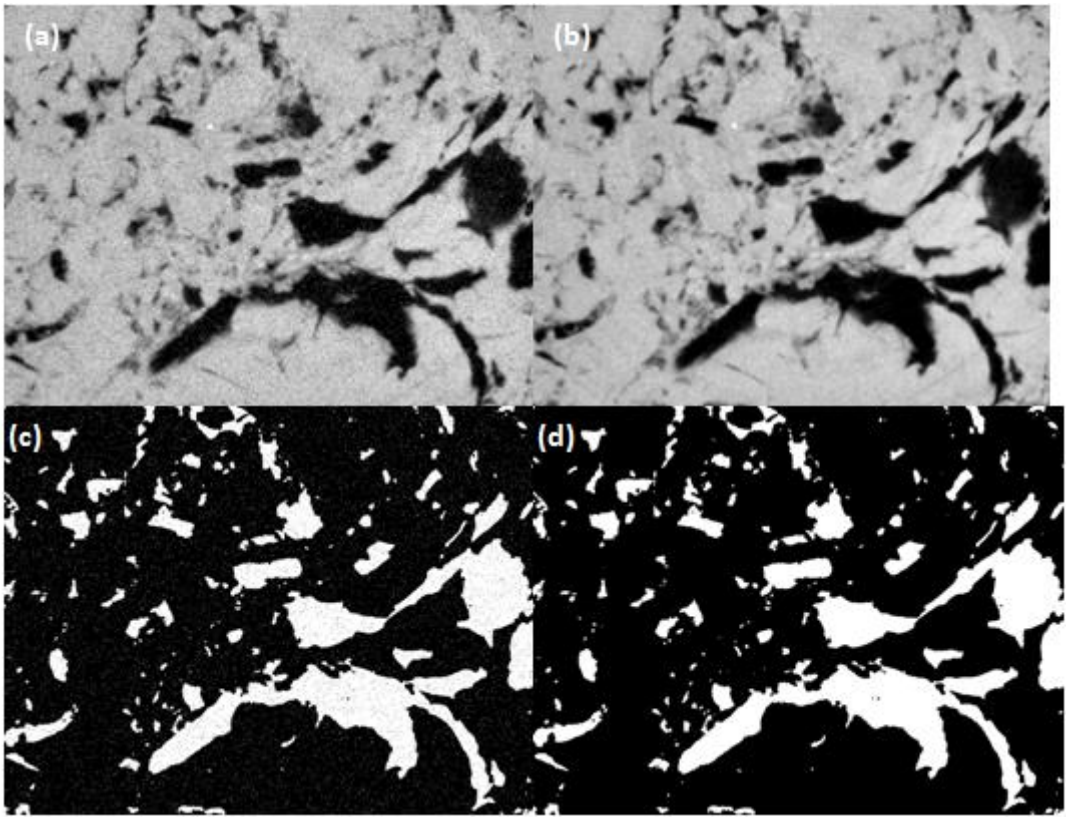

Figure 3.4: Function of median filter shown by comparing the original CT image cross section (a) with the filtered CT images (b) and their related binary image in (c) and (d) respectively.

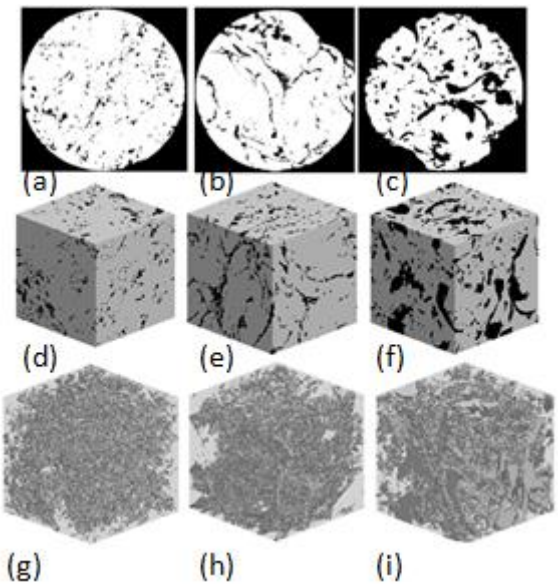

Figure 3.5: The segmentation results of Pet1 (a, d, g), Pet4 (b, e, h) and Pet6 (c, f, i) are shown in cross section (a, b, c), 3D cube (d, e, f) and pore space visualization (g, h, i). The 3D cubes (800^3) for these three samples are chosen from their CT images.

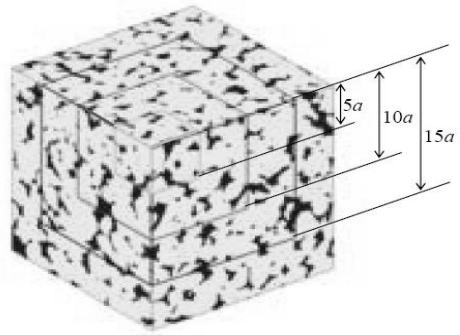

Figure 3.6: REV analysis by porosity calculation over different centred volumes.

3.1.2 Pore Space Images

$\mu-CT$ scans are taken from offcuts of measured plugs instead of the whole of plugs selected for these three samples (Pet1, Pet4 and Pet6) by a micro-tomography SKYSCAN (model 1173 High Energy) (Figure2.3). Figure 3.3 shows the cross sections of these three samples that have been selected to study resistivity and to extract topology (TP) and geometry (GM). In Figure 3.4, the effects of median filtering are shown by applying to a CT image of Pet6. The image resolution is 19.27 μm. The slice (a) is original $\mu-CT$ image of the sample Pet6. After segmentation, the noise in the raw image becomes small grain voxels in the void or the holes in grains shown (c). The picture (b) shows the result after noise is smoothed by using a median filter and its black and white binary image in (d). Comparing the two binary slices in the bottom (c) and (d), it is shown that the median filter preserves the integrity of the grains and the pore space. The binary images of the Pet1, Pet4 and Pet6 are shown in Figure 3.5.

3.2 Representative Elementary Volume (REV) Analysis

$x-CT$ imaging technology provides the images of the samples, thus rendering the representation of their pore structures. However, the reconstruction, visualization, analysis and numerical simulation of such 3D images are limited in computer terms. Thus, it is not always possible to reconstruct the images with the total size of the micro-tomography sample, the representative elementary volume (REV) should be determined which has to be big enough to represent the characteristics of the sample and as small as possible compared with its total volume (Corbett *et al.*, 1999[54]; Vik *et al.*, 2013[206]; Corbett *et al.*, 2014[56]). Meanwhile, the process of the REV determination is a way to better understand the micro-structure of a given material, which is the first step to link

the microstructures to its physical properties (Vik *et al.*, 2013[206]; Corbett *et al.*, 2014[56]).

REV analysis is usually implemented by comparing the porosity of the sub-cube samples extracted from the 3D CT images with the experimental results. These sub-cube samples are built with length of *a* centred on a voxel which is chosen randomly from the 3D images (Figure 3.6). The porosity of these sub-cube samples can be expressed by the percentage of the pore voxels in each whole sub-cube samples. The porosity of each sub-cube sample is related to the length of this sub-sample, with the increase of the length, the porosity should gradually reach a stable value reflecting that the sub-sample with this length is representative. The relationships between porosities of these sub-cube samples and their lengths can be used to analyse representative elementary volume. In Figure 3.7, REV analysis is implemented in the carbonate samples of Pet1, Pet4 and Pet6 taken sandstone Fb22 as a comparison showing the difference between sandstones and carbonates. In each sample, four voxels are randomly chosen as the centre of the sub-samples respectively. Four series of sub-samples located in their relative position with different lengths can be built and the porosity of these sub-cube samples versus the length of each are shown by four curves with different colour and symbols in each cross plot (Figure 3.7).

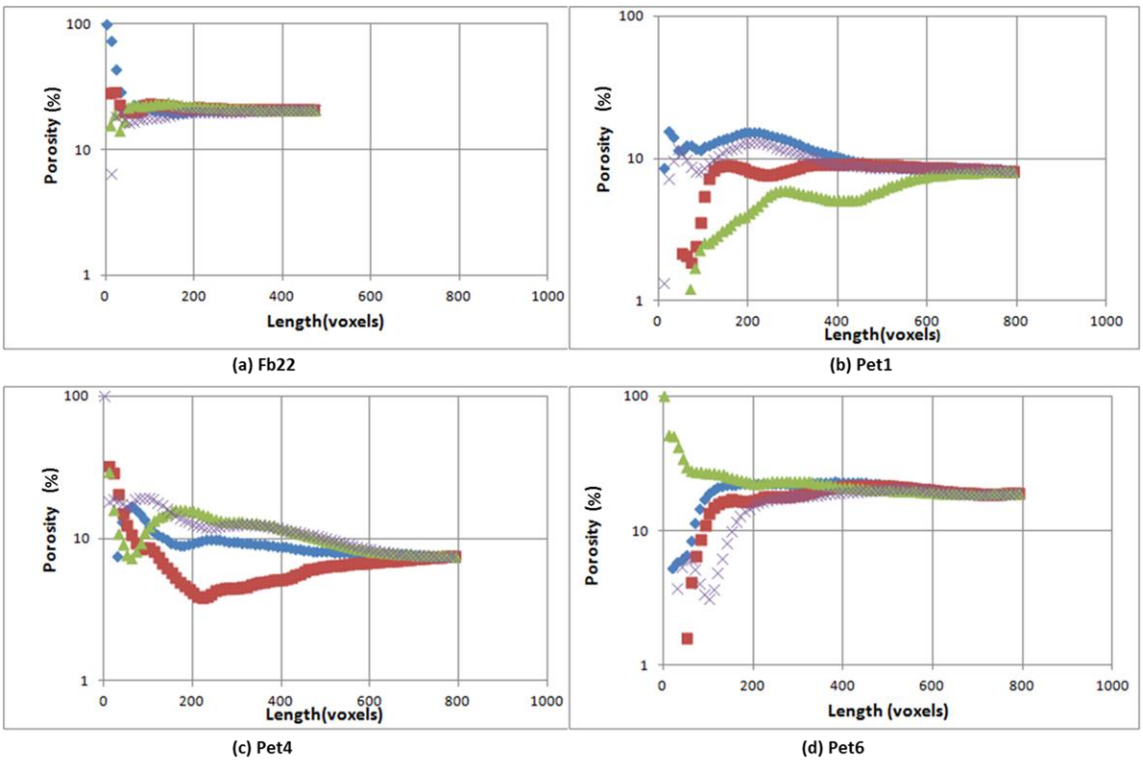

Figure 3.7: REV analysis results based on porosity (%) for three carbonate samples, Pet1 (b), Pet4 (c), Pet6 (d) taken sandstone Fb22 (a) as comparison.

It is shown that when the length of the cube is larger than 60 voxels , the porosities of sandstone Fb22 from four different sub-cube samples are convergent while the porosity for these three carbonates are still divergent even the length of the sub-cube reaches 400 voxels. This result shows that the carbonates are much more heterogeneous than the sandstones. It is noted that the REV analysis results for different rock samples are different and the best size of representative elementary volume of these samples are related to their own pore structure. Even for the same rock sample, the REV analysis results in different resolutions are different. So REV analysis based on porosity could be helpful in qualitative analysis the heterogeneity of the samples because the sub-cubes used for the porosity calculation are chosen randomly from the whole sample.

The size of the REV based on the Figure 3.7 should be equal to 600. However, the porosity in the Figure 3.7 is the reflection of the local properties due to the random location and the limited number of the sub-samples. In order to offer an indicative factor for the REV of the rock images, a preliminary REV analysis based on two-point correlation function has been studied by Dong (2007[63]). The two-point correlation function is calculated by Equation 3.1 (Øren and Bakke, 2002[145]).

$$
\begin{aligned}
Z(x) &= \begin{cases} 1 & \text{if } x \in \text{porespace} \\ 0 & \text{otherwise} \end{cases} \\
\phi &= \langle Z(x) \rangle \\
g2(u) &= \frac{\langle (Z(x)-\phi) \bullet (Z(x+u)-\phi) \rangle}{\phi(1-\phi)}
\end{aligned}
\qquad (3.1)
$$

Where the phase function *Z(x)* is related to the state, solid or void, of the voxel in *x* and the "<> "means the average of this function *Z(x)*. *u* is the length of the segment.

This function reflects the possibility of the two ends points of a segment with a certain length in the same pore or solid space in the image. In his study, the first decay length, equivalent to the lag when the two-point correlation firstly reached zero on the correlogram, was taken as the indicative factor. The transport property of the samples kept stable when the size of the samples is three times more than the first decay length (Figure 3.8).

In Figure 3.8, the absolute permeability starts to converge from the first decay length and the fluctuation of the permeability of the images with the length from once to three times the decay length is negligible. So in this thesis, the size of REV is selected to be less than three times of the decay length and more than first decay length.

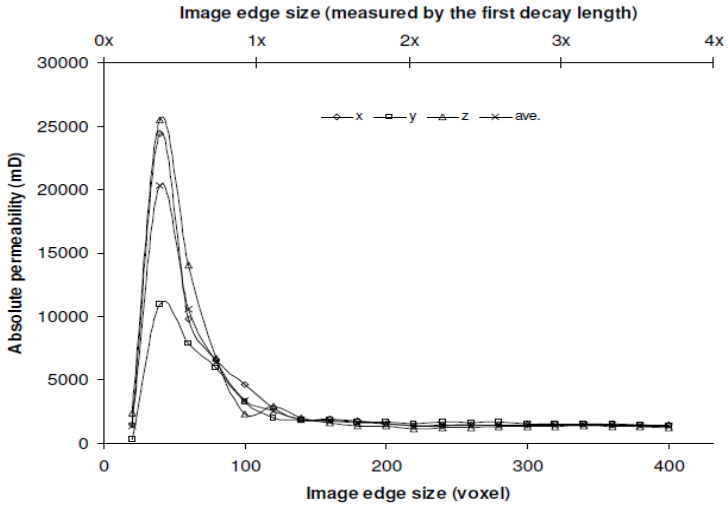

Figure 3.8: The absolute permeability of 20 sub-samples calculated in three directions and their average permeability versus the size of the sub-samples united by voxels in primary x-axis. The secondary x-axis is the ratio of the image size to the first decay length. When the ratio exceeds three, the absolute permeability keeps stable (Dong, 2007[63]).

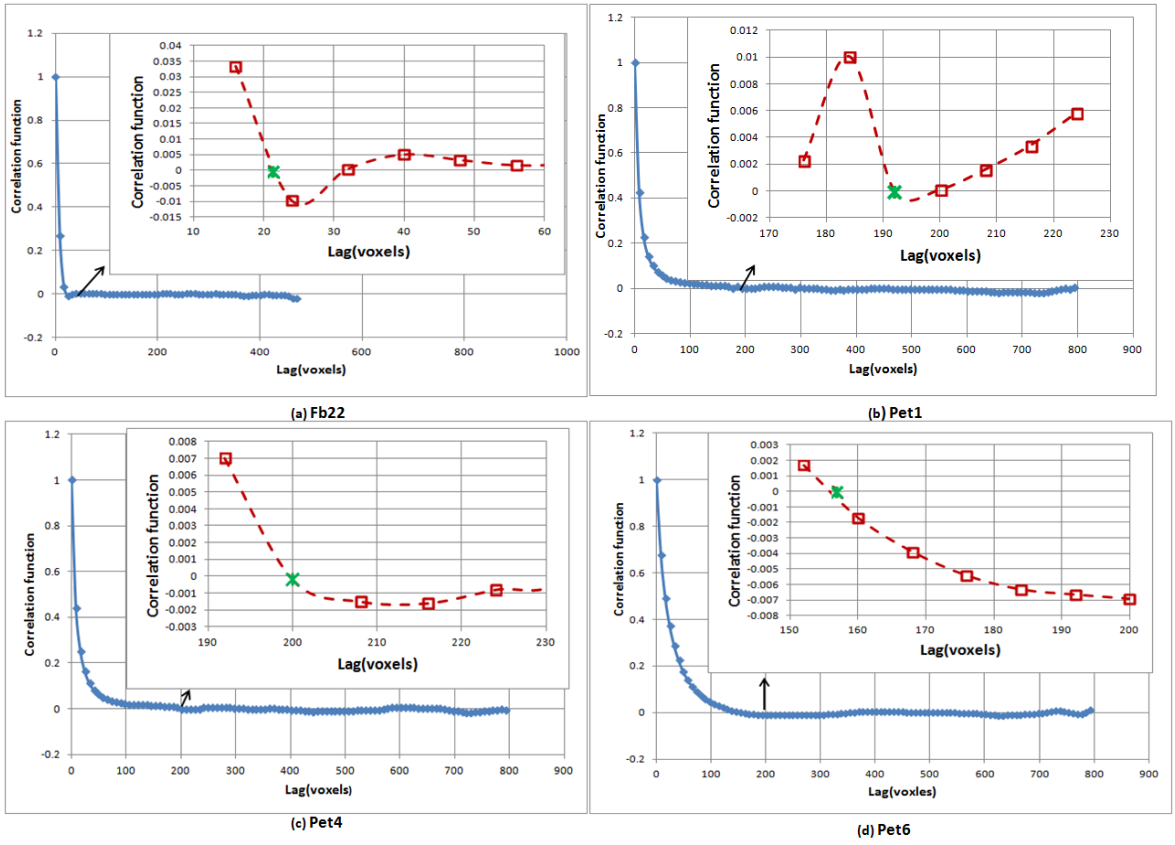

Figure 3.9: The two-point correlation function correlogram which is the average function in three directions for sandstone Fb22 and carbonates Pet1, Pet4, Pet6. The first decay length for sandstone Fb22 (a) with 5.68 μm resolution is 21 voxels; The first decay length for Pet1 is 192 voxels, the resolution of Pet1 is 19.04037μm (b); The first decay length of Pet4 is 200 voxels, its resolution is 20.44 μm (c) and this length for Pet6 (d) is 155 voxels with 19.27 μm as the resolution.

The first decay length of Pet1, Pet4, Pet6 and Fb22 can be shown by two-point correlation function in Figure 3.9. The first decay length for carbonates is about 200 voxels while the length is about 20 voxels for sandstone Fb22. The REV size for carbonates is about twice the first decay length according to a preliminary research based on Pet6 to calculate porosity exponent by the FF from random walk (RW) simulation in Figure 3.10. The size of the sub-cubes reaches 350 voxels, the calculated porosity exponents in x, y, z three directions and their average become stable reflected that sub-cubes are gradually representative.

However, with the increase of the length, the porosity exponents in three directions turn to diverge again while the porosity exponent in each direction keeps stable with less variation. The divergence of the porosity exponents in three directions is due to the anisotropy of the carbonate samples, the anisotropy causes the difference of the porosity exponents in three directions, for Pet6 the porosity exponent in z direction is larger than the porosity exponents in x and y directions. The variation of the porosity exponent in each direction stems from the simulation. The error in the RW estimation, in this thesis, is about 5%, that is, the variation of the simulated porosity exponent in each direction is about 0.1.

The size of the REV based on the porosity distribution (Figure 3.7) is about 600 voxels while its size is about 400 according to the distribution of the porosity exponent (Figure 3.10). The relationship between different sizes can be illustrated in the Figure 3.11 taken Pet6 as an example.

In Figure 3.11, the size of the REV is 600 voxels. When the size of the sub-sample is less than that, the term for this sub-sample is "*Sub REV*" while the sub-sample with the size larger than 600 is named as "*Sup REV*". In this thesis, the sub-samples are all in cube and then their scale or size can be expressed as "*SCnum*", which represents the size of the sub-sample in cube equal to num, shown in Figure 3.11, SC300 stands for that the scale of the sub-sample is $300\times300\times300$.

While for Pet6, the porosities of the sub-samples (SC300, SC400) are convergent and then the resistivity calculation for Pet6 can be based on the SC300 or larger. For the other two carbonate samples, Pet1and Pet4, their resistivity calculations are based on SC400 or even larger.

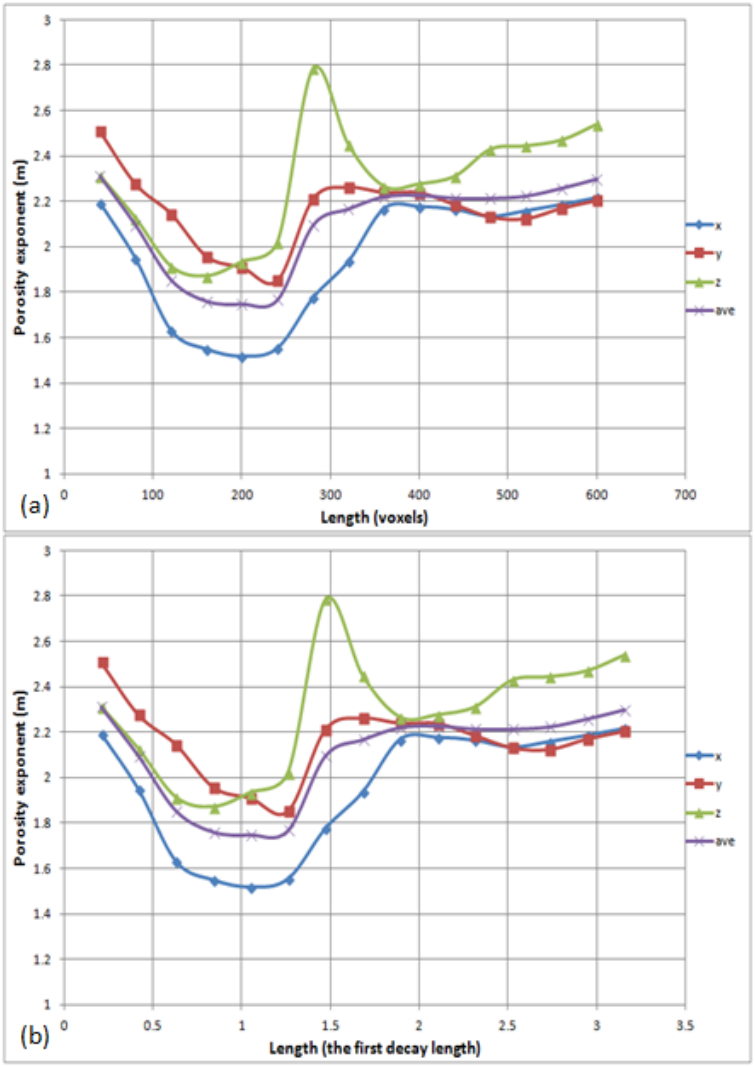

Figure 3.10: The porosity exponents of 15 sub-samples calculated in three directions (x, y, z) and their average (ave) values versus their size united by voxels are in (a) and versus the length of the samples united by the first decay length are in (b). When the ratio reaches about two, the porosity exponents are gradually convergent.

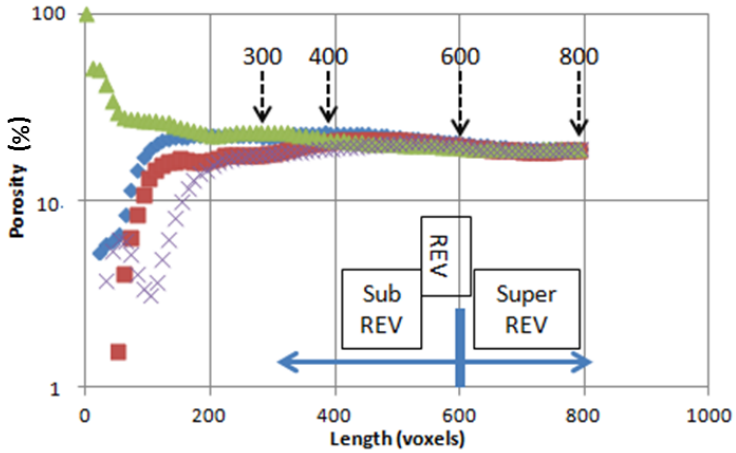

Figure 3.11: The relationship between the types of the representative elementary volume (REV) and their size for Pet6.

3.3 Comparison Resistivity Simulation with Experimental Result

In this section, firstly the experiment results for the Pet1, Pet4 and Pet6 are given. And then the simulated results compare with the experimental results to show the feasibility of the numerical methods. Meanwhile the heterogeneity and anisotropy of the carbonates can be shown by the comparison between the sandstones and carbonates, so the Fontainebleau sandstone with porosity 22% (Fb22) is regarded as comparison again in electrical properties and pore topology and geometry in the following sections.

3.3.1 Experiment Results

The experimental results include their porosities based on different methods, permeability and porosity exponents. The porosity exponents are from two different labs.

Sample	Lithology	Field estimate (%)	Hand scale estimate (%)	Image analysis (%)	Weight of volume (%)	$\mu - CT$ (%)	Hassler measurement (%)
Pet1	Calcirudite	18	17	11	14	9	12
Pet4	Calcirudite	10	7	8	7	7	5
Pet6	Calcirudite	30	20	22	24	15	19.5

Table 3.1: The porosity of the three carbonates measured with different methods (Câmara *et al.*, 2014[42]).

It is clear that the porosity of the Pet4 is least among these three samples. It ranges from 5% to 10% for different experiment methods and the porosity from the $\mu - CT$ image is 7% close to other results reflects that CT images of Pet4 contain the most of the pore space. The porosity of Pet6 is 19.5% where maximum of porosity is 30% and minimum is 15% reflecting that Pet6 has the largest pore space. The porosity of Pet1 is 12% varying from 9% to 18% and the porosity by $\mu - CT$ is 9% without consideration of the pore less than the resolution.

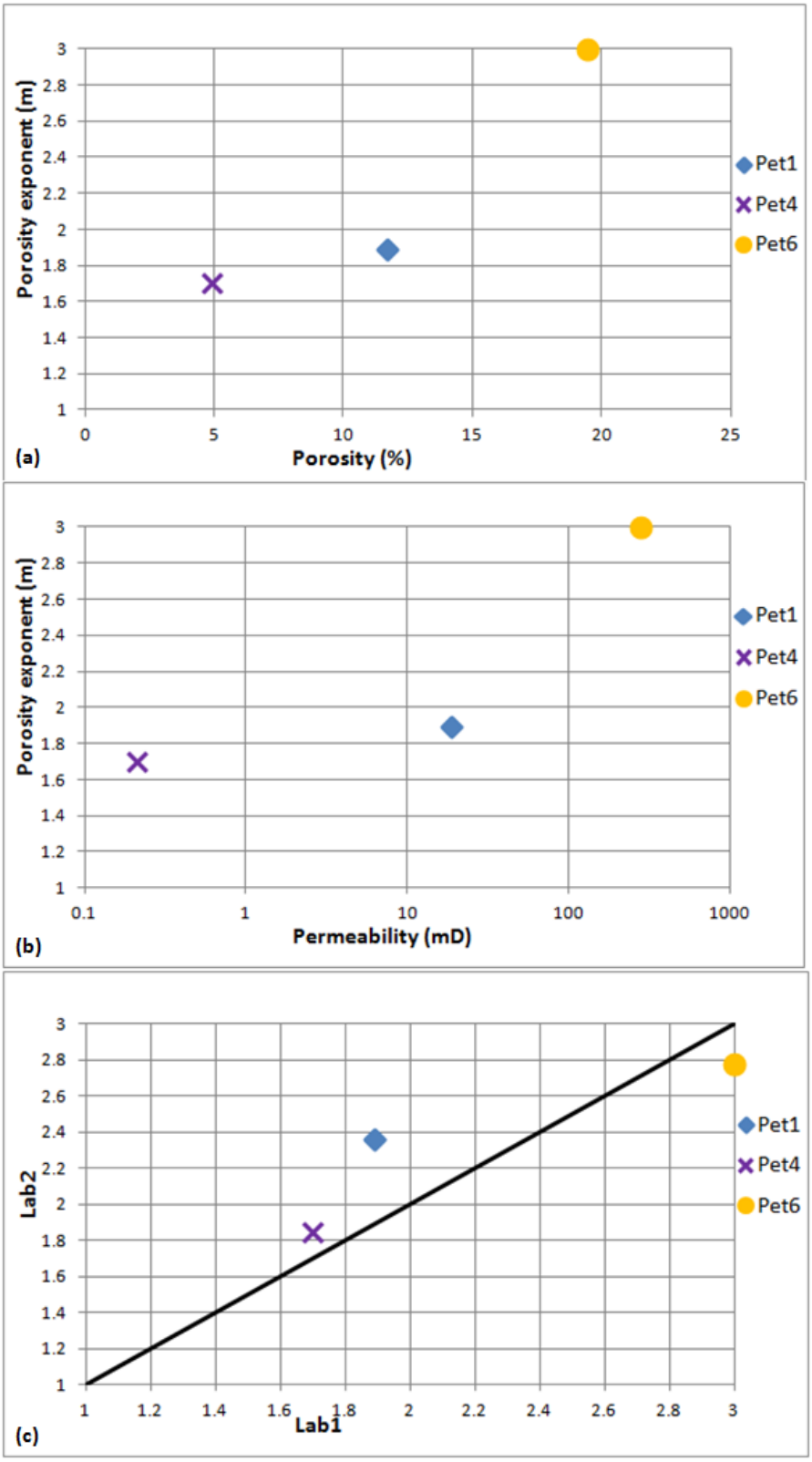

Figure 3.12: The experiment results for Pet1, Pet4 and Pet6. The figure (a) is the cross plot for porosity exponent versus porosity; the relationship between porosity exponent and permeability is in (b) and the porosity exponents for these three samples from two labs in (c), the black line is 1:1.

Figure 3.12 gives their experimental results for porosity exponent and permeability. It is clear that the porosity exponent goes up with the increase of the porosity. The

samples with the less porosity shows smaller porosity exponent, which means better electrical current flow. The correlation between permeability and porosity exponent (in Figure 3.12b) is positive, that is, the rock sample with high porosity exponent shows large permeability. Verwer *et al.* (2011[205]) observed and explained the similar result in carbonates. The increase in porosity exponent indicates that the pore structure for electrical current gradually becomes worse while the improvement in the permeability reflects that the pore structure for fluid flow improves, which contradicts the traditional trend that the permeability is negatively correlated to the porosity exponent. The pore structure for current flow becomes worse and then the flow of the fluid in this pore space should reduce. Experiment results show that the electrical flow is different from fluid flow just as Archie suggests that molecular fluid flow and ionic motion were "different" (Archie, 1947[16]). The porosity exponents for Pet4 and Pet6 from two labs (Lab1 and Lab2) are almost same, close to the diagonal line. In Pet4, the porosity exponent is 1.7 and 1.85 with 8% variation. The discrepancy of the porosity exponent for Pet6 is the same as Pet4 while the minimal porosity exponent of Pet6 is 2.78 whose exponent is the largest among these three carbonates. While the point of Pet1 in the cross plot of Figure 3.12c is far from the diagonal line and the difference of the porosity exponent from the two labs is about 24.8% ((2.36-1.89)/1.89) or 19.9% ((2.36-1.89)/2.36) also, perhaps, reflecting the complexity of its pore space. Note that $\mu - CT$ was performed on offcuts of the measured plugs and this may account for the differences in Pet1.

3.3.2 Simulation Results

The numerical simulation based on Finite Difference (FD) method is used to calculate the porosity exponent of the Pet6 (SC600). The result can match the experimental result shown in Figure 3.13. In this Figure, the experimental results for the same rock sample from two labs are shown by the similar symbols. Circular symbol is used to represent the results of Pet6 and the difference is that one circular is filled and the other one is empty. The same method used for Pet1 with a diamond shape while for the Pet4 two similar symbols *"+"* and *"*x*"* are used to show the experimental data. The simulation result is shown by a red rectangle.

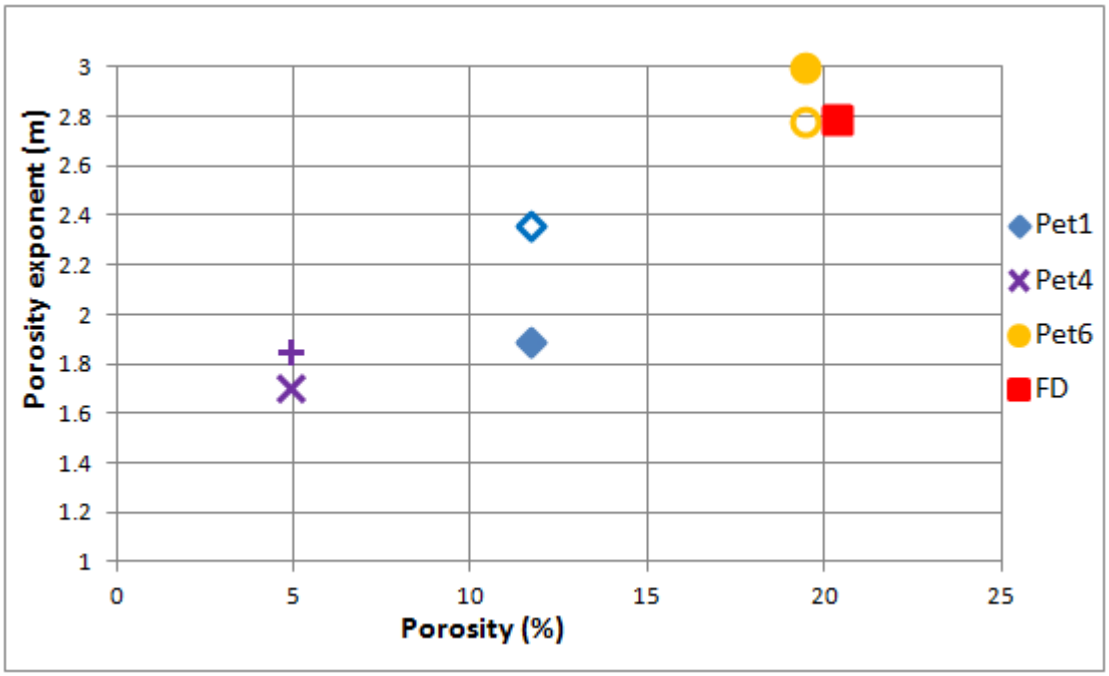

Figure 3.13: The simulation result from (FD) can match the experimental result for Pet6.

However, this size sample is too large for personal computer calculation and this result is calculated by work station which is not always available for some researchers. In order to easily and conveniently obtain porosity exponent, random walk (RW) simulation can be used to calculate the Formation Factor (FF) of the porous medium and then the porosity exponent can be derived by Archie's First Equation, $FF=R_0/R_w=1/\phi^m$ in Equation (1.1) and Equation (2.32), which can accurately predict the porosity exponent of the sandstone Fb22 in Chapter 2(Figure 2.14 and Figure 2.15).

In this section, firstly the simulation results based on random walk for Pet1, Pet4 and Pet6 (SC800) are shown in Figure 3.14. "*RW*" in the legend means random walk simulation for each sample and the results are shown by red triangle. The simulation results for Pet4 and Pet6 can match the experiments while the simulation value for Pet1 is about 8.3% ((2.6-2.4)/2.4) larger than the experimental data while less than 20%, the difference between the two lab results in Figure 3.12, which can be discussed later.

Then the effect of REV on the porosity exponent can be studied by the results of RW based on Sub REV samples with different size for Pet4 and Pet6 (SC800). For Pet4 and Pet6 (SC800), each sample can be divided into eight Sub REV samples (SC400) (shown in Figure 3.15) and the segmentation of the eight Sub REV samples (SC300) is based on a centrally located REV sample (SC600), Additionally, eight REC (SC600) can be similarly segmented from samples (SC800). The porosity exponents from these

different sub-samples can be compared with the experimental results to show the influence of REV on porosity exponent in Figure 3.16.

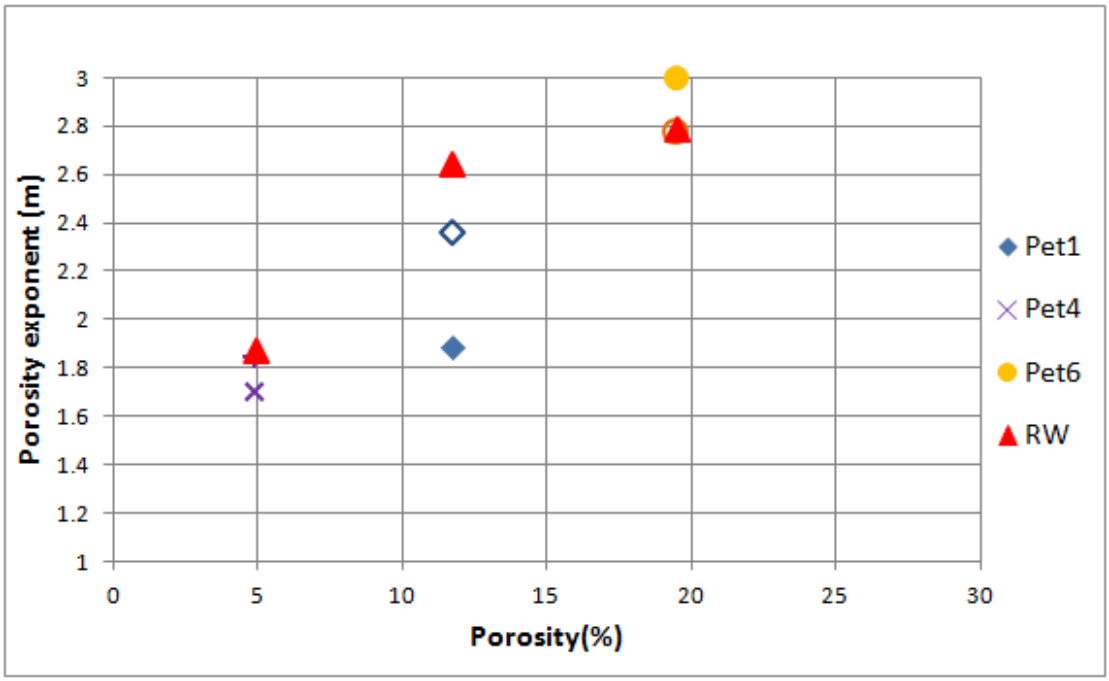

Figure 3.14: The simulation results based on random walk for Pet1, Pet4 and Pet6 (SC800) are compared with the experiments (RW-Random Walk).

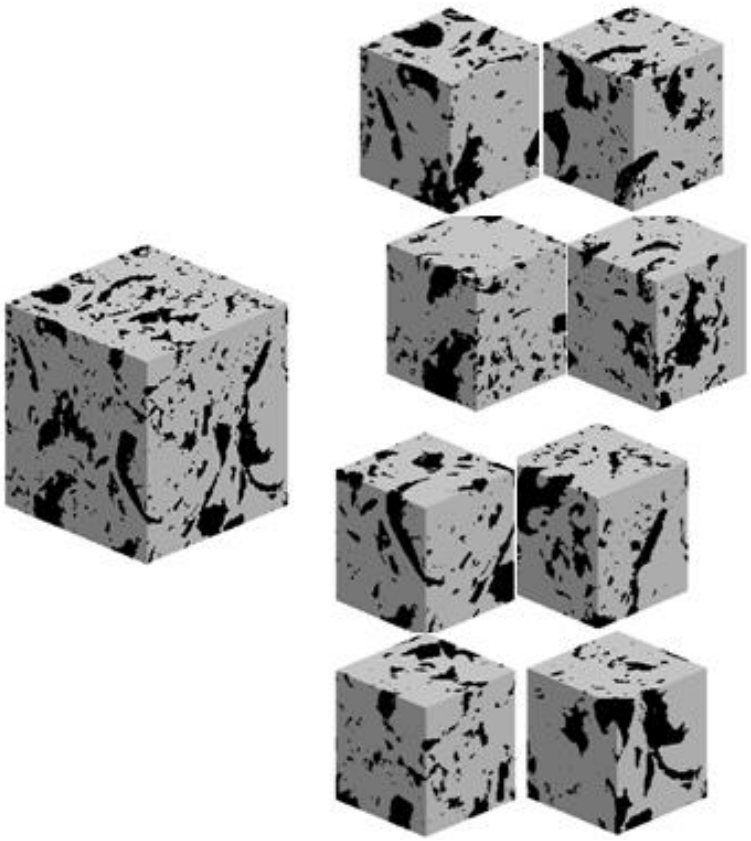

Figure 3.15: The eight Sub REV samples (SC400) distribution in the whole Sup REV sample (SC800) for Pet6.

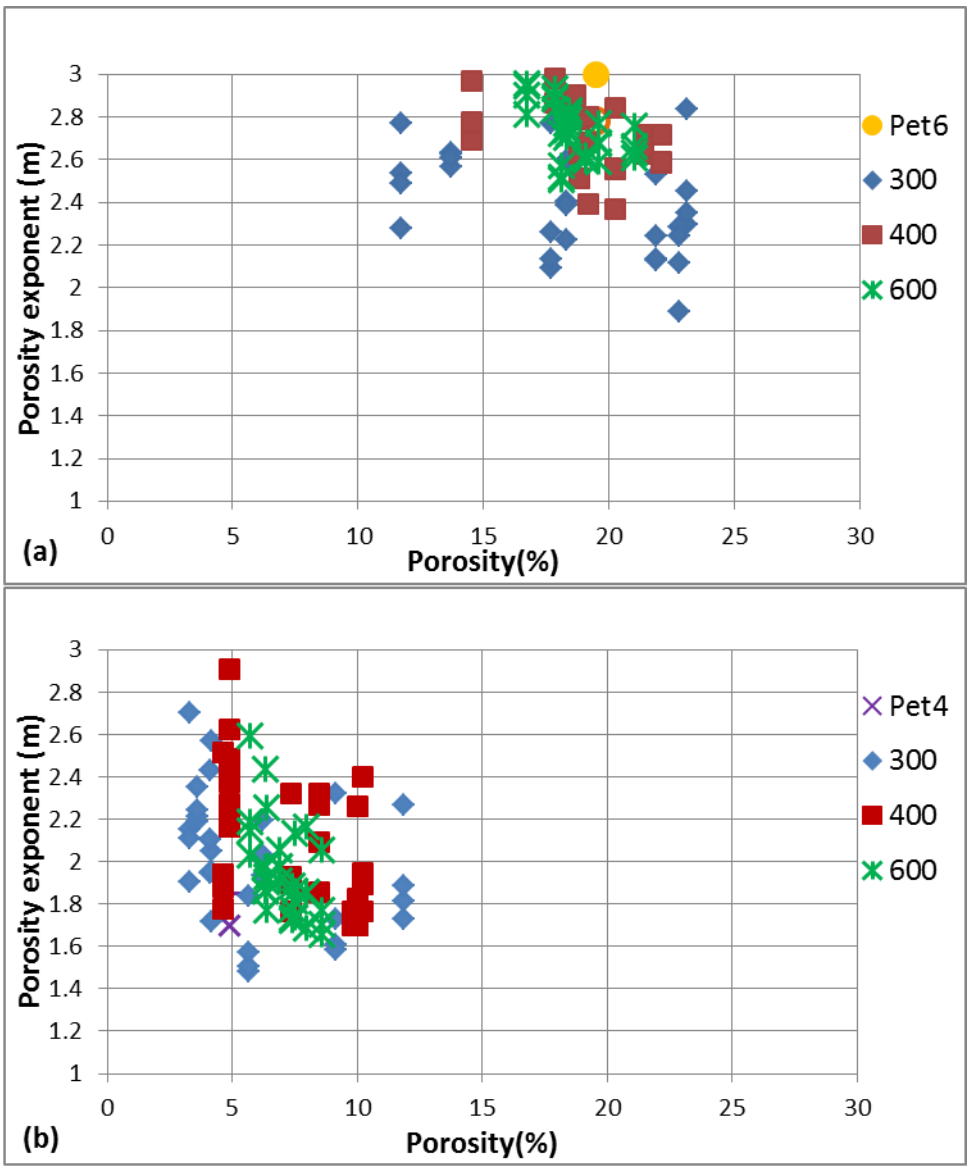

Figure 3.16: The distribution of the three directional porosity exponents for the eight Sub REV samples. The results for these samples (SC300) are shown in blue diamond, the data for the samples (SC400) are expressed by red rectangles and data for SC600 are shown in green symbol.

In Figure 3.16 it is clear that the distributions of the porosity exponents for the larger samples are much better than those of the smaller samples. For Pet6 (Figure 3.16a), the simulated porosity exponents and the porosities of the Sub REV samples (SC400) are much closer to the experimental data, the maximum variation of the simulated porosity exponent is 20% for the porosity exponent 2.4 and the difference between the experimental results and the Sub REV samples (SC400) in porosity is less than 12% while the distribution of the porosities and porosity exponents is much wider for the Sub REV samples (SC300), the minimum of the simulated porosity exponent is about 1.8 and the porosity ranges from about 10% to 23% while the variation of the simulated porosity exponents and porosities are 4.4% and 7.0% respectively for REV

samples (SC600). In Figure 3.16b, the difference of the porosity exponent distribution between the two kinds of Sub REV samples (SC400 and SC300) for Pet4 is trivial, the porosity exponent ranges from 1.5 to 2.9 for both samples. While in porosity, the scatter of the Sub REV samples (SC300) is 5% wider than the distribution of the samples (SC400). The porosities of REV samples (SC600) mostly distribute closely to the experimental results. So the porosity and the porosity exponent based on Sub REV SC600 are closest to the measured data.

Meanwhile the porosity exponent of the whole sample can be estimated by a renormalization method with the help of the porosity exponents from the eight sub-samples. The estimation results based on the sub-samples SC300, SC400 and SC600 respectively are shown in Figure 3.17. In this figure, the estimation porosity exponent for Pet4 from three kinds of sub-samples with different sizes can match the experimental data, 1.8. All of the estimation exponents for Pet1 are close to the experimental exponents, because the difference between the two experimental porosity exponents for Pet1 is about 0.6 which is about 25%, (2.36-1.89)/1.89=0.2486, of the porosity exponent of itself. The better porosity exponent (GP) for Pet6 based on smaller samples (SC300) is 2.4 which is still less than porosity exponent 2.8 in lab by 0.4 while the worst estimation (KK) from the Sub REV samples (SC400) is 2.6 which is the same variation between the two experimental porosity exponents, 2.8 and 3.0 for Pet6. For renormalization, the porosity exponent based on larger Sub REV samples (SC600) is closer to the data.

During the simulation, the current flow density of the 3D samples can be shown to visually inspect the current flow distribution. The current flow density of Pet6 in three directions and its average result can be shown based on a Sub REV sample (SC300) in Figure 3.18. In this figure, high current flow density is shown by red colour and the low density is in blue colour. It is clearly shown that the density of the current is not always denser in centre than in the corner. In Figure 3.18g (2D slice), the centre of the pore space is green while the corner of the pore is orange means the current is concentrated in the corner instead of the centre, which also can be inspected in Figure 3.18f (y direction). Additionally, the small pore may show higher current density than the big pores. That is, the current sometimes dominates the smaller pores which can be shown in the same two 2D cross sections. In the middle area of each cross section (f), (g) and (h), there are three small red spots whose density is larger than the density of the surrounding big pores.

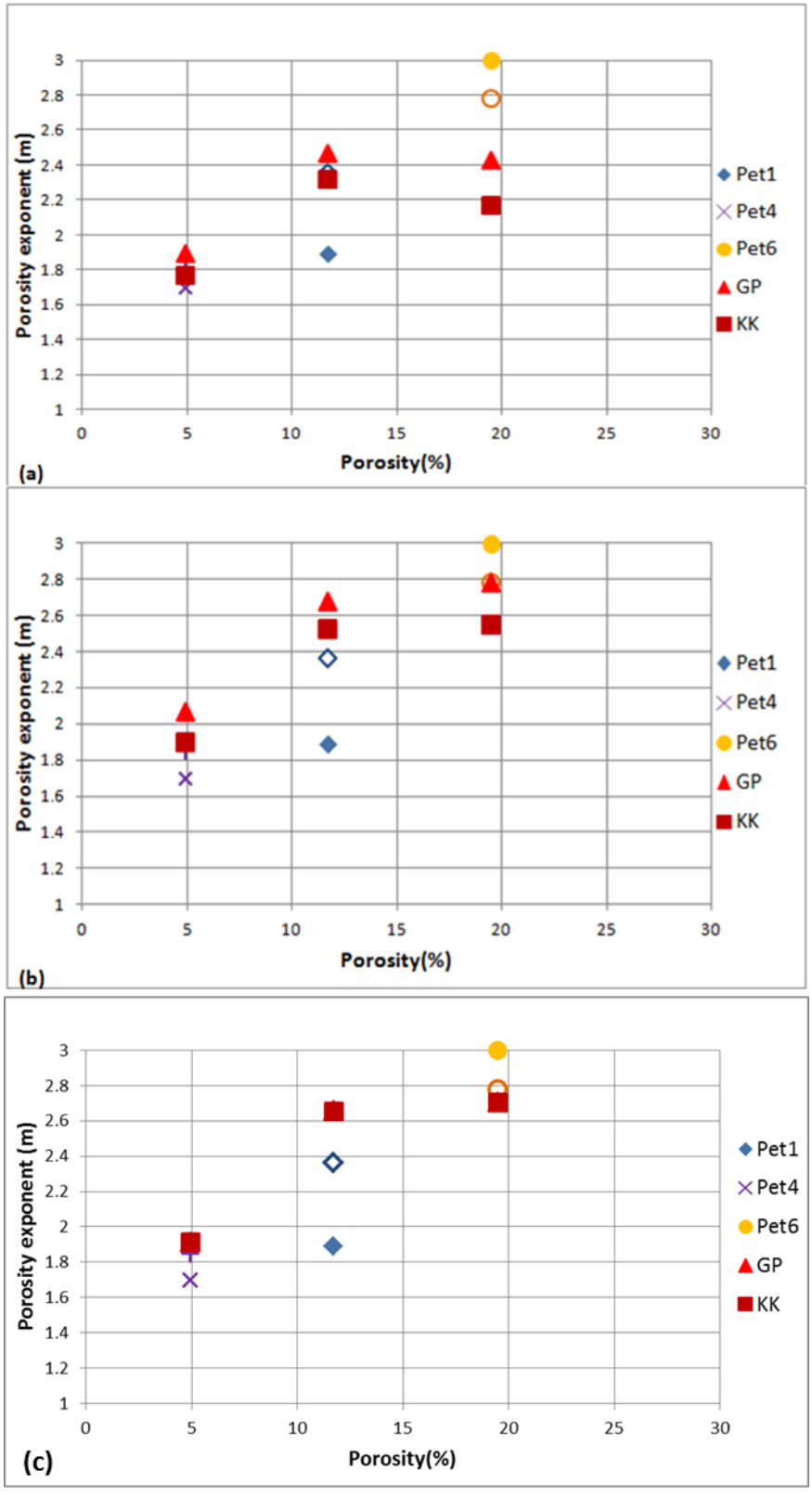

Figure 3.17: The estimation porosity exponents based on a renormalisation method with two calculation algorithms denoted by GP and KK. In (a) the estimation results from eight Sub REV samples (SC300) for each carbonate samples are shown as red triangle and rectangle while the data from the Sub REV samples (SC400) for these carbonates are shown in (b), (C) shows the estimation based on REV samples (SC600).

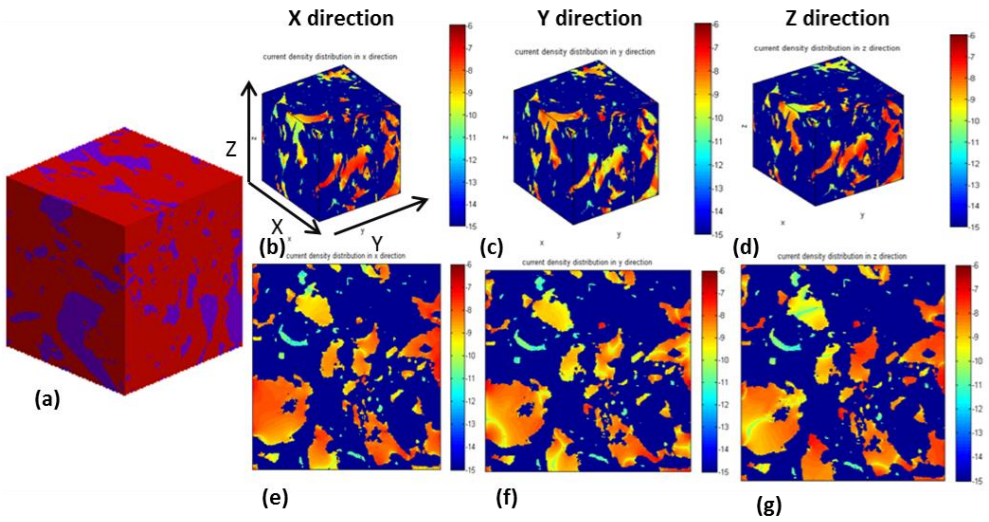

Figure 3.18: The current flow density distribution from a Sub REV sample (SC300) of Pet6. The binary image (a) consists of pore in blue and matrix in red. In the current density distribution, the legend is magnitude of the current density based on logarithm10 scale, the direction of the current flow is in X,Y,Z from (b), (c), (d) respectively, the 2D slice (e, f, g) is a XY plane extracted from Z=150.

3.3.3 Heterogeneity and Anisotropy of Carbonates

The porosity exponents can be correctly simulated by FD, random walk and a renormalization method based on Sub REV. The heterogeneity of the carbonates can be reflected by the comparison the distribution of porosities and porosity exponents of the carbonates Sub REV with these distributions of sandstones which is represented by the Fontainebleau sandstone Fb22.

The heterogeneity of the carbonates can be reflected by the porosity exponent of the Sub REV (SC400) located in different parts of the carbonates. So eight Sub REV can be extracted from each carbonates (Pet1, Pet4 and Pet6) meanwhile the REV sample can be defined in Fb22. The average porosity exponent of each Sub REV sample can be calculated by the exponents in three directions by Equation 3.2. The heterogeneity of the carbonates can be presented by the distributions of the average porosity exponent for sandstone and carbonates in Figure 3.19.

$$\frac{1}{F}=\frac{1}{3}\left(\frac{1}{F_x}+\frac{1}{F_y}+\frac{1}{F_z}\right) \qquad (3.2)$$

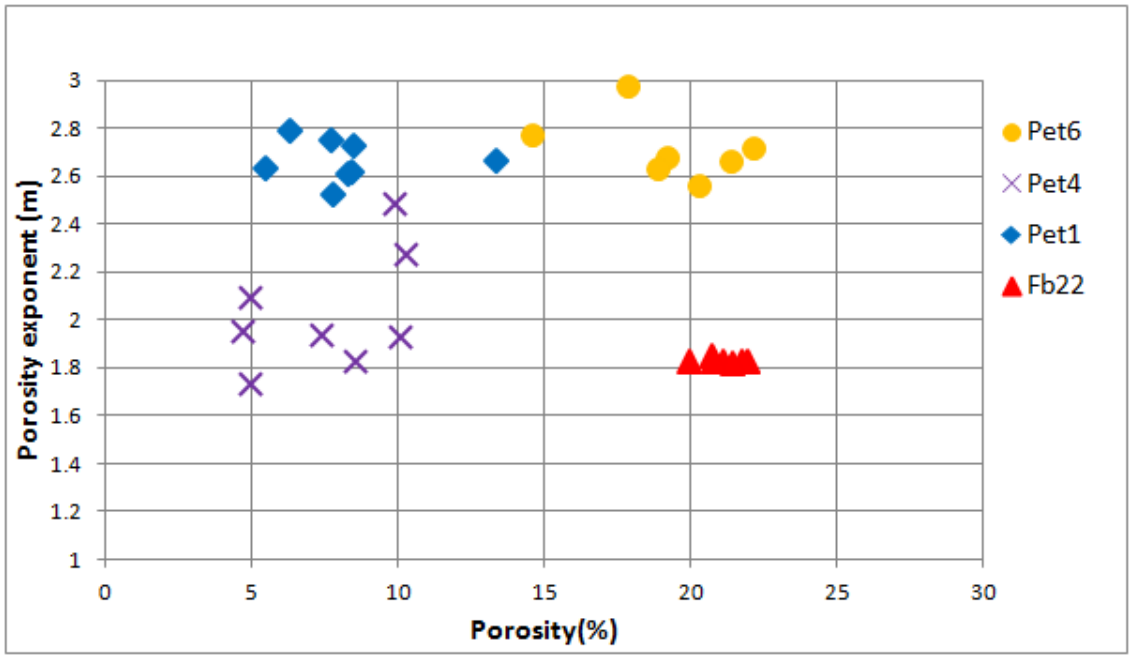

Figure 3.19: The distribution of the average porosity exponents for sandstone Fb22 (SC240) and carbonates Pet1, Pet4 and Pet6 (SC400).

It can be shown that the average porosity exponents for Fb22 are almost equal to 1.8 with porosity from 20% to about 23% while the distributions of the porosity exponents for carbonates are much wider with 0.4 in the porosity exponent bound for Pet1 (2.4-2.8) and Pet6 (2.6-3.0) and about 0.8 from 1.7 to 2.5 in Pet4.

For three carbonates samples, the variation of the porosities for each Sub REV sample (SC400) is the same, about 5%. The Sub REV samples (SC400) for Pet4 show the similar porosities from 5% to 10% while its porosity exponents change greatly from 1.7 to 2.5. For Pet1 and Pet6, both spans of the porosities are about 7% with all porosity exponents close to 2.7. The heterogeneity of the carbonates can be reflected by the distribution of their porosities and porosity exponents. The coefficient of the heterogeneity can be calculated by the standard variation divided by its mean for the porosity and porosity exponent in Figure 3.20. It is clear that carbonates are much more heterogeneous than sandstones. The heterogeneity coefficient of the porosity and porosity exponent for sandstone Fb22 are 0.05 and 0.01 respectively. While the smallest heterogeneity coefficient of the porosity and porosity exponent are 0.25 and 0.06 respectively in Pet1 and the largest in Pet4 is about ten times larger than the coefficient of sandstone.

The anisotropy of the carbonates can be presented by the variation of the porosity exponents in three directions for each Sub REV samples (SC400) in Figure 3.21. The results of Fb22 (SC240) can be taken as a comparison. It is clear that in Fb22, the

variation of the porosity exponents in three directions for the same Sub REV sample (SC240) is less than 0.1 close to 1.8 and the maximal variation of these exponents is 3% of the porosity exponent from itself. The fluctuation of the porosity exponents in carbonates is larger compared with the results of Fb22. The largest difference is Pet4 (Figure 3.21c), the minimum of porosity exponent is in y direction about 1.8 and the maximal porosity exponent is about 2.8 in z direction. The differences of the porosity exponents in three directions for Pet1 and Pet6 are the same about 0.6 from 2.4 to 3.0.

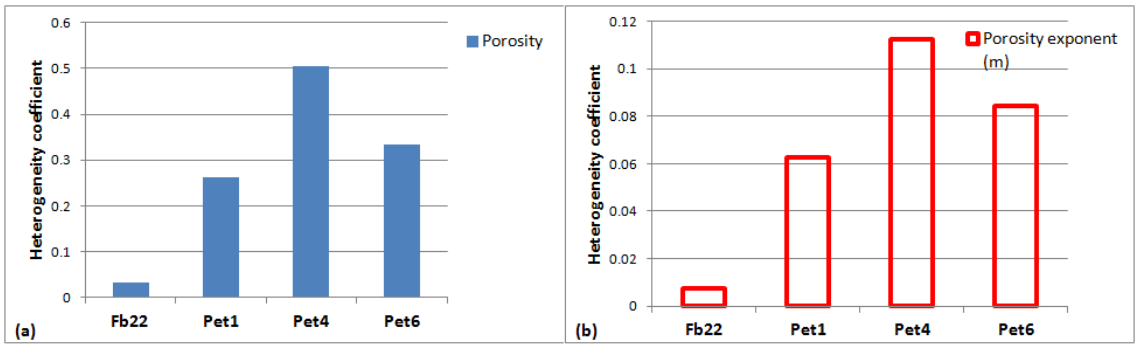

Figure 3.20: The heterogeneity of the porosity and porosity exponent for the sandstone Fb22 (SC240) and carbonates Pet1, Pet4 and Pet6 (SC400).

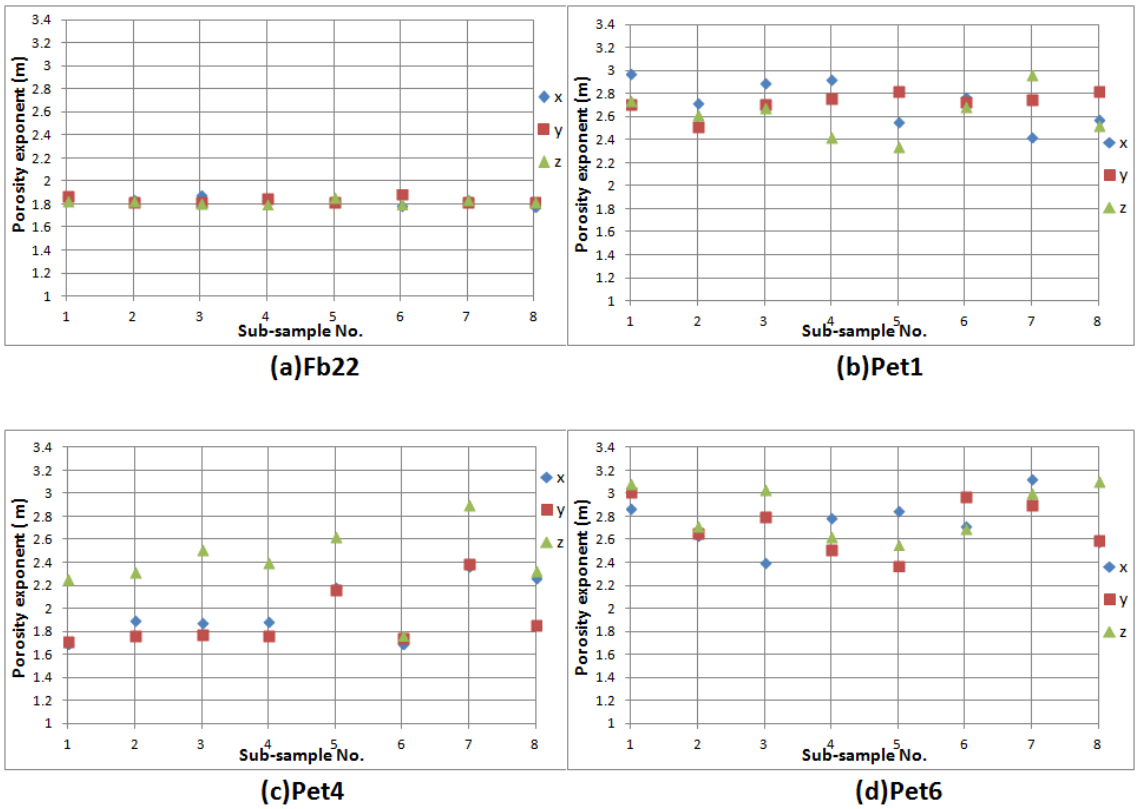

Figure 3.21: The distribution of the porosity exponents in three directions for the eight Sub REV samples (SC400) in Pet1 (b), Pet4 (c) and Pet6 (d). The results of Fb22 (SC240) are used as a comparison in (a). The x, y, z in the legend denotes the porosity exponents in three directions and the x-axis denotes the eight Sub REV samples (SC400) from 1 to 8.

The anisotropy can be quantified by the coefficient defined as the maximal porosity exponent and the minimum in three directions for each Sub REV samples in Equation 2.33 (Salem and Chilingarian, 1999[173]). The anisotropic coefficients for Fb22 and three carbonates are shown in Figure 3.22. In Figure 3.22, the anisotropy of Fb22 is the smallest and its average is about 1.08. While Pet4 presents the strongest anisotropy in these three carbonates taking 2.02 as its average. The anisotropy for Pet1 and Pet6 are moderate with the average anisotropic coefficient of 1.53 and 1.33 respectively. The anisotropy coefficients for carbonates (Pet1, Pet4 and Pet6) are significantly larger than those for sandstone Fb22. So for the sandstones, one porosity exponent can be used to represent the porosity exponents for three directions in water saturation calculation with minimal error while the porosity exponents in three directions for carbonates vary greatly giving rise to different saturations so the porosity exponents for carbonates should be directional.

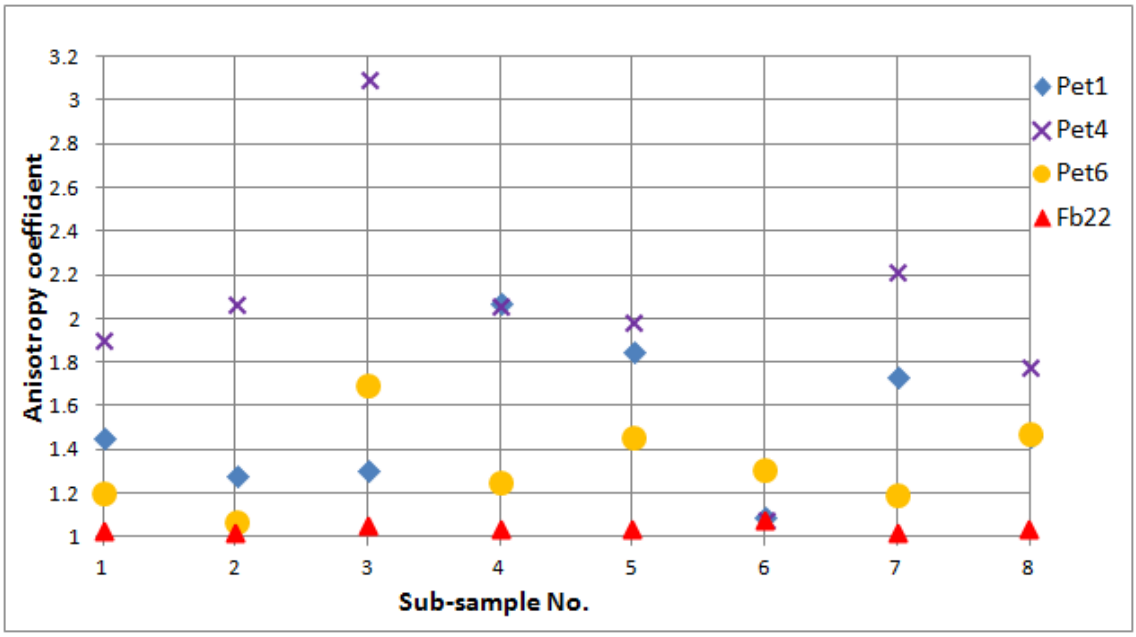

Figure 3.22: The distribution of the anisotropic coefficients for the eight Sub REV samples of Fb22 (SC240) and carbonates Pet1, Pet4 and Pet6 (SC400). The x-axis denotes the eight Sub REV samples from 1 to 8.

In the above sections, the simulation results can match the experiment results showing the feasibility of the simulation methods meanwhile the effect of the REV size on the simulation can be researched and then the heterogeneity and anisotropy of the carbonates are presented by comparing with sandstones.

The porosity exponent is related to the porosity and the resistivity of the fully brine-saturated porous media. The resistivity of the porous media with the same brine is

only related to its pore structure. Hence, the porosity exponent is directly linked to the pore structure. The properties of the pore structure can explain their porosity exponent distribution. In the next section, the properties of the pore structure include topology (TP) and geometry (GM) can be extracted from the pore space of the porous media and these properties can be used to explain the electrical results.

3.4 Topology and Geometry of the Pore Space

Obviously, the electricity of the porous media fully saturated with brine is directly linked to the structure of the pore space which is reflected by its TP and GM.

In this section,

- Firstly, the connectivity reflected by Euler number is illustrated and then applied in a Sub REV sample (SC300) from Pet6 (3.4.1);
- Secondly, the geometrical (3.4.2) and topological properties (3.4.3) of the pore network based on maximal ball (MB) method for one comparison sandstone Fb22 (SC400) and three carbonate samples Pet1, Pet4 and Pet6 (SC800) are shown.
- Thirdly, the porosity exponents for three carbonates samples should be explained by their geometry and topology (3.4.4).

3.4.1 Minkowski Functions Application

This section firstly illustrates the relationship between the Euler number and pore connectivity and then investigates the effect of segmentation and pore space on porosity exponent. In order to explain the relationship between the Euler number and the topology (connectivity) of the pore space, a simple model with the various pore sizes can be built and then be used to calculate Euler number of the pore space with different pore sizes shown in Figure 3.23. In this figure, the x-axis is the minimal pore radius of the pore space, with the decrease of this pore radius, the volume of the pore space increases then raising the porosity.

It is clear that with the decrease of the pore radius from 20, the number of isolated pore clusters (red cubes) gradually increases from 1 to 8 with the porosity from 5% to 32%, the Euler number raises from 1 to 8. In this case, the Euler number reflects the number of the isolated pore clusters. When the pore radius further decreases from 13 to 1, the porosity of the pore space increases by the emergence of the blue channels, the

isolated pore cluster decreases and then the Euler number decreases from 8 to 0,with the pore radius equal to 9, and then to -16.

The relationship between Euler number and connectivity of the pore space describes qualitatively that the positive Euler number is related to the number of the predominantly isolated pore clusters while the negative Euler number is related to the number of the channels which comprise the main pore space. The increase of the positive Euler number presents the worse connection of the pore space and the decrease of the positive Euler number shows that the isolated pore clusters are gradually connected by the channels; The decrease of the negative Euler number illustrates the better connection of the pore space and the increase of the negative Euler number is related to the increase of the isolated pore clusters.

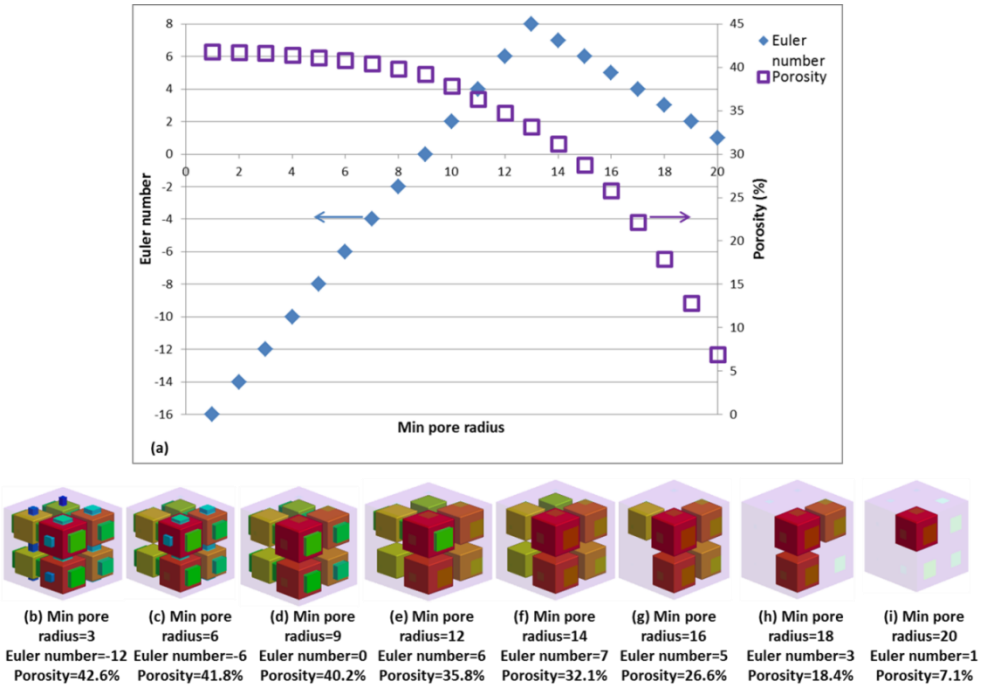

Figure 3.23: The Euler number (in primary axis) and Porosity (%) (secondary axis) versus Min pore radius which is the minimum of the pore sizes (a). The pore space related to the pore size including the Euler number and porosity is shown in the bottom from b to i.

The Euler number calculated by Minkowski Functions reflects the pore connectivity of the pore space which is related to the porosity exponent. Additionally, the binary images are segmented from the grey scale CT images based on the threshold value. So different threshold values can generate various binary images with different pore space and then the Euler numbers and porosity exponents of these images are different. In order to study the relationship between the porosity exponent and the Euler number as well as the effect of the threshold on the porosity exponent, a series of binary

images (from a Pet6 sample SC300) can be generated based on different threshold values and then their Euler number can be calculated by Minkowski Functions and the porosity exponent can be obtained by finite difference (FD) method.

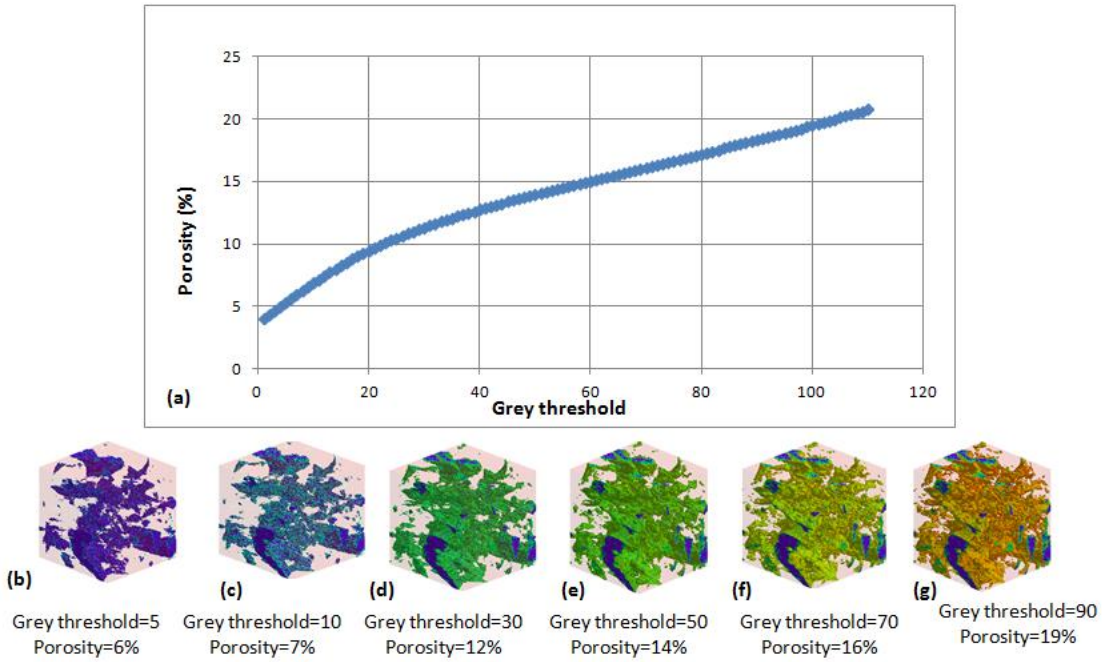

Figure 3.24: The porosity versus threshold is shown in (a) and the pore spaces for different thresholds of grey scale are presented from (b) to (g).

Figure 3.24 gives the relationship between porosity of the binary image and the threshold based on a Sub REV sample (SC300) of Pet6. With the decrease of the threshold, the number of the voxels classified into pore reduces and then the porosity declines. The images in the bottom show their pore space for different thresholds. The pore space is reduced by firstly removing the pore corners and then gradually towards the pore centres, because the grey scaled (0-255) data of the pore corner and edge is usually larger than that in the pore centre which is shown in Figure 3.25. In this figure, the pore area confined by the circle is a big pore in blue reflecting low grey scale data while the sections defined by the triangle are close to the pore corners or the irregular edges which are green and the grey scale data is 100. So the more the pore space is blue, the simpler the pore space while the pore space becomes complex when the colour of the pore space turns to red.

The pore structure becomes simple by keeping the big pores and removing the irregular corners. The percolation of the pore space should be examined because with the decrease of the pore space, the pore space may be blocked in one direction which would affect the resistivity in this direction and then the porosity exponent. The results of the percolation with the threshold in three directions are shown in Figure 3.26 with

the results of the porosity exponents and Euler number calculated according to the 26 and 6 connections (the basic concepts about the binary images and connection can refer to Appendix D).

From the image in Figure 3.26a, it is clear that the porosity exponent gently increases to 3.0 with the decrease of the threshold. The decrease of the threshold reduces the porosity by removing the irregular corners. The pore space becomes simpler while the porosity exponents increase in all directions. During this process, the positive Euler number keeps stable. When the threshold value is less than 29, the pore space is not percolated in x direction, the porosity exponent in x direction firstly raises to a peak and then the exponent in y direction goes up to a maximum representing the block in y direction. Meanwhile Euler number reaches a plateau reflecting the increase in the amount of the isolated pore clusters. When the threshold further reduces, the change of the resistivity of the porous medium fully with brine is trivial while the porosity of the porous medium consequently reduces as a result the porosity exponent would decrease which is shown in Figure 3.26 (a) at the low porosity section.

It is clear, in Figure 3.27, that the pore space becomes simple by preserving the big pores and removing the irregular corner when the threshold gradually reduces. The current gradually dominates the smaller pores according to the current changes from (d), (h), to (l), the current is mainly distributed in pore centre by red colour in Figure 3.27d while the current finally is in the corner of this pore in orange colour with the rest is in blue (Figure 3.27l).

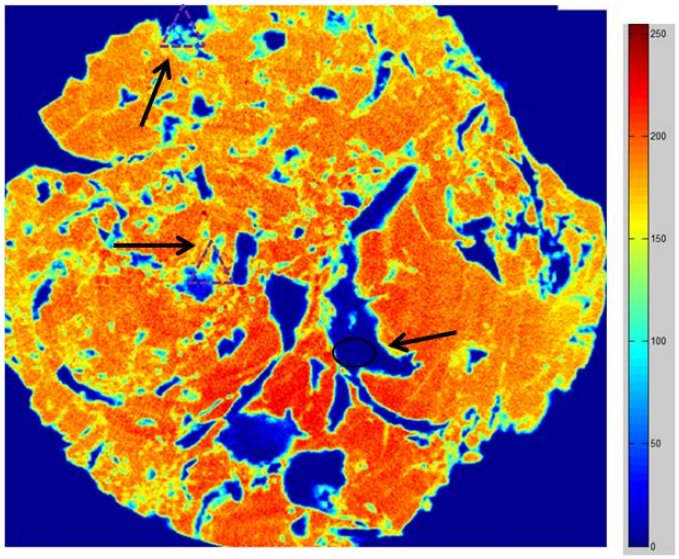

Figure 3.25: A cross section of Pet6 in grey scale is shown in a colourful image with its colour map on the right. There are three symbols (located by black arrows) in this image. One circular is in a big pore centre which is blue and the rest are located in a green area by triangle showing the irregular pore corners and edges in green colour.

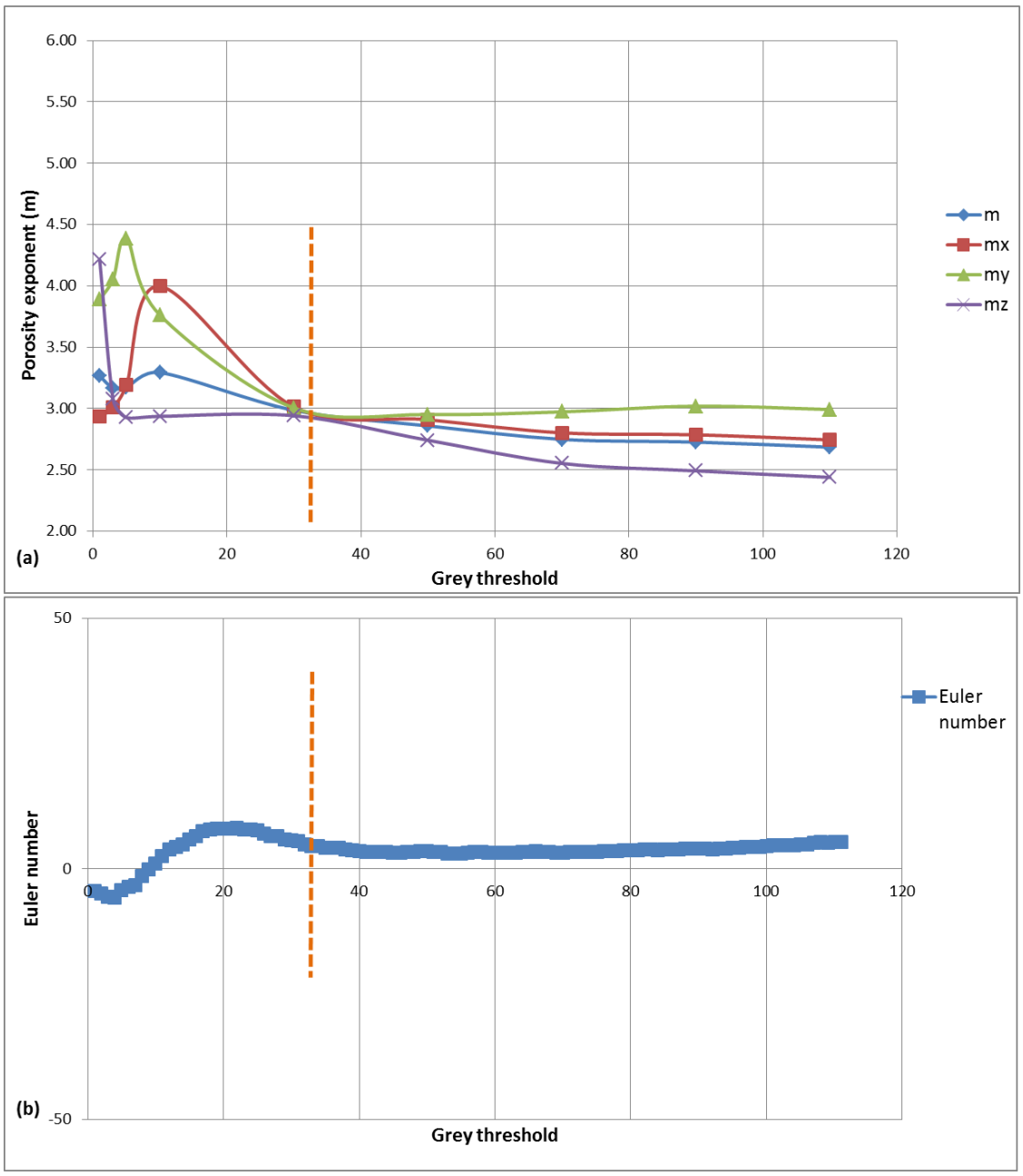

Figure 3.26: The relationship between the porosity exponents and threshold is shown in (a). The exponents include the exponents in three directions and their average exponent. The Euler number is in (b). The percolation is expressed by a dash segment in orange and the related threshold is 29 in grey scale. When the threshold value is less 29, the pore space generated is firstly not percolated in x direction and then in y direction.

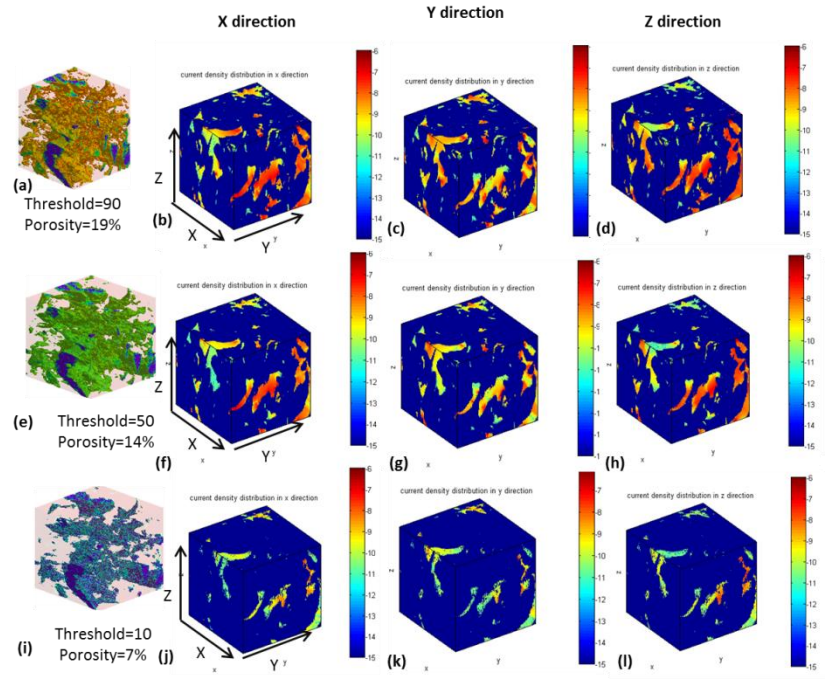

Figure 3.27: The flow current density in 3D for different thresholds. (a), (e), and (i) are the pore space and its porosities; (b), (f) and (j) are the current density distribution for the current flow in x direction; (c), (g), and (k) are for the current flow in the y direction and the results of the current flow in z direction are in (d), (h) and (l); The legend is the magnitude of the current density on logarithm 10.

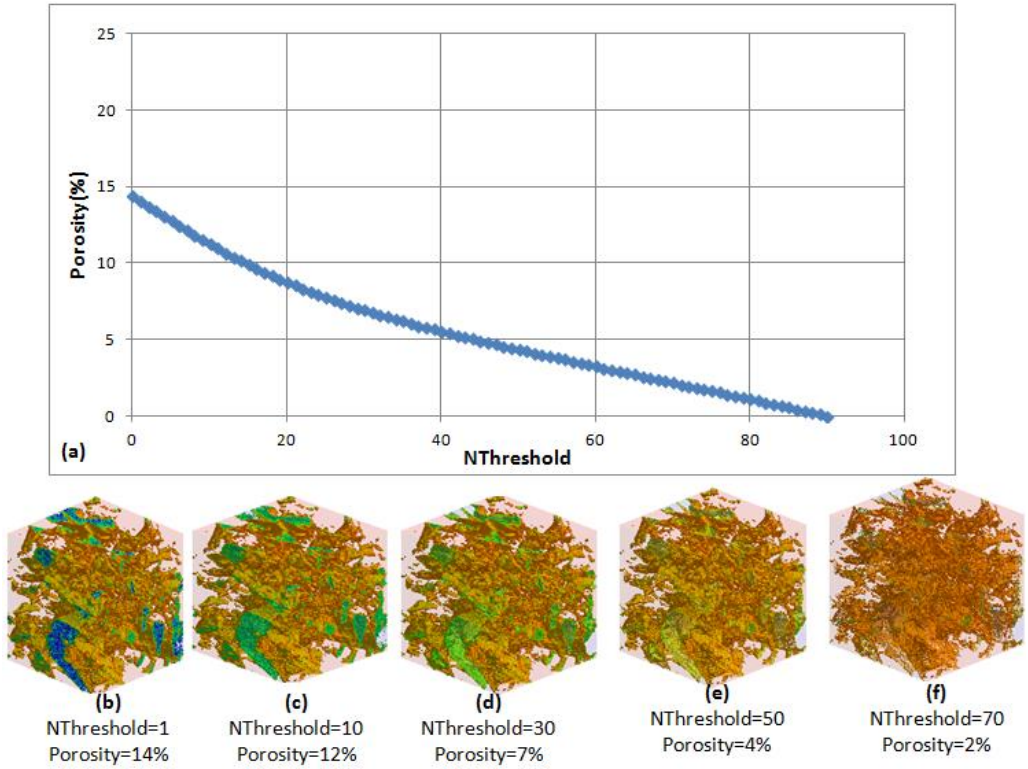

Figure 3.28: The porosity versus new threshold is shown in (a) and the pore spaces for different new threshold are presented from (b) to (f).

The porosity exponent gradually increases with the simplification of the pore space. What happens to the porosity exponent when the pore space becomes complex? So a series of binary images with different porosities by removing the pores from their centre are generated in Figure 3.28. In these samples, the initial threshold for binary images is 90. In order to get these binary results, a new threshold, expressed by "NThreshold" should be used to segment the original grey scale images. The voxels whose grey scale data in this range [NThreshold, 90] are classified as pore and the rest are void. With the increase of this new threshold, the ranges in the grey scale images for pores becomes narrower and then the pore space is mainly composed of the irregular pore corners due to the fact (Figure 3.25) that the large and obvious pore in grey scale image is close to zero.

So the percolation, Euler number and porosity exponent of these models can be calculated and their results are shown in Figure 3.29(b) and Figure 3.29(a). The porosity exponents in three directions all decrease from about 2.8 to the minimum 2.2, the related new threshold increases to 40. The pore space consists of the voxels whose grey scale ranges from 40 to 90. In this process, the Euler number reduces to the minimum meaning the best connectivity of the pore space at this point. As the threshold further increases, the porosity exponents rapidly increases to 4.0 and the Euler number also dramatically raises from negative to positive. The connectivity of the pore space becomes worse in this process. The negative Euler number means the pore space is connected while the positive Euler number means the pore space is not connected. The transition from unconnected to the connected state for pore space is reflected by whether the Euler number declines to zero or not. Euler number equal to zero is the critical point. So the increase of the Euler number means the connectivity becomes worse and the decrease of the Euler number represents the better connectivity of the pore space.

In Figure 3.30, it is clear that the pore space becomes complex from top to bottom due to the segmentation of the big pores and the preservation of the irregular pore edges and corners. The current mainly flows along the corners and edges of the pores which show as red colour even the porosity decreases to 7%.

So the pore systems with simple, big pores result in poor structure for current flow with a high porosity exponent, while the complexity of the pore space does not mean poor structure for current flow.

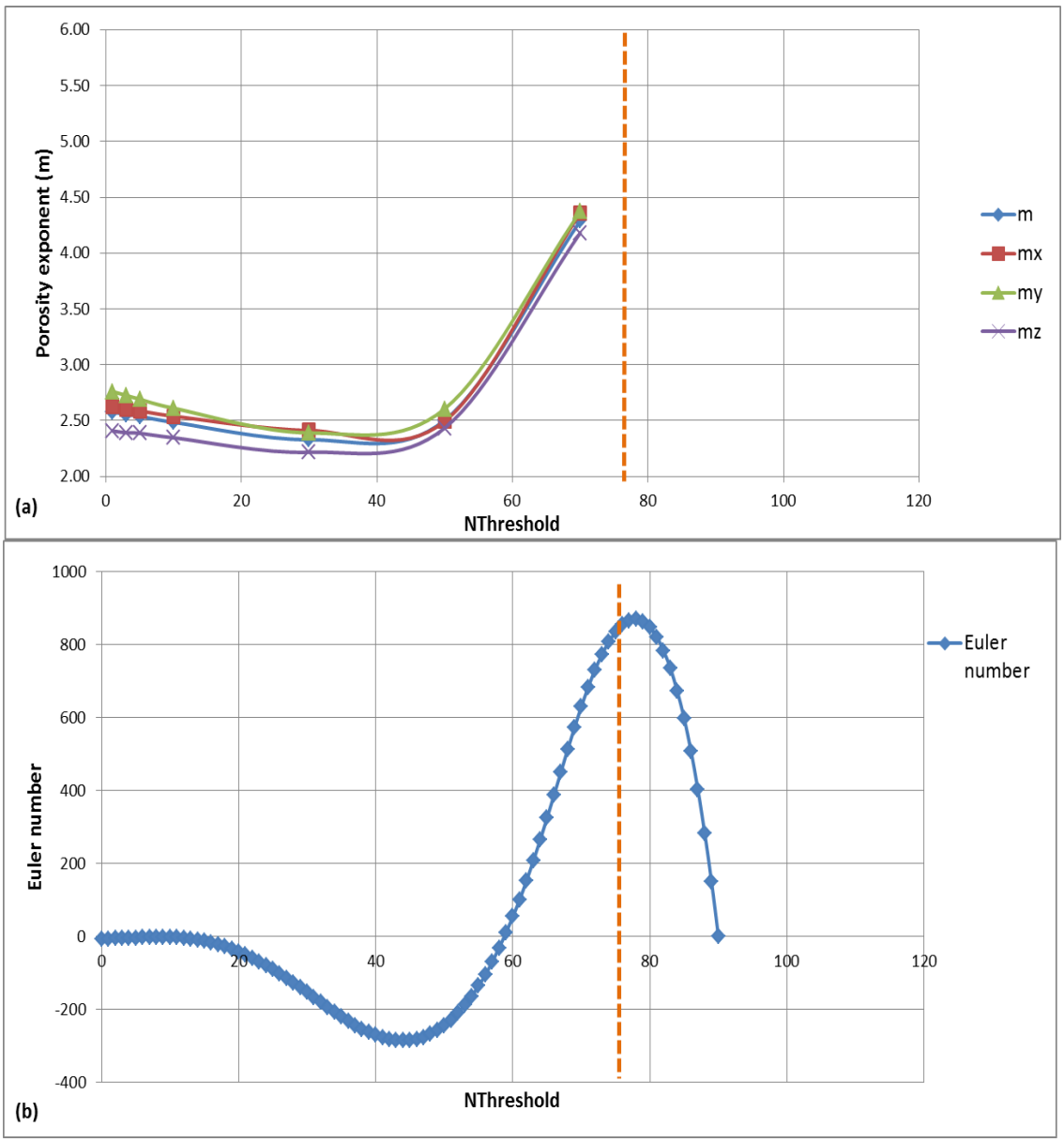

Figure 3.29: The relationship between the porosity exponents and new threshold *"NThreshold"* is shown in (a). The porosity exponents include the exponents in three directions and their average exponent. The Euler number is in (b). The percolation is expressed by a dash segment in orange and the related threshold is 76 in grey scale. When the new threshold value is less 76, the generated pore space is percolated until the new threshold *"NThreshold"* >76.

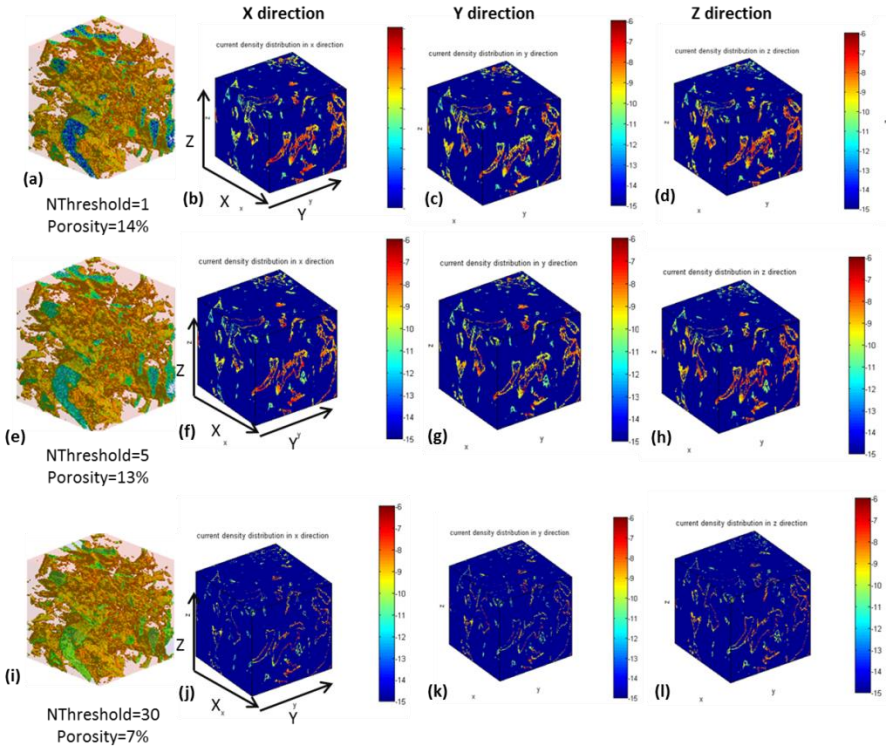

Figure 3.30: The flow current density in 3D for different thresholds. (a), (e) and (i) are the pore space and the porosities; (b), (f) and (j) are the current density distribution in x direction; (c), (g) and (k) are in the y direction and the density in z direction are in (d), (h) and (l); The legend is the magnitude of the current density on logarithm 10.

As already discussed above, Minkowski densities are average quantification of the pore structure without considering the information about pore size distribution which is important for the physical properties of the porous media. This information is considered in a connectivity function presented by Vogel (1997[208]) which links the connectivity to the pore size. This function in fact is a relationship between pore size and Euler number. The Euler number in this function is calculated based on the pore fractions whose pore size (radius) is equal to or larger than a given value (Figure 3.26). Pore clusters with pore size in a specific range can be extracted from pore space by morphological operation including erosion and dilation (Serra, 1982[181]) while the Euler number of the pore cluster with this pore size can be calculated by the Minkowski Functions m_3 above. This similar idea is used in the pore network. Next section introduces geometrical and topological properties.

3.4.2 Pore Geometrical Properties

In this section, the calculation of pore geometry is listed as follows.

The histogram of the pore size can be plot in Figure 3.31 for Pet1, Pet4, Pet6 (SC800) and Fb22 (SC400). The x-axis is the radius of the pore size and the y-axis is

the percentage of each pore size which is calculated by the ratio of the volumes of the pore with this size to the total volume of the pores. It is clear that the pore size for Fb22 is the smallest in four samples because the resolution for Fb22 is 5.68 μm smaller than the resolution of carbonates which is about 20 micron. The pore size distribution for the Pet1 and Pet4 are almost same with a peak at about 100 micron while the pore size of the Pet6 is largest and the pore size is dominated in 1000 micron which is about ten times larger than the size of Pet4 and Pet1.

Meanwhile the throat size distribution for Pet1, Pet4, Pet6 and Fb22 is shown in Figure 3.32. The throat size of the Fb22 is still the smallest and Pet1 and Pet4 show the same throat size distribution while the Pet1 has more medium throats with the size of 30 *um* than Pet4. The throat size of the Pet6 is mostly larger than 100 *um*.

According to the pore and throat size distribution for Pet1, Pet4 and Pet6, the permeability for Pet1, Pet4 and Pet6 can be explained by the radius distribution. The Pet4 has the worst permeability which is about 0.21 mD and the permeability of the Pet1 is about 18.6 mD. Their throat size and pore size distribution are similar while the number of the larger size of pore and throat for Pet1 is more than that in Pet4. The throat and pore size for Pet 1 and Pet4 are both about ten percent of the size for Pet6 so the permeability for Pet6 is 282 mD which is about ten times larger than the permeability of the Pet 1 and Pet4. So the permeability is related to the pore and throat size distribution. The pore space with larger size of pores and throats is likely to present better permeability.

The throat shape factor distribution for Pet1, Pet4, Pet6 and Fb22 can be shown in Figure 3.33. It is shown that the curve of the throat shape factor distribution for these four samples are almost the same, most of the throat cross sections with the shape factor of 0.03 (triangular cross section) and the very irregular and smoothed cross section are less for throat cross section. The number of throats with the cross sections of G=0.03 in Pet 6 and Pet1 are much more numerous than those in Pet4 and Fb22. The sample Pet4 reaches the smallest throat cross section region presenting the most irregular throat cross section in these three carbonates samples.

The pore shape factor for these samples is shown in Figure 3.34. Compared with the throat shape factor in Figure 3.33, the pore shape factors move towards small values reflecting that the cross sections of the pores are much more irregular than the cross sections of the throats for these samples. The difference between sandstones and carbonates is obvious in low shape factor section. Compared with sandstone Fb22, the

pore throats of the carbonates have much more complexity. In the carbonates the irregular cross sections in Pet6 are much more various than these in Pet1 and Pet4.

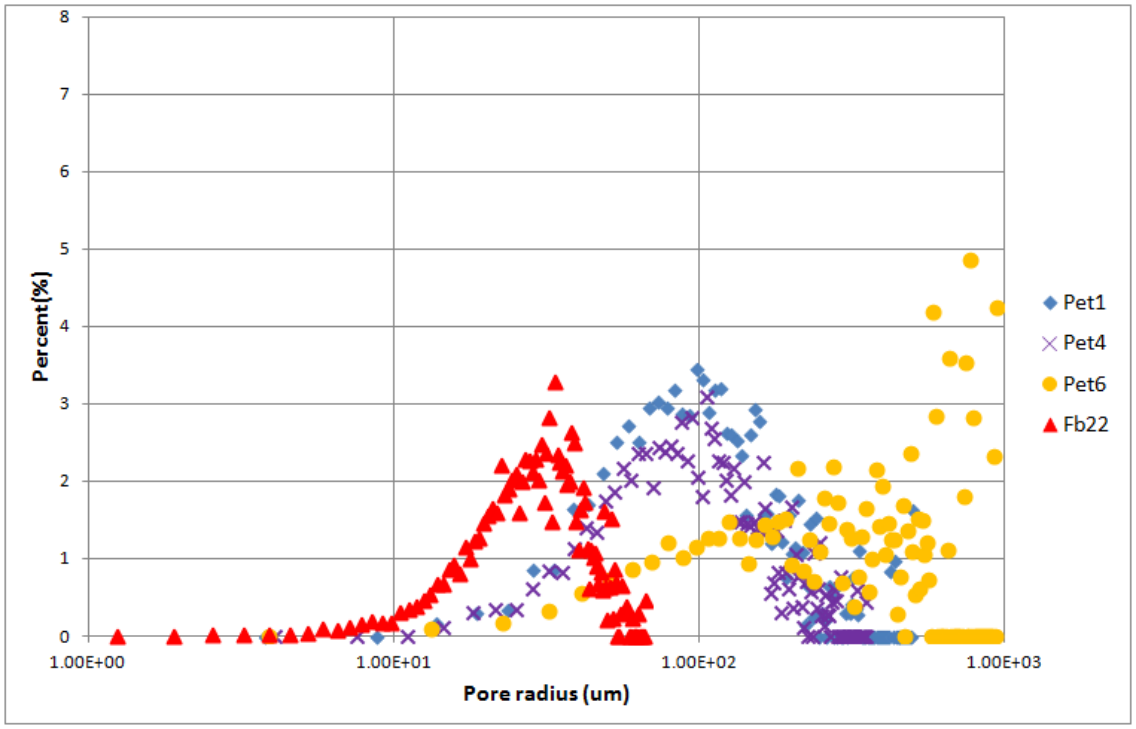

Figure 3.31: The pore size distribution for Pet1, Pet4, Pet6 (SC800) and Fb22 (SC400). The x-axis is shown in logarithm and y-axis is the percentage (%) of each radius. Fb22 has a much smaller distribution.

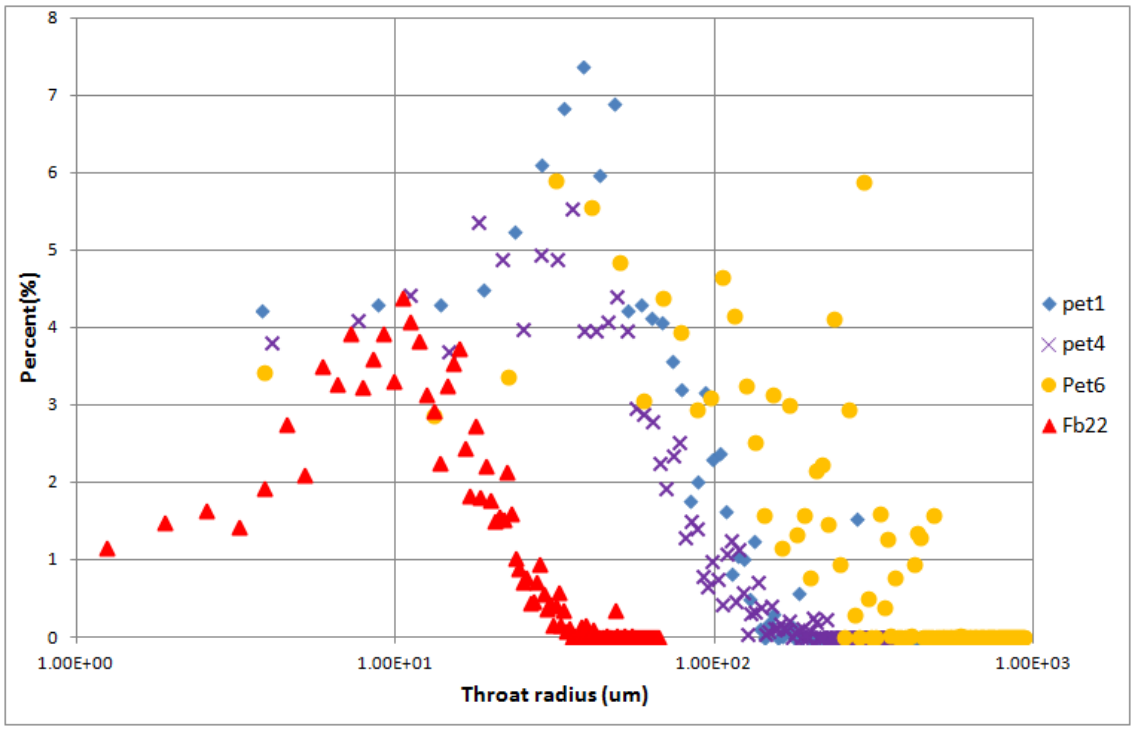

Figure 3.32: The throat size distribution for Pet1, Pet4, Pet6 (SC800) and Fb22 (SC400). The x-axis is shown in logarithm.

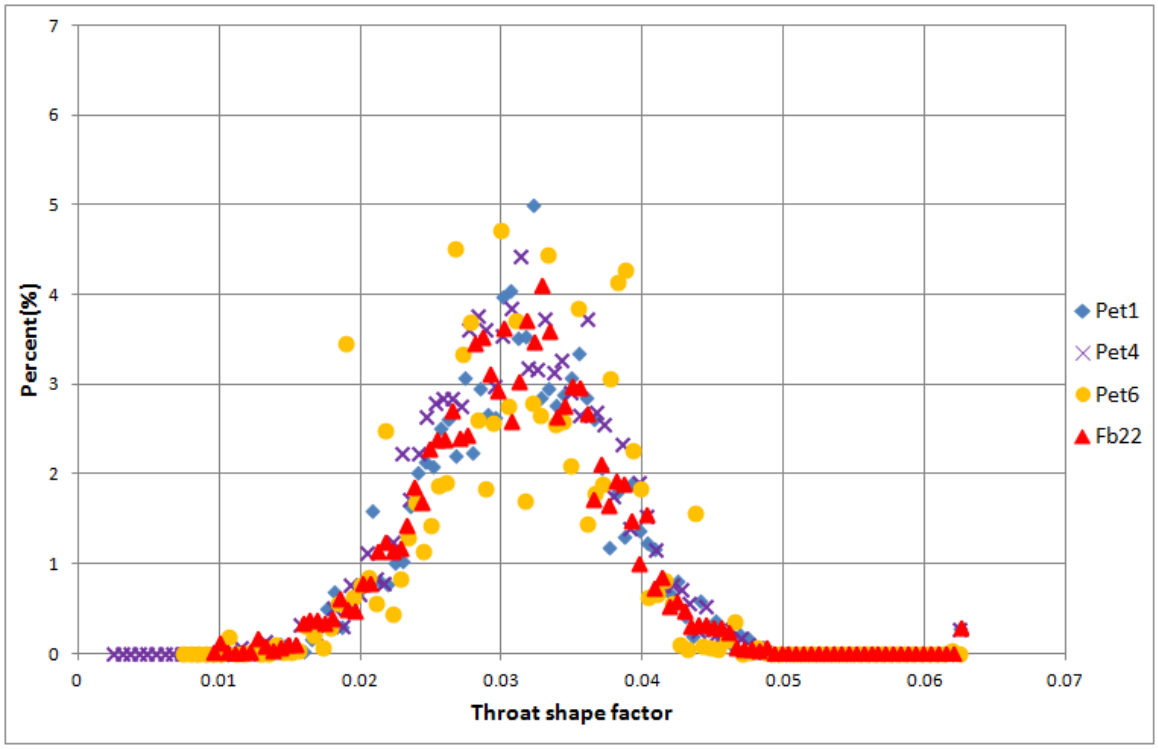

Figure 3.33: The throat shape factor distribution for Pet1, Pet4, Pet6 (SC800) and Fb22 (SC400).

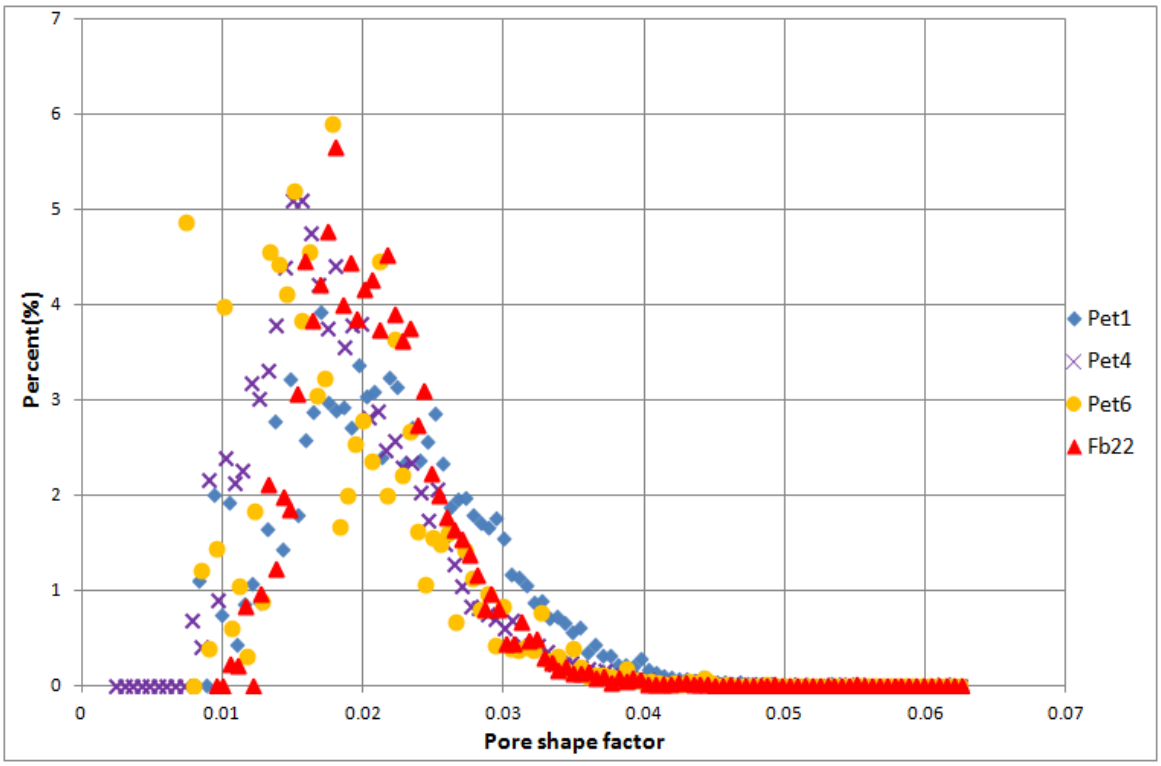

Figure 3.34: Pore shape factor distribution for Pet1, Pet4, Pet6 (SC800) and Fb22 (SC400).

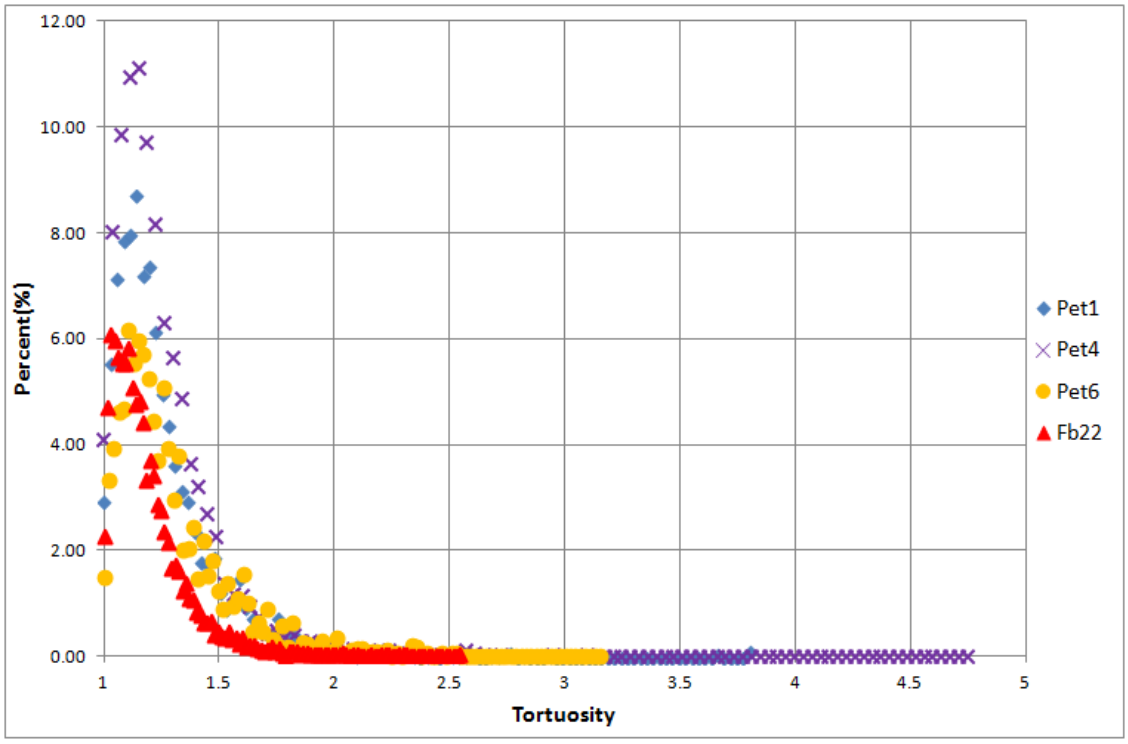

Figure 3.35: The distribution of tortuosity for Pet1, Pet4, Pet6 (SC800) and Fb22 (SC400).

The tortuosity distribution for sandstone Fb22 (SC400) and three carbonate samples Pet1, Pet4 and Pet6 (SC800) can be shown in Figure 3.35. The tortuosity mostly distributes from 1 to 2.5. The percentage of each tortuosity from 1 to 2.5 for Pet4 is the largest, the second largest is Pet1 while the Pet6 shows the smallest percentage for each tortuosity which are almost the same as the Fb22. Additionally, Pet4 can reach the largest tortuosity, 4.75, this largest tortuosity for Pet1 and Pet6 are about 3.7 and 3.2 respectively. While for Fb22, the percentage of each tortuosity and the largest tortuosity are the smallest among these samples. So the tortuosity in carbonates is larger than that in sandstones.

3.4.3 Pore Topology

The topological properties of the pore network are reflected by connection number (Z) and Euler characteristic (Euler number). The network of the pore space consists of nodes and bonds and the nodes are connected by bonds. So the connectivity of such pore network can be described by the coordination number (connection number). The coordination number of each node is the number of bonds connected to this node which is shown in Figure 3.36.

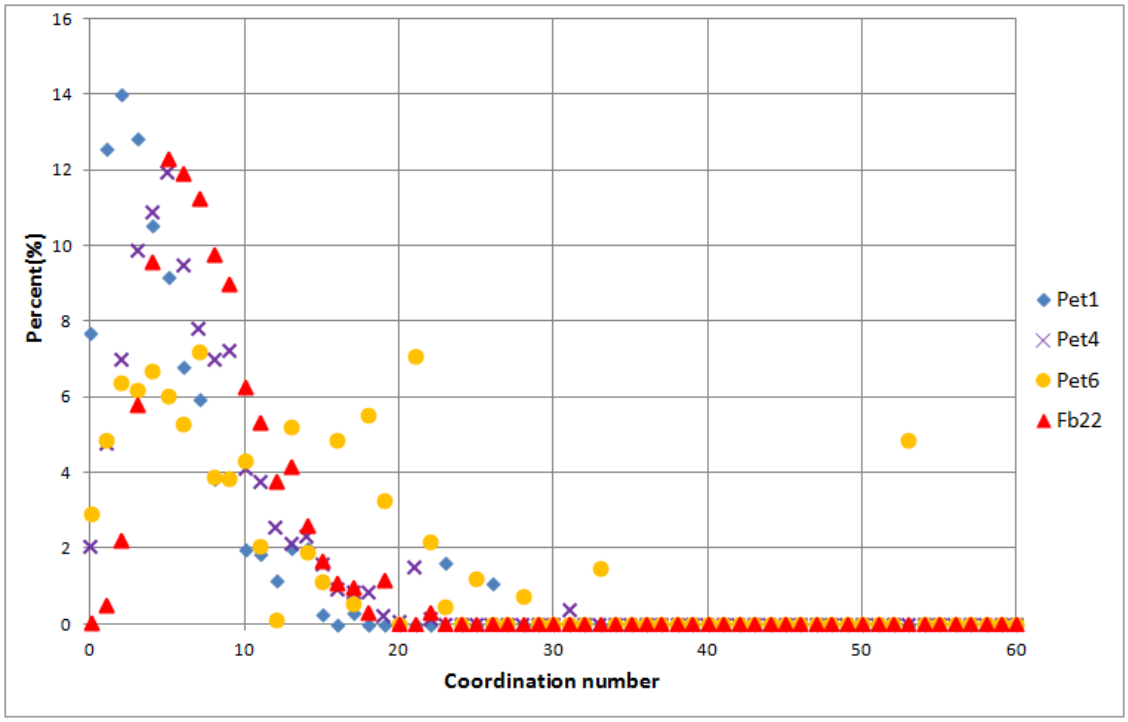

Figure 3.36: The coordination number for Pet1, Pet4, Pet6 (SC800) and Fb22 (SC400).

For the coordination number distribution, two kinds of distribution is shown in Figure 3.36. Fb22, Pet1 and Pet4 are in the same group, the coordination of this group ranges from one to 20, the dominant number is about 5 for Fb22 and Pet4 and this number is 3 for Pet1, the number of the bonds connecting to the nodes for Pet1 is less than that for Pet4; for the second group, the coordination number distribution of Pet6 shows almost three peaks at the coordination numbers of 6, 16 and 53. Larger coordination number results from the larger pore existing in the pore space. These larger pores are usually presented by the merge of several pores. This merging process can increase the coordination number shown in Figure 3.37 (Dong, 2007[63]). The large connection number and variation on its distribution reflect that there are relatively large pore clusters in its pore space which is proved by its CT images in Figure 3.38(c). While Pet1 and Pet4 have only one peak and the number for both of them is almost concentrated in the range below 10 reflecting the variation of the pore space in these two samples is minimal compared with Pet6 which can also be proved by their CT images in Figure 3.38 (a) and (b). However, the samples with larger coordination number should have a better topology property.

Euler number related to different sizes of the pore system including pore body (node) and throat (bond) is given in Figure 3.39. In this figure, the Euler number is related to the size of the pore system. The minimal radius in the x-axis means that the

size of this pore system is larger than this radius denoted by "*Min radius*". With the decrease of the Min radius, the pore space used to calculate Euler number becomes larger until reaches the whole pore spaces. So the Min radius stands for the minimal size in the current pore space.

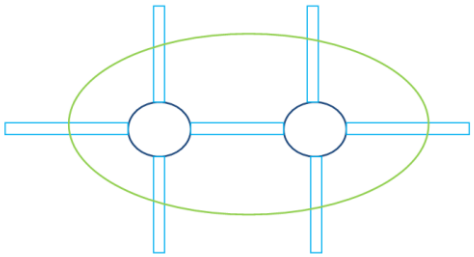

Figure 3.37: The coordination number of the pores increases from four to six when the two pores are merged together.

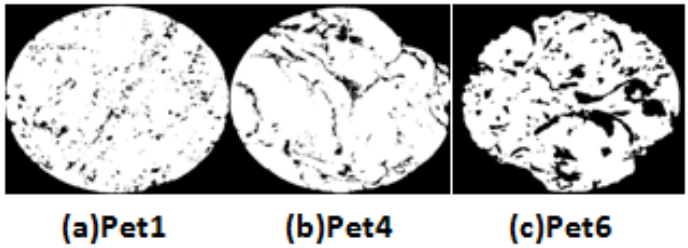

Figure 3.38: The binary cross section slice for Pet1 (a) (2240x2240), Pet4 (b) (1440x1440) and Pet6 (c) (1968x1968) from left to right (in Figure 3.3). The pore is black and the void is white. The size of the pore in the same cross section is close for Pet1 and Pet4 while the pore size is various in Pet6 with different size scales.

From the below image in Figure 3.39, it is clear that the Euler number of Fb22 is the least among the four samples. For Euler number, the more negative the better. Because negative Euler number represents the good connection of the pore space and the positive Euler number stands for the unconnected pore space, that is, the isolated pore clusters are not totally linked by bonds. Zero in Euler number means the isolated pore clusters are just joined together and then the pore space is connected. So the negative Euler number should represent a good pore structure with low porosity exponent. In the expanded image Figure 3.39(b), it is obvious that the property of the Euler number for Pet4 is much better than the numbers for Pet1 and Pet6, so the pore structure for Pet4 is the best in all three carbonates and meanwhile the porosity exponent of the Pet4 is the lowest from 1.7 to 1.85 according to the two experimental results. While the porosity exponents for Pet1 are 1.89 and 2.36, the experimental data for Pet6 are 2.78 and 3. The Euler number can explain the low porosity exponent for

Pet4 but this number can not totally explain the experimental results for Pet 1 and Pet6. In the image (b), the Euler number of Pet6 is less than that of Pet1 while the porosity exponent of Pet6 is greatly larger than the exponent of Pet1. Meanwhile a question in this image is that when the "Min radius" is close to zero, the pore space related to this "Min radius" is almost the whole pore space which should be percolated and connected, while the Euler number of Pet1 is still positive, which is the same as the Euler number from Minkowski Functions in Figure 3.26(b), this means that there are isolated pore clusters which are not linked to the main pore cluster to form one connected pore cluster. The main reason for this result is the existence of too many isolated pore clusters. These isolated pore clusters should be removed to give accurate and reasonable Euler number to closely reflect the connectivity of the pore space which contributes to the current flow. This work will be discussed in next section about labelling pore clusters to get a connected pore cluster dominating in current flow as input to study its pore topology and geometry.

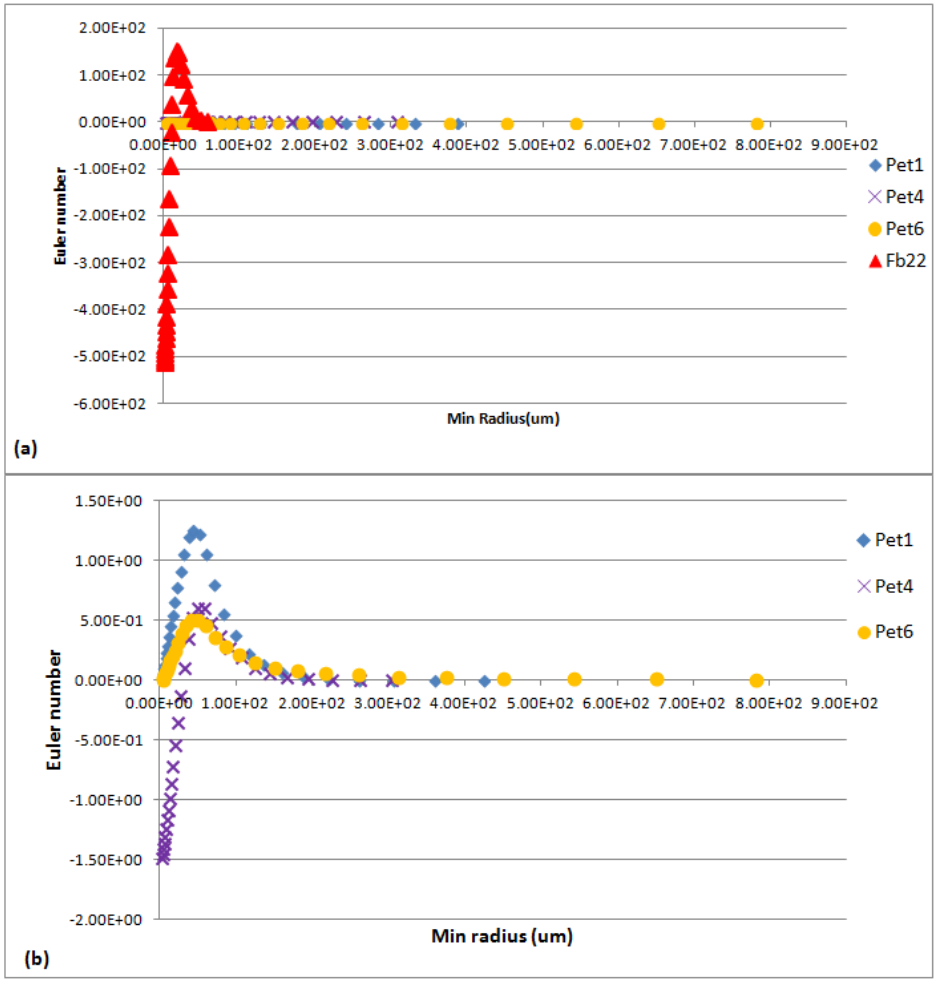

Figure 3.39: The Euler number considering with size of the pore system presented by "Min radius" for Pet1, Pet4, Pet6 (SC800) and Fb22 (SC400) is shown in the figure of (a) and the expanded image for Pet1, Pet4 and Pet6 is in (b).

3.4.4 Explain Porosity Exponent by Geometry and Topology

Until now, the topology and geometry extracted parameters can not totally explain the porosity exponent for these three carbonates. The correlation between the permeability and porosity exponent is positive which contradicts traditional wisdom. Traditionally, it is believed that a higher porosity exponent relates to a higher amount of vuggy porosity and a lower porosity exponent indicates well connected pore network positively effecting on the permeability.

Verwer *et al.* (2011[205]) met the same experimental results when studying their seventy one carbonate plugs. The samples with small pores and an intricate pore network have low porosity exponent, whereas samples with large pores and a simple pore network have high values for porosity exponent. According to the concept of "apparent cross section area" (Adisoemarta *et al.*, 2000[2]) available to flow of electric charge, the importance of the cross sectional area of the pore throats has caused their attention. The pore throat cross section is the main factor affecting the porosity exponent by introducing the influence of the number of the pores and connections. In their studies, the number of pores has a high impact of the cross sectional area of the pore throats. By reducing the amount of the pores, the apparent cross sectional area decreases causing increase of resistivity. Conversely, the increase in the absolute number of the pores can reduce the difference between throat cross sectional area and the total cross sectional area of the pore consequently decreasing the resistivity. The reason is that the total number of the pore increases and then the volume and cross section for each reduces. As a result, the apparent cross sectional area becomes better to reduce resistivity and increase conductivity.

The cross sectional area of the throat, paid attention by Adisoemarta *et al.* (2000[2]), was the same as argued by Etris *et al.* (1989[70]). In their early case, the major contribution to the porosity exponent is the distribution of the pore-throat area which is only related to the throat radius. It is believed that the real meaning of the apparent cross section area should be related to the ratio of the pore radius to the throat radius (PTRR), which was suggested by Ehrlich and others (1991[68]), instead of the throat area. The porosity exponent was effectively a measure of ratio of the logarithm of the pore body cross sectional area to the pore throat cross sectional area (PTAR). This thought is similar as the pore-throat conjunction theory (Chen and Zhang, 1987[46]) to explain the relationship between the porosity exponent to the ratio of the pore cross sectional area to the throat cross sectional area (PTAR) in Figure 3.40.

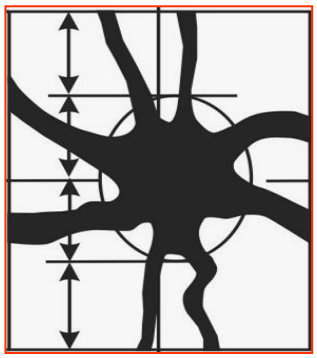

Figure 3.40: The structure of the pore and throats in a pore-throat conjunction point (Chen and Zhang, 1987[46]).

Porosity exponent (m)	Pore-throat size
1-1.3	
1.3-2.0	
2.0-3.5	
3.5-6	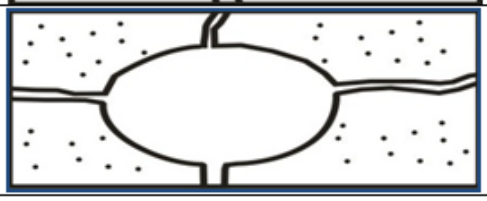

Figure 3.41: The porosity exponent distribution for different pore-throat shapes (from Chen and Zhang, 1987[46]).

The porosity exponent of the pore space is determined by the parameters in the conjunction points. The relationship between the porosity exponent and its shape is listed in Figure 3.41. The aspect ratio of the Pet1, Pet4, Pet6 and Fb22 is shown in Figure 3.42. This aspect ratio is the ratio of the pore radius to the throat radius (PTRR) and the cross sectional area ratio of the pore to the throat (PTAR). The PTRR and PTAR are small meaning that the difference of the pore and the throat is minimal and then the apparent cross sectional area is large so the porosity exponent is small while the

ratio increases, the cross sectional area difference between pore and throat goes up and then the apparent cross sectional area reduces causing increase of the porosity exponent.

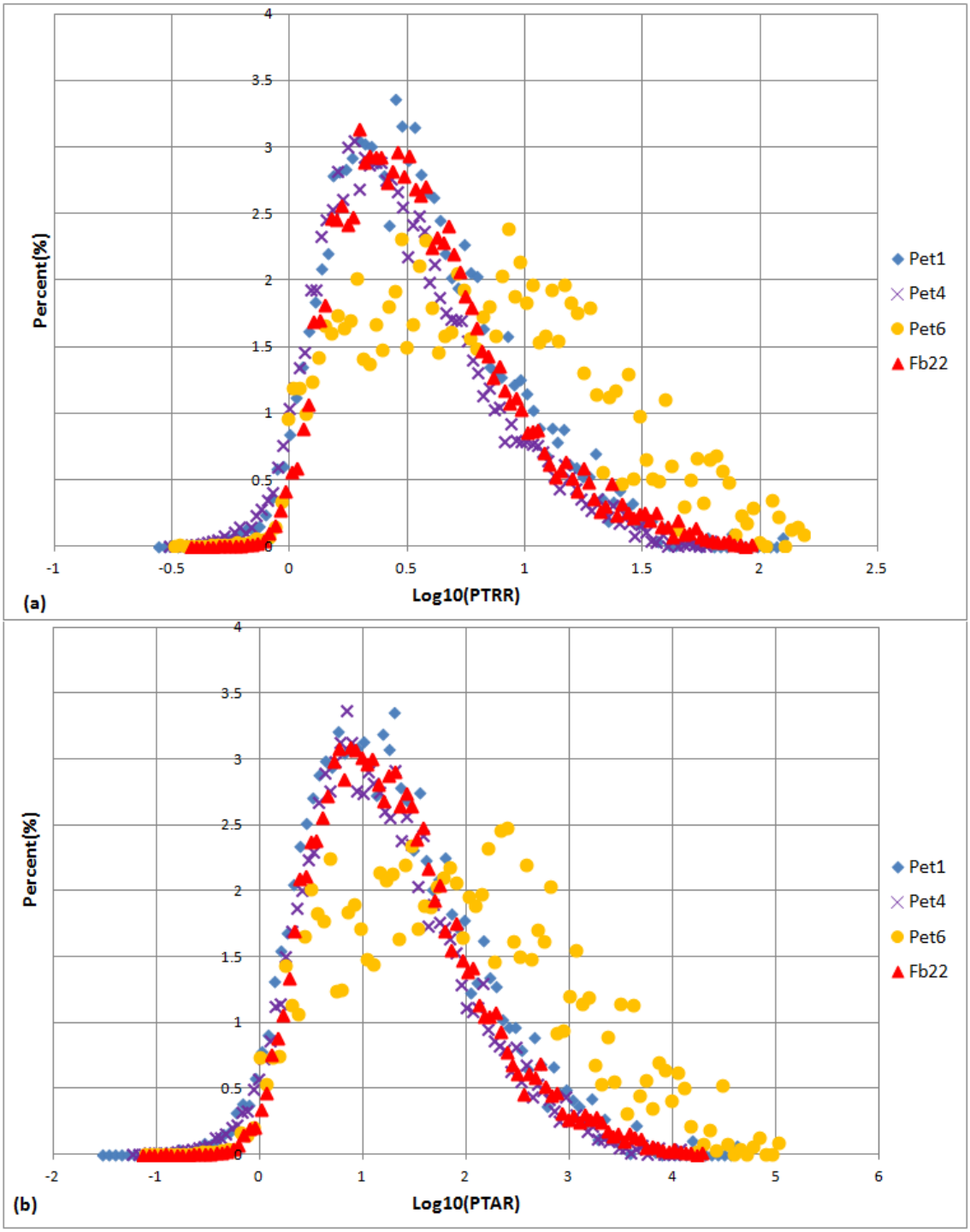

Figure 3.42: The distribution of the PTRR (a) and PTAR (b) for Pet1, Pet4, Pet6 (SC800) and Fb22 (SC400). PTRR is defined as the ratio of the pore radius to the throat radius and PTAR is the cross sectional area ratio of the pore to the throat.

In Figure 3.42, the PTRR and PTAR for Pet1, Pet4 and Pet6 can be classified into three groups. The first group is for Pet6 with greatest ratio and then the porosity exponent for Pet6 should be largest because the ratio of the pore radius to the throat

radius is the largest so the apparent cross sectional area is the smallest and then the resistivity increases causing the increase of the porosity exponent. This ratio for Pet4 is the smallest so the resistivity for Pet4 is lowest and then the smallest of the porosity exponent. So the PTRR can explain the porosity exponent results from laboratory. This relationship can be proved by simple models preserving the connectivity and changing the PTAR, which is the cross sectional area ratio of the pore to throat, to calculate the porosity exponents in Figure 3.43.

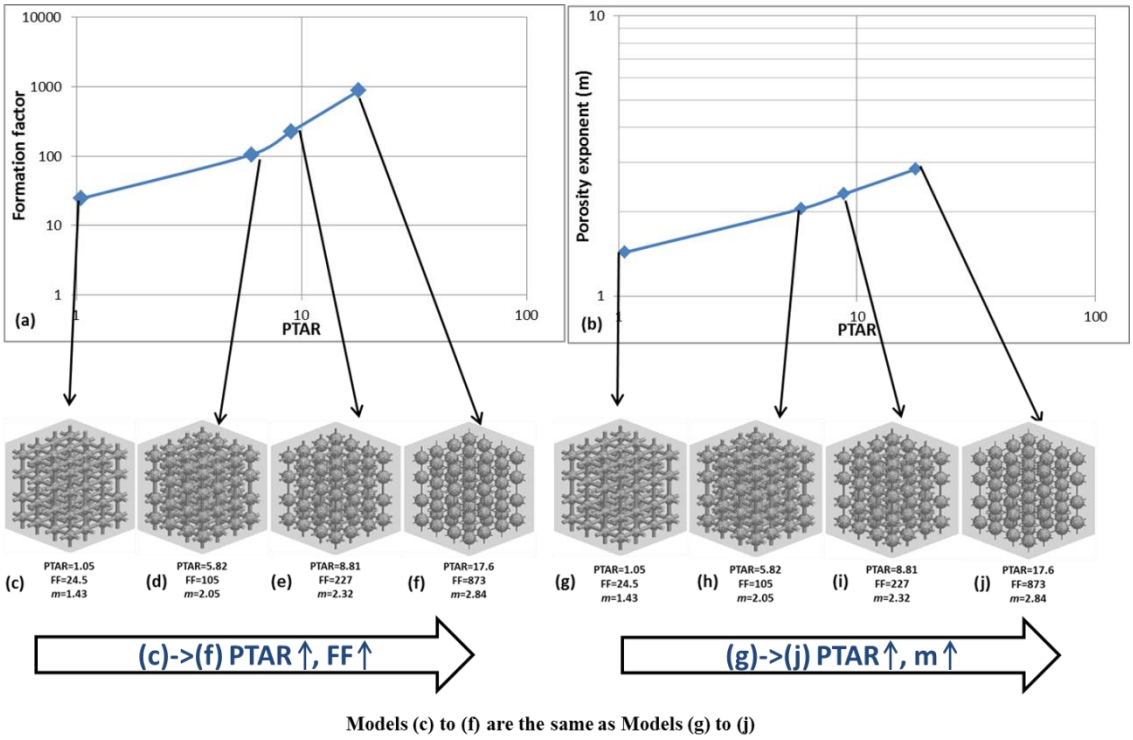

Figure 3.43: The simple models for porosity close to 10% with various PTAR (pore–throat cross sectional area ratio) are shown from (c), (d), (e) to (f) as well as from (g), (h), (i) to (j), these models in two sereis respectively from (c), (d), (e) to (f) and from (g), (h), (i) to (j) are the same. The simulated Formation Factors and porosity exponents versus PTAR based on these models are shown in (a) and (b) respectively.

In Figure 3.43, the PTAR goes up from (c), (d), (e) to (f) and from (g), (h), (i) to (j) for the models in the bottom and their simulated Formation Factors and porosity exponents increase with the increase of ratios. The PTAR is positively related to the porosity exponent. Based on that, the experimental results for Pet1, Pet4 and Pet6 can be explained by the geometrical and topological properties extracted from the pore network. The permeability distribution for these three carbonates is related to their pore and throat size distribution. The porosity exponent can be explained by PTRR which is the ratio of the radius of the pore to the radius of the throat or PTAR as well as the pore connectivity. The pore connectivity can be reflected by the Euler number calculated by

Minkowski Functions or from pore network, the negative Euler number indicates good pore connection while the positive Euler number represents that there are isolated pore clusters outside the main connected pore cluster and the zero in Euler number means the whole pore space just join together.

However topology calculated by Minkowski Functions and expressed from pore network based method are always positive so the connectivity of the pore network from the image can not reflect the connection of the pore space mainly contributing to the current flow. The isolated pores existing in the pore space cause the increase of the Euler number. In order to prove and solve this problem, scanning pore cluster is needed to extract the predominant cluster for flow. This process is implemented by component labelling.

3.5 Component Labelling

In this section,

- Firstly, the component labelling is introduced to extract the predominant pore cluster (3.5.1);
- Then the geometry (GM) and topology (TP) of the predominant pore cluster can compare with the GM and TP of the whole pore space (3.5.2);
- Based on difference of the GM and TP between the predominant pore cluster and the whole pore space, the effect of the pore clusters on the porosity exponent can be investigated (3.5.3);
- Considering the contribution of different pore clusters to the resistivity, a better porosity exponent may be obtained (3.5.4);
- With the help of the influence of different pore clusters and comparison with the published work, the key pore type in each carbonate sample can be examined (3.5.5);

3.5.1 Component Labelling Algorithm

There are many algorithms for searching and labelling the components in 3D binary image (Park and Rosenfeld, 1971[152]). These algorithms scan only half neighbourhoods and they need a table to record labels for the scanned voxels. This table is used to solve the dispute when a voxel belongs to more than one pore cluster.

An important breakthrough occurred in 1976, this attributes to the introduction of the cluster multiple labelling for both 2D and 3D images by Hoshen and Kopelman

(1976[88]) known as the Hoshen-Kopelman algorithm (HKA). This algorithm can determine the number and the size of components (clusters) in just a single scan with consideration of diverse adjacencies (basic concepts for image processing used here can be referred toAppendix D). Three kinds of adjacencies are used in 3D：6, 18 and 26 adjacencies which means a voxel belonging to its 6, 18 and 26 nearest surrounding neighbours respectively while 4 and 8 adjacencies are the only two kinds of connection for 2D.

The main idea of HKA can be described as follows. For a binary image $P(V,B)$ in 3D, B is the set of pore voxels and these pore voxels are α -adjacent. The α -neighbours of p voxel are denoted by $\mathrm{N}_{\alpha}^{*}(\mathrm{p})$. In the pore cluster labelling algorithm, the process of labelling voxel *p* is shown as follow:

For each $q \in N_{\alpha}^{*}(p)$ can be scanned in a certain order. A set named $N_L(p)$ is used to store the α -adjacent neighbour voxels of p which have been labelled. The set $N_L(p)=\{q_1,q_2,\cdots,q_m\}$.The label of each element in the set of $N_L(p)$ are $L(q_1),L(q_2),\cdots,L(q_m)$.

If the set $N_L(p)$ is empty after scanning α -adjacent neighbours of p voxel, a new pore cluster labelled as *NewLbl* should be generated. Otherwise, p should be labelled according to the minimum label $(MinL)$ in set $N_L(p)$.

$MinL=\min\{L(q_1),L(q_2),\cdots,L(q_m)\}$. The label of each element is recorded by an array LId. Meanwhile these pore voxels in set $N_L(p)$ should be relabelled as $-MinL$ by setting $LId(L(q_i))=-MinL, i=1,2,\cdots,m$. In the array LId, the value of the positive element stands for the total number of pore voxels in the pore cluster labelled as this value while the value of the negative element is $-MinL$ applied to find the final proper label for this pore cluster.

The labelled image is stored in an array named $LI\ \mathrm{m}g$.

Input:

Binary image $P(V,B)$;

B is the set of pore voxels (foreground);

$V \setminus B$ is the set of background voxels;

α -adjacency;

Output:

Labelling image $LI\,\mathrm{m}\,g$;

Temporary variations:

Number of pore clusters sum;

An array LId recording the total number of pore voxels in each pore cluster for positive value and the proper pore cluster label for the negative element;

An array $Rindex$ with the same size as LId is to record the sequential label for each pore cluster after scanning all the voxels in the image.

$NewLbl$ is the label for the new generated pore cluster. It is also the total number of the labelled pore clusters and some pore clusters' label may be not proper and the LId value for these pore labels entries is negative;

lbl is the variation standing for the label of the pore cluster which pore *voxel* q belonged to;

$Nlbl$ is the same as lbl;

$N_a(p)$ represents the a-adjacent neighbours of voxel p including itself; $N_a(p) = N_a^*(p) \bigcup \{p\}$;

$L(q)$ is the pore cluster label for voxel q;

The flow chart is shown in Figure 3.44. In this flow chart, the label of a pore voxel is set according to its α-adjacent neighbours. If all of its neighbours have not be labelled, this voxel needs a new label; if some of its neighbours have been scanned, then the minimal label of these scanned voxels has to be obtained by a searching process. The rest of the scanned voxels with different labels have to renew their labels by this minimal label. Meanwhile the total number of these minimal labels should be calculated again after this process. The labelling process ends until all the pore voxels have been scanned.

This process can be explained by a 2D image shown in Figure 3.45. Figure 3.45 shows a 2D binary image for pore cluster labelling process, the white 0 are the background pixels while the grey 1 are the foreground. The sequence of the pixels scanned in this process is determined by the ordered number in each pixel (in Figure 3.45b). The one dimensional array LId is used to record the current existing labels by its entries, the number of pixels (voxels) in the labelled pore cluster or the appropriate label for the labelled pore cluster by value of LId. For example $LId(m)$, m is the entry number, standing for the current existing label, and the LId value of this entry is present by $LId(m)$. If $LId(m) > 0$, this value represents the number of the pore elements

in the pore cluster labelled as $LId(m)$; if $LId(m) < 0$, this value indicates the appropriate label for this labelled pore cluster.

At the beginning, the pixel ordered 1 is firstly scanned and its related neighbours are checked. Then the first label 1 emerges and the number of the pixel in the pore cluster labelled 1 is one, so $LId(1) = 1$ and $LId(m) = 0, m > 1$ which is shown in the first row in the Figure 3.46. pixel 2 is checked due to its 8-adjacent connectivity to pixel 1, there is not new label emerging while the number of the pixel in pore cluster 1 increases by 1, $LId(1) = 1+1 = 2$, $LId(m) = 0, m > 1$.

A complex case happens when the pixel 15 is scanned. This pixel is 8-adjacent connected to the pixel 11 and pixel 14. Both of them respectively belong to pore cluster 1 and 3. In this condition, new label is not needed and the label of the pore cluster including the current scanning pixel 15 is determined by the minimal label of the two connected pore clusters. The $MinLbl = 1$, and then the number of the pixels in the pore cluster 1 should be increased by the number of the pixels in the pore cluster 3 and 1 relating to pixel 15, $LId(MinLbl) = LId(MinLbl) + LId(3) + 1$. Additionally, the label 3 is not a valid pore cluster label, and its appropriate label for the pixels in the pore cluster 3 is equal to $MinLbl$, $LId(3) = -MinLbl$. This process is shown in the 15th row of the Figure 3.46**(**a**)**.

In the next work, the total number of the real pore clusters should be recorded and then the labelled image in sequential can be generated according to the real pore cluster numbers and the value of each label in the array LId. The positive value LId records the total number of the pore voxels in this cluster while the negative value in LId is related to its proper labels. These processes are shown in Figure 3.47 and Figure 3.48.

After fully scanned all the object pixels in Figure 3.45, the initial labels in the image are shown in Figure 3.49 for the 8- (a) and 4-adjacent (b) to the object pixel. These initial labels are not totally valid and their validity depends on the value in the array LId. If the value is positive, this label is valid otherwise this valid is not appropriate. Additionally, these new labels should be sequential. This process can be implemented by a new one dimensional array $Rindex$, which is based on the value of LId, shown in Figure 3.50.

The Figure 3.50(a) is for the 8- adjacent and (b) is for the 4-adjacent labelling. LId and $Rindex$ share the same entries. The entry for LId also represents the pore cluster label, When the value of the entry in LId is positive, this label is valid and its final

sequential label is the value of the related entry in $Rindex$. In the 8-adjacent pore cluster labelling in Figure 3.50(a), $Entry = 2$ is valid in LId and its final pore cluster label in $Rindex$ is $Rindex(2) = 2$. When the value of the entry in LId is negative, this label is not valid while its appropriate label can be obtained by this value. Taken this appropriate label as the entry of index, the final label for this case can be got. In the same labelling process, $Entry = 3$ is not valid in LId due to $LId(3) = -1 < 0$, while its appropriate label can be given by this negative value, the appropriate value=1 and then the final label is $Rindex(1) = 1$. The label 3 in Figure 3.49(a) should be labelled as 1. The final labels for the 8- and 4- adjacent pore cluster labelling are shown in the (a) and (b) of Figure 3.51 respectively.

In Figure 3.52, the labels of the pore clusters and their relative percentages for Pet1, Pet4 and Pet6 (SC800) are shown in the (a), (b) and (c) respectively. The pore cluster labelled as 1 for Pet4 and the pore cluster labelled as 3 for Pet6 are the predominant pore cluster. The relative percentage of the pore voxels in both clusters for Pet4 and Pet6 are about 75% of the total pore voxels. In Pet1, the pore cluster labelled as 2968 is the main component of the pore space with the relative percentage of 35% and the pore cluster labelled as 925 is the second largest cluster in Pet1 with 5% relative percentage. So Pet4 and Pet6 can extract a predominant pore cluster while the pore cluster from Pet1 represents a part of the pore space.

The pore space, biggest pore cluster and the rest pore space for these three carbonate samples are shown in Figure 3.53. It is clear that the pore cluster after the component labelling algorithm in Pet6 and Pet4 occupy the most pore space while the pore cluster for Pet1 is a much limited part of the pore space. In the following sections, the largest pore clusters for these three carbonate samples Pet1, Pet4 and Pet6 are denoted as “Pcl1”, “Pcl4” and “Pcl6” respectively and their related labels after component labelling in Pet1, Pet4 and Pet6 are 2968,1 and 3 expressed by “Pet1_cl2968”, “Pet4_cl1” and “Pet6_cl3” representing the related pore cluster labels in each carbonate sample. The topology and geometry of these pore space in the main pore clusters (Pcl1, Pcl4 and Pcl6) listed in (c), (g) and (k) of Figure 3.53 can be shown in Figure 3.54, Table 3.2 and Table 3.3.

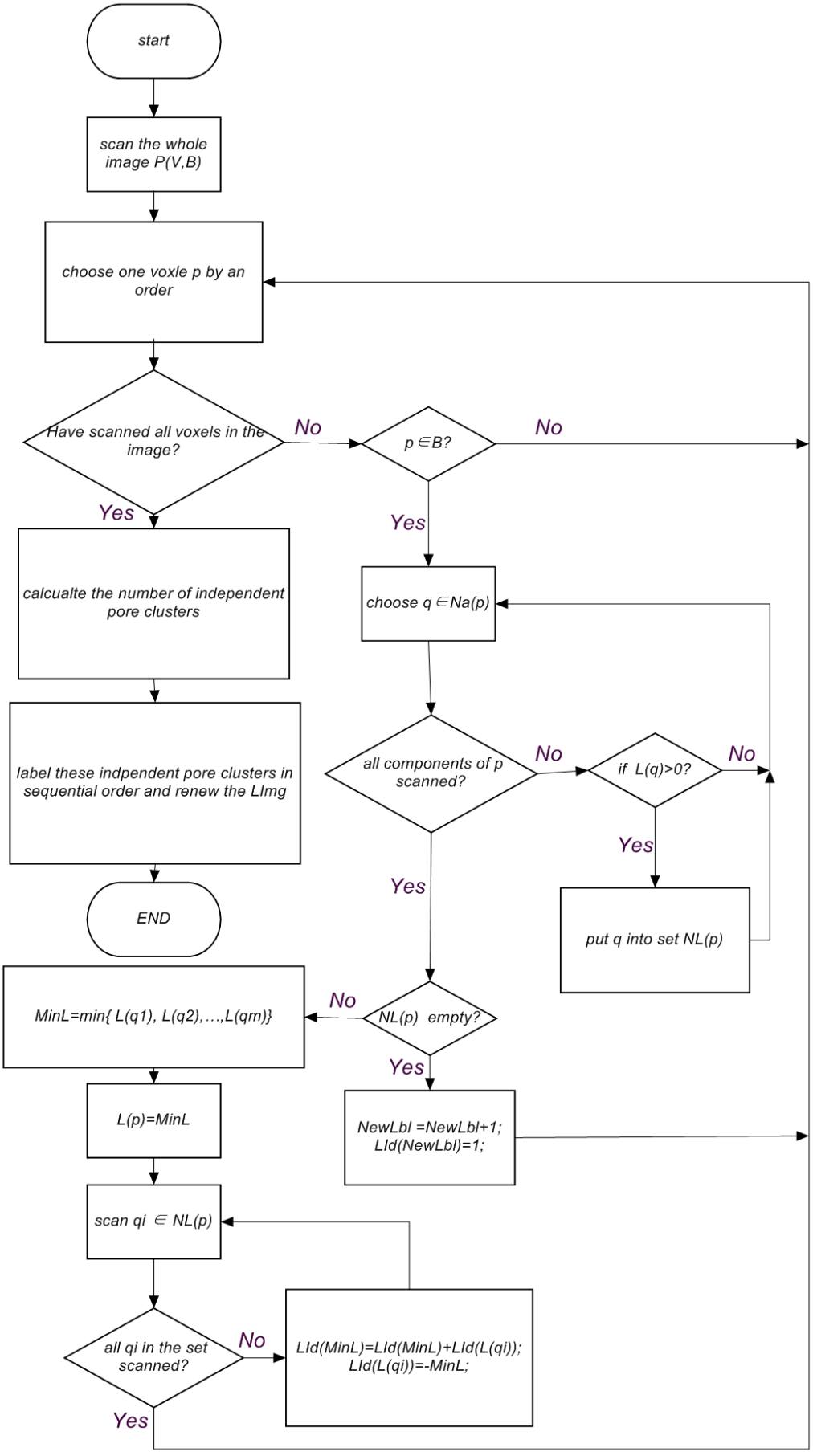

Figure 3.44: The workflow for the component labelling.

(a)

Y\X	1	2	3	4	5	6	7	8	9	10
1	0	0	0	0	0	1	1	1	1	0
2	0	1	0	0	0	1	0	0	0	1
3	0	1	0	0	0	0	0	0	1	0
4	0	0	1	0	0	0	0	1	0	0
5	0	0	1	0	1	1	1	0	0	0
6	0	0	0	0	0	1	0	0	0	0
7	0	0	0	0	1	0	0	1	1	0
8	1	0	0	1	0	0	0	0	1	0
9	0	0	0	0	0	0	1	1	1	0
10	0	0	0	0	0	0	0	0	0	0

(b)

Y\X	1	2	3	4	5	6	7	8	9	10
1	0	0	0	0	0	1	2	3	4	0
2	0	5	0	0	0	6	0	0	0	7
3	0	8	0	0	0	0	0	0	9	0
4	0	0	10	0	0	0	0	11	0	0
5	0	0	12	0	13	14	15	0	0	0
6	0	0	0	0	0	16	0	0	0	0
7	0	0	0	0	17	0	0	18	19	0
8	20	0	0	21	0	0	0	0	22	0
9	0	0	0	0	0	0	23	24	25	0
10	0	0	0	0	0	0	0	0	0	0

Figure 3.45: 2D illustration for 8- and 4- adjacent pore cluster labelling. The (a) is the original binary image, 1 is object pixel and 0 is the background. In the picture of (b), the sequential number of the objects is related to the scanning process.

(a)

	1	2	3	4	5	6
1	1	0	0	0	0	0
2	2	0	0	0	0	0
3	3	0	0	0	0	0
4	4	0	0	0	0	0
5	4	1	0	0	0	0
6	5	1	0	0	0	0
7	6	1	0	0	0	0
8	6	2	0	0	0	0
9	7	2	0	0	0	0
10	7	3	0	0	0	0
11	8	3	0	0	0	0
12	8	4	0	0	0	0
13	8	4	1	0	0	0
14	8	4	2	0	0	0
15	11	4	-1	0	0	0
16	12	4	-1	0	0	0
17	13	4	-1	0	0	0
18	13	4	-1	1	0	0
19	13	4	-1	2	0	0
20	13	4	-1	2	1	0
21	14	4	-1	2	1	0
22	14	4	-1	3	1	0
23	14	4	-1	3	1	1
24	14	4	-1	5	1	-4
25	14	4	-1	6	1	-4

(b)

	1	2	3	4	5	6	7	8	9	10	11	12
1	1	0	0	0	0	0	0	0	0	0	0	0
2	2	0	0	0	0	0	0	0	0	0	0	0
3	3	0	0	0	0	0	0	0	0	0	0	0
4	4	0	0	0	0	0	0	0	0	0	0	0
5	4	1	0	0	0	0	0	0	0	0	0	0
6	5	1	0	0	0	0	0	0	0	0	0	0
7	5	1	1	0	0	0	0	0	0	0	0	0
8	5	2	1	0	0	0	0	0	0	0	0	0
9	5	2	1	1	0	0	0	0	0	0	0	0
10	5	2	1	1	1	0	0	0	0	0	0	0
11	5	2	1	1	1	1	0	0	0	0	0	0
12	5	2	1	1	2	1	0	0	0	0	0	0
13	5	2	1	1	2	1	1	0	0	0	0	0
14	5	2	1	1	2	1	2	0	0	0	0	0
15	5	2	1	1	2	1	3	0	0	0	0	0
16	5	2	1	1	2	1	4	0	0	0	0	0
17	5	2	1	1	2	1	4	1	0	0	0	0
18	5	2	1	1	2	1	4	1	1	0	0	0
19	5	2	1	1	2	1	4	1	2	0	0	0
20	5	2	1	1	2	1	4	1	2	1	0	0
21	5	2	1	1	2	1	4	1	2	1	1	0
22	5	2	1	1	2	1	4	1	3	1	1	0
23	5	2	1	1	2	1	4	1	3	1	1	1
24	5	2	1	1	2	1	4	1	3	1	1	2
25	5	2	1	1	2	1	4	1	6	1	1	-9

Figure 3.46: Array LId for pore cluster labelling by 8-adjacent (a) and 4-adjacent (b) of object pixels. The column numbers present the entry of the array LId, which is also the current used labels and the row numbers are the scanned order for each object pixels.

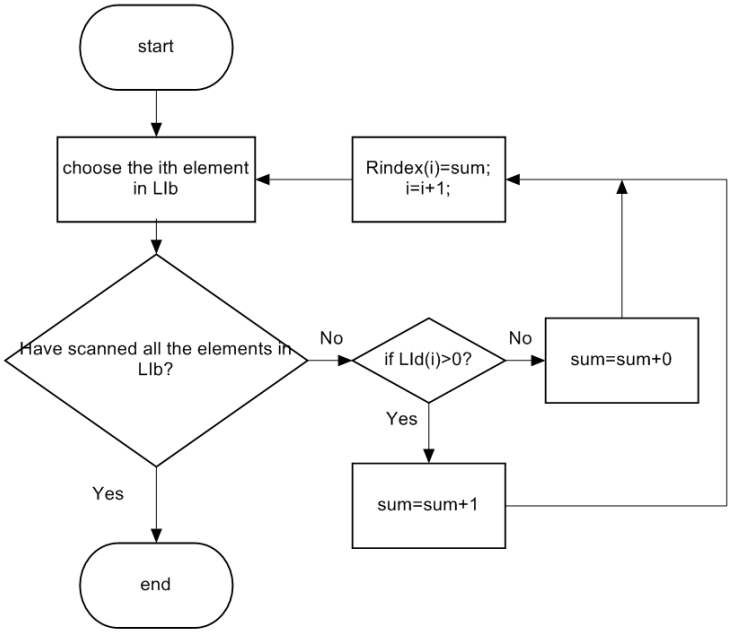

Figure 3.47: The process of calculating the total number of the independent pore clusters is shown in this flow chart. *sum* records the total number and the array *Rindex* records the sequential label for each pore cluster in *LId*.

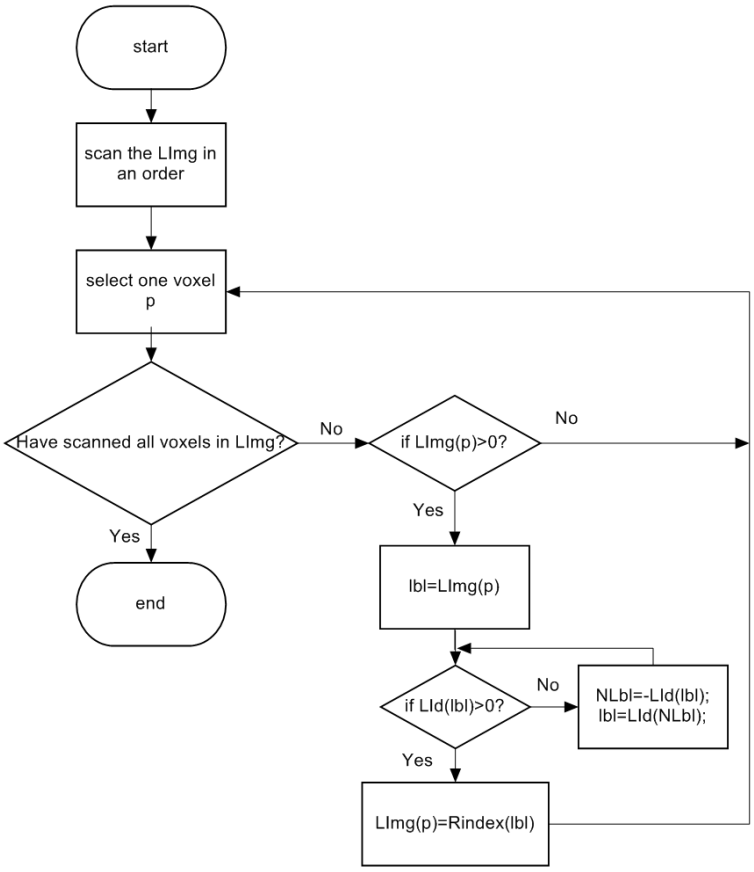

Figure 3.48: The labelled image can be renewed according to this process. *lbl* and *Nlbl* are two temporary variations to record the proper label of the pore clusters which are negative in array *LId*.

(a)

Y\X	1	2	3	4	5	6	7	8	9	10
1	0	0	0	0	0	1	1	1	1	0
2	0	2	0	0	0	1	0	0	0	1
3	0	2	0	0	0	0	0	0	1	0
4	0	0	2	0	0	0	0	1	0	0
5	0	0	2	0	3	3	1	0	0	0
6	0	0	0	0	0	1	0	0	0	0
7	0	0	0	0	1	0	0	4	4	0
8	5	0	0	1	0	0	0	0	4	0
9	0	0	0	0	0	0	6	4	4	0
10	0	0	0	0	0	0	0	0	0	0

(b)

Y\X	1	2	3	4	5	6	7	8	9	10
1	0	0	0	0	0	1	1	1	1	0
2	0	2	0	0	0	1	0	0	0	3
3	0	2	0	0	0	0	0	0	4	0
4	0	0	5	0	0	0	0	6	0	0
5	0	0	5	0	7	7	7	0	0	0
6	0	0	0	0	0	7	0	0	0	0
7	0	0	0	0	8	0	0	9	9	0
8	10	0	0	11	0	0	0	0	9	0
9	0	0	0	0	0	0	12	12	9	0
10	0	0	0	0	0	0	0	0	0	0

Figure 3.49: Initial labels for the pore cluster labelling 8- and 4- adjacent with 25 pixels in Figure 3.45 scanned.

	1	2	3	4	5	6
LId	14	4	-1	6	1	-4
Rindex	1	2	2	3	4	4

(a)

	1	2	3	4	5	6	7	8	9	10	11	12
LId	5	2	1	1	2	1	4	1	6	1	1	-9
Rindex	1	2	3	4	5	6	7	8	9	10	11	11

(b)

Figure 3.50: The final labels for the pore cluster labelling which are related to the value of *LId*.

(a)

Y\X	1	2	3	4	5	6	7	8	9	10
1	0	0	0	0	0	1	1	1	1	0
2	0	2	0	0	0	1	0	0	0	1
3	0	2	0	0	0	0	0	0	1	0
4	0	0	2	0	0	0	0	1	0	0
5	0	0	2	0	1	1	1	0	0	0
6	0	0	0	0	0	1	0	0	0	0
7	0	0	0	0	1	0	0	3	3	0
8	4	0	0	1	0	0	0	0	3	0
9	0	0	0	0	0	0	3	3	3	0
10	0	0	0	0	0	0	0	0	0	0

(b)

Y\X	1	2	3	4	5	6	7	8	9	10
1	0	0	0	0	0	1	1	1	1	0
2	0	2	0	0	0	1	0	0	0	3
3	0	2	0	0	0	0	0	0	4	0
4	0	0	5	0	0	0	0	6	0	0
5	0	0	5	0	7	7	7	0	0	0
6	0	0	0	0	0	7	0	0	0	0
7	0	0	0	0	8	0	0	9	9	0
8	10	0	0	11	0	0	0	0	9	0
9	0	0	0	0	0	0	9	9	9	0
10	0	0	0	0	0	0	0	0	0	0

Figure 3.51: The images with the finally sequential labels for 8-adjacent and 4-adjacent object pixels.

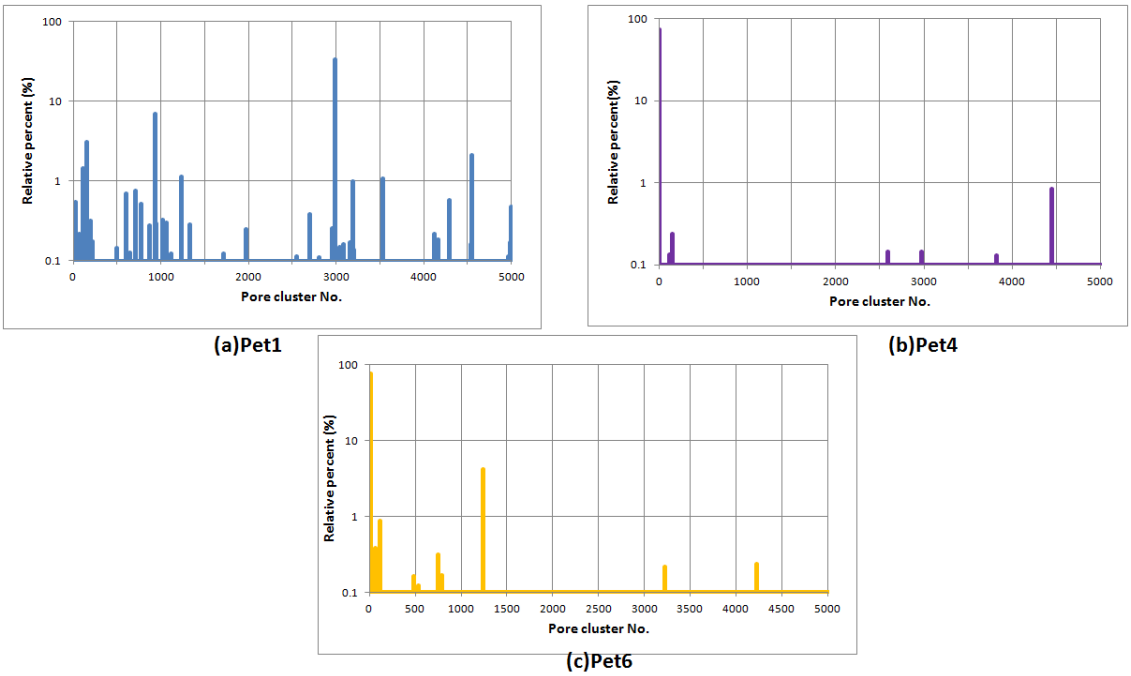

Figure 3.52: The histograms of the pore cluster labels for Pet1 (a), Pet4 (b) and Pet6 (c) (SC800) after component labelling algorithm. The relative percentage (shown by logarithm scale) is calculated by the ratio of the number of the pore voxels in this pore cluster to the total number of the pore voxels. In two cases for Pet4 (b) and Pet6 (c), one main cluster has about 70% of the porosity.

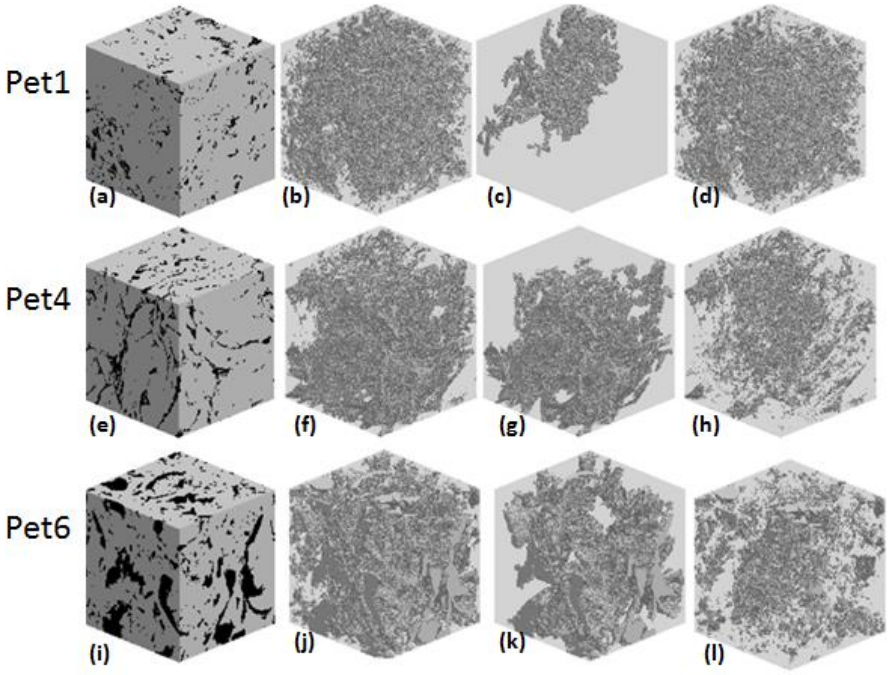

Figure 3.53: The pore space distribution for the original samples in (b), (f) and (j) for Pet1, Pet4 and Pet6 (SC800), the results after the labelling algorithm are shown in (c), (g) and (k) and the right column including (d), (h) and (l) are the pore space of the remaining labels. (a), (e) and (i) are the binary images in 3D for Pet1, Pet4 and Pet6 from top to bottom, white is solid and the black is void. The relative percentage of the porosity for the main pore cluster from (c), (g) to (k) for Pet1, Pet4 and Pet6 (SC800) are 30%, 75% and 77% respectively.

	Pore						Throat						Z			PTRR		
	r (μm)			G (10^{-3})			r (μm)			G(10^{-3})								
	min	ave	max	min	ave	max	min	ave	max	min	ave	max	min	ave	max	min	ave	max
Pet1	15.8	145	500	8.34	22	57.2	3.81	58.6	277	9.33	31.5	62.5	0	5.02	26	0.278	5.46	124
Pet4	16.9	127	354	7.91	18.8	62	4.09	51.2	250	2.49	31.4	62.5	0	6.84	31	0.31	4.59	61.9
Pet6	16	444	940	7.4	18.7	60.2	3.87	154	599	7.91	31.5	62.5	0	12.3	53	0.322	13.2	154

Table 3.2: The geometrical properties for Pet1, Pet4 and Pet6 (SC800) before component labelling.

	Pore						Throat						Z			PTRR		
	r (μm)			G (10^{-3})			r (μm)			G(10^{-3})								
	min	ave	max	min	ave	max	min	ave	max	min	ave	max	min	ave	max	min	ave	max
Pcl1	15.9	163	454	9.45	19.9	54.8	3.82	67	290	11.5	31.1	62.5	1	6.27	17	0.339	5.42	71.6
Pcl4	16.9	130	358	8.15	18.2	56.2	4.11	53.5	271	2.49	31.4	62.5	1	7.84	32	0.313	4.46	61.1
Pcl6	16.3	484	938	7.88	17.5	58.7	3.90	170	498	11.6	30.8	62.5	1	14.1	51	0.390	13.8	172

Table 3.3: The geometrical properties for Pcl1, Pcl4 and Pcl6 (SC800) after component labelling.

3.5.2 Topology and Geometry of the Predominant Pore Cluster

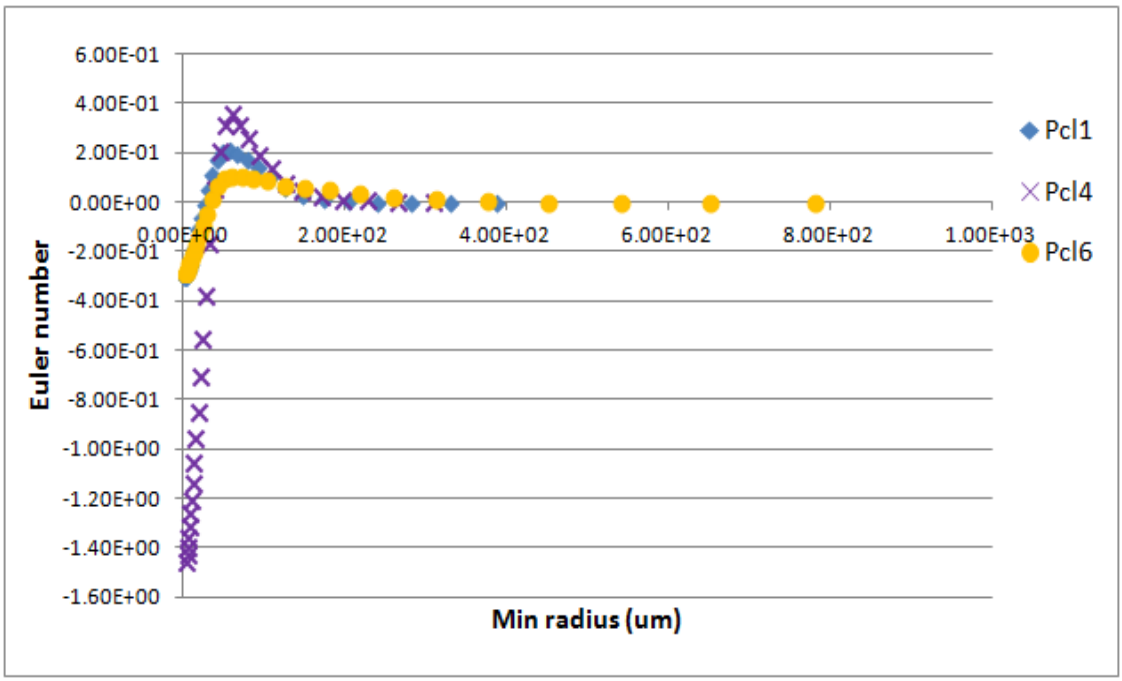

Figure 3.54: The Euler number versus the minimal radius of the pore space for the largest clusters.

The topology of the Pcl1 and Pcl6 (SC800) become better after labelling the component compared with the topology of the whole pore system in Figure 3.39 and the

Euler number turn to negative for both of them and the Euler number of Pcl4 still keeps negative. The problem explained by these results is that the remaining isolated small pore clusters can seriously undermine the connectivity of the whole pore space (Pet1, Pet4 and Pet6). So the necessity of the pore cluster labelling can be reflected by these results.

The topologies (Figure 3.39 and Figure 3.54) of these three carbonates prove that the connectivity of the whole pore system in Pet4 is better than the connectivity of the Pet1 and Pet6. These results can not directly explain the porosity exponent or permeability distribution for Pet1, Pet4 and Pet6, while these results can prove that the good connectivity of the pore system contributes to the current flow, the porosity exponent of Pet4 is smaller than the porosity exponents of Pet1 and Pet6 probably relating to its connectivity (which can be studied in Chapter 4).

It is acceptable for Pet4 and Pet6 that the geometrical properties keep stable before and after labelling pore clusters, because the pore cluster determined by the component labelling algorithm is predominant so it can reflect the geometry of the original pore space. While the pore cluster for Pet1 after labelling is only 35% of the original pore space, its geometry is similar to that of the original pore space. The only explanation is that this largest pore cluster has the same geometrical properties as the smaller pore clusters, and then the geometrical properties of the whole pore space are the same as the part of the pore space. This is can be proved by comparing the geometry of both of them, which is shown in Figure 3.55.

It is clear that firstly, the topology of the largest pore cluster labelled as 2968 is much better than that of the second largest pore cluster in Figure 3.55(c), this is due to the reality that the pore cluster with less pore space can not form a good connected pore space while the pore cluster with more pore voxels can generate good connected pore system. Secondly, the geometrical properties of these two pore clusters are almost same in Figure 3.55(a), (b) and (d). The same geometry in each larger pore cluster forms the similar geometry of the whole sample. The current should mainly flow among this largest pore cluster instead of the remaining isolated pores.

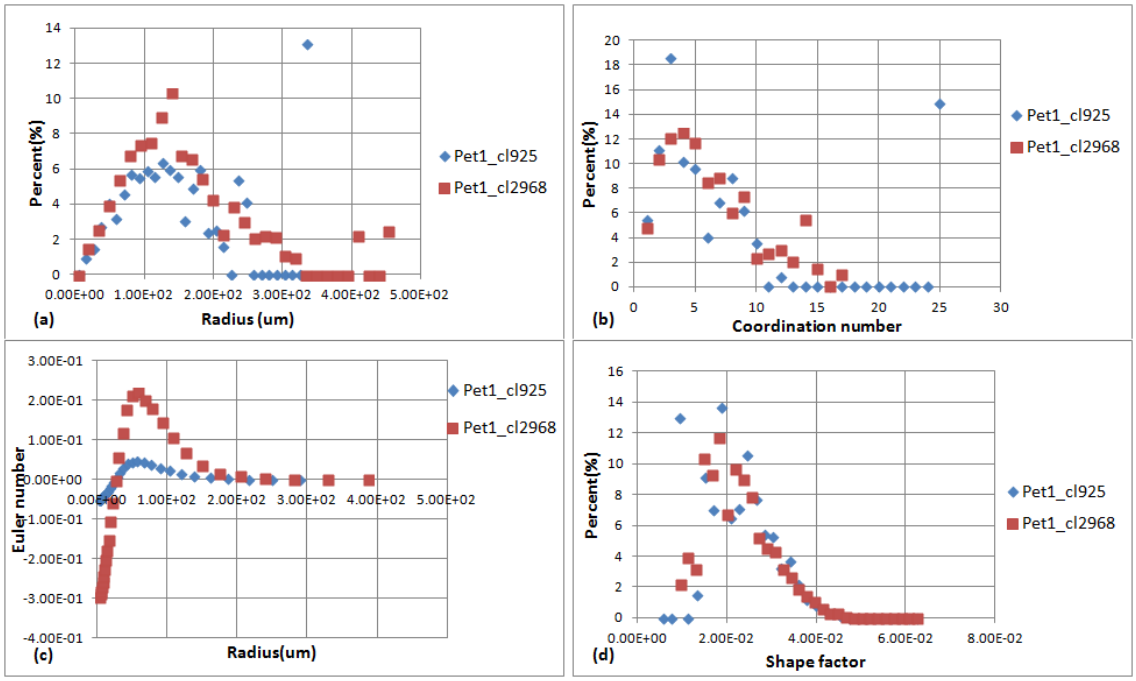

Figure 3.55: The geometry and topology extracted by pore network method for the largest pore cluster labelled as Pet1_cl2968 (SC800) and the second largest pore cluster labelled as Pet1_cl925 (SC800) in Pet1.

Based on this point, the remaining isolated pores can be regarded as the isolated vug (IVG) while the pore structure of the main pore cluster is the mutual effect of the intergranular (IG), fracture (FT) and connected vug (CVG). The overestimation of the porosity exponent for Pet1 can be examined by firstly simulating the random walk to calculate the Formation Factor (FF) in the largest pore cluster assuming the trivial contribution of the isolated pore clusters to current flow. Formation Factor (FF) in this case can be accurately simulated by the porosity and the result of the random walk based on the largest pore cluster (Equation 2.23) and then the porosity exponent can be determined by the FF based on the largest pore cluster and the total porosity of the whole sample according to Archie First Law in Equation (1.1) and Equation (2.32). In this process, the effect of the remaining pore clusters on the porosity exponent of the porous medium can be researched to reflect contribution of the dominate pore clusters to this medium.

3.5.3 The Effect of Pore Clusters on the Porosity Exponent

The simulation based on random walk simulation for the main cluster Pcl1, Pcl4 and Pcl6 are shown in Figure 3.56. The Pcl1, Pcl4 and Pcl6 in the legend stand for the pore clusters for the FF (the resistivity of the 100% brine saturated rock sample).

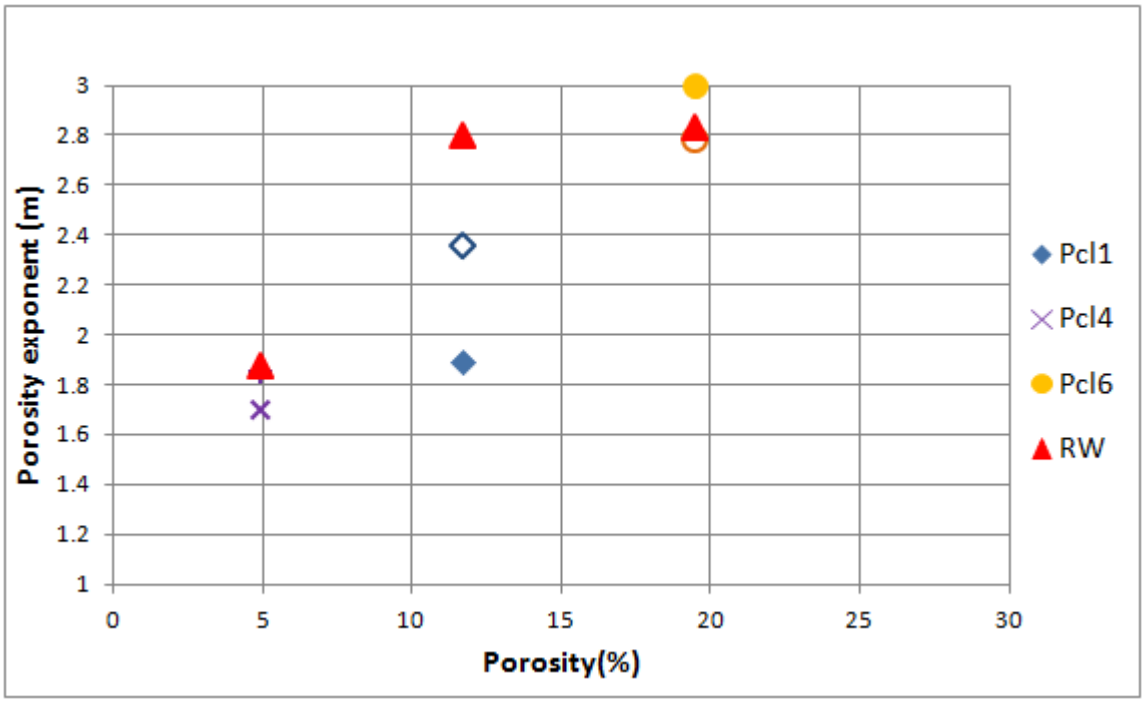

Figure 3.56: The simulated porosity exponents based on the Formation Factor (FF) of the largest pore cluster after component labelling algorithm and the total porosity of the whole sample. Now the simulated porosity exponents from random walk can compare well with the experimental data for Pet4 and Pet6 (SC800), not well for Pet1 which will be discussed further in the text.

It is clear that this method works well for the simulation in Pet4 and Pet6, this means that taken the rest of the pore clusters as the isolated vug (IVG) is reasonable, the high porosity exponent of Pet6 with large pore size is mainly due to the existence of such isolated vug (IVG). While the simulated porosity exponent for Pet1 is 2.8, much larger than the experimental results, 1.89 and 2.36, taking these remaining pore clusters as IVG does not work for Pet1. So for Pet6, the existence of vug explains the high porosity exponent while this is not the case for Pet1.

In this condition for Pet1, the porosity exponent based on the FF and porosity of this largest pore cluster should be firstly considered to research the effect of the main pore cluster on the porosity exponent and then to further study other effects of the whole pore space. The simulation porosity exponent based on the largest pore cluster should be less that the porosity exponent simulated on the whole pore space. Because the pore structure of the largest pore cluster is better than the structure of the whole pore space without consideration of the isolated pore clusters. This simulation results based on the predominant pore cluster for Pet1, Pet4 and Pet6 are shown in Figure 3.57.

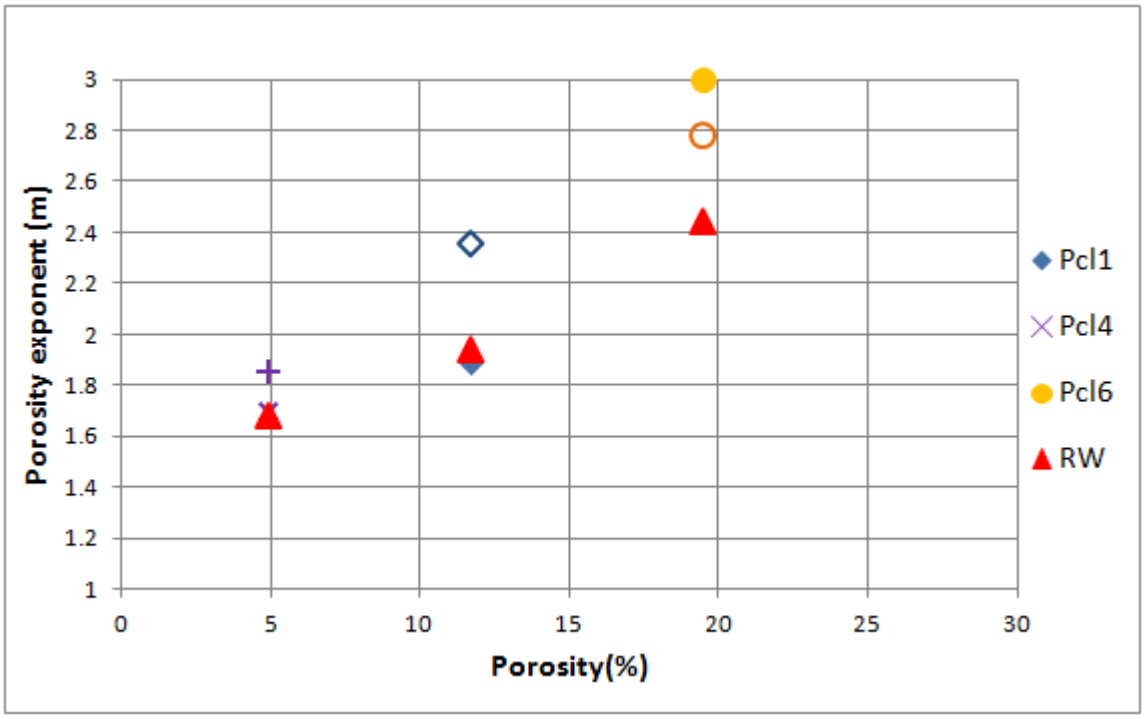

Figure 3.57: The simulated porosity exponents based on the FF and porosity of the largest pore cluster (Pcl1, Pcl4 and Pcl6 (SC800)) for each carbonate sample. Then the simulated porosity exponents from random walk can compare better with the experimental data.

Obviously, the simulation results in Figure 3.57 compared with these results in Figure 3.56 agree better with the above analysis. The simulation result for Pet1 can match the experimental results while the porosity exponent for Pet6 is about 0.4 lower than the experimental data. So without considering the effect of the isolated pore clusters, the simulated porosity exponent is less than the experimental result showing that the existence of the IVG is the critical factor for the porosity exponent of Pet6. While for Pet1, without considering the effect of the isolated pore clusters, the simulated porosity exponent is 1.9 close to the lab data while the simulation result is larger than the real data when taking the remaining clusters into consideration. The difference between the two simulation results is about 0.9 reducing from 2.8 to 1.9, this indicates that the porosity exponent of Pet1 mainly depends on this connected pore cluster. So the key point for the porosity exponent of Pet1 is the existence of the connected pore cluster, with less porosity but greater effect on decrease of the porosity exponent. Due to the successful percolation of this connected pore cluster (Figure 3.53c) in one direction, the porosity exponents of Pet1 may be greatly variable in different directions. So the porosity exponent variation for Pet1, based on the two laboratory data 1.89 and 2.36, is great about 20% (Figure 3.12c), which is the largest among these three

carbonates. This variation for the rest two carbonates Pet1 and Pet4 both are about 8% (Figure 3.12).

The change of the simulated porosity exponents for Pet4 in these two conditions is minimal, from about 1.9 down to 1.7, which is about 10%, less variation compared with Pet1. To some extent, the porosity exponent is the interaction result of the largest pore cluster and the remaining pore clusters. The effect of the remaining pore clusters on the porosity exponent is not so obvious compared with the results from Pet1 and Pet6. The effect on Pet4 is about 0.2 while this change for Pet1 and Pet6 are 0.9 and 0.4, so the connection of the largest cluster is a key point for the porosity exponent in Pet4.

3.5.4 Prediction Porosity Exponent Considering the Influence of Different Pore Clusters

Conversely, based on the above idea, a better simulation result based on random walk can be obtained by comparing the three different simulation results from varied pore space including the porosity exponent (FF and porosity) just based on the predominant pore cluster, the porosity exponent based on the FF from the main pore clusters and the total porosity as well as the porosity exponent based on the FF and the porosity from the whole pore space. The porosity exponent based on the FF from the main pore clusters and the total porosity just considers the effect of the remaining pore clusters on porosity while the porosity exponent based on the FF and the porosity from the whole pore space includes the effect of the isolated pore clusters on the FF and porosity. This comparison is to consider the effect of the isolated pore clusters on the FF and then on the porosity exponent.

Firstly the simulation can be implemented directly on the whole pore space of the samples, the results are shown in Figure 3.58(a), the porosity exponent is the combined results of different pore clusters in the pore space including the largest pore cluster and the remaining.

Secondly, the porosity exponent can be estimated by the FF and the porosity on the largest pore cluster in Figure 3.58(b). This porosity exponent should be reasonably reduced due to the removing of the isolated pore clusters. It is the exponent of the main pore cluster in the pore space.

Thirdly, the porosity exponent based on the FF from the largest pore cluster and the total porosity of the pore space can be obtained in Figure 3.58(c) with assumption that the contribution of these isolated remaining pore clusters to electrical current is zero. In

this case, the porosity exponent should be the second largest among these three exponents with the smallest for the porosity exponent in the second case. Because the porosity for first and third case are both same, while the FF or the R_0 (R_w constant for three carbonate samples) from the first is larger than the third one, due to effect of the isolated pore clusters on the random walk simulation increasing the FF and R_0. So the first exponent is the largest and the third is the second largest.

The implicit assumption for the first and the third simulation about the effect of the isolated pore cluster (isolated vug, IVG) on the porosity exponent are respectively that the first simulation assumes that the IVG can affect the resistivity, R_0 while the third one assumes that the IVG can not affect the resistivity, R_0.

If the simulated porosity exponent from the largest pore cluster and total porosity, is close to the exponent from the whole pore space and total porosity (Pet6 close to 2.8) and the fluctuation of the porosity exponents based on the largest pore cluster, respectively considering its porosity and the total porosity, is intermediate (about 0.4 for Pet6), the effect of the isolated pore clusters is reasonable case which should be considered in the modelling to get a better result. This is the case for Pet6 and Pet4 with about 0.2 in fluctuation meaning the less effect of the isolated pore clusters compared with Pet6.

If the porosity exponent based on largest pore cluster and total porosity is larger than the porosity exponent based on whole pore space and total porosity, this incorrect result indicates that consideration of the isolated pore clusters in the porosity exponent calculation is not suitable. So the porosity exponent based on the largest pore cluster and its porosity may be best one without consideration of the isolated pore clusters. In Figure 3.59 the better porosity exponent based on this analysis is given.

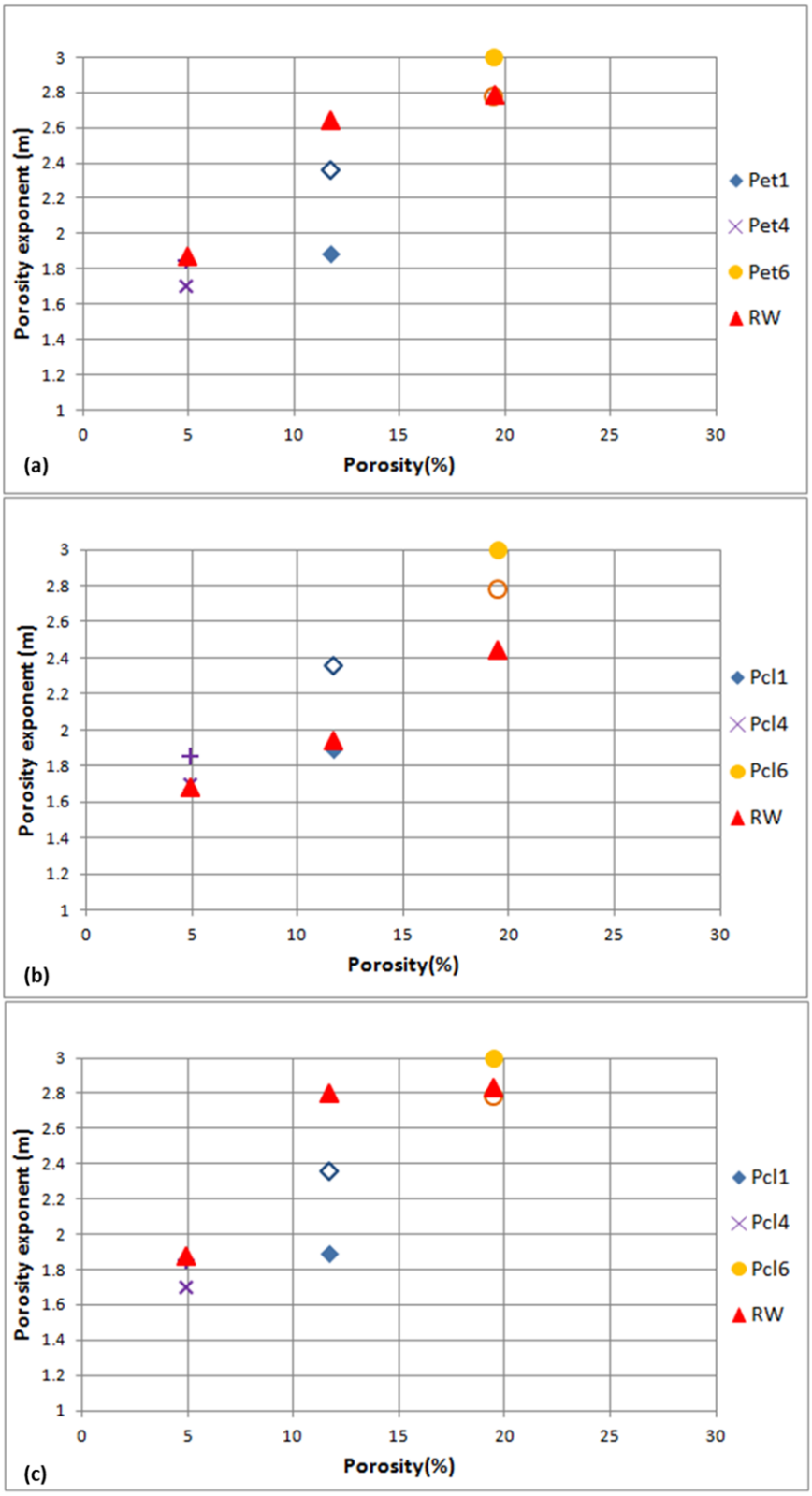

Figure 3.58: The random walk simulation based on different input pore spaces. The captions in the legend identify the pore space used for Formation Factor (FF) or the resistivity of the fully brine saturated sample. (a) is for the FF simulated on the whole pore space and the total porosity; (b) is for FF and porosity from the largest pore cluster; (c) is based on FF from the largest pore cluster and the total porosity assuming no contribution of the remaining pore clusters to the resistivity.

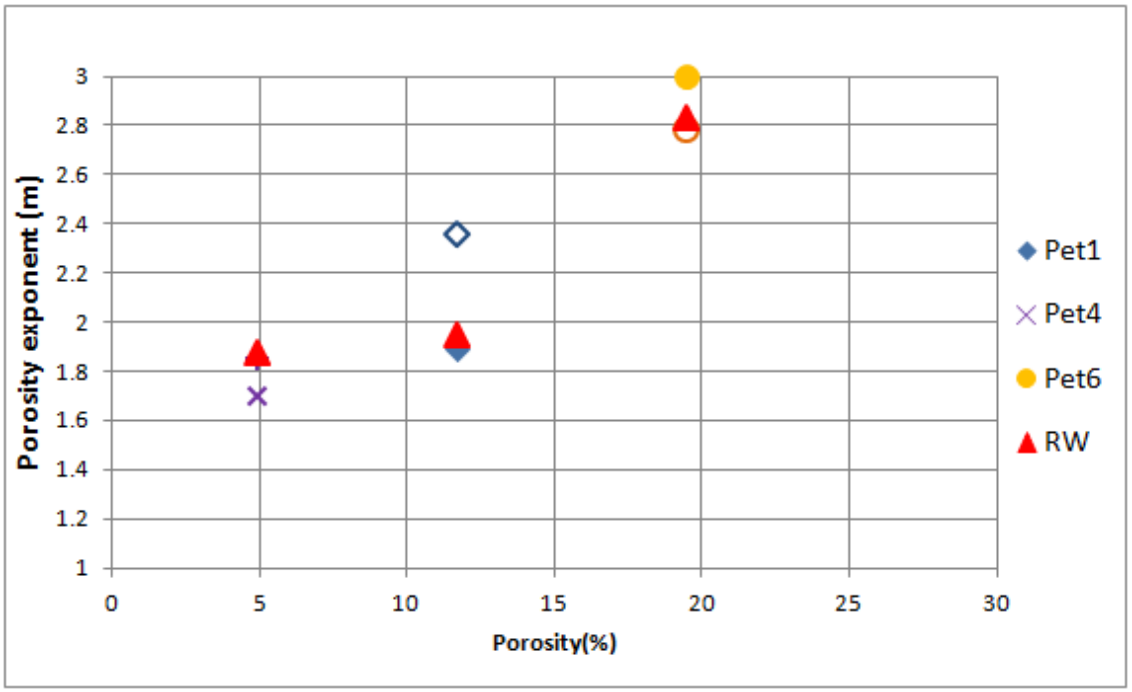

Figure 3.59: The best simulation of porosity exponent for Pet1, Pet4 and Pet6 (SC800). The porosity exponent for Pet1 is based on the largest pore clusters and the porosity exponent for Pet4 is based on the Formation Factor (FF) from the whole sample and its total porosity and the Pet6 is the same as for Pet4.

3.5.5 Main Pore Type for Three Carbonates

Besides, the porosity exponent for Pet6 mainly controlled by vugs and the key factor for Pet4 is fracture can be shown by the dual porosity model (Aguilera and Aguilera, 2003[5]), the total porosity of the whole sample and the porosity of the largest pore cluster. The distributions of the Pet 4 and Pet 6 in dual porosity model are in Figure 3.60. The total porosity, the porosity of the largest pore cluster and the porosity of the rest is shown in

Table 3.4.

	Total Porosity (%)	Largest cluster Porosity $\phi_{cluster}$ (%)	Remaining cluster Porosity $1-\phi_{cluster}$ (%)
Pet1	**8.2**	**2.7**	**5.5**
Pet4	**7.5**	**5.6**	**1.9**
Pet6	**19.1**	**14.7**	**4.4**

Table 3.4: Total porosity, the porosity of the largest pore cluster and the porosity of the rest pores for Pet1, Pet4 and Pet6 (SC800).

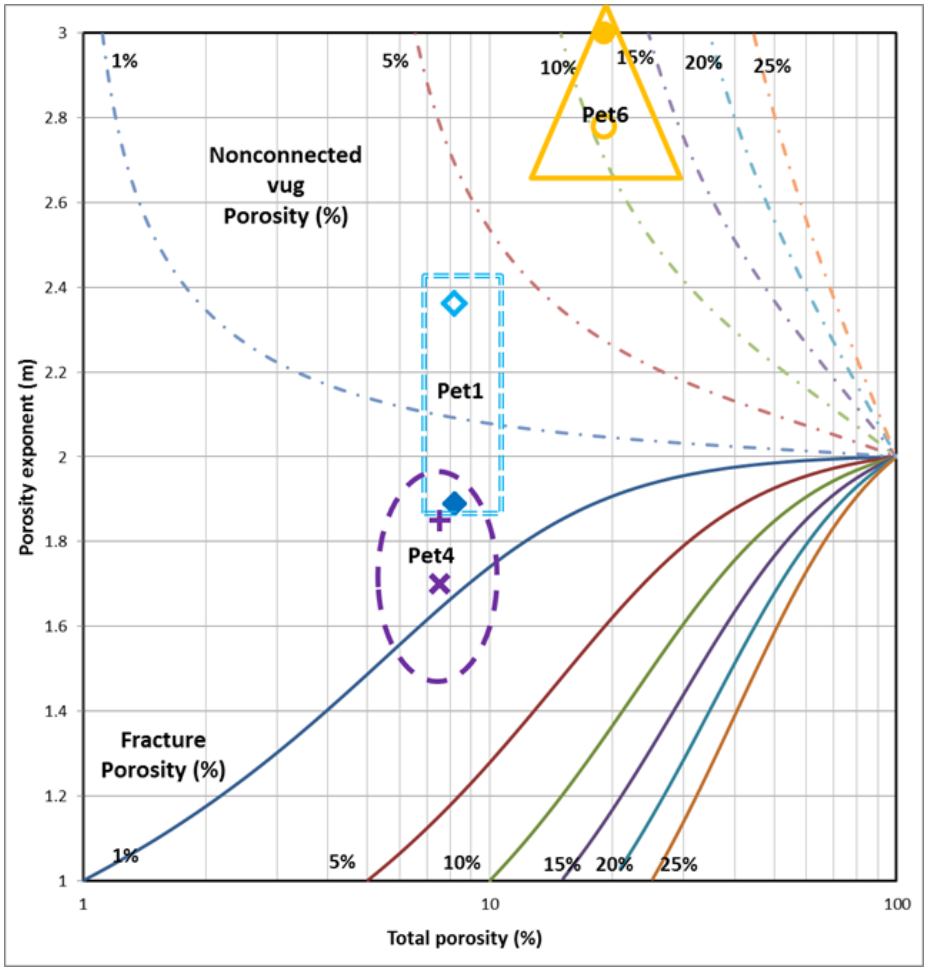

Figure 3.60: The distribution of the Pet1, Pet4and Pet6 in the dual porosity model (Aguilera and Aguilera, 2003[5]).

For Pet1, the total porosity is 8.2%, the porosity of the largest pore cluster is 2.7% and the porosity of the remaining pore voxels is 5.5% in

Table 3.4. Its porosity exponent is 1.89 or 2.36 located in the rectangular area in the Figure 3.60. For Pet4, the total porosity is 7.5% with the porosity of the largest pore cluster equal to 5.6%, The fracture porosity of its location is about 1% which is possible for Pet4. Because the porosity of the largest pore cluster, where pore cluster is not the same size, is 5.6% so the maximal porosity for facture is 5.6%, when the fracture porosity is less than 5.6%, it is possible for Pet4 to reach this requirement. For Pet6, the porosity of the remaining pore voxels is 4.4% and the porosity of the largest pore cluster is 14.7%. Due to the largest pore and throat cross sectional area ratio in this sample, the trap or dead-end in the largest pore cluster of the Pet6 can raise the porosity of vugs from 4.4%. In the Pet6 triangle region, the porosity of vugs is about 10% which is available for Pet6.

Based on that, the pore space trimmed by component labelling algorithm can improve the topology of the pore space by removing the isolated pore clusters. The geometry of the pore space keeps stable before and after the labelling process showing that the pore geometry for different pore clusters may be same. Finally, a reasonable porosity exponent based on random walk simulation can be given by the comparison of simulation results based on three different input pore systems and the key point effect on the porosity exponent can be predicted by the change of the simulated porosity exponents for three different inputs and their location in the cross plot of porosity exponent versus total porosity based on dual porosity models.

This analysis has been shown that the effect of the pore types (vugs or fractures) on porosity exponent is significant. However, the pore structures and types are fixed for the CT images which are related to resolution. It is not convenient to get CT images at various resolutions to contain all the pore types, which need $x-CT$, $\mu-CT$ and $n-CT$ in the future, while this is easily available for pore scale modelling method. So in the next chapter, simplified pore scale models can be used to study the effect of pore types on porosity exponent which is difficult for complex CT images. Thus porosity exponent affected by pore types can be related to their effect on the formation factor (FF) as well as their effect on the geometry (GM) and topology (TP) of the pore system.

3.6 Discussion

3.6.1 Variation of Porosity Exponents in REV Analysis

Porosity exponents from RW simulation in Figure 3.10 are convergent in x, y, z three directions and their average become stable reflecting the sub-cube is gradually representative when the size of the sub-cubes reaches 350 voxels. However, with the increase of the length, the porosity exponents in three directions turn to be divergent again while the porosity exponent in each direction keeps stable with less variation. The divergence of the porosity exponents in three directions is due to the anisotropy of the carbonate samples, the anisotropy causes the difference of the porosity exponents in three directions. The porosity exponent in z direction is larger than the porosity exponents in x and y directions. The variation of the porosity exponent in each direction stems from the simulation method, the error existing in the RW estimation about 5%, the variation of the simulated porosity exponent in each direction is about 0.1.

3.6.2 Resistivity Simulation

Comparing the simulation results with experimental data, FD, RW and renormalisation methods can match the experimental data. FD can best simulate the porosity exponent while it needs lots of time and it is a challenge for computer. RW estimates the porosity exponent with error determined using less time and memory of computers. Renormalisation is a successful estimation of the porosity exponent when the sub-sample is representative.

In this thesis, RW is an efficient method to simulate the porosity exponent of the REV and Sup REV samples due to its less requirement of memory in computer and less consumption of time. FD is applied in the Sub REV sample with the requirement of the current density distribution. Renormalisation is not directly applied to estimate porosity exponent due to the calculation of all the samples still in the capacity of the computer while its feasibility has been validated by considering the effect of size of sub-samples on the simulation results.

3.6.3 Pore Types Influence on the Geometry and Topology

The geometry and the topology of the three carbonate samples are related to the pore types in their pore systems. Pore size and throat size can not compare with Fb22 due to the differences in resolution. For Pet1, Pet4 and Pet6, fracture can reduce the size (Figure 3.31**,** Figure 3.32) and the PTRR (Figure 3.42) of the pore system while the vug can increase the pore size and PTRR, so Pet6 shows the largest pore size and PTRR while Pet4 is the smallest in pore and throat size as well as PTRR and PTAR. Meanwhile, the fracture (FT) which is more irregular than the intergranular (IG) pore can effectively affect the pore compared with the effect on the throat, so the pore shape factor (Figure 3.33 and Figure 3.34) for Pet4 is less than the throat shape factor and the pore shape factor can reach the smallest region while the vug (VG) do not generate irregular cross section but introduces various cross section because the cross section for VG and IG is different, so the shape factor of Pet6 scatters widely.

Additionally, fracture (FT) increases the length of the throat causing the large tortuosity (Figure 3.35) while the vug (VG) increases the volume of the pore body to some extend reducing the tortuosity but increasing the coordination number (Figure 3.36) due to the merging of the pore body (in Figure 3.37).

3.6.4 Explanation the Porosity Exponent by Pore-Throat Conjunction

The pore-throat conjunction can explain the porosity exponent for three carbonates. According to the relationship between porosity exponent and pore-throat size in Figure 3.41, the porosity exponent is related to the size of the pore and throat which can be expressed by the pore-throat cross sectional radius ratio (PTRR) or the pore-throat cross sectional area ratio (PTAR), with the increase of PTRR or PTAR, the porosity exponent increases. The PTRR of these three carbonate samples Pet1, Pet4 and Pet6 (SC400) can be shown by the schematic pore-throat structure with the pore in red and throat in blue in Figure 3.61.

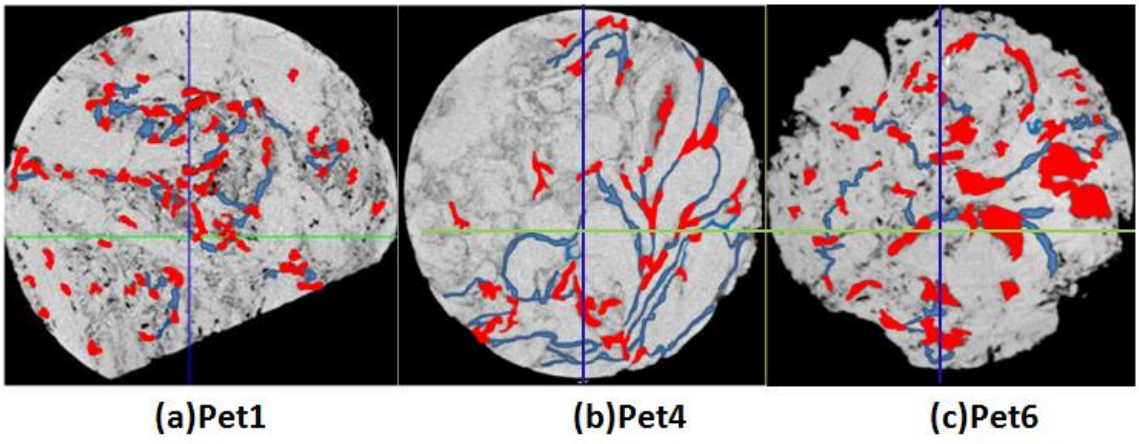

Figure 3.61: The schematic of the pore throat structure for the three carbonate samples Pet1 (a), Pet4 (b) and Pet6 (c). Red identifies pores and blue is pore throat.

From the above pictures in the Figure 3.61, it is clear the similarity of the pore (red) and throat (blue) in size reduces from Pet4 (b), Pet1(a) and Pet6 (c). The largest variation in the pore and throat size lies in Pet6 and the pore and throat size are almost equal for Pet4 with the intermediate variation for Pet1. This result conforms to the porosity exponents for these three carbonates.

These variations in pore and throat size for these three samples can be shown by their nodes and bonds in the pore network models shown by Rhinoceros (http://www.rhino3d.com/) in Figure 3.62.

3.6.5 Length and Size of the Pore Space effect on Porosity Exponent

The porosity exponent is related to the length and size of the pore system consisting of pore (node) and throat (bond).

The porosity exponent is the mutual effect of length and size of the pore space including the nodes and bonds and the pore types according to the comparisons between

the pore network for Pet1, Pet4 and Pet6 and the comparisons between these three pore networks before (a, b, c) and after segmentation (d, e, f) in Figure 3.62.

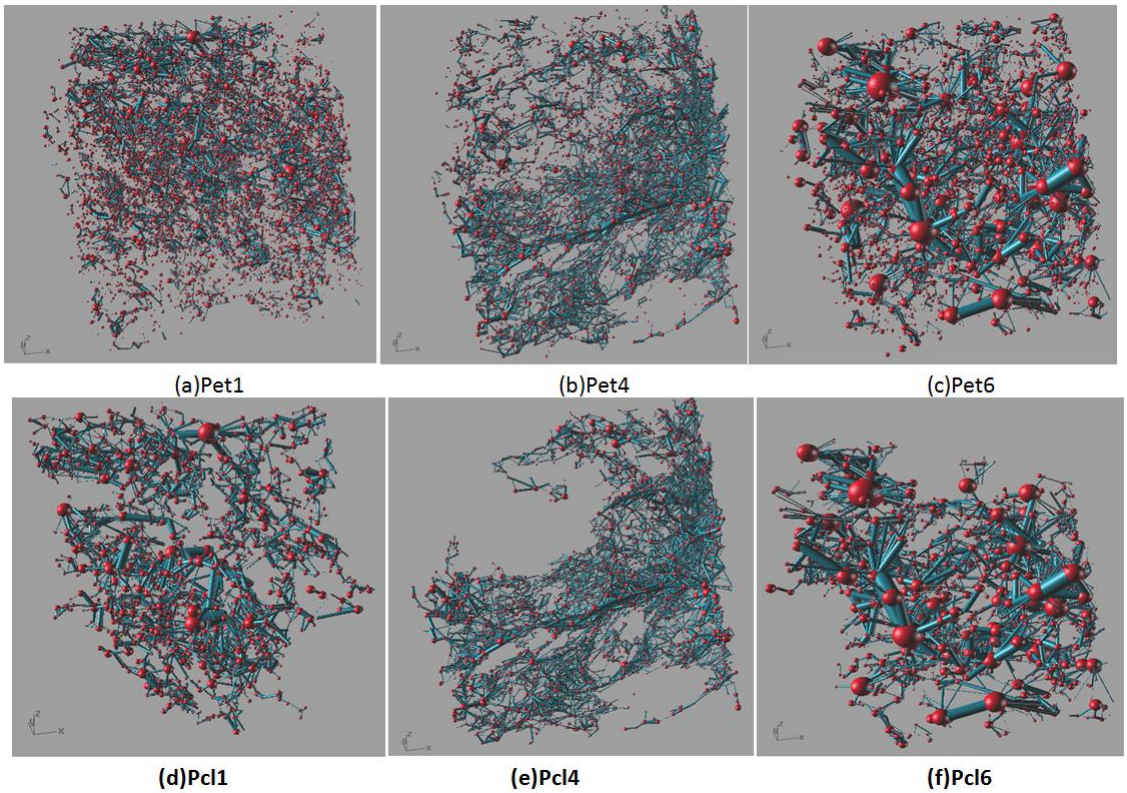

Figure 3.62: The pore network for the three carbonate samples Pet1 (a), Pet4 (b) and Pet6 (c) (SC800) and their predominant pore clusters after component labelling process denoted as Pcl1 (d), Pcl4 (e) and Pcl6 (f) (SC800).

In the top pictures (a), (b) and (c), the pore network presents the pore throat cross sectional area ratio and the pore types with the predominantly connected pore space and the isolated pores (IVG). From this comparison, *it is presented that the porosity exponent was controlled by the geometrical properties, which are affected by the pore types, of the mainly connected pore network as well as the pore types*.

While the contribute of the pore throat cross sectional areal ratio (PTAR) or pore throat cross sectional radius ratio (PTRR) to the porosity exponent (Figure 3.58, Table 3.2 and Table 3.3) was obvious in the visual comparisons (Figure 3.62) and numerical comparisons (Table 3.2 and Table 3.3 in pore, throat and PTRR) of these three carbonate samples in (d), (e) and (f) after the segmentation showing the dominant pore network.

3.6.6 Relation between Pore Types and Porosity Exponent

The porosity exponent is related to the pore types. The effect of the pore types on the porosity exponent can be illustrated by the comparison of the porosity exponents for these three carbonate samples before and after segmentation in Figure 3.58.

It is clear that the porosity exponent of the Pcl6 presenting the mainly connected pore space of Pet6 by segmentation is 2.4 which is larger than 2.0, typical value for the intergranular pore (IG). This is due to the effect of the PTAR or PTRR on the porosity exponent. The porosity exponent for Pcl6 increased to 2.8 for Pet6 resulting from the pore types. *The additional isolated pores (moldic or vug) cause the increase of the porosity exponent, which is, on one hand, the pore types effect on the porosity exponent. On the other hand, the pore type effect on the porosity exponent can change their geometrical or topological properties such as the PTAR or PTRR or Euler number* (Table 3.2 or Table 3.3 from Pet4, Pet1 to Pet6, the difference of the pore or throat or PTRR to some extent are related to the pore types and Figure 3.61**,** Figure 3.39 and Figure 3.54). The connected vug or moldic pores which are larger than the intergranular pore can increase the PTAR or undermine the connectivity of the pore system and then affect the porosity exponent.

The effect of the pore types on the porosity exponent can be directly reflected by the isolated large moldic or vuggy pores or indirectly presented by the increase of the pore throat cross sectional area (PTAR) or radius ratio aspect (PTRR) and the Euler number (Figure 3.54). This result is also acceptable for fracture whose effect lies in the direct decrease of the porosity exponent and the enhancement of the similarity of the pore and throat relating to the PTAR (PTRR) (Table 3.2 and Table 3.3) then influence the porosity exponent.

The PTAR (PTRR) effect on the porosity exponent for the predominant pore network of Pet4 (Figure 3.58) caused the porosity exponent equal to 1.6 while it just increased by 0.2 to 1.8 with consideration of the isolated pores (moldic or vugs). The isolated pores, which is equal to the size of the intergranular pore, in Pet4 increases the porosity exponent while the contribution of the fracture to the porosity exponent lies in the PTAR, the similarity of the pore and throat reduces the porosity exponent to about 1.7.

For the carbonate sample Pet1 which is mainly the intergranular (IG) pore, the porosity exponent of the IG is close to 2.0 shown in Figure 3.58**(**b**)**, which is the reflection of the geometrical and topological properties of the mainly connected pore

(Pcl1) obtained by the segmentation. This result conforms to the traditional porosity exponent for the IGs. While the IVG can dramatically increases the porosity exponent to 2.8 by numerically and to 2.4 by the experimental result. The effect of the IVG on the porosity exponent can be reflected by the increase of the porosity exponent both in numerical simulation and experiment (Figure 3.12**,** Figure 3.14**,** Figure 3.56 and Figure 3.58).

3.6.7 Explanation the Large Simulation Result in Pet1

The numerical simulation is larger than the experimental result for Pet1 in this lower porosity (<10%) can be explained by the existence of the small pores whose size is smaller than the resolution of the CT without consideration in the CT images reflected by the porosity difference between experimental results and $\mu - CT$ (Table 3.1) or by the threshold chosen in the binary segmentation. This threshold is a bit less than the critical threshold causing the porosity (8%) less than the experimental data (12%) in Table 3.1, according to the effect of threshold on the porosity (Figure 3.24) and porosity exponent (Figure 3.26) causing the larger value of the porosity exponent by the simulation.

Based on the discussion, the porosity exponent is controlled by the pore length, size and pore types. On one hand, pore types to some extent can affect the geometrical properties such as pore size including the size of the pore and throat, the pore throat cross sectional area ratio (PTAR) or PTRR and the topological property (Euler number). These effect on the TP and GM of the pore system can affect the FF (resistivity of the 100% brine saturated samples), and then the porosity exponent. On the other hand, the pore types can increase the total porosity. By these two aspects, the pore types can affect the porosity exponent. And the key pore type for these three carbonate samples can be shown in Figure 3.60 with earlier published work (Aguilera and Aguilera, 2003[5]).

In the next chapter, the pore scale models can be used to study the effect of pore size, length and pore types on porosity exponent. In this process, the effect of pore types on the Formation Factor (FF) and the geometry (GM) and topology (TP) of the pore system can be researched inspired by these carbonate samples.

3.7 Conclusion

The main conclusions can be obtained from this Chapter 3 are:

- Finite difference (FD), Random Walk (RW) and a Renormalisation simulation can match the experimental results (Figure 3.13, Figure 3.14, Figure 3.17). Considering the consumption of time and memory of computer, RW is an efficient method to estimate porosity exponent with error determined for REV and Sup REV samples. With requirement of current density, FD is suitable for Sub REV samples.
- The carbonate samples are much more heterogeneous and anisotropic than sandstones in porosity and porosity exponent (Figure 3.19, Figure 3.20, Figure 3.21 and Figure 3.22); the porosity exponent for carbonates should be a vector (regional and directional).
- The porosity exponent is the mutual effect of the size and length of the pore system (Figure 3.42, Figure 3.43 and Figure 3.62).
- According to effect of the main connected clusters and the whole pore system, the pore type for these three carbonates are that Pet6 is the vug (IG+VG), Pet4 is fracture (IG+FT) and Pet1 is intergranular (IG) pore (Figure 3.60).

There are several other findings in this chapter:

- The porosity exponents for the larger Sub REV are more robust than the smaller Sub REV (Figure 3.16 and Figure 3.17) and then the porosity exponents from the Sup REV samples are the best. The length of REV cube sample for coquinas is 600 voxels.
- The positive Euler number shows worse connection of the pore space, predominantly occupied by isolated clusters, comparison with the negative Euler number presenting better connection resulting from the channels as the main component in the pore space (Figure 3.23, Figure 3.26 and Figure 3.29).
- Simple, big pore system $\neq$ small porosity exponent; Complex pores in the pore system $\neq$ large porosity exponent (Figure 3.27 and Figure 3.30);
- The pore and throat radius is: Pet6>Pet1>Pet4, the permeability KPet6>KPet1>KPet4. The samples with larger pores and throats present larger permeability. The permeability is related to the pore and throat size (Figure 3.12b, Figure 3.31 and Figure 3.32).
- The geometry and topology of the pore system is related to the pore types (Figure 3.31, Figure 3.32, Figure 3.33, Figure 3.34, Figure 3.35, Figure 3.36, Figure 3.39 and Figure 3.62)

- The cross sections of the pore are much more irregular than the cross sections of the throats (Figure 3.33 and Figure 3.34).
- Fractures cause the irregularity of the cross section (shape factor) and vugs result in the variety of the cross sections (Figure 3.33, Figure 3.34 and Figure 3.62).
- The pore system of carbonates is much more tortuous than the sandstones (Figure 3.35).
- The effect of fractures (FT) and vugs (VG) on the tortuosity lies in the increase and decrease respectively (Figure 3.35 and Figure 3.62).
- Vugs can cause the increase of the connection number (Figure 3.36 and Figure 3.62).
- Fractures can reduce the PTRR while vugs increase the PTRR (Figure 3.42 and Figure 3.62).

Chapter 4

Model Investigation of the Impact of Pore Types on the Porosity Exponent

From the study of carbonates in Chapter 3, it is apparent that these rocks include dissolution seams and micro-fractures that can be considered generically as "fractures (FT)" and also over-large moulds, macro-pores or vugs that can be considered as "vugs (VG)" in the sense of Aguilera and Aguilera (2003[5]). And these pore types affect the porosity exponent by their influence on the geometry (GM) and topology (TP) of the pore system and then on the porosity exponent with the increase of the total porosity when these different pore types merges in the pore systems. These conform to the conclusions by some researchers (Wardlaw, 1980[215]; Ransom, 1984[164]; Rasmus, 1986[167]) that the porosity exponent is largely affected by secondary porosity (pore types), pore throat size and the tortuosity.

Due to the flexibility of modelling pore structures and pore types, pore scale modelling method and resistivity calculation are used to investigate the effect of pore geometry and pore types on the porosity exponent. In the pore scale models, the capillary tubes and pore network models are both easy to mathematically derive the electrical flow equations. However, the major weakness of the capillary tubes lies in the absence of pore connectivity (Abousrafa *et al*., 2009[1]). Pore network model is used to theoretically derive the porosity exponent of a pore-throat conjunction based on Ohm's law and electrical arrangement of pore node and bonds. This model is used to investigate the effect of pore geometry on the porosity exponent conforming to the experimental porosity exponents and the calculated pore geometrical properties in Chapter 3. Due to the convenience of the capillary tubes in building models with various geometries, based on the results from pore network models the capillary tubes with different geometries can be built to represent different pore types according to their porosity exponents and then these capillary tubes are used to model the pore types of IG+FT and IG+VG mainly existing in three coquina samples to validate the accuracy of the dual porosity model and to investigate the effect of pore types on the porosity exponent. However, the capillary tubes and pore network models can not represent the characteristics of the FT and VG (Mousavi *et al.*, 2012[139]). The models based on grain packs are used to simulate the FT and VG according to Mousavi *et al.* (2012[139]) with the IG simulated by a Fontainebleau sandstone. Due to grain packs models better representing pore structure for IG+FT and IG+VG, these models are used to investigate the effect of the pore types on the porosity exponent, formation factor and the anisotropy. With consideration of these electrical properties related to the pore structures, these models based on grain packs are also used to investigate the effect of

the pore types on the pore geometry and topology by comparing with the geometrical and topological properties of the models representing different pore types. For modelling the IG+FT and IG+VG by capillary tubes and grain packs models, the IG models are regarded as host media and inserted by the models of FT or VG. The resistivity is numerically calculated by FD.

This chapter firstly presents the theoretical models for porosity exponent based on pore-throat conjunction, this model is used to study the effect of the size and length of pore system on the porosity exponent and secondly builds pore scale models based on capillary tubes and models from process-based grain packs to simulate pore types such as IG, FT and VG, these models are used to investigate the effect of pore types on the pore geometry and topology, formation factor and then on porosity exponent.

4.1 Theoretically Electrical Models for Pore-Throat Conjunction

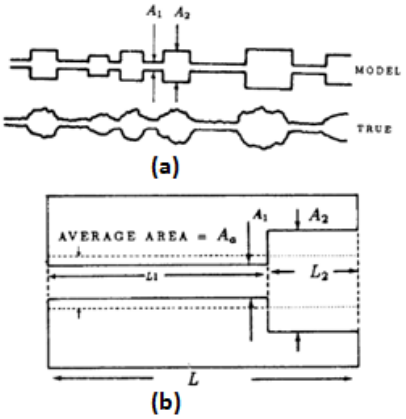

Figure 4.1: The theoretical model for tube model with consideration of the pore size and length (from Watfa and Nurmi, 1987[216]).

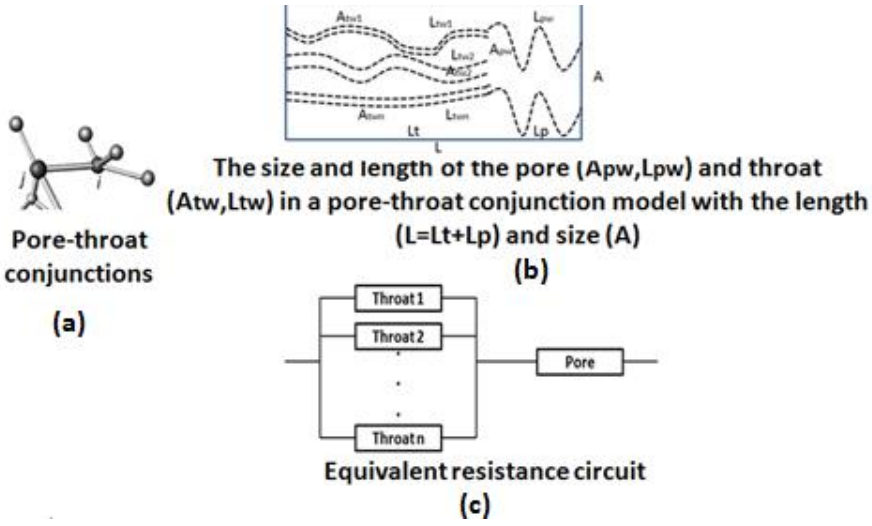

Figure 4.2: Pore-throat conjunctions in the pore network (a) and its pore-throat conjunction electrical model (b) considering the size and length of the pore system as well as its equivalent resistance circuit (c).

This section presents the porosity exponent theoretically derived from pore-throat conjunction based on Ohm's law and the equivalent resistance for resistors in series or parallel or both and investigates the effect of pore size, length and cross sectional area difference on the porosity expoenent.

The Pore-Throat conjunction is the basic unit for the pore network, the effect of the size, length and pore throat cross sectional area ratio (PTAR) on the porosity exponent could be helpful to explain the relationship between the geometry properties and porosity exponent. This basic pore-throat conjunction consists of pore and throat with parallel throats serially connected to a pore cell. This is an improvement compared with the simple tube-bundle model only considering one pore and one throat in series resistance network shown in Figure 4.1.

In the pore-throat conjunction electrical model, the equivalent resistors for throats are in parallel and then they are connected to pore node in series, the resistance is calculated by Ohm's law. Based on the resistance and Archie First Equation 2.32, the porosity exponent can be derived. And then the effect of the pore size, length and relative cross sectional area ratio in this basic conjunction in Figure 4.2 is investigated. In this model, the length of the pore system including the pore and throat is expressed by tortuosity (TT or τ). It is related to the length of the pore (TTp or τ_p) and throat (TTt or τ_t) shown in Equation 4.1. The pore and throat size is related to the cross sectional areal ratio (CSAR or ψ) which is defined by the ratio of the cross sectional area of the pore space to the cross sectional area of the conjunction in Equation 4.2.

$$\begin{aligned} &\tau = \tau_p + \tau_t, \tau \geq 1 \\ &\tau_p = L_{wp}/L, \tau_p > 0 \\ &\tau_t = L_{wt}/L, \tau_t > 0 \end{aligned} \tag{4.1}$$

$$\psi = A_w/A, 0 < \psi < 1 \tag{4.2}$$

The relative cross sectional area ratio (RCSAR or ψ_r) is in Equation 4.3 which is similar to the definition of the pore throat cross sectional area ratio (PTAR).

$$\begin{aligned} &RCSAR_{12} = CSAR_1/CSAR_2 \\ &\psi_{r12} = \psi_1/\psi_2 \end{aligned} \tag{4.3}$$

The terms in capital are used in the figure as axis title and legend while the Greek symbols are used in the formula.

The derivation of the porosity exponent of this model can be given in Appendix F .

$$m = -\frac{\log\left(\frac{\tau_p}{\psi_p} + \frac{1}{\sum_{i=1}^{n}\frac{\psi_{ti}}{\tau_{ti}}}\right)}{\log\left(\psi_p\tau_p + \sum_{i=1}^{n}\psi_{ti}\tau_{ti}\right)} \quad (4.4)$$

4.1.1 Size and Length of the Pore System Effect on the Porosity Exponent

This section presents the effect of pore size and length on the porosity exponent, the porosity exponent (Equation 4.4) derivative to the tortuosity (length) and cross sectional area ratio (size) is positive meaning that with the increase of the tortuosity, the porosity exponent raises and when the size of the pore space goes up, the porosity exponent of the pore system increases instead of decreasing.

Figure 4.4 shows the effect of the size and length on the porosity exponent for a simple pore-throat conjunction model in Figure 4.3 with the total porosity less than 40%. In Figure 4.4(a), the x-axis is the tortuosity denoted as TT, the porosity exponent of the model, with the cross sectional area ratio fixed as 0.01, increases from 1 to 9 when the TT ranges from 1 to 40. And the slope of the curve, reflecting the relationship between the porosity exponent and TT, increases with enhancement of the cross sectional area ratio (CSAR) from 0.01 to 0.25. The effect of the cross sectional area ratio (CSAR) on the porosity exponent is shown in Figure 4.4(b). The porosity exponent becomes large when the logarithm of this ratio increases while the exponent always keeps stable as 1 only if the TT is equal to 1, that is, the pore space is a straight tube channel.

Based on that, the porosity exponent is the mutual effect of the pore length (TT) and pore size (cross sectional area ratio). The effect of TT and pore size on the porosity exponent is the same lying in increasing the porosity exponent with the increase of the length or size of the pore space.

4.1.2 Relative Cross Sectional Area Ratio Effect on the Porosity Exponent

This section presents the effect of the relative cross sectional area ratio on the porosity exponent. For a pore-throat conjunction with n throats, the number of the pore throat cross sectional area ratio or this relative cross sectional area ratio is n, which is difficult to study the effect of each ratio on the porosity exponent. However, the parallel throat resistance circuit in Figure 4.2(b) and (c) can be presented by one resistance

circuit in Figure 4.5. The effect of the relative cross sectional area ratio can be reflected by this equivalent resistance model in series with one pore and one throat.

The porosity exponents of the systems with different TTs and CSARs for this equivalent resistance model consisting of one pore and one throat are shown in Figure 4.6. The legend in this figure is the porosity exponent and the colour is from blue to red with the increase of the exponent. It is clear that the porosity exponent distribution is related to the TT in each channel. The red colour is almost distributed in the margin of each slice, where the difference between the two CSARs of the two channels is large. The relationship between the relative cross sectional area ratio (RCSAR) and the porosity exponent can be given based on the porosity exponent distribution in Figure 4.7.

For the two pictures (a) and (b) in Figure 4.7, the minimal porosity exponent for each TT combination lies in the middle of the range of the logarithm of the relative RCSAR. It is obvious that the value in horizontal axis for the minimum of the porosity exponent is not always equal to zero, that is, the same cross sectional area for both cells. This critical value in horizontal axis is related to the TT of the two components (one pore and one throat) in the model, which is much more obvious in Figure 4.7(a), this critical value can be either positive or negative. Based on pore-throat conjunction electrical model in this section, the effect of the relative cross sectional area ratio on the porosity exponent is related to the length of the pore and throat. The similarity of the pore and throat size for the three carbonate samples with the TT ranging from 1 to 3 means low porosity exponent.

In this section, the theoretical conclusion for the effect of the length, the size and the RCSAR of the pore system on the porosity exponent have been studied. The results from this analysis can support the interpretation of the porosity exponents and geometrical properties for these three carbonate samples in Chapter 3 (Figure 3.42 and Figure 3.43).

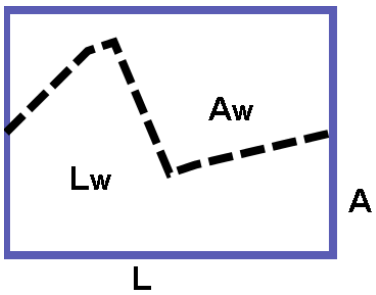

Figure 4.3: The schematic of a simple pore-throat conjunction model, its length is L and its cross section area is A. The length and cross sectional area of the pore space in this cell model are L_w and A_w respectively.

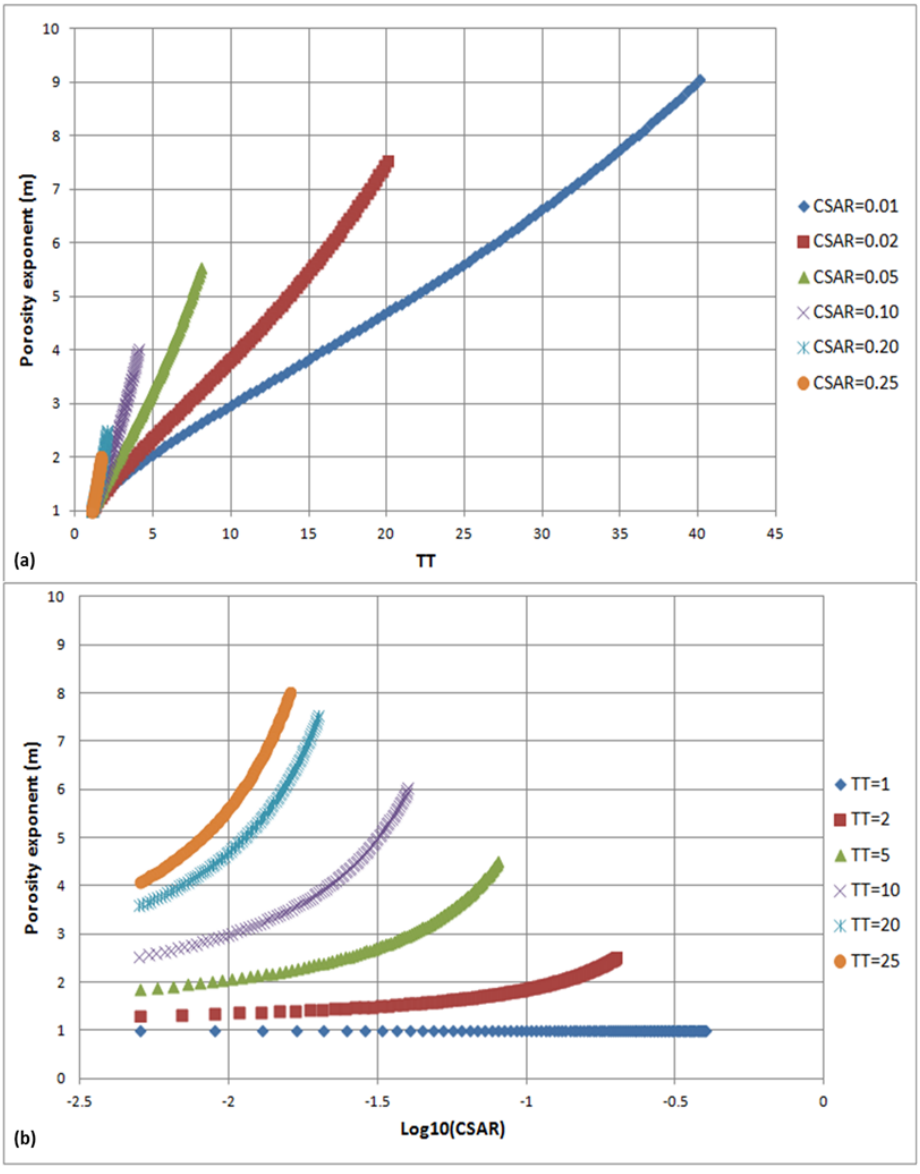

Figure 4.4: Porosity exponent versus tortuosity (TT) (a) and porosity exponent versus the logarithm of the cross sectional area ratio (CSAR) (b).

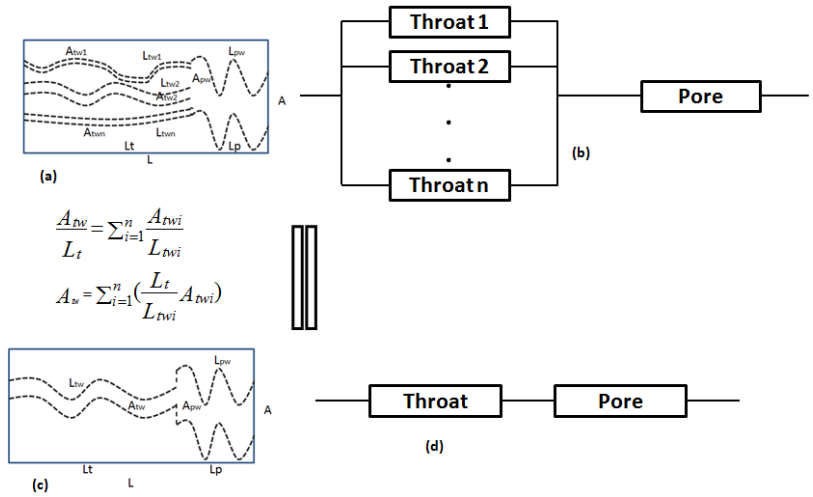

$$\frac{A_{tw}}{L_t} = \sum_{i=1}^{n} \frac{A_{twi}}{L_{twi}}$$

$$A_{tw} = \sum_{i=1}^{n} \left(\frac{L_t}{L_{twi}} A_{twi}\right)$$

Figure 4.5: The equivalent resistance model (c), including two pore channels respecting throat and pore respectively, and circuit (d) for a pore-throat conjunction (a) and (b) with several throats in parallel connected to a pore in series. The cross sectional area of the equivalent throat is the weighted average of the cross sectional area, the weight of each throat is related to the reciprocal of its length.

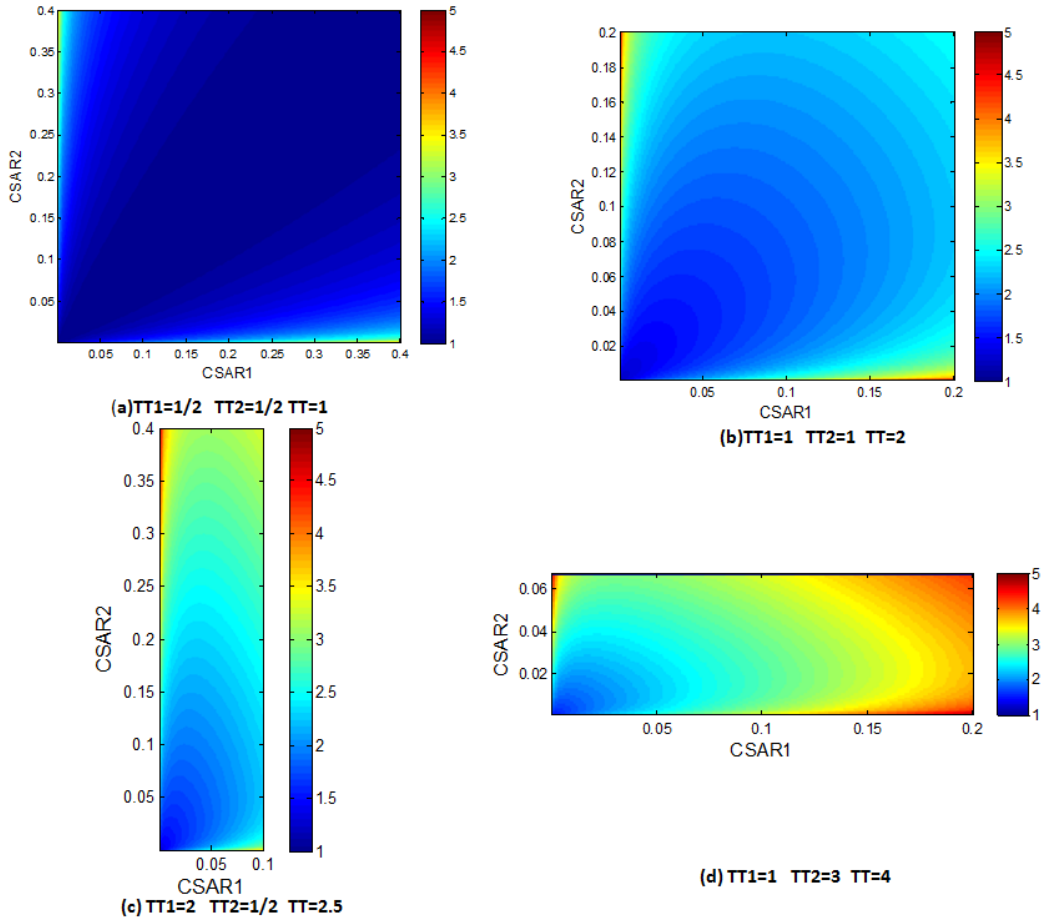

Figure 4.6: Porosity exponent distribution in 2D slices and the axes of each picture respectively reflect the cross sectional area ratio (CSAR) of the two pore channels in the system. The porosity exponent distribution in the two dimensional slice is related to the TT of each channel (TT1 and TT2).

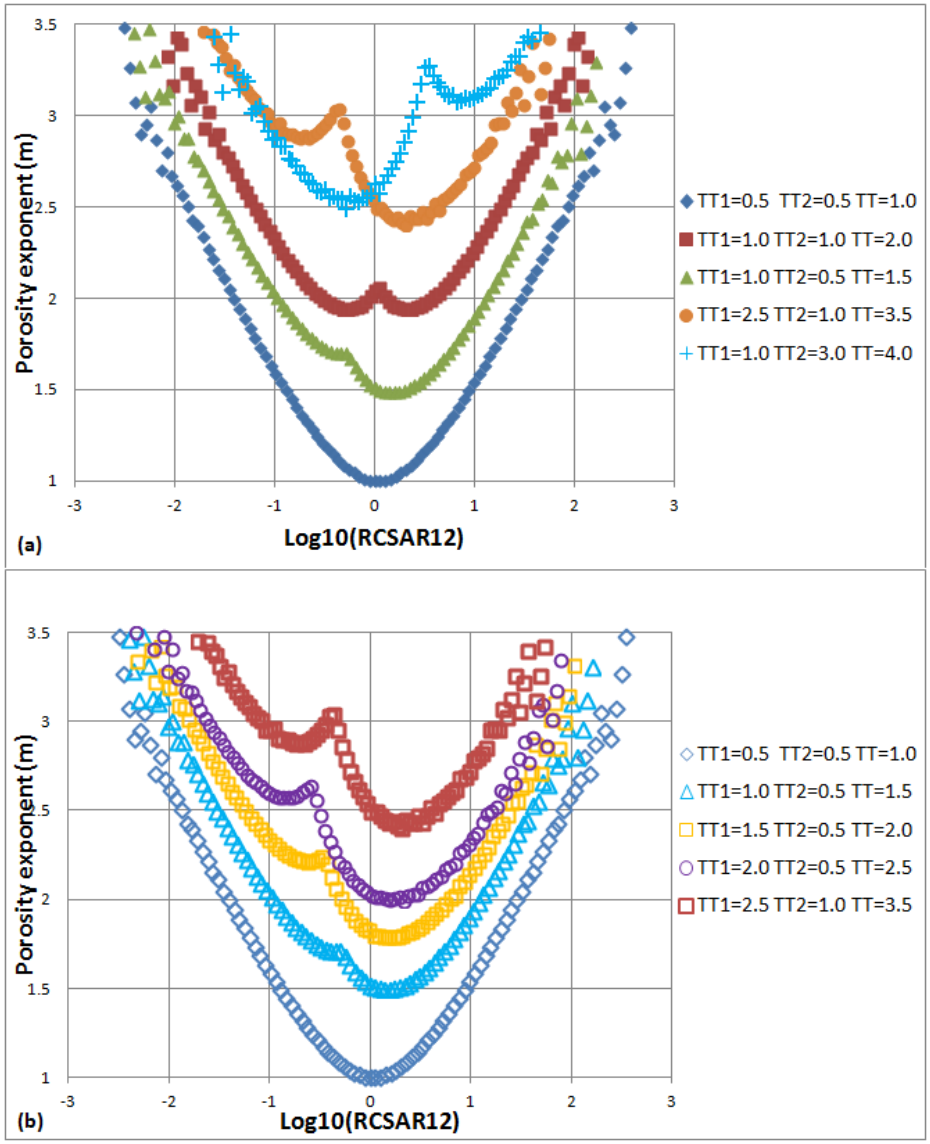

Figure 4.7: Porosity exponent versus the logarithm of the relative cross sectional area ratio (RCSAR) for different combinations of the TTs of the two channels in the pore-throat junction with one pore and one throat.

4.2 Effect of Pore Types on Porosity Exponent by Pore Scale Modelling

This section presents the key pore types existing in the CT images and their schematics for the following discussion. Due to the resolution of the CT images, the micro-pores cannot be distinguished in the images and therefore are not included in the following sections. While the pore types such as VG and FT affect significantly the porosity exponent of these three carbonate samples especially for Pet6 and Pet4. The models of IG, FT and VG can be simulated by capillary tubes and grain packs from the process-based method. In the modelling processes by these two methods, the tortuosity is not the main issue in this study due to the similarity in three carbonate samples. The

schematic for these models in the grain random pack, pore trap and channel and simple pore network is given in Figure 4.8. These schematic can be used in the following sections.

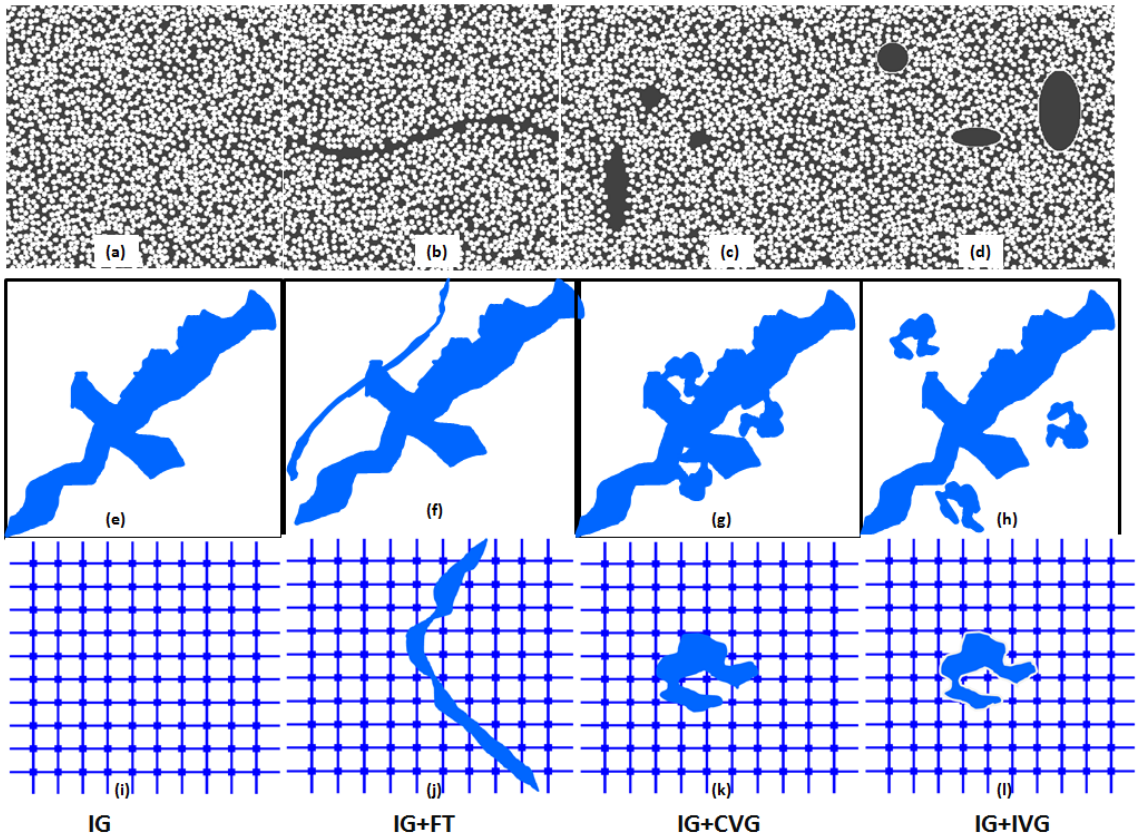

Figure 4.8: The schematics for IG, IG+FT, IG+VG including connected vug (CVG) and not connected or isolated vug (IVG) from the aspects of random grain pack (a), (b), (c) and (d), pore trap and channel (e), (f), (g) and (h) as well as simple pore network (PNW), the square is node and the line is bond in (i), (j), (k) and (l). In the random grain pack (top), the white is grain and the black is pore; for the pore trap and channel as well as the simple pore network, the white is void and the blue is the pore space.

4.3 Effect of Pore Types on Porosity Exponent by Simple Tubes

This section investigates the effect of the pore types on the porosity exponent and validates the accuracy of the dual porosity model (Aguilera and Aguilera, 2003[5]). From the viewpoint of capillary tubes, the FT and VG are firstly reflected by the tubes with different sizes. A series of simple tubes with various pore sizes along their same pore length can be built to represent IG, FT and VG according to their porosity exponents calculated by FD. Secondly the pore types of IG+FT and IG+VG are built based on the models of IG, FT and VG. Thirdly, the models for IG+FT and IG+VG are used to validate the accuaracy of the dual porosity model and investigate the effect of pore types on the porosity exponent. In this process, the resistivity is calculated by FD.

4.3.1 Representation of the IG, FT and VG by Simple Tubes

This section builds a series of simple tubes with various pore sizes along the same direction to present different pore types. Figure 4.9 presents the porosity exponents of these tubes. It is clear that with the PTAR close to one, the porosity exponent reduces to 1.00 conforming to the theoretical results for the two pore electrical channels in series in Figure 4.7 with the TT of each cell equal to 1. So the tubes taken as IG, FT and VG can be determined by their porosity exponents in the plot of Figure 4.9(a). The current density distributions of the four tubes in Figure 4.9 (b), (c), (d) and (e) are shown in the Figure 4.10 with the legend as magnitude of the current density by logarithm 10 scale. it is obvious that the red denser current mainly distributes in the channel and central part of the large pore space, the current density in the central space of the pore is higher showing orange and green while in the edge of the pore space, the colour turns to blue reflecting that this pore space is less useful for the current flow equivalent to the trap pore space.

The porosity for the tubes in these series above is close to 10%. In order to study the effect of the pore types on the porosity exponent in low porosity, it is necessary to build the models with the porosity close to 2%, another series of the tubes can be built and their porosity exponents are shown in Figure 4.11. In these models, the size of the tubes is much less than that in above series and then their related porosity is close to 2%. The relationship between the porosity exponent and the PTAR conforms to the theoretical results in Figure 4.7. And the current density distribution in these related tubes can be shown in Figure 4.12. The similar current density distribution can be observed in the Figure 4.12 that current mainly focuses on the channel while the edge of the large pore space can be taken as trap pore with less current density. From the current density distribution, it is can be concluded that with the increase in the PTAR, the pore space taken as trap pore, which is meaningless to the current flow, increases resulting in the large porosity exponent with the current flow along the channel.

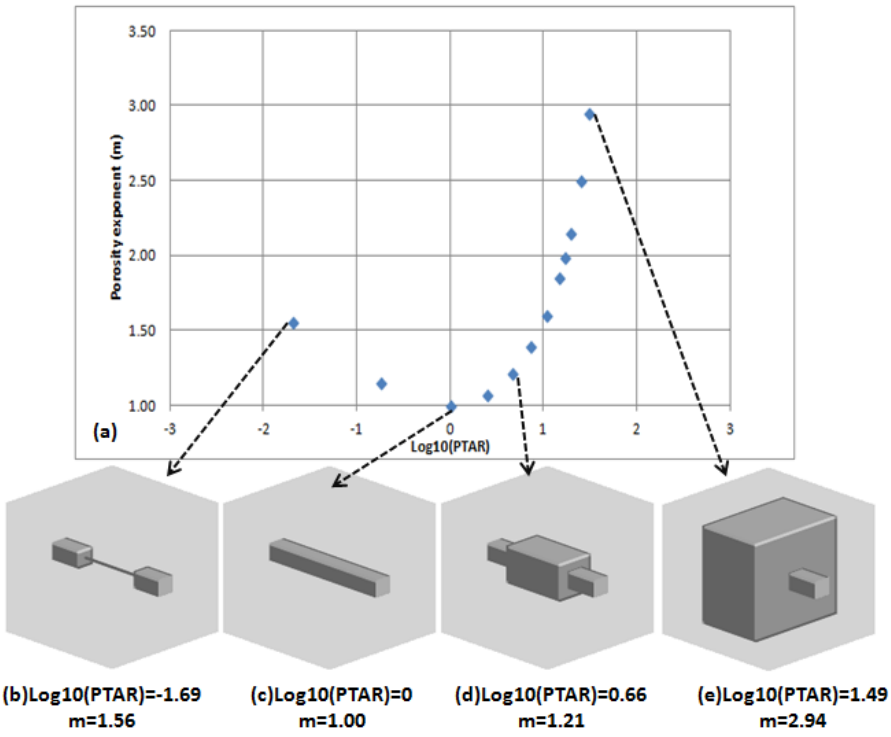

Figure 4.9: The tubes are used for simulating pore types with different pore sizes and same length from (b) to (e). Their relative porosity exponents versus the logarithm of the pore throat area ratio (PTAR) are shown in (a).

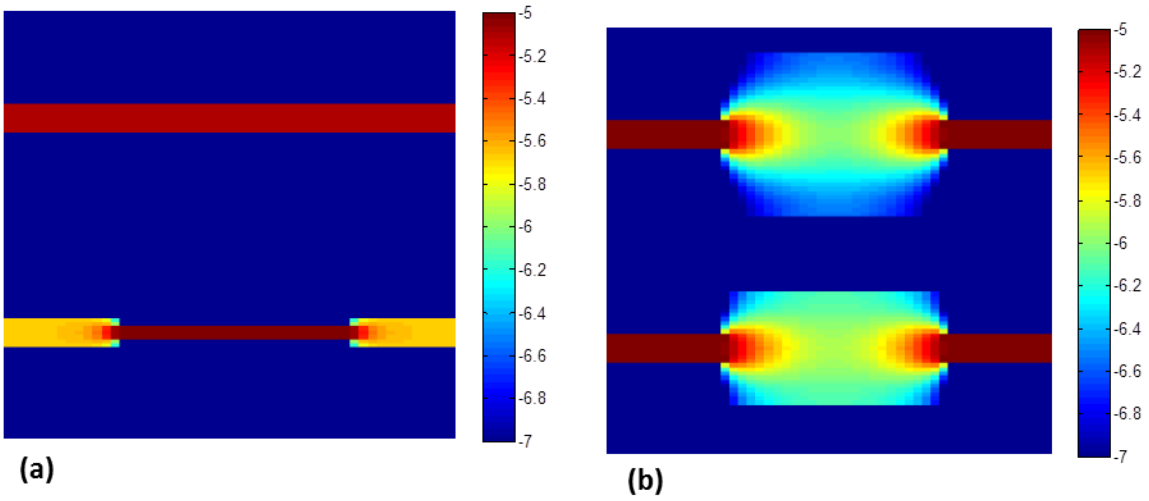

Figure 4.10: The current density distribution of the four tubes with logarithm of the current density in the legend shown by a finer colour map.

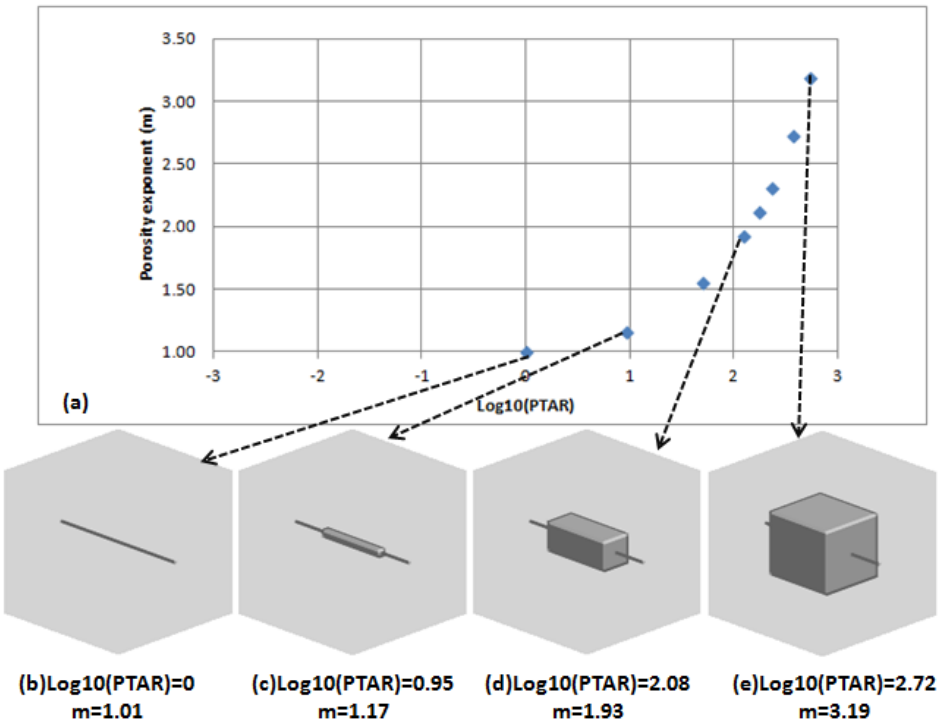

Figure 4.11: The tubes are used for simulating pore types with different pore size and same length (b) to (e). Their relative porosity exponents versus the logarithm of the pore throat area ratio (PTAR) are shown in (a).

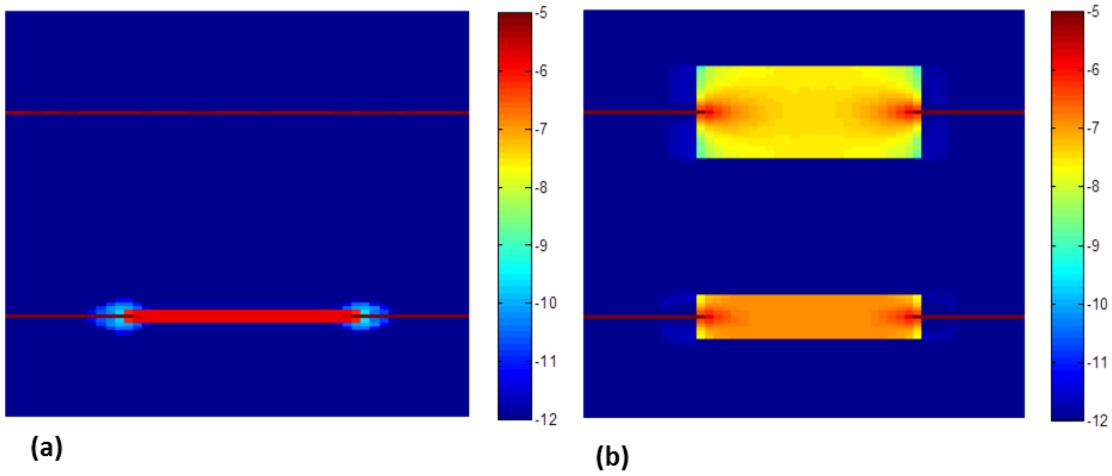

Figure 4.12: The current density distribution in the four tubes with logarithm of the current density in the legend.

4.3.2 Generation the Models of IG+FT and IG+VG

This section builds the IG+FT and IG+VG models based on capillary tubes for IG, FT and VG. The models for the pore types of intergranular (IG) and fracture (FT) and the models for the pore types of intergranular (IG) and vug (VG) both take IG model

with porosity about 2% as host medium inserted by the FT and VG. The arrangement of the IG and FT satisfies the assumption of the dual porosity model that IG and FT are in parallel, the VG is not connected to the IG. Pore types simulated by capillary tubes are shown in Figure 4.13.

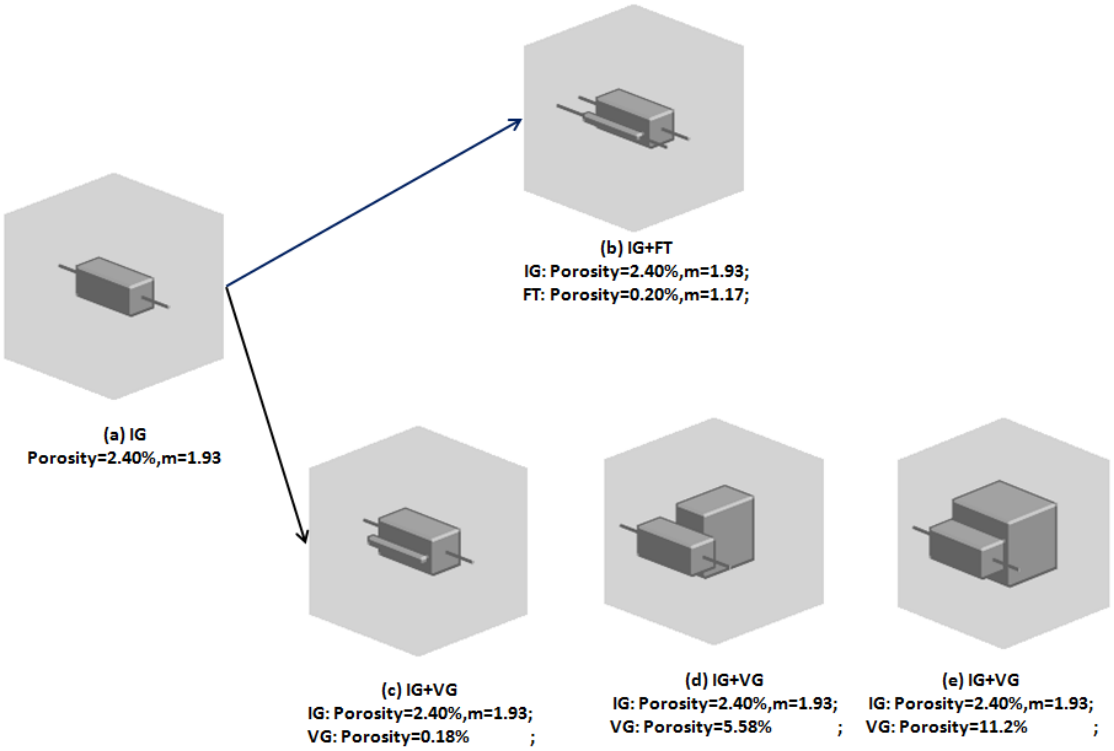

Figure 4.13: The models for IG (a), IG+FT (b) and IG+VG (c), (d), (e) with consideration of their porosities and porosity exponents.

4.3.3 Effect of the Pore Type on the Porosity Exponent and Formation Factor

This section presents the porosity exponent and Formation Factor (FF) based on the pore types models calculated by FD. These simulation results reflect the effect of the pore types on the porosity exponent and FF and validate the dual porosity model by comparing to the porosity exponent and FF from porosity model.

The effect of the FT and VG on the porosity exponent can be compared with the earlier published work (Aguilera and Aguilera, 2003[5]) by showing the porosity exponents in their theoretical porosity versus porosity exponent cross plot against the possibilities for the porosities of the inserted FT and VG in Figure 4.14.

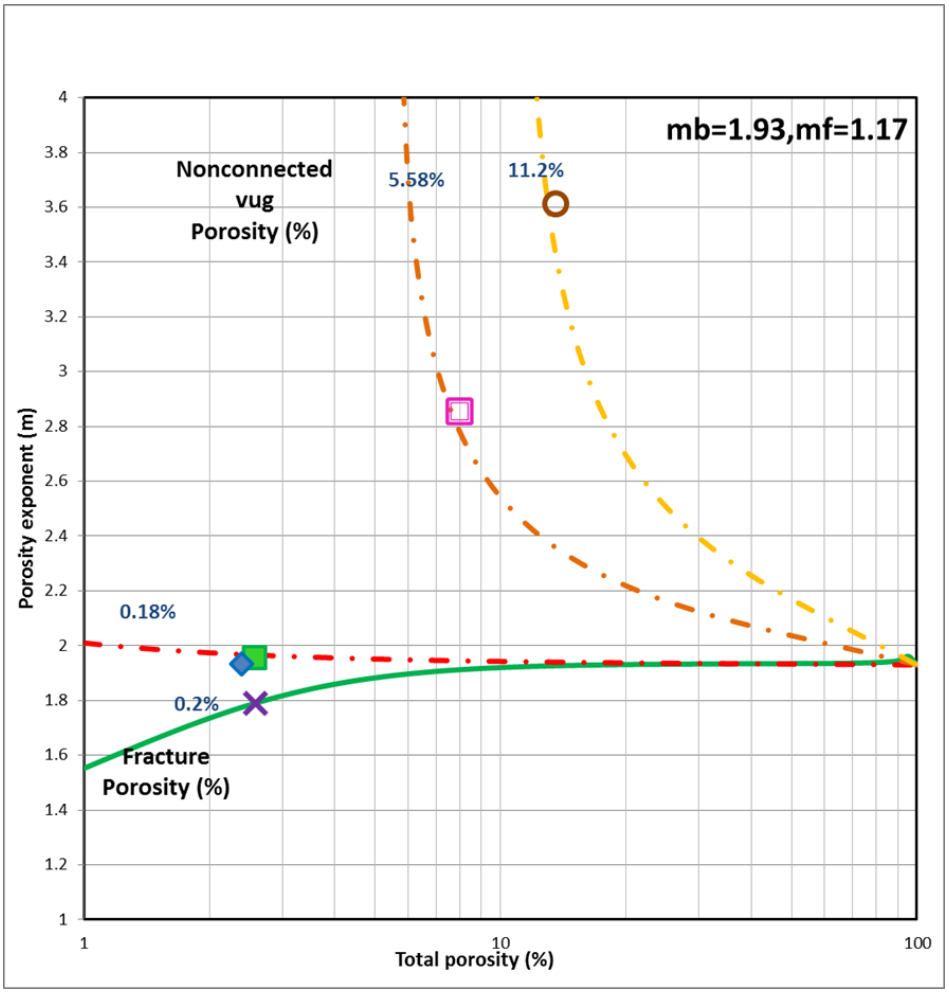

Figure 4.14: The porosity exponent versus the total porosity against the porosity of the FT and VG in the published work (Aguilera and Aguilera, 2003[5]). In their work, the porosity exponent of the IG is expressed by m_b and the porosity exponent of the FT is m_f.

The blue diamond "◆"symbol represents the IG with porosity close to 2.39% and porosity exponent equal to 1.93. The porosity exponents reduces to 1.8 in purple cross "✕" for the IG+FT model, in this mode, the porosity of the embedded FT is about 0.2% and its porosity exponent is equal to 1.17. The porosity exponent for this model matches the theoretical result for fracture porosity equal to 0.2% in green curve.

For IG+VG models, with the increase of the VG porosity from 0.18%, 5.58% to 11.2%, the porosity exponent increases from 1.96, 2.85 to 3.61 shown respectively by green square "■", unfilled pink square "□"and unfilled red circle "○". These three simulation results agree well with the theoretical results in Figure 4.14.

Based on the simulation results from IG+FT and IG+VG in Figure 4.14, the theoretical results of Aguilera and Aguilera (2003[5]) are correct when the models satisfying their assumption that the FT and IG are in parallel resistance network while the VG and IG are in series resistance network. The above IG+FT and IG+VG models

satisfy their assumption shown by schematic of the simple pore trap and channel model in Figure 4.15 and then their simulation results match their theoretical data.

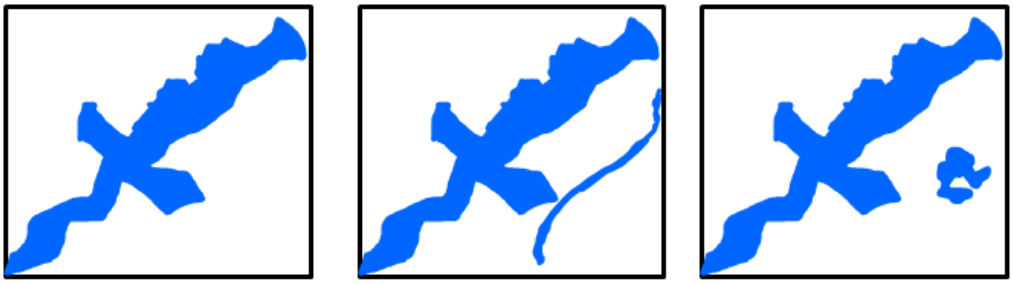

Figure 4.15: Schematic for the models of IG (a), IG+FT (b) and IG+IVG (c). IG+IVG schematic responds to the model for the IG and not connected vug (IVG) in series resistance network in Aguilera and Aguilera (2003[5]).

In Figure 4.15, it is clear that the electrical arrangement of the IG and FT is parallel and FT does not affect the pore structure of the IG. And the not connected vug (IVG) is not connected to the IG without influence of the pore structure of the IG.

Meanwhile, the effect of the pore type effect on the Formation Factor (FF) can be shown in Figure 4.16. It is clear that FT reduces FF while the effect of the IVG on the FF is trivial, FF almost keeps stable. According to the schematic in Figure 4.15, FT contributes to the electrical current flow with the decrease of FF while the IVG does not obviously affect the electrical current flow just increasing the total porosity to increase the porosity exponent.

Based on the results in Figure 4.14 and Figure 4.16, the accuracy of the published work (Aguilera and Aguilera, 2003[5]) was proved. Then the pore types effect on the porosity exponent was shown: the effect of the FT lies in the increase of the total porosity as well as decrease of the FF resulting in the decrease of the porosity exponent while the effect of the IVG contributes to the increase of the porosity exponent by the obvious increase of the total porosity and less influence on FF.

Are these correct for the models from random grain packs? The answer can be shown in the next section.

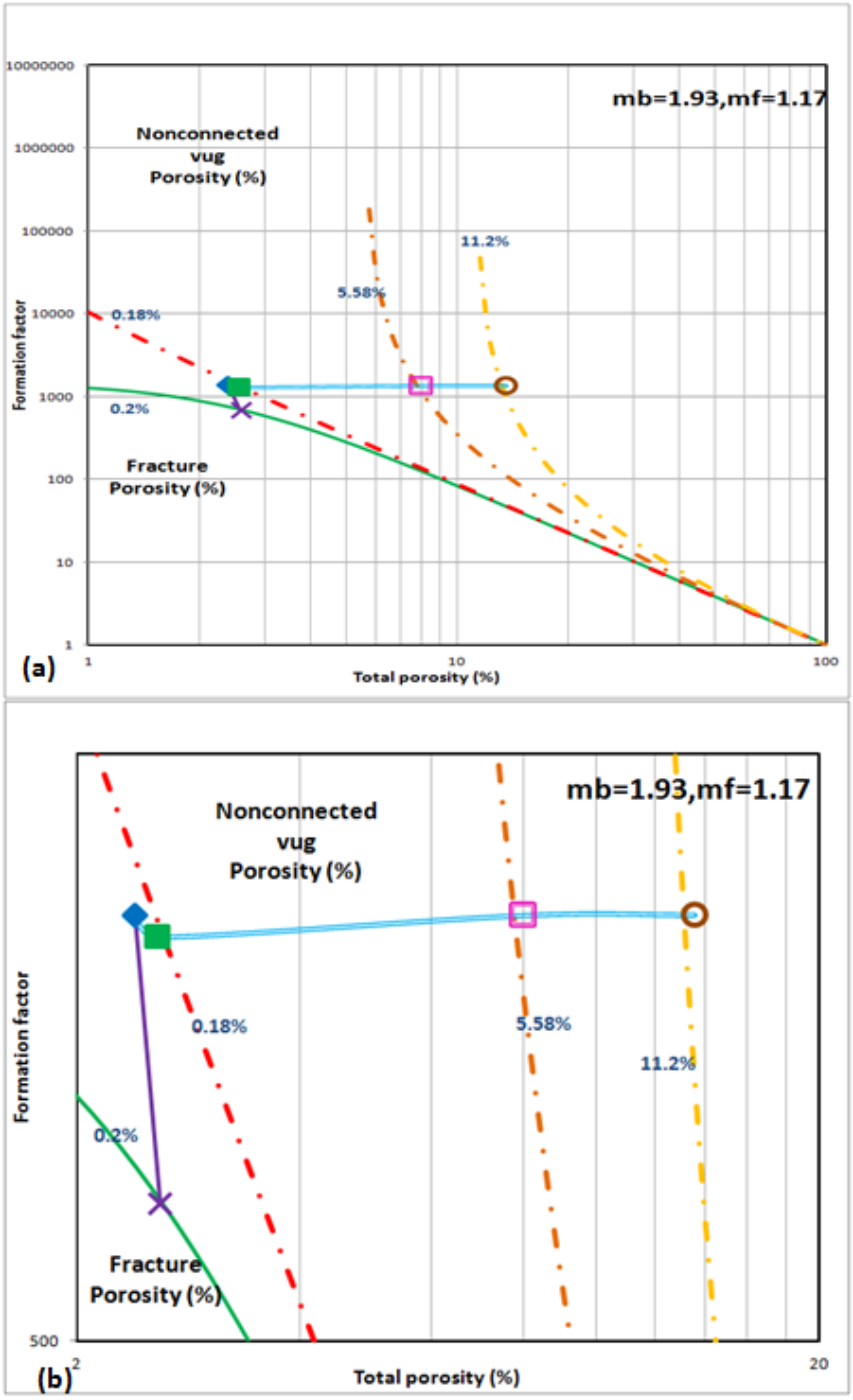

Figure 4.16: The Formation Factor (FF) of the IG, IG+FT and IG+VG models in the published work (Aguilera and Aguilera, 2003[5]). In their work, the porosity exponent of the IG is expressed by m_b and the porosity exponent of the FT is m_f. (b) is the expanded image of (a).

4.4 Effect of Pore Types on Porosity Exponent Based on Rock Models

This section builds pore types by grain pack models and applies these models to investigate the effect of pore types on the porosity exponent, anisotropy and Formation Factor (FF). The porosity exponent and FF are simulated by FD based on these pore

type models. These two pore types can be generated by grain pack (showing three kinds of pictures for models, grain pack, pore trap and Pore network, PNW, for IG IG+FT, IG+VG). In this section,

- Generation of IG, FT, VG models (4.4.1);
- Generation of IG+FT, IG+VG models (4.4.2);
- The pore type effect on the porosity exponent in FT percolation direction based on these models can be shown by comparison with the tested work of Aguilera and Aguilera (2003[5]). And their effect on the porosity exponent for the models of IG+FT, IG+CVG and IG+IVG is illustrated in section (4.4.3).
- Meanwhile, the effect of the pore types on the Formation Factor (FF) in FT percolation direction can be shown in this process (4.4.4). Their effect can be illustrated by their contribution to current flow (4.4.5)
- For the porosity exponent in three directions, the effect of pore types on the anisotropy is investigated (4.4.6).

4.4.1 Representation of the IG, FT and VG

This section introduces how to represents the IG, FT and VG by the models based on grain pack. The IG model is taken the pore space of Fontainebleau sandstone termed as Fb13 (SC200) as input shown in Figure 4.17.

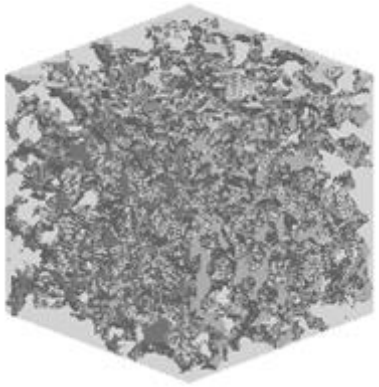

Figure 4.17: IG pore space represented by the pore space of the Fontainebleau sandstone Fb13 (SC200) with the porosity as 13%. The pore type in this kind of sandstone is typically IG.

The FT, VG can be generated based on the method introduced by Mousavi *et al.* (2012 [139]). This method is to generate fracture with rough surface from the random grain pack by randomly removing the grains in a randomly chosen sub volume in the pack shown in Figure 4.18. The VG can be simulated by randomly choosing the grains

in the pack and then directly taking these chosen grains as vuggy pores. When these vuggy pores are mixed with the IG pore space, these vuggy pores represent the connected vug (CVG). While the grains keep an outside matrix layer surrounded itself with regarding of the inside space as a vug pore, the vuggy space is isolated (not connected) vug (IVG). The related processes can be shown in Figure 4.19. When the chosen grain totally converts into the pore space, the pore space may connect to the IG pore forming the CVG in Figure 4.19(a). If the outside layer of these chosen grain are matrix shown in Figure 4.19(b), the inside pore space of these grains never connect to the IG pores generating the IVG. The IG, FT and VG can be simulated by related methods shown in Figure 4.20. In the sections below, the models for the IG+FT and IG+VG including IG+CVG as well as IG+IVG are firstly generated and then their effect on the porosity exponent of the models can be studied.

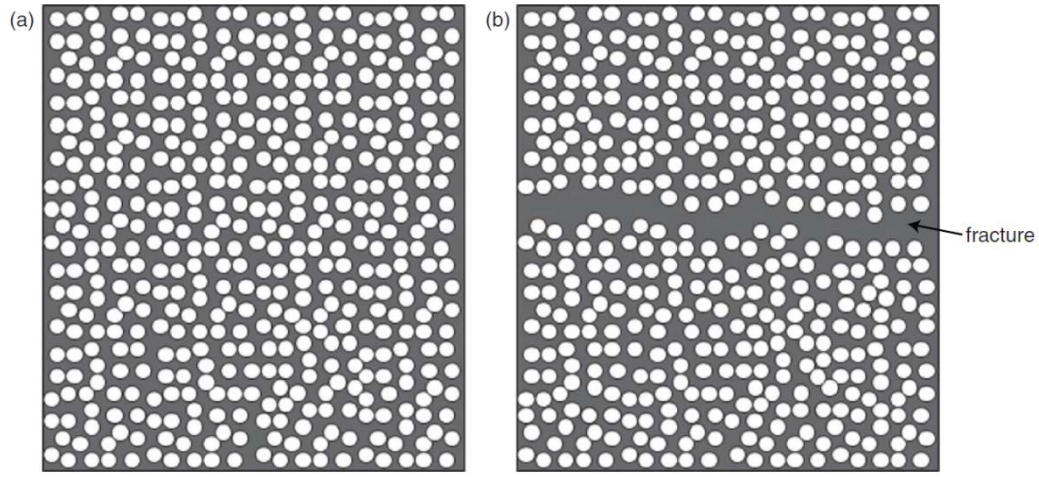

Figure 4.18: The process of the FT generation from the random grain pack. (a) is the small-grained packing and (b) is the FT generated by the same pack. Grey is pore space and white is grain (after Mousavi *et al.*, 2012[139]).

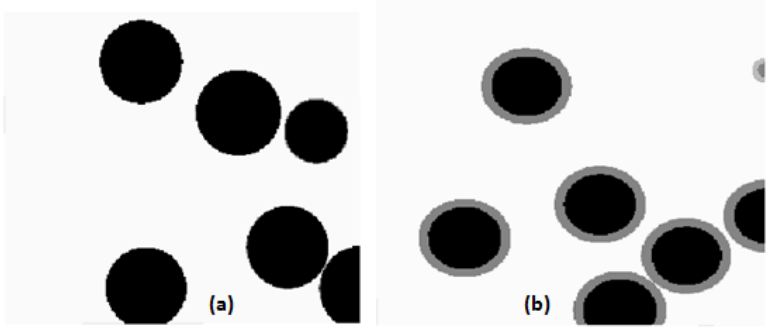

Figure 4.19: The process of the generation of the CVG (a) and IVG (b). The grains in black and grey are the chosen ones converted into VG with the white being the pore space. The black in the grain totally becomes pore space while the grey part is still as matrix.

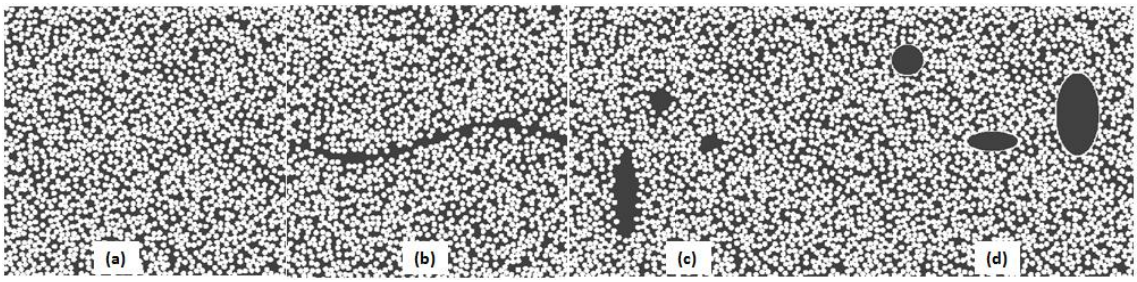

Figure 4.20: The process of the IG (a), FT (b), CVG (c) and IVG (d) generation from the random grain pack. The black is pore space and white is grain

4.4.2 Generation the Models for IG+FT and IG+VG

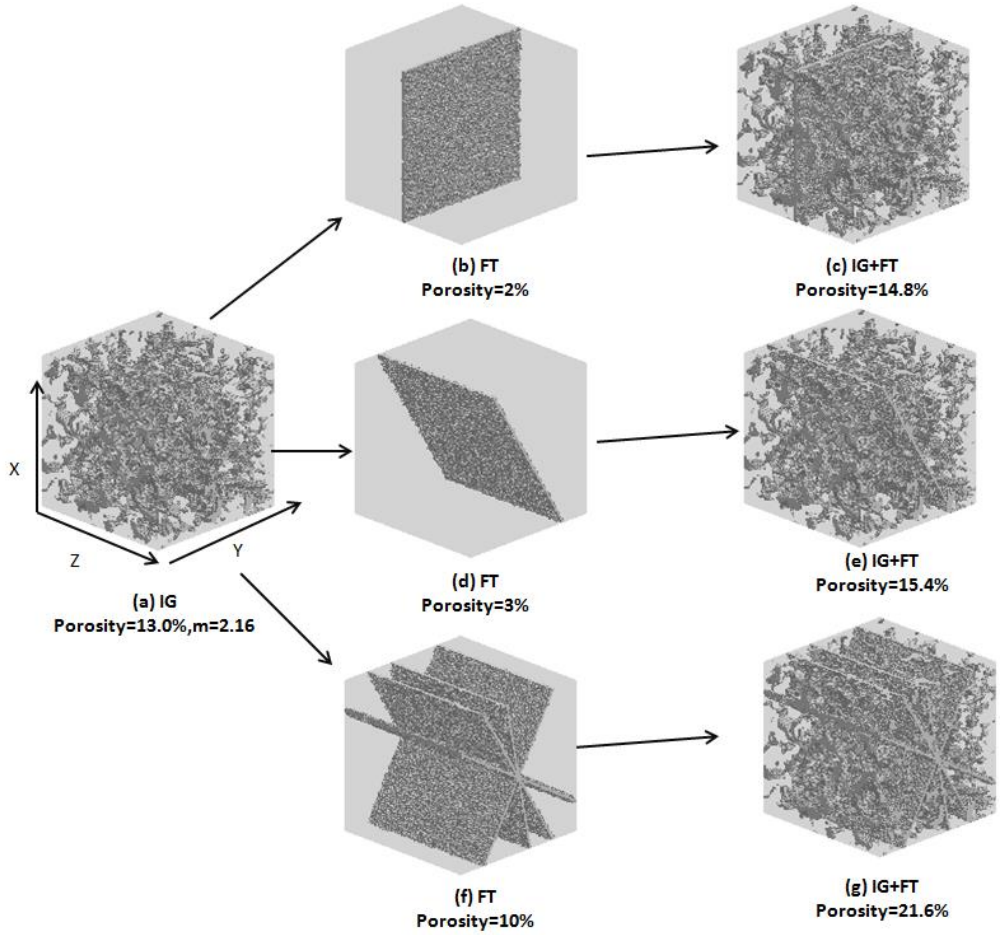

Figure 4.21: The models of IG+FT (c), (e) and (g) are built by combination of the IG (a) and FT (b), (d) and (f).

This section describes the process to build the models for IG+FT and IG+VG, these models take IG as host medium inserted by FT and VG model. The process of building the IG+FT model is shown in Figure 4.21. Considering the pore network visualization of Pet1, Pet4 and Pet6 in Figure 3.62, there are two kinds of VG in their pore system, one is larger pores with less numbers and the other one is small isolated pores with

numerous amounts. So for the IG+VG models, two kinds of VG models are built for each CVG and IVG, one model is large and less numerous and the other one is tiny and much numerous, to reflect their effect on GM and TP and then FF as well as porosity exponent. The process of building the IG+VG model for the tiny more numerous VG model is shown in Figure 4.22. The large VG model with less numbers is shown in Figure 4.23. Based on these models, the porosity exponents of these models can be shown in next section.

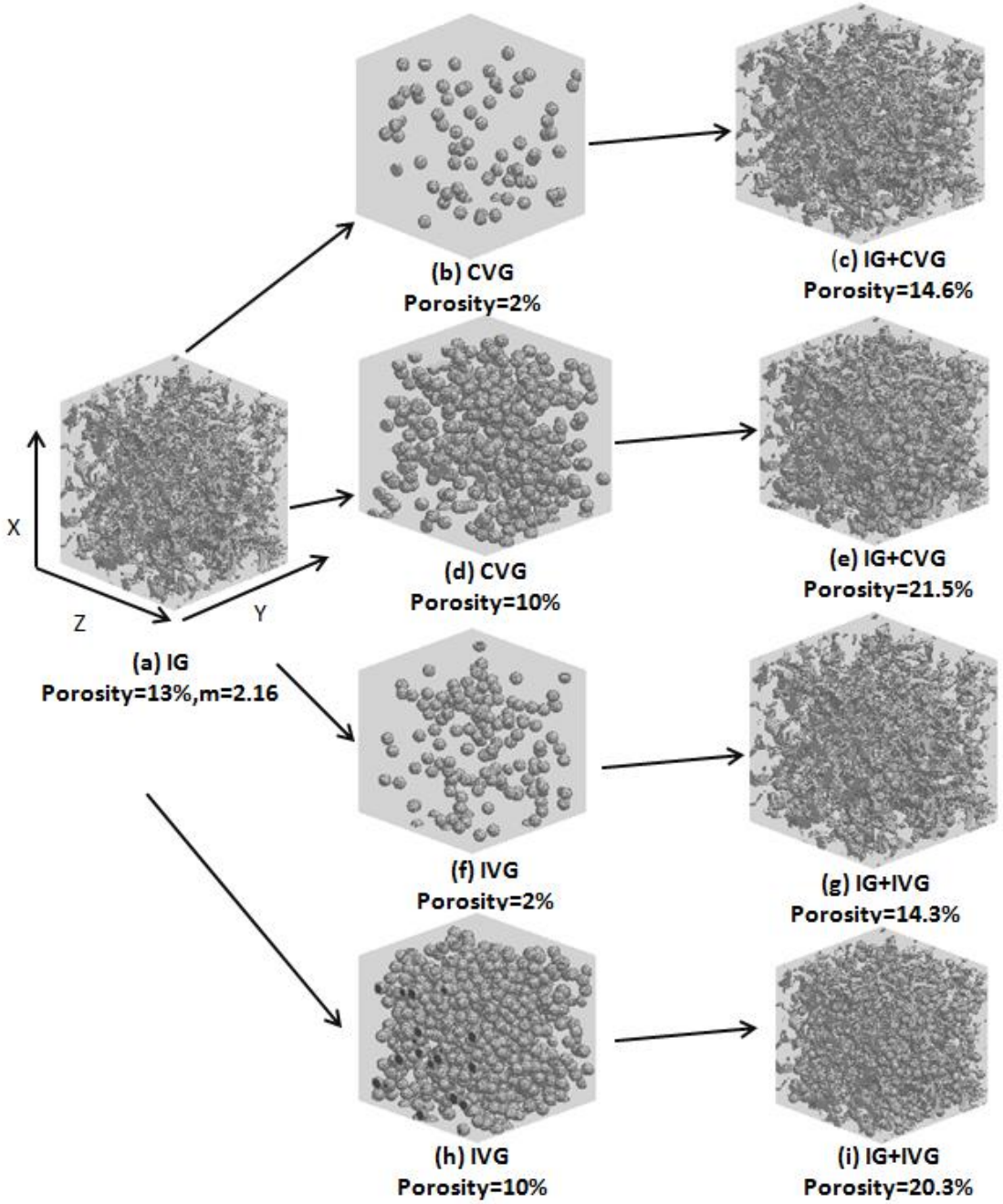

Figure 4.22: The IG+VG models including IG+CVG (c), (e) and IG+IVG (g), (i) are built by combination of the IG (a) and VG with (b), (d) for CVG and (f), (h) for IVG. For these IG+VG models, the VG is small size with numerous amounts.

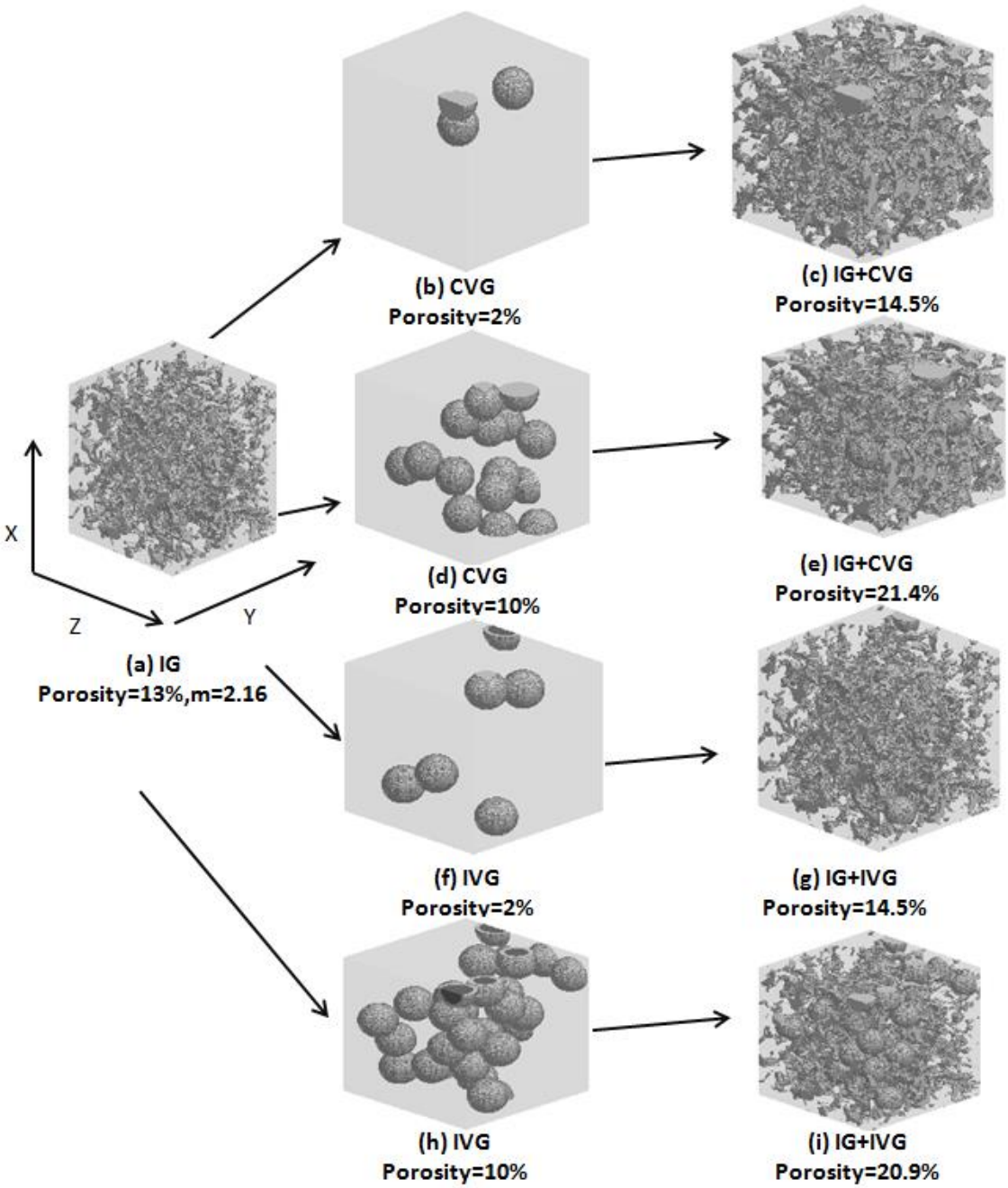

Figure 4.23: The IG+VG models including IG+CVG for (c), (e) and IG+IVG for (g), (i) are built by combination of the IG (a) and VG consisting of CVG (b), (d) and IVG (f), (h). For these IG+VG models, the VG is large size with less numbers.

4.4.3 Pore Type Effect on the Porosity Exponent

In this section, the porosity exponent of the IG+FT models in the one FT percolation direction and the porosity exponent in the same direction for the IG+VG models are shown in Figure 4.24 with the published work of Aguilera and Aguilera (2003[5]), which has been validated by the simple tube models. It is clear in Figure 4.24 that the effect of the FT lies in the decrease of the porosity exponent while the effect of

the tiny more numerous VG lies in increase of the porosity exponent. The same effect of the FT and the large less numerous VG on porosity exponent is shown in Figure 4.25.

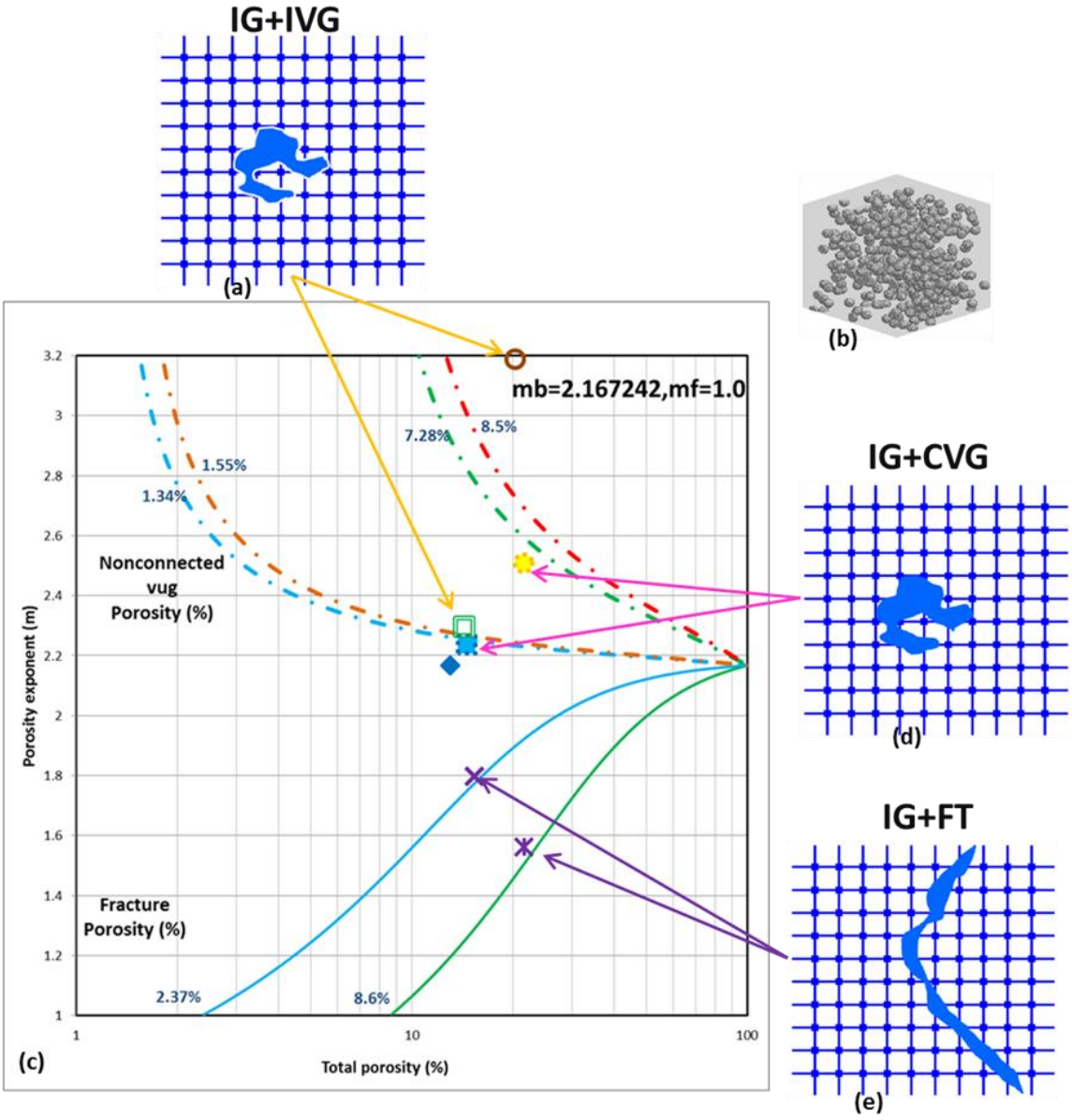

Figure 4.24: The porosity exponent for IG (filled blue diamond), IG+FT (purple cross), IG+CVG (filled makers with dotted maker line), IG+IVG (unfilled makers) for the VG model with small size and numerous numbers shown in (b). The porosity exponent of the IG is m_b=2.16 and the porosity exponent for FT is m_f=1.0 for Aguilera and Aguilera (2003[5]) theoretical model.

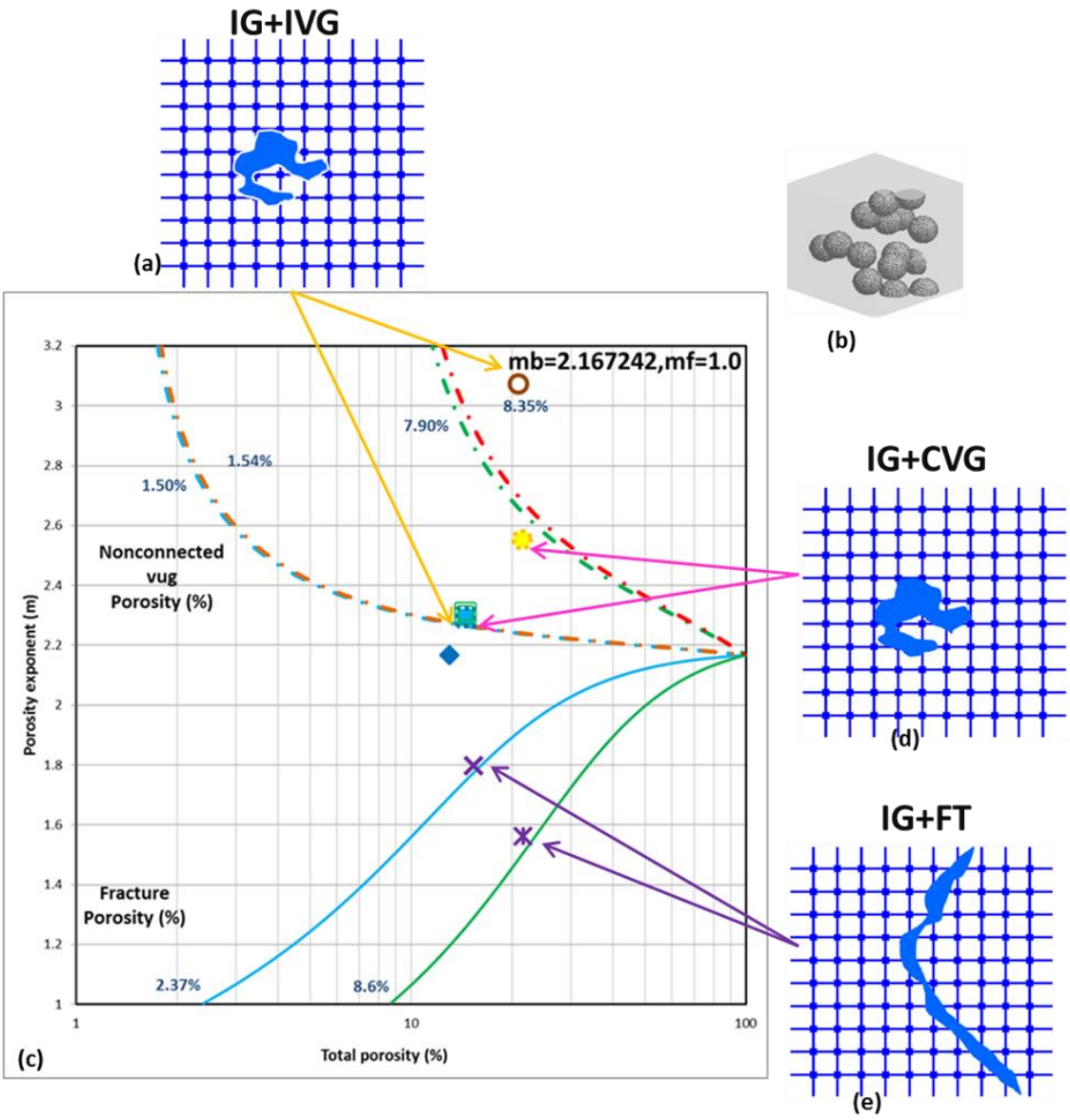

Figure 4.25: The porosity exponent for IG (filled blue diamond), IG+FT (purple cross), IG+CVG (filled makers with dotted maker line), IG+IVG (unfilled makers) for the VG model with large size and less numbers shown in the top right corner. The porosity exponent of the IG is m_b=2.16 and the porosity exponent for FT is m_f=1.0 for Aguilera and Aguilera (2003[5]) theoretical model.

From Figure 4.24 and Figure 4.25, Firstly, it is clear that the porosity exponent of the IVG is larger than the porosity exponent of the CVG (This is can be explained by their contribution to the current flow in Figure 4.30, the current flow distribution in the IG+CVG and IV+IVG , the CVG can offer the current flow path while IVG is meaningless for the current flow just increase the total porosity) and the porosity exponent of the IG+IVG models with small size and numerous numbers in Figure 4.24 is larger than the porosity exponent for the IG+ IVG models with large size and less numbers (this can be explained by their effect on the GM+TP in discussion and then on

the resistivity and porosity exponent). Based on that, the *IVG can have a stronger effect on the porosity exponent compared with the effect of the CVG especially for the IVG with small size and large numbers*.

Secondly, the porosity exponents of the IG+FT model still match the theoretical results while the porosity exponents of the IG+VG models are different from their results. This is due to the fact that the IG+FT model can still satisfy the IG and FT in parallel resistance network while for the IG+VG models, CVG and IVG are inserted into the IG, the VG and IG are not the simple resistance circuit in series just shown in Figure 4.26 by pore trap and channel model.

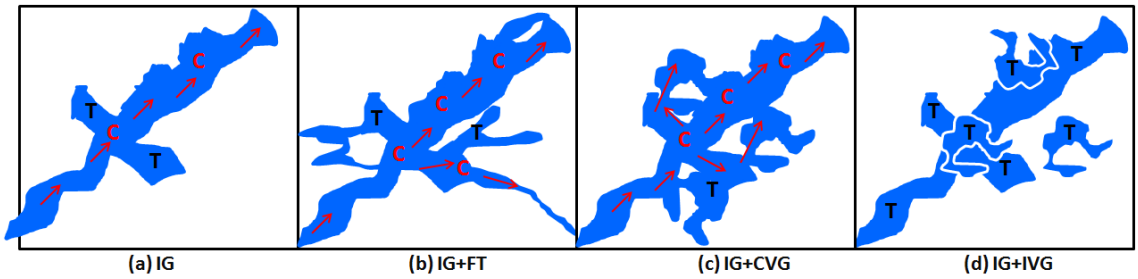

Figure 4.26: Pore trap and channel schematic for IG (a), IG+FT (b), IG+CVG (c) and IG+IVG (d) models.

In this figure, for the IG+FT model, the FT and IG can satisfy the parallel arrangement while the CVG and IVG dramatically affect the IG pore system, their arrangement in resistance network are not simple in series (in Figure 4.15c) resulting in the difference between the simulated porosity exponent and their theoretical data.

The porosity exponent is calculated by the Formation Factor (FF) reflecting the resistivity, R_0, of the 100% brine saturated rock samples and the total porosity, ϕ, according to Archie Law, $FF = R_0/R_w = 1/\phi^m$ in Equation (1.1) and Equation (2.32). The pore type effect on the FF is useful for understanding their contribution to FF and the total porosity to the porosity exponent.

4.4.4 Pore Type Effect on the Formation Factor (FF)

This section presents the effect of the pore types on the Formation Factor (FF) in the same FT percolation direction for IG+FT and IG+VG compared with the published work of Aguilera and Aguilera (2003[5]). Figure 4.27 presents the FF for the IG+FT and the IG+VG with the tiny more numerous VG. Figure 4.28 presents the FF for the IG+FT and the IG+VG with the large less numerous VG. From Figure 4.27 and Figure 4.28, the effect of the FT on the FF is decrease, which is the same for both, that is, FT

contributes to the current flow and then reduces the resistivity, R_0. As a result, FF as the ratio of the R_0 to the constant water resistivity, R_w, reduces. The CVG effect on the FF lies in the decrease shown in the dotted pink line with filled square and circle makers while the contribution of the IVG to the FF is increase shown in the filled green line with unfilled square and circle markers in both Figures. The difference between the two figures can be shown by the arrows in Figure 4.28, the FF of the large less numerous IVG (unfilled circle) + IG model is less than that for the tiny more numerous IVG + IG model in Figure 4.27. The effect of FT, CVG and IVG on the FF can be to the illustrated by their contribution to the current flow in the next section.

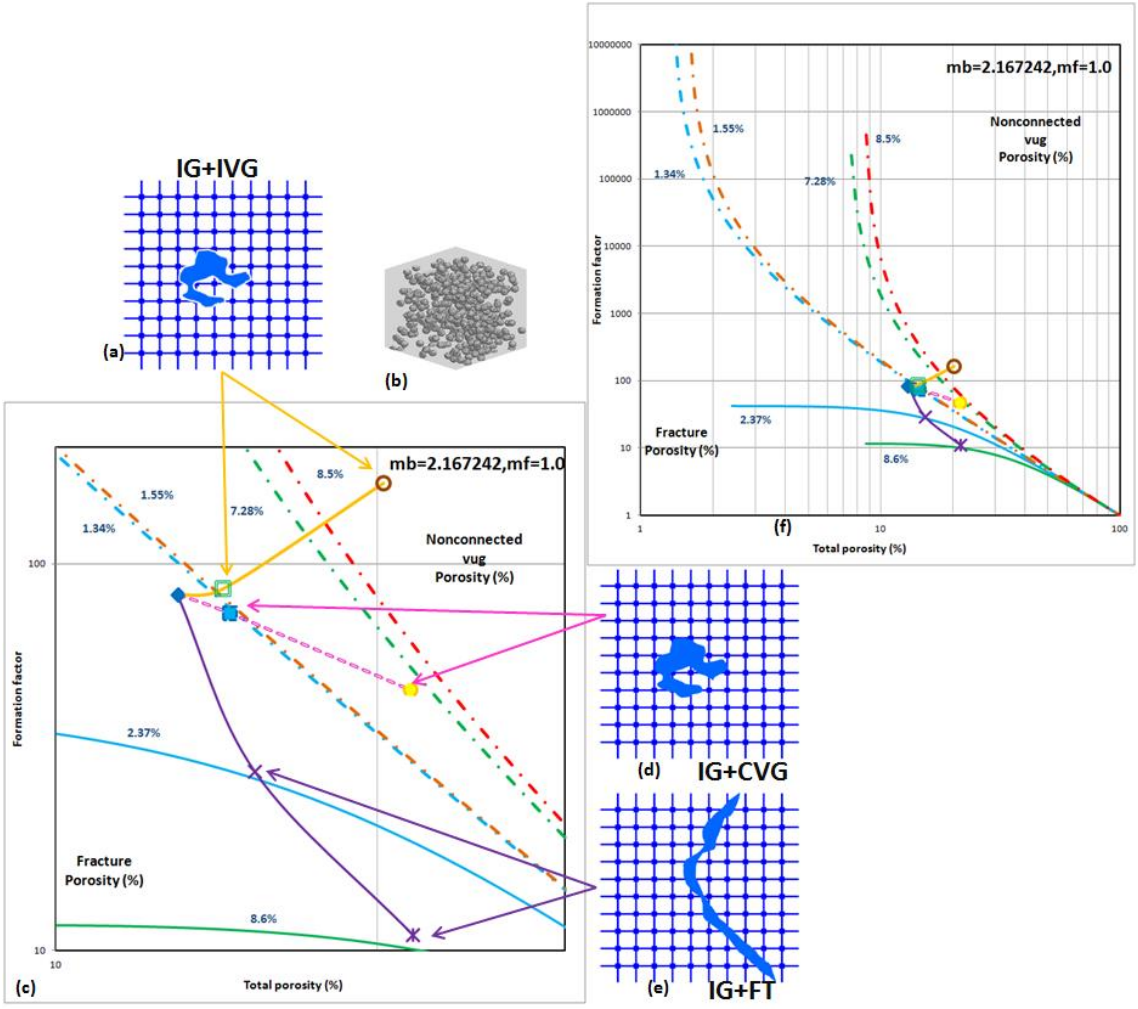

Figure 4.27: The Formation Factor (FF) for the IG (blue filled diamond), IG+FT (purple cross), IG+CVG (filled maker with dotted maker line) and IG+IVG (unfilled maker) models. The VG (b) in this figure is numerous with tiny size. (c) is the expanded of the (f) with consideration the theoretical FF from Aguilera and Aguilera (2003[5]) with m_b=2.16 for IG, m_f=1.0 for FT. The porosity exponent for the same porosity possibilities are in coloured line and dotted line.

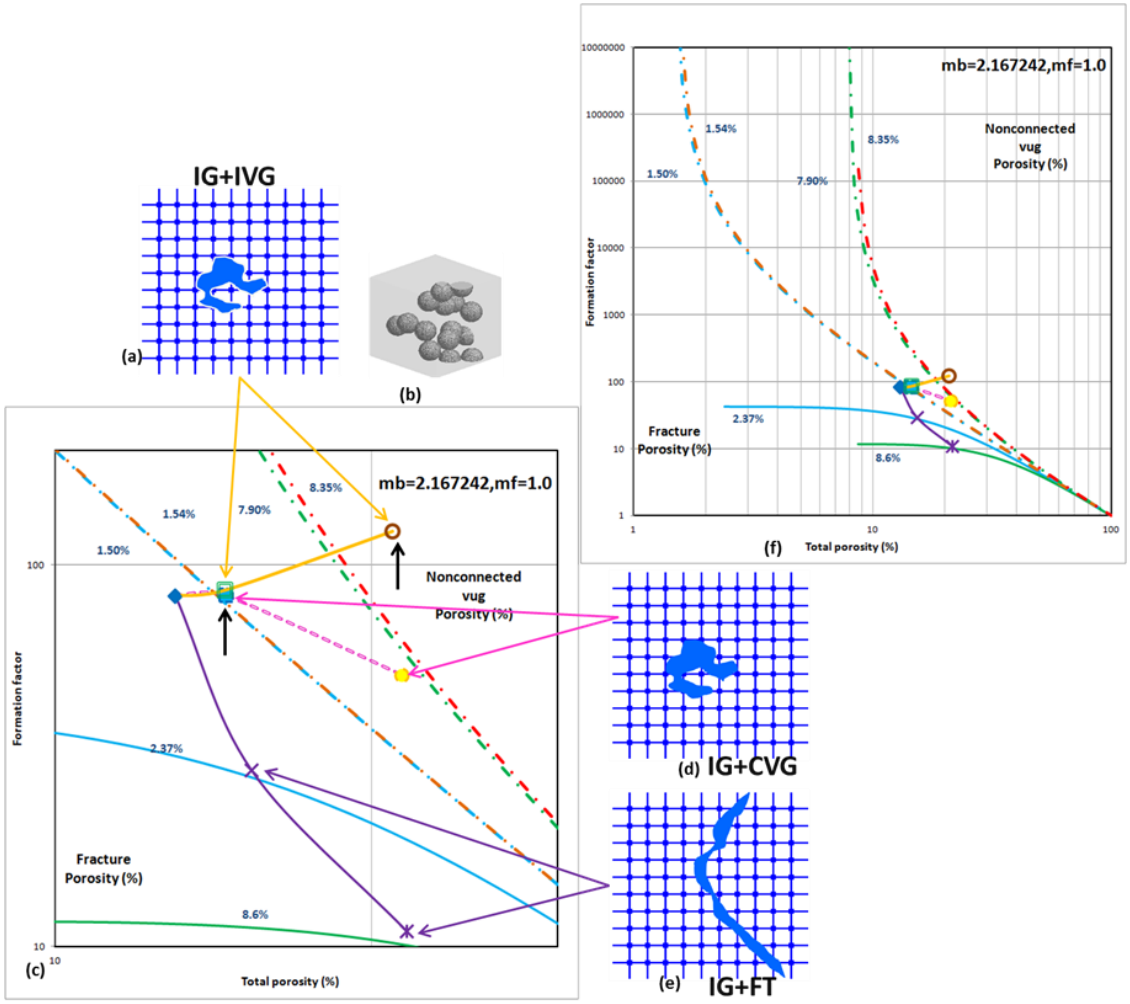

Figure 4.28: The Formation Factor (FF) for the IG (blue filled diamond), IG+FT (purple cross), IG+CVG (filled maker with dotted maker line) and IG+IVG (unfilled maker) models. The VG (b) in this figure is large size with less number. The (c) is the expanded of the (f) with consideration of the theoretical FF from Aguilera and Aguilera (2003[5]), with m_b=2.16 for IG, m_f=1.0 for FT and the FF for the same porosity possibilities are in coloured line and dotted line.

4.4.5 Contribution of the FT, IVG and CVG to Electrical Current

This section illustrates contribution of pore types to the current flow by the current density distribution in the FT percolating directions in Figure 4.29. From the current density distribution, it is clear that the FT is the main current flow path by the red colour resulting in the decrease of the resistivity and FF. The CVG effect on the FF lies in the decrease while the contribution of the IVG to the FF is increase. Their different contribution to the FF (or R_0) can be shown by their current density distribution in Figure 4.30.

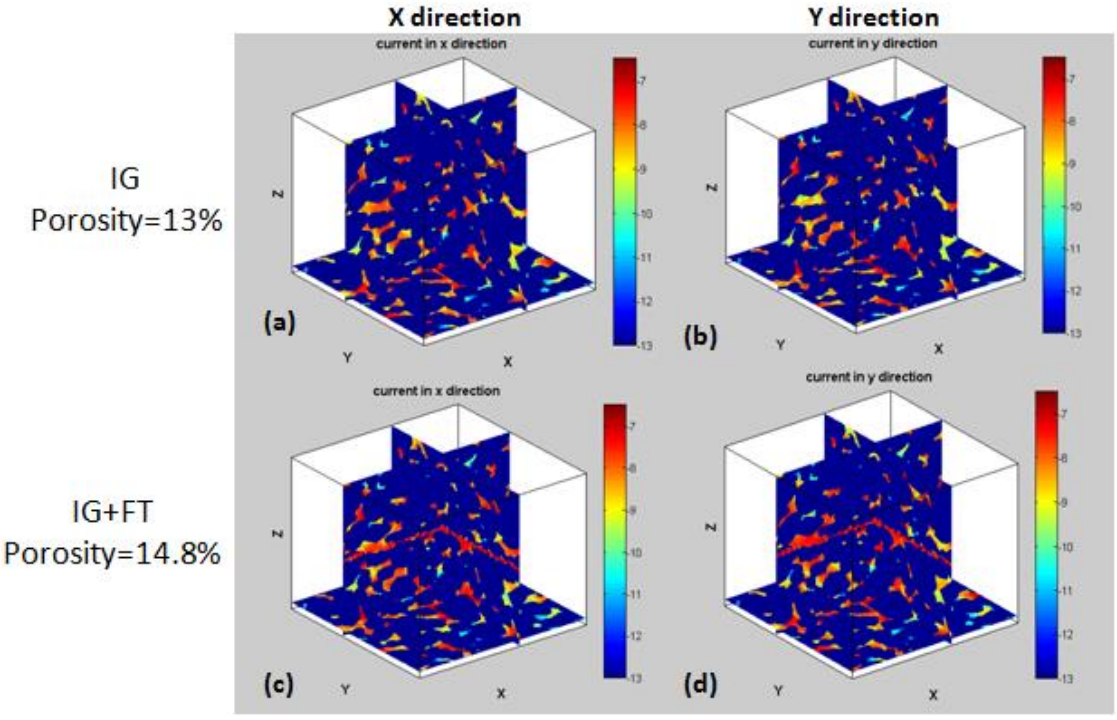

Figure 4.29: The current density distribution for IG (a), (b) and IG+FT (c), (d) in FT percolating directions. The legend is the magnitude by the logarithm of the current density from -13 to -7.

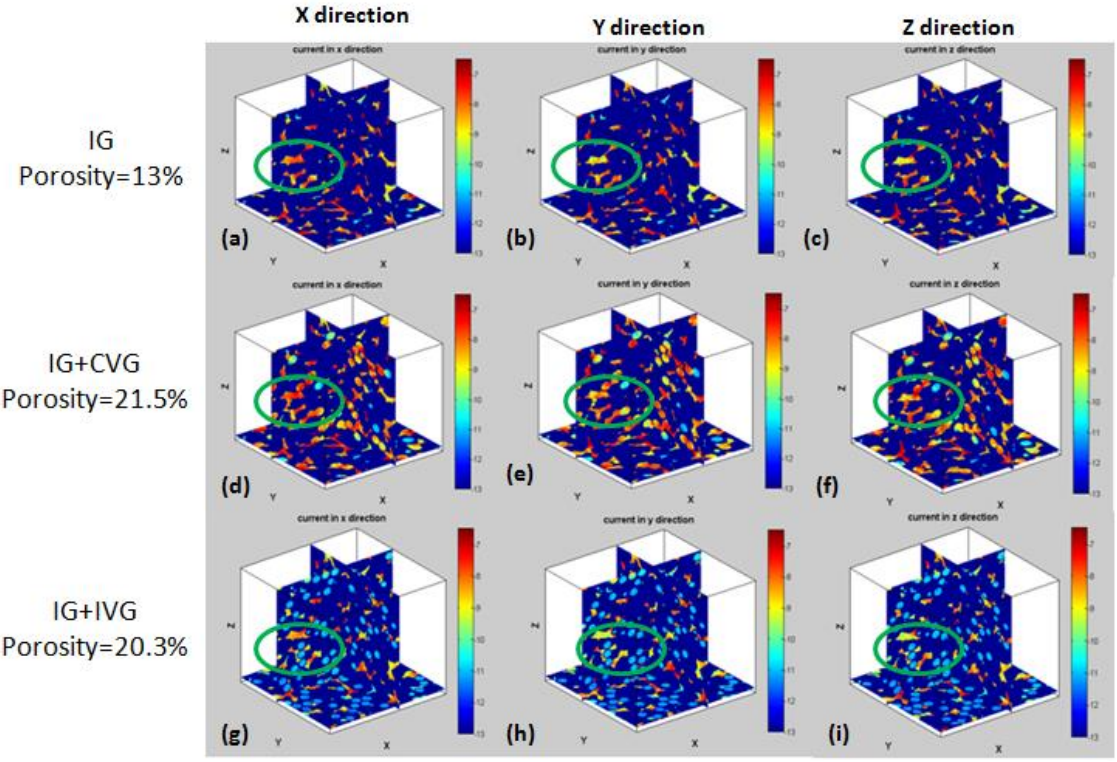

Figure 4.30: The current density distribution for IG (a), (b), (c), IG+CVG (d), (e), (f) and IG+IVG (g), (h), (i) for the VG with tiny size and large numbers in three directions. The legend is the magnitude by the logarithm of the current density from -13 to -7. Green circle discussed in text.

From the current density distribution, it is clear that CVG can contribute to the current flow and most of CVG space is colourful and the density of the original IG pore space (in green circle in a, b, and c) in IG+CVG model become larger by their colour towards red in Figure 4.30 (d), (e) and (f) While the colour of the IVG space is blue without contribution to the current flow and the current density in the IG pore space (green circle) in the IG+IVG model in Figure 4.30 (g), (h) and (i) becomes less by the colour turning toward blue compared with its colour in IG in first row (green circle).

The effect of the pore type on the FF can be illustrated by their contribution to the electrical current in Figure 4.29 and Figure 4.30. Whilst how the effect on the FF cannot been thoroughly explained by the current density distribution, this needs to consider the pore type effect on the pore geometry (GM) and topology (TP) which determine the FF and porosity exponent.

The FF is directly controlled by the pore geometry (GM) and topology (TP) which also affects the porosity exponent, the GM and TP for IG, IG+FT and IG+FT models need to be extracted to illustrate how the pore type affect the FF and *m* from their influence on GM and TP. The pore type effect on GM and TP is in section 4.5 and the pore type effect on FF and *m* by their influence on GM and PT is in section 4.6 to explain the results in the modelling.

While for this section, the FF and porosity exponent is just shown in the percolation direction. The porosity exponent in three directions for IG+FT, IG+CVG and IG+IVG compared with them for IG can reflect the pore type effect on the anisotropy of the porosity exponent in next section.

4.4.6 Pore Type Effect on the Anisotropy of the Porosity Exponent

This section calculates the anisotropy of the porosity exponent for different pore types. The porosity exponents in three directions for IG+FT as well as the anisotropy of the model are shown in Figure 4.31. The anisotropy is related to the squared ratio of the maximum to the minimum of the porosity exponents in three directions, $\sqrt{m_{\max}/m_{\min}}$ (in Equation 2.33). In Figure 4.31 (a), the porosity exponent in x direction for IG is less than that in y and z direction, m_x reduces from IG to IG+FT (total porosity=14.8%) due to the FT percolation in this direction while m_z increases from IG to IG+FT (total porosity=14.8%) in the non-percolation direction. For IG+FT (total porosity=15.4%) and IG+FT (total porosity=21.6%), the main percolation direction is z, m_z reduces from

2.2 to 1.8 and then to 1.6. while m_y in non-percolated direction firstly keeps 2.0 stable and then increases to 2.2. it is clear that in the percolation direction, FT reduces the porosity exponent. The anisotropy of the porosity exponent for IG+FT is the Figure 4.31: The porosity exponent in three directions (a) and its anisotropy coefficient (b) for IG+FT compared with IG. (b), the anisotropy of the IG is 1.10 while the anisotropy for IG+FT ranges from 1.12 to 1.40. FT causes the anisotropy of the porosity exponent.

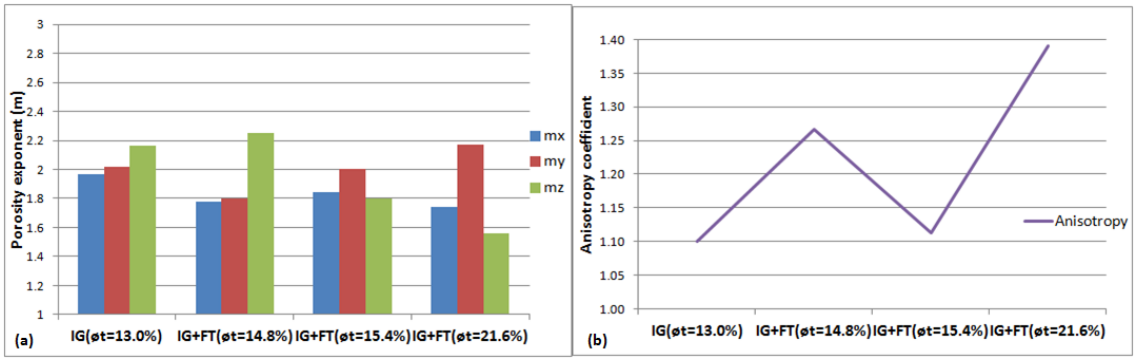

Figure 4.31: The porosity exponent in three directions (a) and its anisotropy coefficient (b) for IG+FT compared with IG.

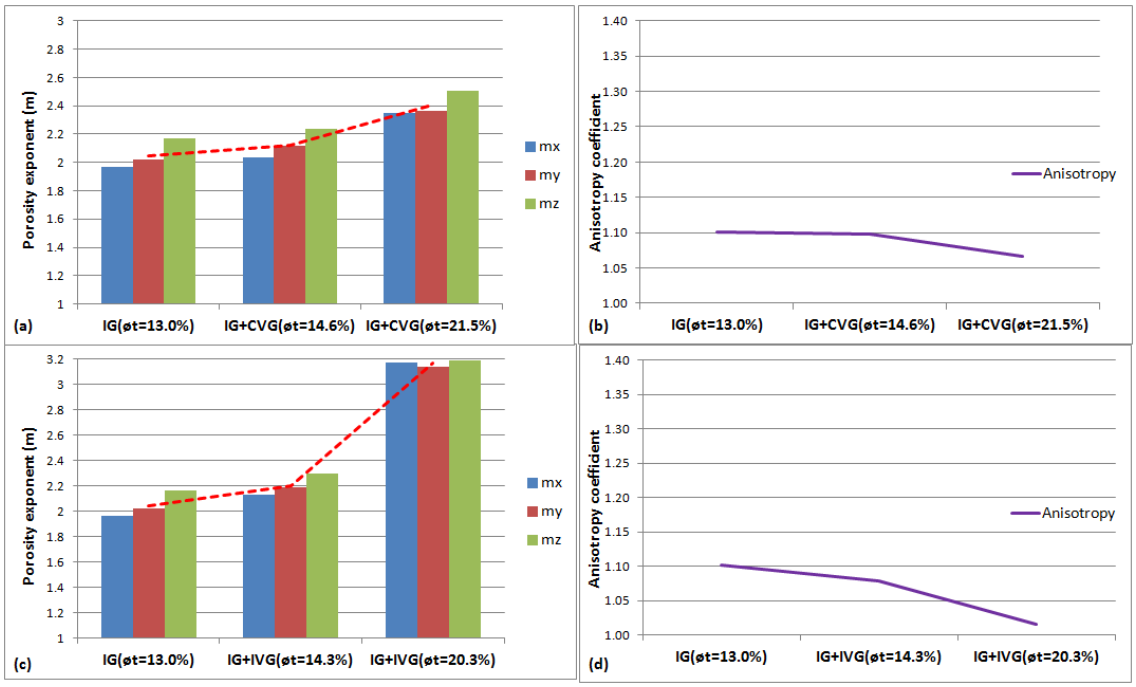

Figure 4.32: The porosity exponent in three directions (a) and (c), its average (red dotted line)as well as anisotropy(b) and (d) for IG+CVG (a), (b) and IG+IVG(c), (d) for the tiny VG with large numbers.

The porosity exponents in three directions as well as the anisotropy for IG+CVG and IV+IVG for the tiny more numerous VG are show in Figure 4.32. From the Figure 4.32 (a) and (c), the VG effect on the porosity exponent lies in the increase. For CVG in (a), the average porosity exponent increases from 2.0 to 2.1 and then to 2.4 with the

porosity ranging from 13.0% to 14.6% and then to 21.5%. For IVG in (c), the average porosity exponent increases from 2.0 to 2.2 and then to 3.2 when the porosity increases from 13.0%, to 14.3% and then to 20.3%. The effect of the IVG on the porosity exponent is much stronger than the influence of the CVG. The anisotropy of the IG, IG+CVG and IG+IVG is shown in the Figure 4.32 (b) and (d). It is clear that the anisotropy for IG+CVG (b), 1.06, and IG+IVG (d), 1.02, with porosity larger than 20% is lower than the anisotropy of the IG, about 1.10.

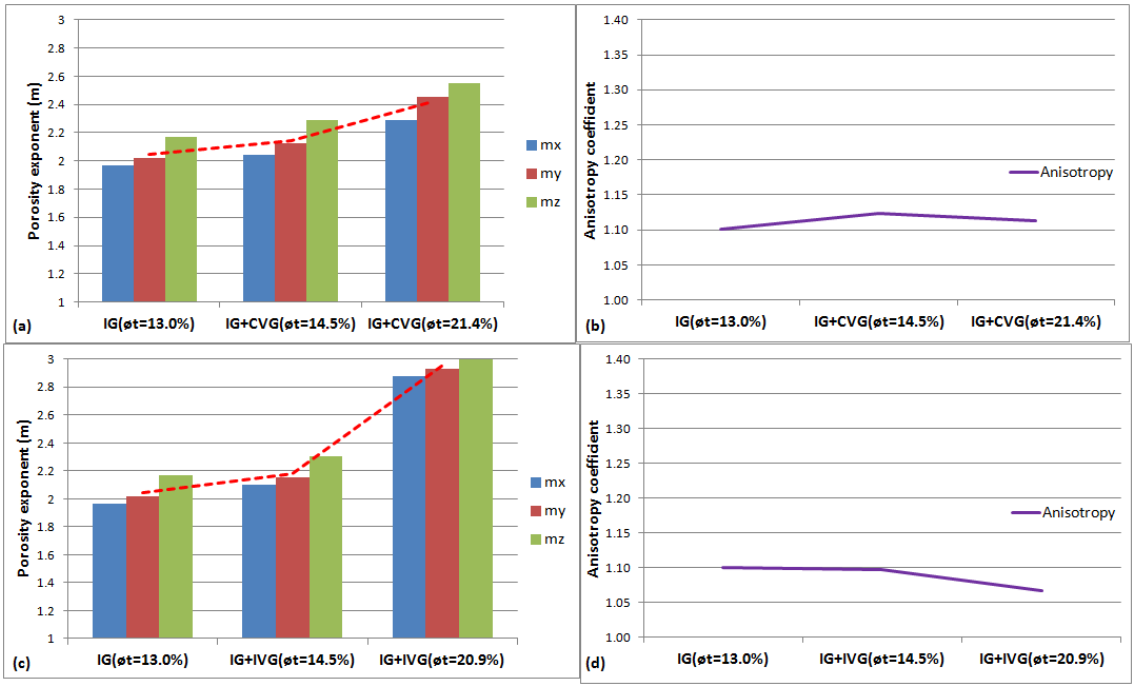

Figure 4.33: The porosity exponent in three directions (a) and (c), its average (red dotted line) as well as anisotropy (b) and (d) for IG+CVG (a),(b) and IG+IVG (c), (d) for the large VG with less numbers.

The porosity exponents in three directions as well as the anisotropy for IG+CVG and IV+IVG for the large and less numerous VG model are shown in Figure 4.33. From the Figure 4.33 (a) and (c), the VG effect on the porosity exponent lies in the increase. For CVG in (a), the average porosity exponent increases from 2.0 to 2.1 and then to 2.4 with the porosity from 13.0% to 14.5% and then 21.4%, which is the same as the porosity variation in Figure 4.32 (a) for the tiny CVG with numerous numbers. For IVG in (c), the average porosity exponent increases from 2.0 to 2.1 and then to 2.9 when the porosity increases from 13.0%, to 14.5% and then to 20.9%, the increase of the porosity exponent is less compared with the fluctuation in Figure 4.32 (c) for the tiny IVG with numerous numbers. The effect of the IVG on the porosity exponent is much stronger than the influence of the CVG, which is suitable for both kinds of VG in Figure 4.32 and Figure 4.33. The anisotropy of the IG, IG+CVG and IG+IVG is in the Figure 4.33

(b) and (d). It is clear that the anisotropy for IG+CVG in (b), 1.11, and IG+IVG in (d), 1.06, with porosity larger than 20% close to the anisotropy of the IG, about 1.10.

Based on Figure 4.31, Figure 4.32, and Figure 4.33, FT can dramatically cause the anisotropy of the porosity exponent while the VG effect on the anisotropy of the porosity exponent is minimal and prone to reduce the anisotropy. The impact of the FT on the anisotropy of the porosity exponent can be illustrated by the current density distribution in three directions in Figure 4.34. It is obvious that in the percolation directions of the FT, x and y, the colour in the FT (d) and (e) is red while the colour in the FT for the non-percolation direction (f) is orange reflecting that the contribution of the FT to the current flow in the percolation directions is larger than its contribution in the non-percolation direction resulting in great variation of the porosity exponent in different directions, that is, anisotropy.

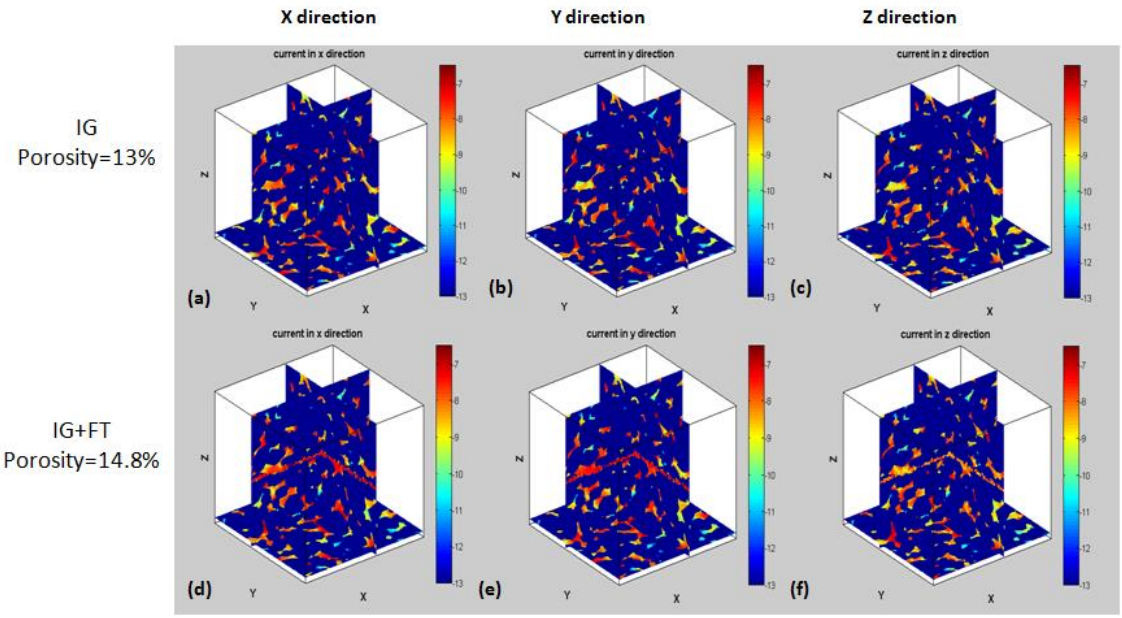

Figure 4.34: The current density distribution for IG (a), (b), (c) and IG+FT (d), (e), (f).

In this section, the pore type effect on the porosity exponent, Formation Factor (FF) in the percolation direction of the FT and anisotropy of the porosity exponent had been investigated.

FT causes the decrease of the porosity exponent and FF as well as anisotropy; CVG increases the porosity exponent while decreases the FF; IVG increases the porosity exponent and FF. The effect of IVG on the porosity exponent is larger than the effect of CVG. The impact of the VG including CVG and IVG on the anisotropy lies in the decrease which is minimal.

The porosity exponent and FF are related to the geometry (GM) and topology (TP) of the pore system, the pore type effect on the porosity exponent and FF depending on their influence on the GM and TP. Knowing the pore type effect on the GM and TP is helpful to understand how the pore type affect the FF and *m*. The next section is to introduce the effect of the pore type effect of GM and TP based on the above IG, IG+FT, IG+CVG and IG+IVG models.

4.5 Pore Type Effect on GM and TP

In this section, the pore type effect on GM and TP is reflected by the characteristics of GM and TP for each pore type. The GM including the radius, shape factor of the pore and throat, pore-throat cross sectional area ratio (PTAR) and tortuosity and TP consisting of coordination number and Euler number for IG+FT, IG+CVG and IG+IVG are presented taken these properties of IG as comparison.

The obvious GM and PT properties for each model can be reflected by their pore network visualization in 3D with the help of Rhinoceros (https://www.rhino3d.com/download).

4.5.1 GM and TP of the IG+FT Model

This section presents the geometry and topology of the IG+FT model.

The radius of the pore and throat for IG+FT models are given in Figure 4.35. It is clear that the pore radius of the IG+FT decreases with the increase of the FT while the throat radius keeps stable. The shape factor of the pore and throat is shown in Figure 4.36. The decrease of the pore shape factor is obvious while the effect of FT on the shape factor of throat is trivial. From Figure 4.35 and Figure 4.36, FT mainly affects the pore body compared with its influence on throat. Its influence causes the irregularity of the pore with the decrease in the radius and shape factor of pore body.

From Figure 4.37, the FT effect on the PTAR is minimal although its influence on the pore radius is decrease. While FT brings the increase in the tortuosity which increases the porosity exponent based on the theoretical analysis in Section 4.1.1.

The TP includes the coordination number reflecting the number of the throat connected to a pore body and Euler number representing the connectivity of the pore system, the negative data indicates good connectivity compared with the positive value. It is clear that FT increases the coordination number in Figure 4.38(a), which is

discussed later, and the channels to enhance the connectivity of the pore system in Figure 4.38 (b). Based on GM and TP as well as the pore network 3D visualization in Figure 4.39, the effect of the *FT on GM lies in the decrease of the pore radius and shape factor increasing its irregularity and the increase of the tortuosity increasing the length of the current flow. Its influence on the TP is the improvement of the connectivity of the pore system by increasing the coordination number and reducing the Euler number*. There are two kinds to CVG based on its size and number. One CVG is tiny size and more numerous while the other CVG is large size and less numerous.

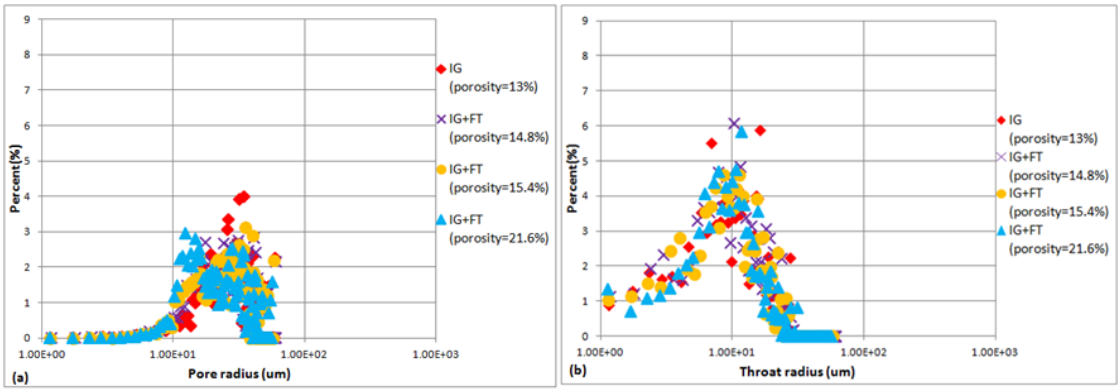

Figure 4.35: Pore radius (a) and throat radius (b) for the IG+FT models as well as IG.

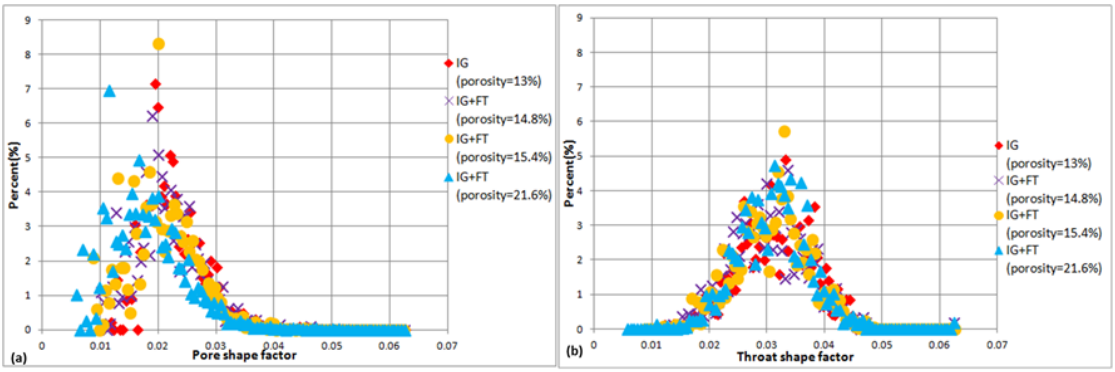

Figure 4.36: The shape factor of the pore (a) and throat (b) for IG+FT models and IG model.

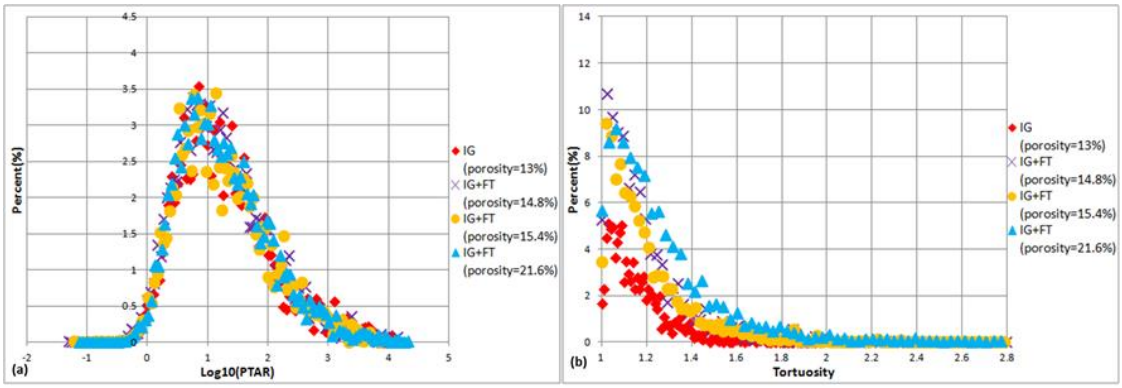

Figure 4.37: The pore throat cross sectional area ratio (PTAR) (a) and tortuosity (b) of the IG+FT models and IG model.

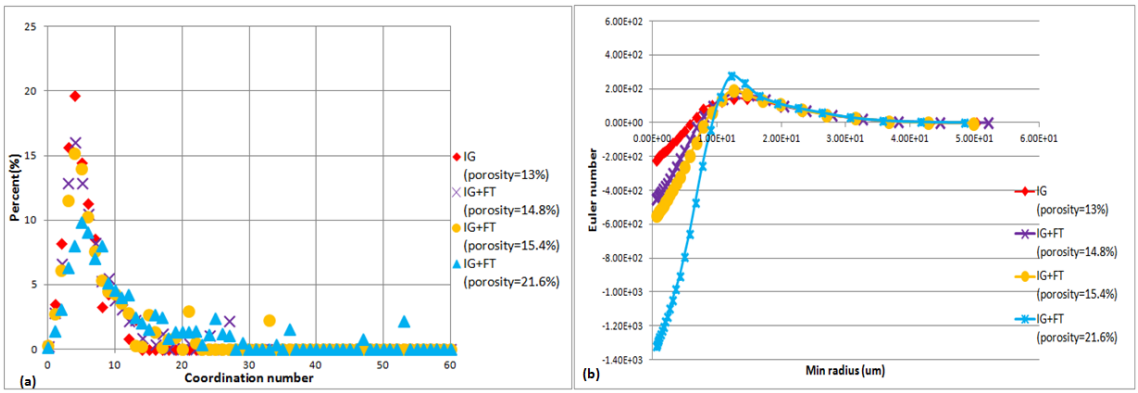

Figure 4.38: The coordination number (a) and Euler number (b) of the IG+FT models and IG model.

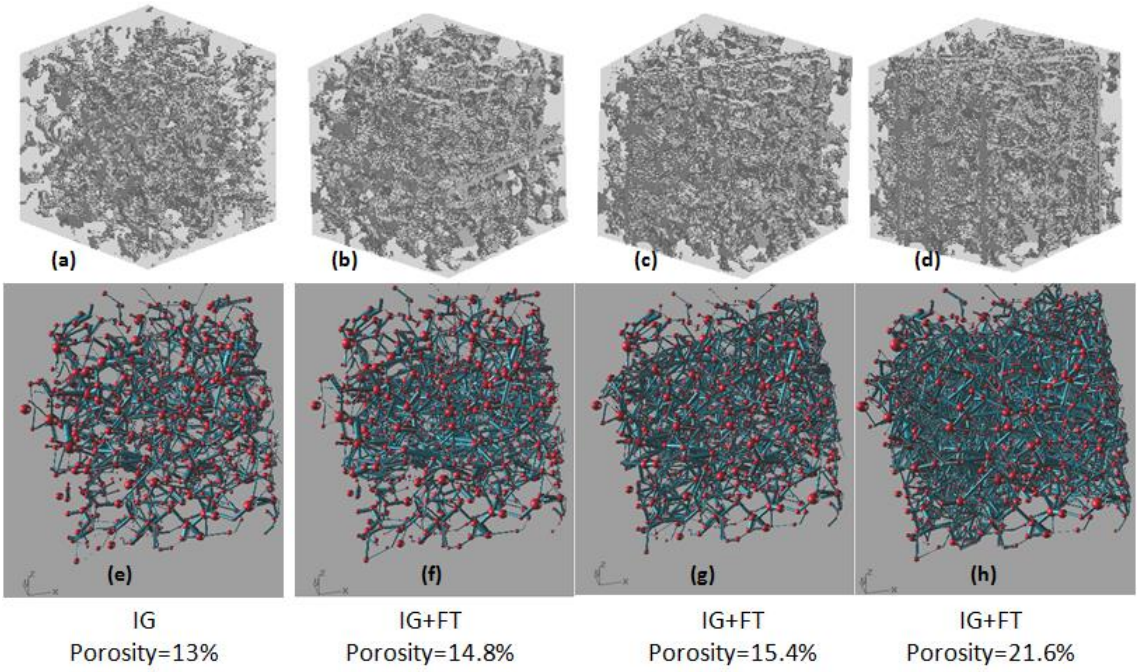

Figure 4.39: The pore network visualization for IG model (a), (e) and IG+FT models (b), (c), (d), (f), (g), (h).

4.5.2 GM and TP of the IG + Tiny CVG Models

This section shows the geometrical and topological properties of the IG+CVG models, the CVG is tiny and numerous.

It is clear that CVG increases the pore radius and pore shape factor in Figure 4.40 (a) and (c) reflecting the enhancement of the simplicity and regularity of the pore body with trivial impact on the throat in Figure 4.40 (b) and (d). CVG can increase the PTAR and tortuosity (Figure 4.41) both of which increase the porosity exponent according to the study in section 4.1.1 and section 4.1.2.

The TP is shown in Figure 4.42, it is clear that the influence of the CVG on the coordination number and Euler number is minimal *while its influence lies in improving the connectivity reflected by the trivial decrease of the Euler number* Figure 4.42 (b).

The visualization of the IG and IG+CVG models for the CVG with tiny size and numerous numbers is shown in Figure 4.43. From the 3D visualization, its increase on the pore radius and PTAR is clear.

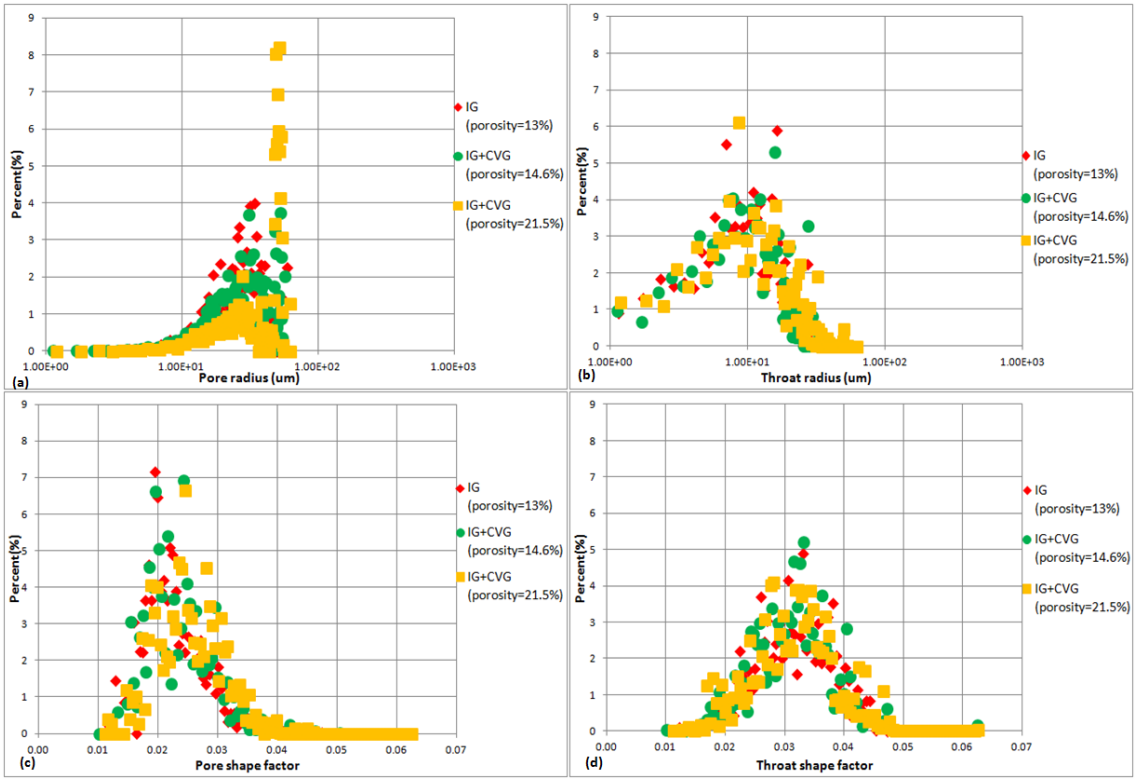

Figure 4.40: The radius and shape factor of the pore (a), (c) and throat (b), (d) for IG+CVG models as well as IG model.

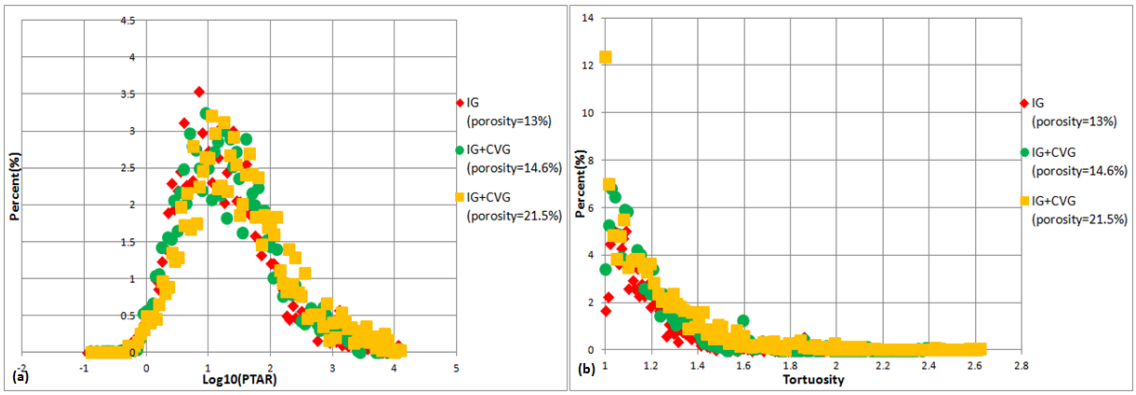

Figure 4.41: The pore throat cross sectional area ratio (PTAR) (a) and tortuosity (b) of the IG, IG+CVG models.

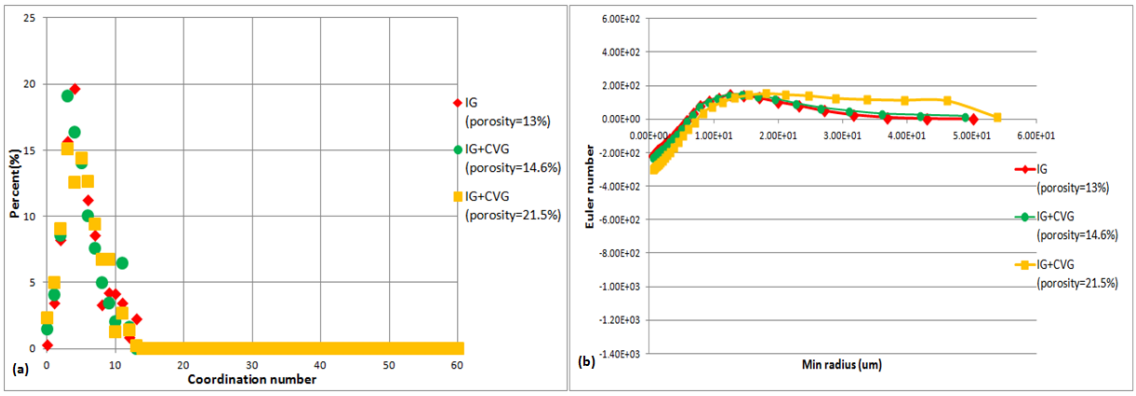

Figure 4.42: The coordination number (a) and Euler number (b) for IG and IG+CVG models with tiny and more numerous CVG.

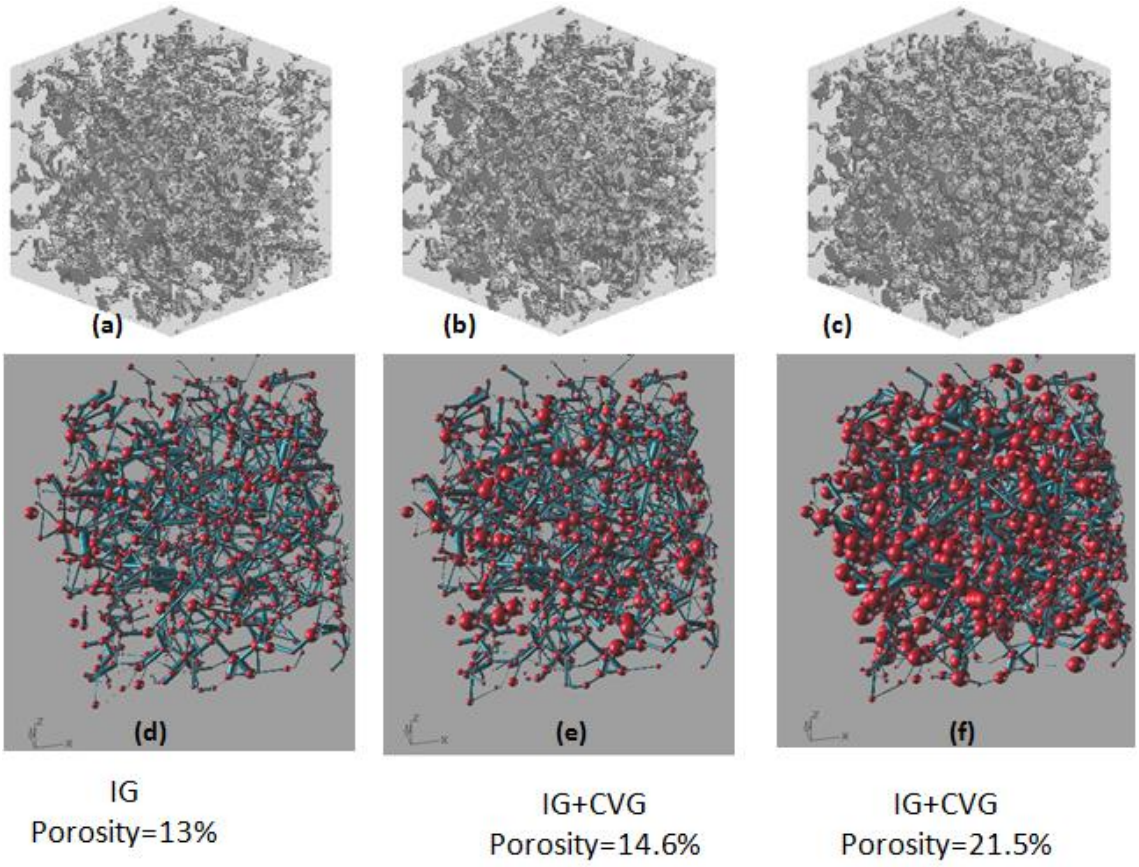

Figure 4.43: The pore network 3D visualization for the IG (a), (d) and IG+CVG (b), (c), (e), (f) models for the tiny CVG with large numbers.

4.5.3 GM and TP of the IG + Large CVG Models

In this section, the geometry and topology for IG+CVG models is presented, the CVG is large with less numbers.

The radius and shape factor of the pore and throat is shown in Figure 4.44. Compared with the pore radius and shape factor in Figure 4.40 for tiny CVG with large

numbers, the pore radius and shape factor in Figure 4.44 (a) and (c) are larger resulting in simpler and more regular pore. Additionally, this CVG can increase the percentage of the small throat in Figure 4.44 (b).

The increase of the pore size and decrease of the throat results in the increase of the pore throat cross sectional area (PTAR) which cause large porosity exponent. The increase of the PTAR is shown in Figure 4.45 (a) as well as the increase of the tortuosity (b), the increase in both is much more obvious in comparison with the results for the tiny CVG with large number in Figure 4.41.

The coordination number and Euler number reflecting the TP is shown in Figure 4.46. Compared with the decrease of Euler number and minimal variation of the coordination number for the tiny CVG (Figure 4.42), the fluctuation of the Euler number is trivial while the increase of the coordination number is obvious for the large CVG. This is due to the existence of large pore merging surrounding pore resulting in the increase of the coordination number (Figure 3.37), which can be discussed later and compared with the increase from the FT (Figure 4.38).

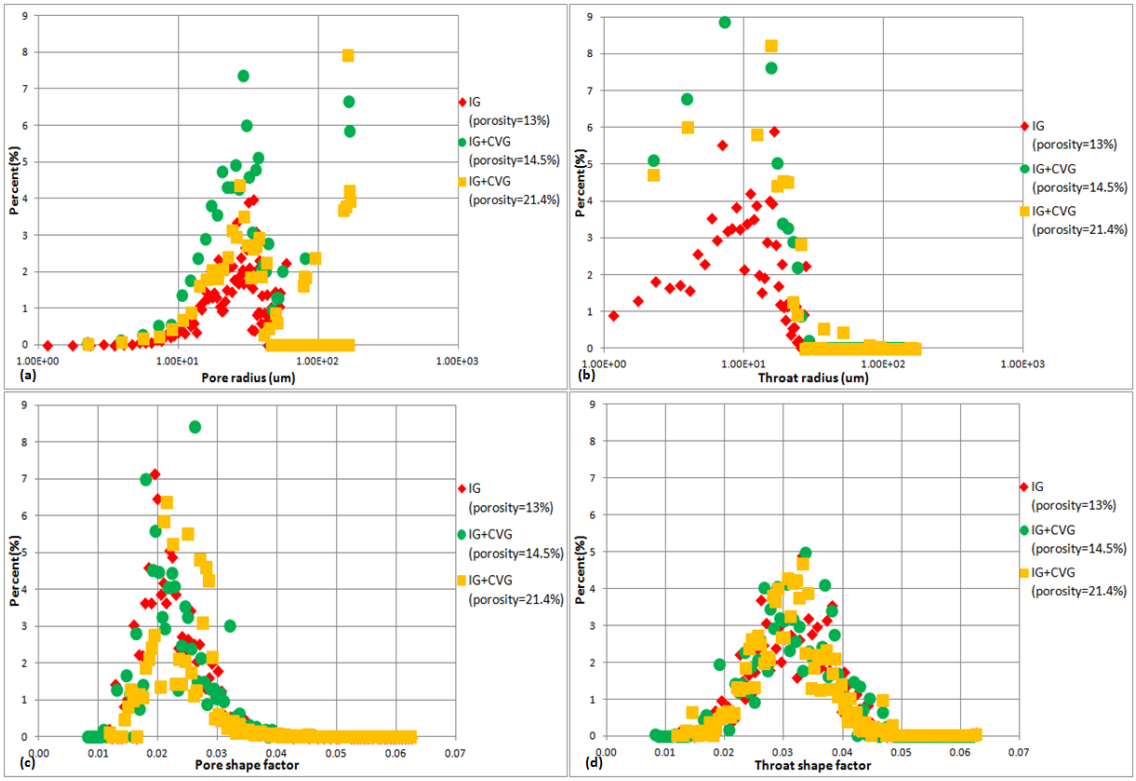

Figure 4.44: The radius and shape factor of the pore (a), (c) and throat (b), (d) for IG and IG+CVG models. The CVG is large and less numerous.

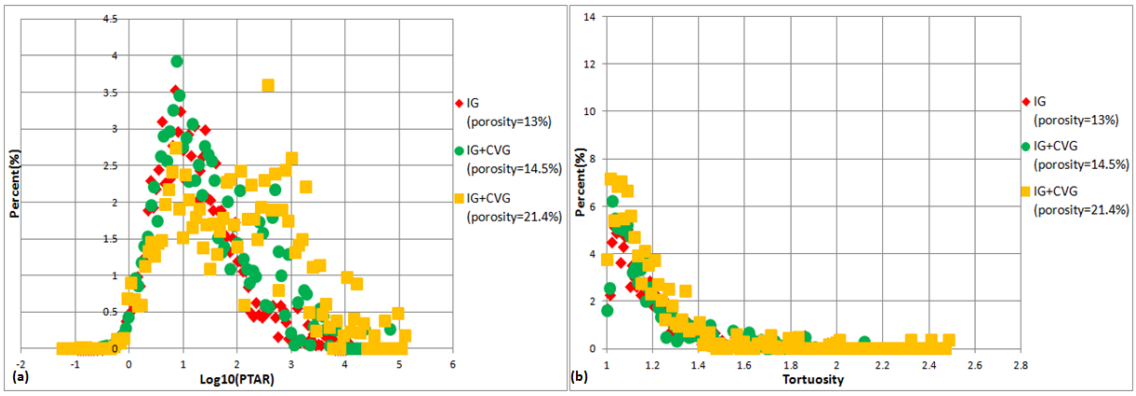

Figure 4.45: The pore throat cross sectional area ratio (PTAR) (a) and tortuosity (b) of the IG and IG+CVG models for the CVG with large size and less numbers.

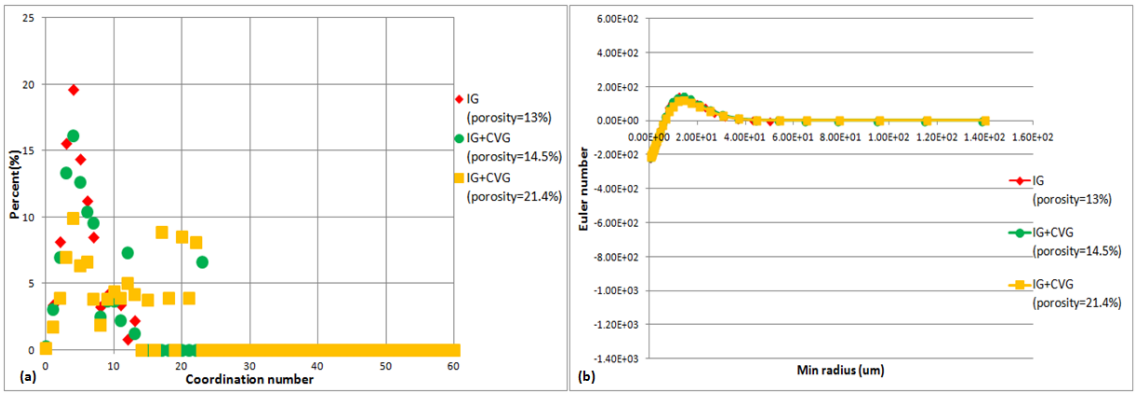

Figure 4.46: The coordination number (a) and Euler number (b) for IG and IG+CVG models. The CVG is large and less numerous.

The visualization of the IG and IG+CVG models for the CVG with large size and less number is shown in Figure 4.47. From the visualization, the effect of the CVG on the pore radius and PTAR obviously is increase. Based on the GM and TP as well as the pore network visualization for both kinds of CVG, it is clear that the CVG effect on the GM lies in the increase of the pore size, PTAR as well as tortuosity. Its effect on the TP lies in the decrease of the Euler number and the increase of the coordination number to improve the connectivity of the pore system. The same two kinds of IVG with tiny and large size are built respectively for the generation of IG+IVG models.

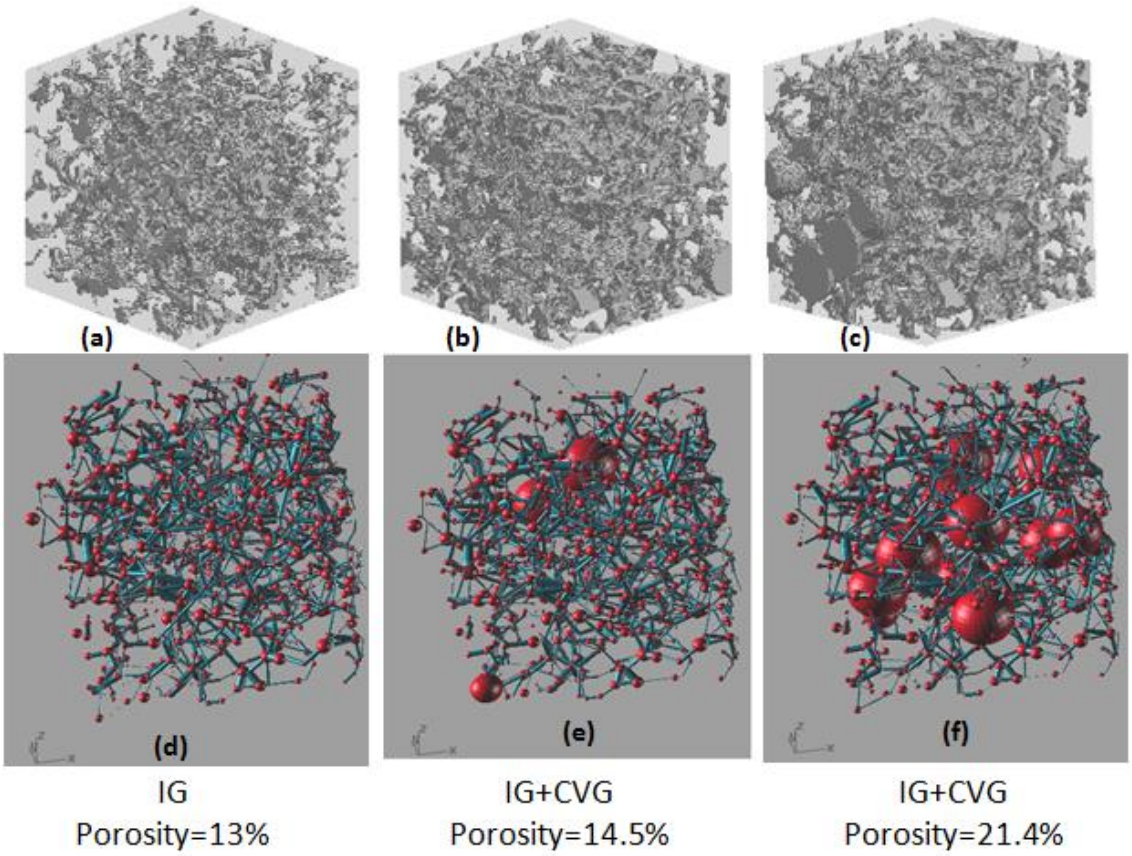

Figure 4.47: The pore network visualization in 3D for IG (a), (d) and IG+CVG models (b), (c), (e) and (f), the CVG is in large size and less numbers.

4.5.4 GM and TP of the IG + Tiny IVG Models

This section shows the radius, shape factor of the pore and throat, tortuosity, PTAR, coordination number and Euler number of the IG+IVG models, the IVG is tiny and numerous.

It is clear that the IVG effect on the radius (Figure 4.48) and shape factor (Figure 4.49) of the pore and throat as well as the PTAR (Figure 4.50a) is trivial while IVG increase the tortuosity (Figure 4.50b). The shape factor of the pore in 20% is related to the inserted IVG in Figure 4.49 (a) and its expanded image in Figure 4.49 (b). The TP comprised of coordination number and Euler number is shown in Figure 4.51. The IVG lowers the coordination number in Figure 4.51 (a) with its expanded image in (b). This effect on Euler number is obvious with the increase of the Euler number for the IG+IVG presenting the worse connectivity of the pore system. Its significant effect on the TP can be reflected by the pore network visualization in 3D in Figure 4.52. The inserted IVG seriously destroys the connectivity of the pore space resulting in the increase of the Euler number and the percentage of the coordination number equal to 0, that is, isolated

pore without throat connected to it and decrease of the percentage of other coordination number (Figure 4.51a).

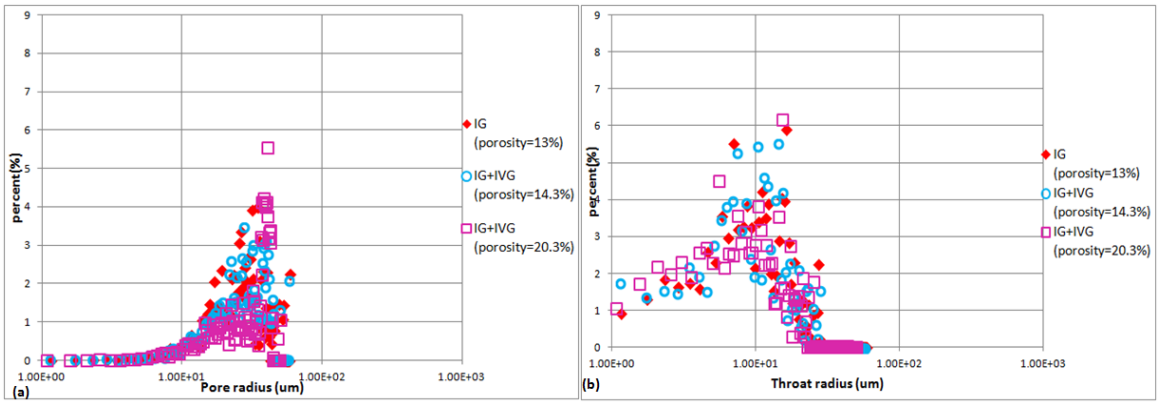

Figure 4.48: The radius of the pore (a) and throat (b) for the IG and IG+IVG models for the tiny numerous IVG.

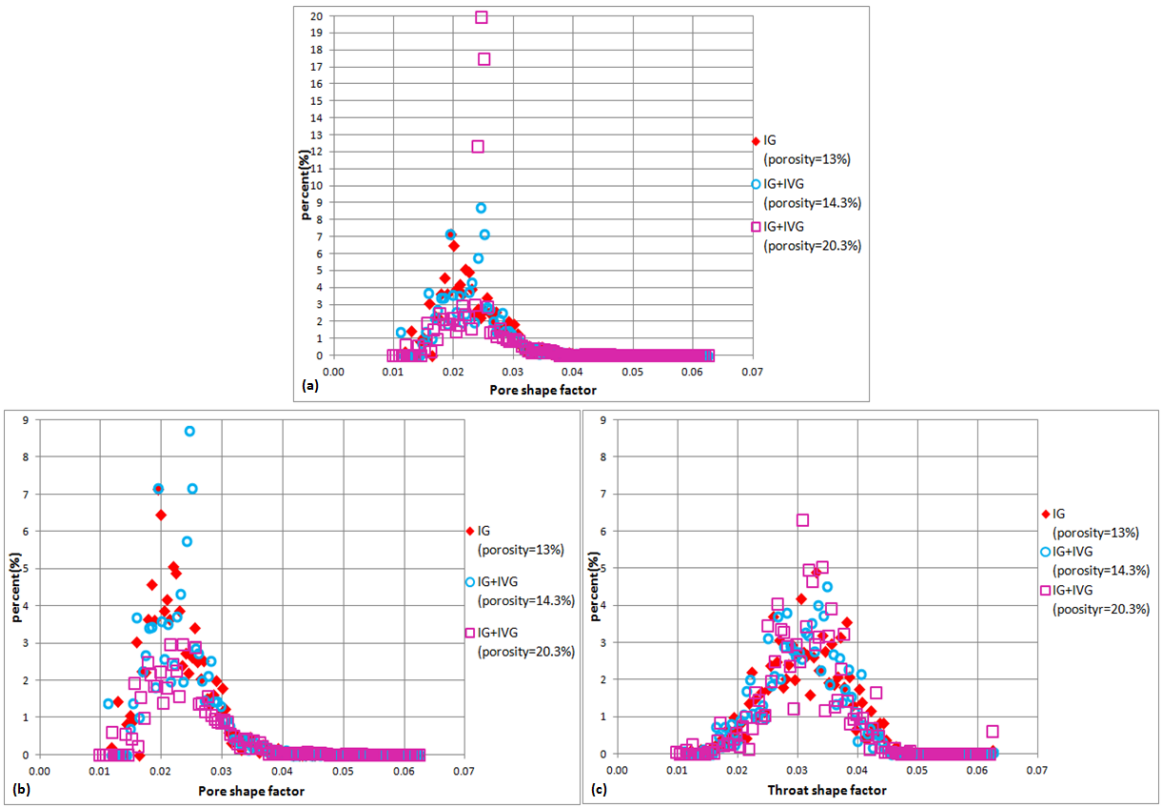

Figure 4.49: The shape factor of the pore (a), (b) and throat (c) for the IG and IG+IVG models for the tiny numerous IVG. (b) is the expanded image of (a).

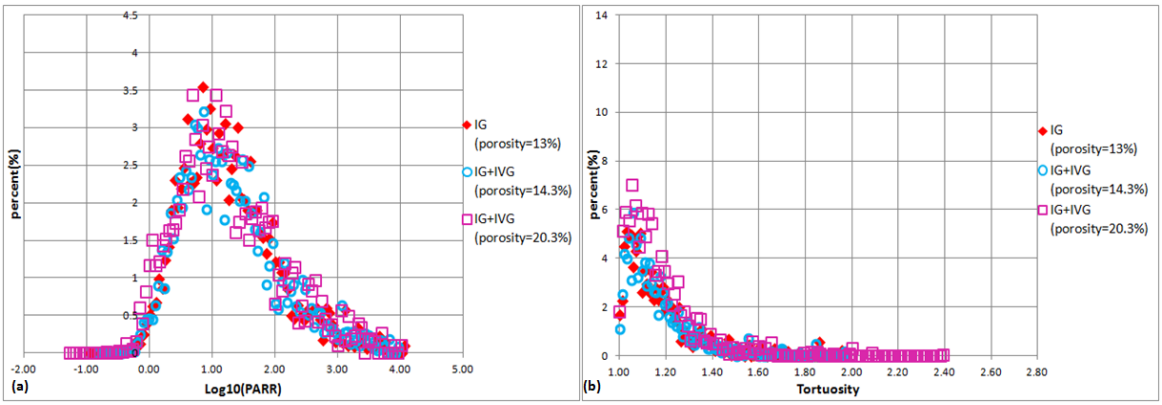

Figure 4.50: The pore throat cross sectional area ratio (PTAR) (a) and tortuosity (b) of the IG and IG+IVG models for the tiny numerous IVG.

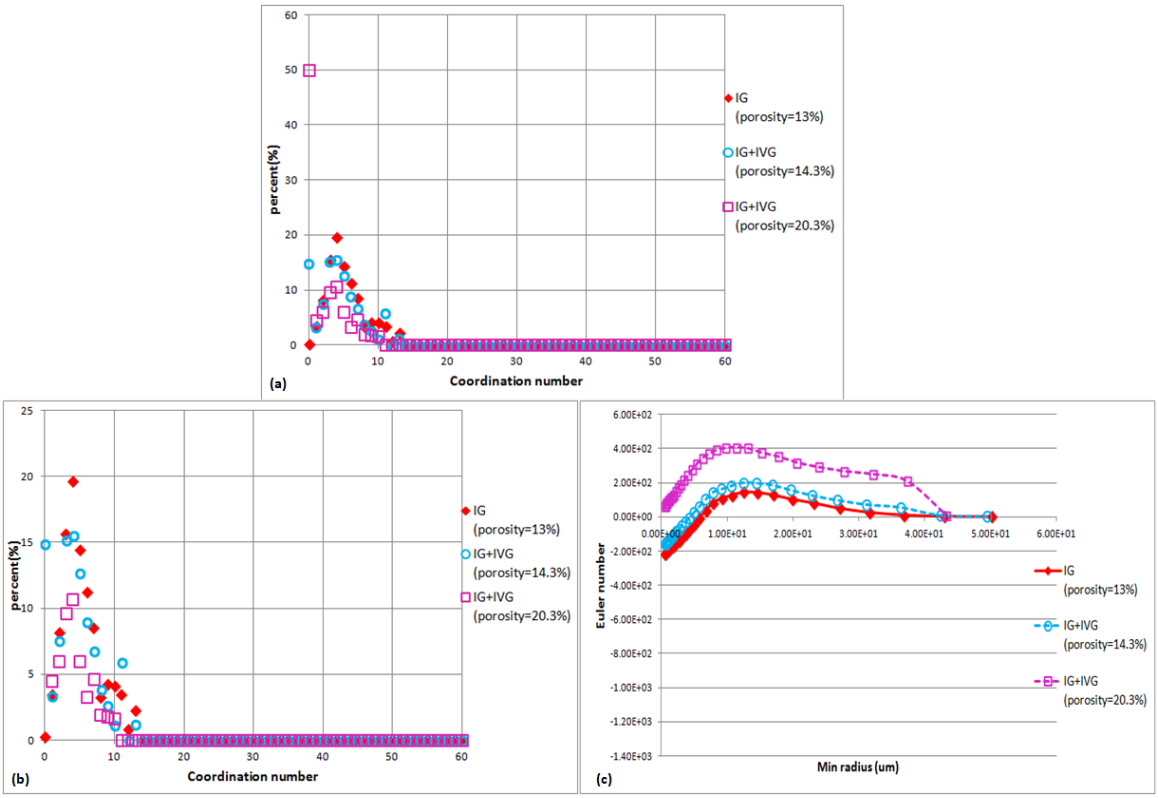

Figure 4.51: The coordination number (a), (b) and Euler number (c) of the IG and IG+IVG models for the tiny numerous IVG. (b) is the expanded image of (a).

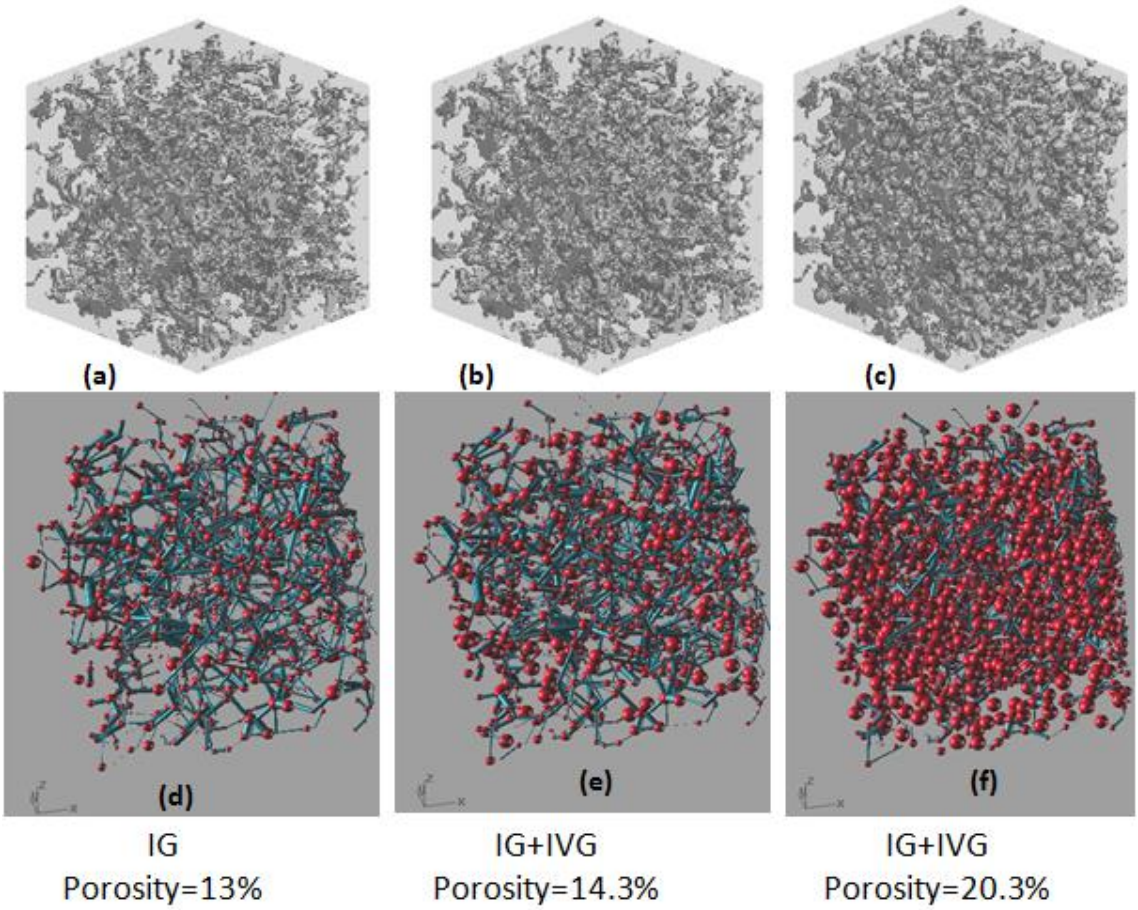

Figure 4.52: The pore network visualization in 3D for IG and IG+IVG models for the tiny numerous IVG.

4.5.5 GM and TP of the IG + Large IVG Models

This section compares the geometry and topology of the IG+IVG models, the IVG is large with less numbers.

The radius of the pore and throat for the IG and IG+IVG models for the IVG with large size is shown in Figure 4.53. The large IVG can increase the pore radius and reduce the throat radius. The large radius of the pore in Figure 4.53 (a) is the reflection of the size of the inserted IVG and this process changes the pore structure resulting in the increase of the throat in small size. Its effect on the shape factor of the pore and throat is not obvious (Figure 4.54). The PTAR and tortuosity of the IG and IG+IVG models is presented in Figure 4.55. It is clear that the effect of this IVG on the PTAR and tortuosity is minimal. The PTAR for the IG+IVG almost match the PTAR of the IG. The large percentage for the pore and throat in the same size is introduced by the insert of the IVG resulting in the emergence of the new pore from the end part of the blocked throat by IVG shown in Figure 4.56. When the IG model is inserted by IVG, the end part of the throat which is cut off by IVG should be regarded as pore due to the fact that

throat should connect two pores, that is, there is isolated pore while there is not isolated throat. Therefore these end parts turn into new pore shown by unfilled square which is the same size as the throat. So in Figure 4.55, there are 8% for the PTAR=1. The TP of the IG and IG+IVG is shown in Figure 4.57. It is clear that the coordination number decreases with about 40% of the coordination number equal to 0. Its effect on Euler number lies in the increase which is minimal. Its minimal effect on the GM and TP can be shown by their pore network in 3D visualization in Figure 4.58. It is clear that this kind of IVG with large size and small numbers slightly affect the GM while it can reduce the connectivity of the pore system. The extent of the influence is related to the number of the IVG by comparing with the results in Figure 4.51 and Figure 4.57 for the IVG in different sizes and numbers. Base on the above results, the impact of the IVG on the GM is trivial and its main effect lies in reducing the connectivity of the pore system.

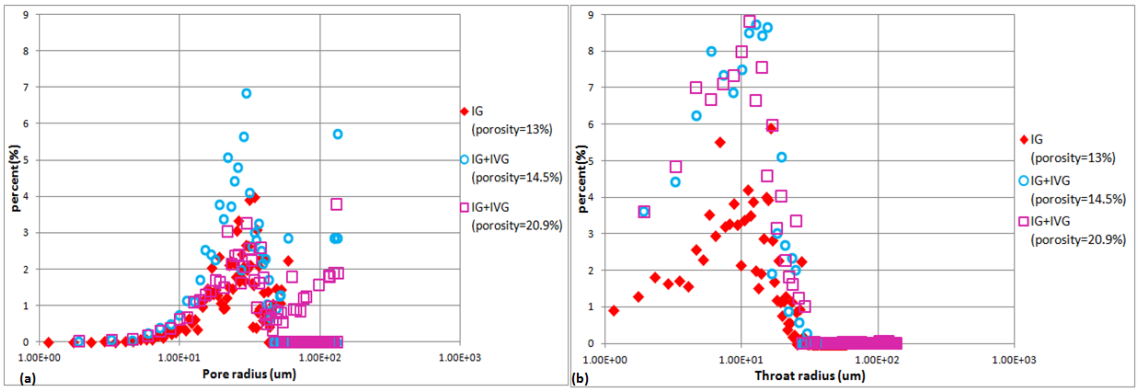

Figure 4.53: The radius of the pore (a) and throat (b) for IG and IG+IVG models for the large less numerous IVG.

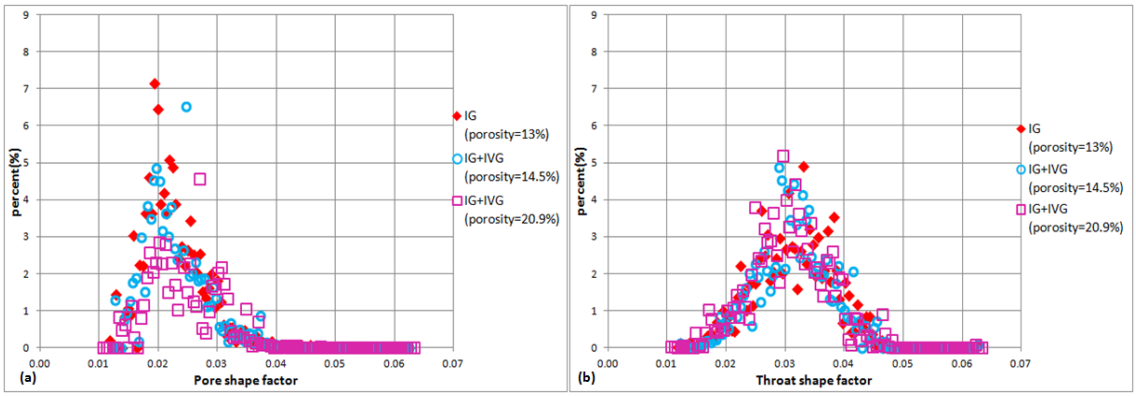

Figure 4.54: The shape factor of the pore (a) and throat (b) for IG and IG+IVG models for the IVG with large size and less numbers.

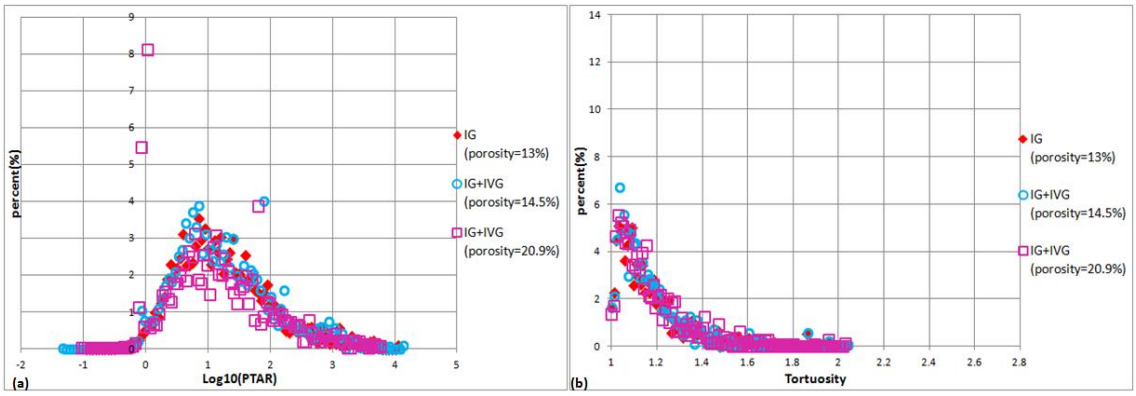

Figure 4.55: The pore throat cross sectional area ratio (PTAR) (a) and tortuosity (b) of the IG and IG+IVG models for the large IVG with less numbers.

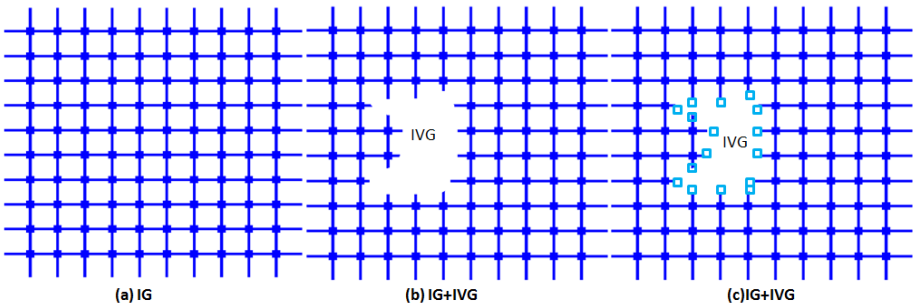

Figure 4.56: Schematic pore network for IG (a), IG+IVG (b) and (c) to explain the pore and throat in the same size.

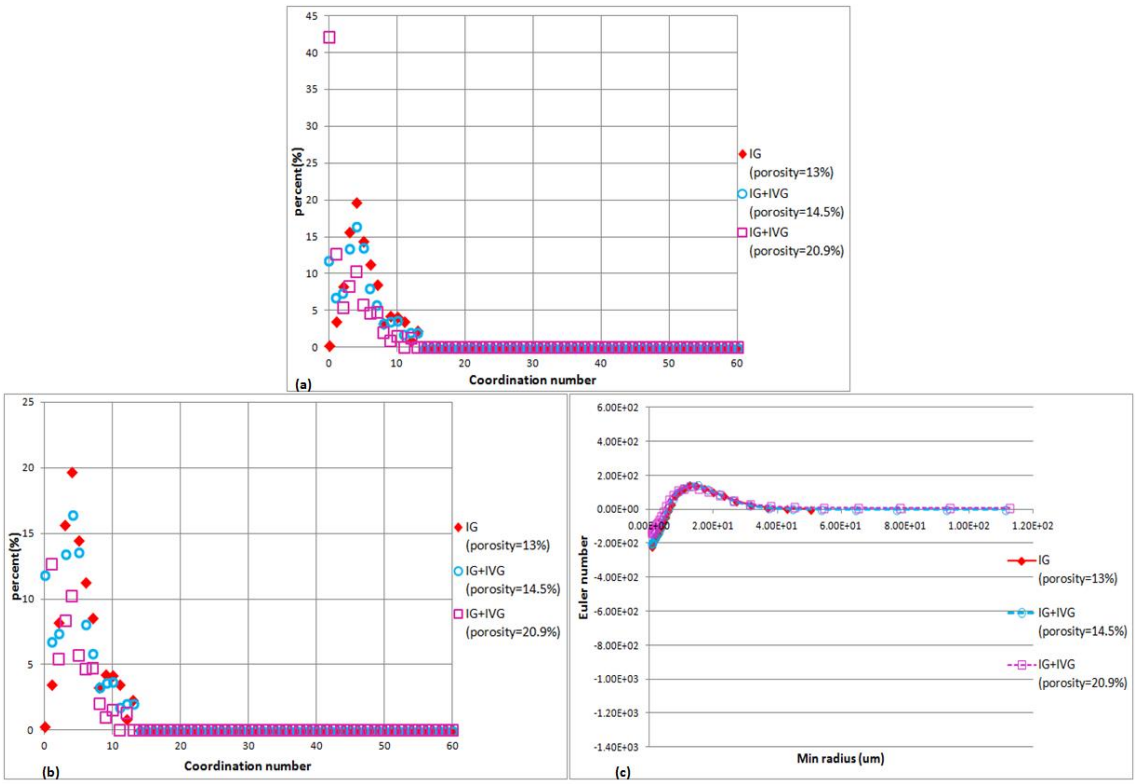

Figure 4.57: The coordination number (a), (b) and Euler number (c) of the IG and IG+IVG models for the large IVG with less numbers. The expanded picture for coordination number (a) is in (b).

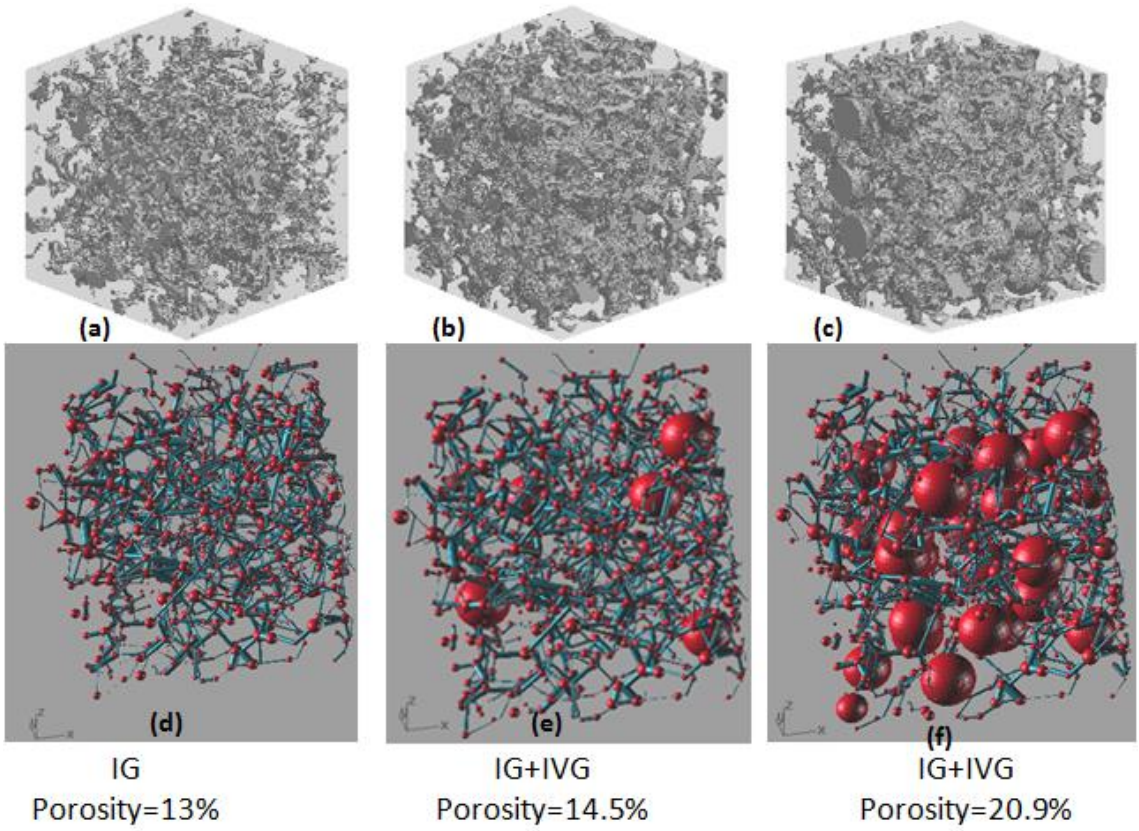

Figure 4.58: The pore network visualization in 3D for IG and IG+IVG models for the IVG with large size and less numbers.

From above several sections, the effect of the pore size and length on the porosity exponent based on theoretical analysis (section 4.1), the effect of the pore type on the porosity exponent based on simple tubes as well as the validation of the published work of Aguilera and Aguilera (2003[5]) (section 4.3), the effect of the pore type on the porosity exponent, Formation Factor and anisotropy (section 4.4) as well as on GM and TP (section 4.5) are given. In the next section, several discussions are presented.

4.6 Discussion

4.6.1 Effect of the IVG on the Porosity Exponent

In Figure 4.24 and Figure 4.25, the porosity exponents of IG+IVG models for the IVG with tiny size and large number are larger than the porosity exponents of IG+IVG models for the IVG with large size and less number. This can be explained by the difference of their effect on lowering the connectivity of the pore system.

For the IG+IVG models, their effect on decreasing the connectivity of the pore systems is much more obvious for the IVG with small size and large number than the

IVG with large size and less number. This can be explained by the schematic in Figure 4.59.

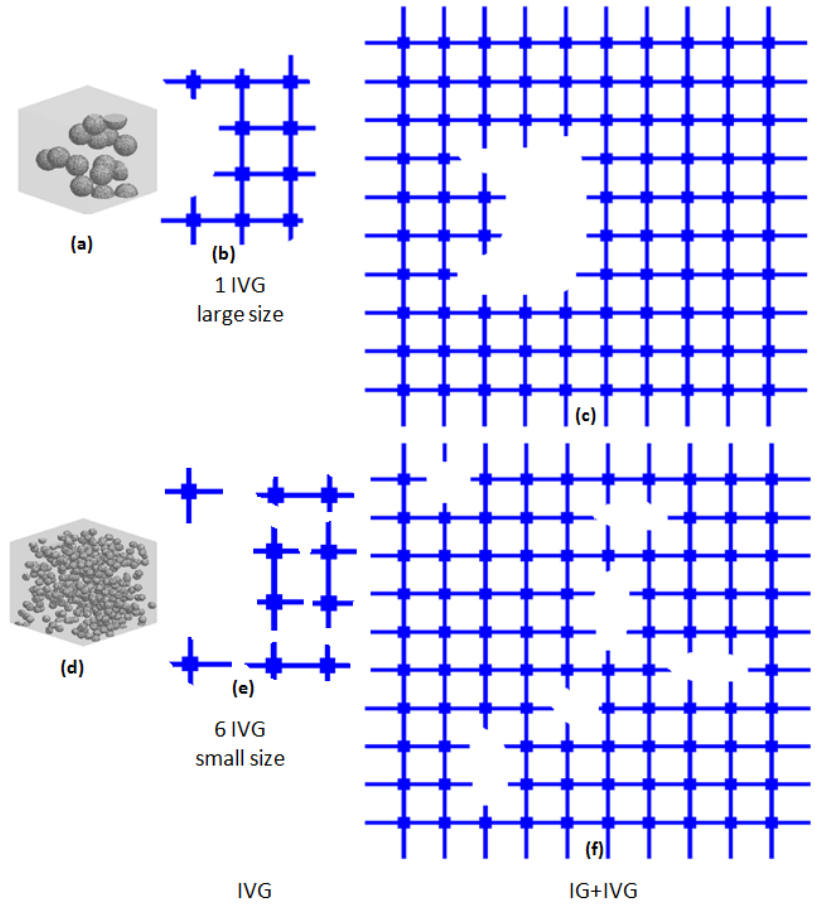

Figure 4.59: Schematic for the effect of the IVG on the connectivity of the pore system.

It is clear that for the same porosity (10 pore bodies), the connectivity of the IG+IVG for large size IVG (top) is better than the bottom IG+IVG model, and then the porosity exponent (top) is less than the porosity exponent (bottom). The effect of increasing the porosity exponent of the IG+IVG model is much more obvious for the small size IVG with numerous number than the IVG with large size and less numbers.

4.6.2 Coordination Number Increase for IG+FT and IG+CVG models

In Figure 4.38 for IG+FT and Figure 4.46 for IG+CVG, the coordination number for both models increases while the difference lies in that coordination number of the IG+FT is larger than the coordination number of the IG+CVG. The increase of the coordination number is the same in Figure 3.37, the difference lies in the difference of the shape of the FT and CVG. Compared with the shape of FT, CVG is much more

regular with the width and length similar resulting in the different arrangement of the merged pores hence resulting in different coordination number in Figure 4.60.

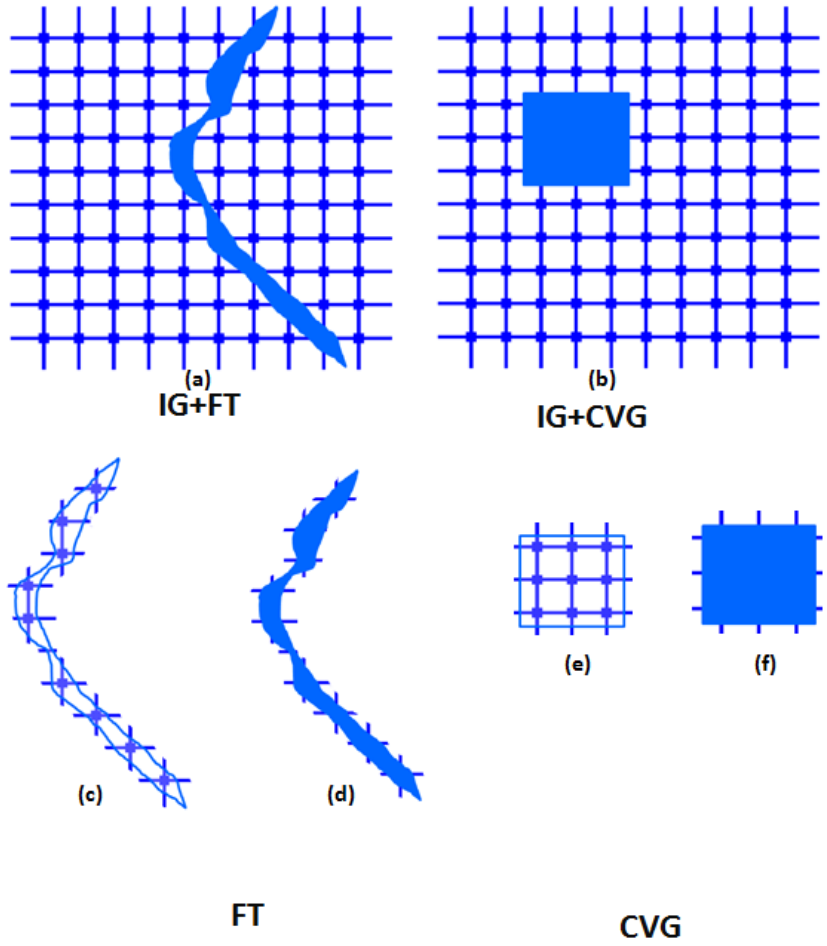

Figure 4.60: Schematic for the coordination number of IG+FT (a), (c) and (d) and IG+CVG models (b), (e) and (f). The bottom shows the coordination number of the FT (32) in (c) and (d) and CVG (12) in (e) and (f) with 9 pore bodies.

It is clear that the difference of the shape for FT and CVG results in the different of the coordination number. The irregularity in the pore shape can contribute the increase of the coordination number.

Based on the schematic of pore trap and channel and simple pore network, the explanation of the GM and TP effect on Formation Factor (FF) and the total porosity and then on the porosity exponent are given.

4.6.3 Effect of the FT on the GM, TP, FF and Porosity Exponent

The FT effect on the geometry (GM) and topology (TP) mainly lies in the decrease of radius and shape factor of the pore body and increase of the tortuosity causing the

irregularity of the pore body with less influence on the throat while building well connectivity of the pore system by decreasing the Euler and increasing the connection number. These effects generate an intricate pore system with good connectivity to decrease the FF and porosity exponent.

These effect on the GM and TP result in the decrease of the Formation Factor (FF) and then the porosity exponent which is shown in Figure 4.61 with the geometrical and topological properties in the square with filled line while the FF and porosity exponent which are the properties of resistivity in the square with dotted line. The increase of the properties presented by red colour and up arrow, the decrease is in green and down arrow and the yellow is for the properties which are stable.

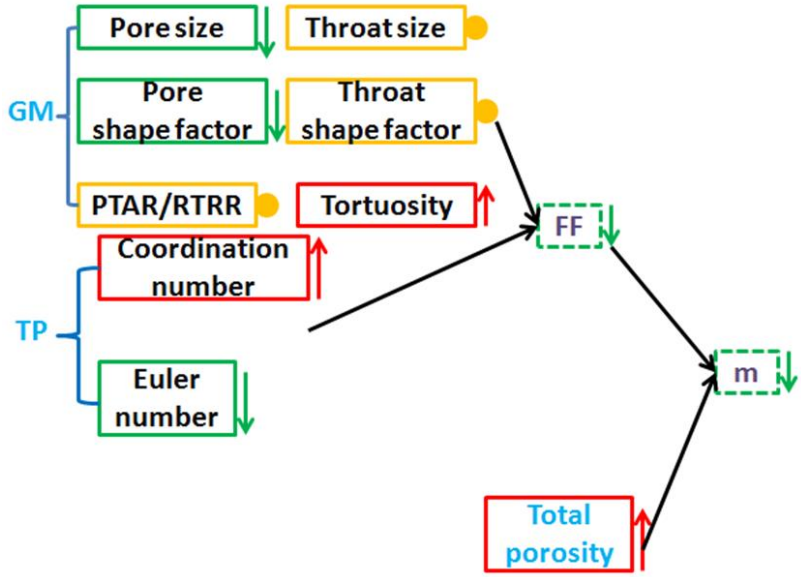

Figure 4.61: The effect of the FT on the GM and TP and then on the FF and porosity exponent.

4.6.4 Effect of the CVG on the GM, TP, FF and Porosity Exponent

The CVG effect on the GM and TP mainly lies in the increase the size and shape factor of the pore, PTAR and tortuosity generating a large and simple pore system. The CVG tends to cause well connectivity of the pore system by increasing the coordination number and decreasing the Euler number while this effect in connectivity is slight. Its effect on GM and TP causes the decrease of the formation factor and the increase of the porosity exponent in Figure 4.62. These effects are sensitive to the size of the CVG with less influence from the number of CVG.

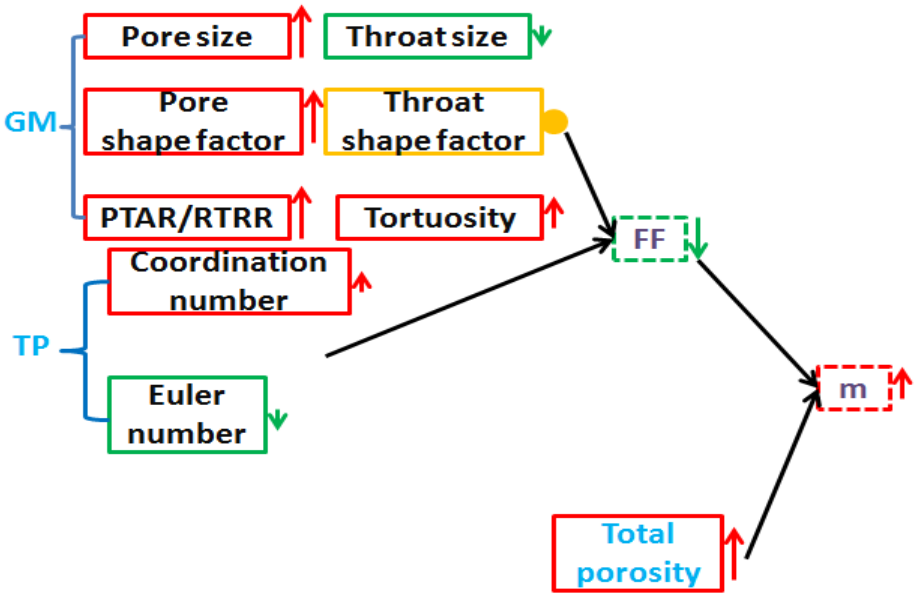

Figure 4.62: The effect of the CVG on the GM and TP and then on the FF and porosity exponent.

4.6.5 Effect of the IVG on the GM, TP, FF and Porosity Exponent

The effect of the IVG on the GM is minimal merely changing the radius distribution of the pore with less influence on the throat and PTAR due to its isolation. While it effect on the TP is obvious in undermining the connectivity of the pore system to improve the resistivity FF and porosity exponent for both kinds of IVG models. These effects are sensitive to the number of the IVG instead of its size.

These effects are shown in Figure 4.63.

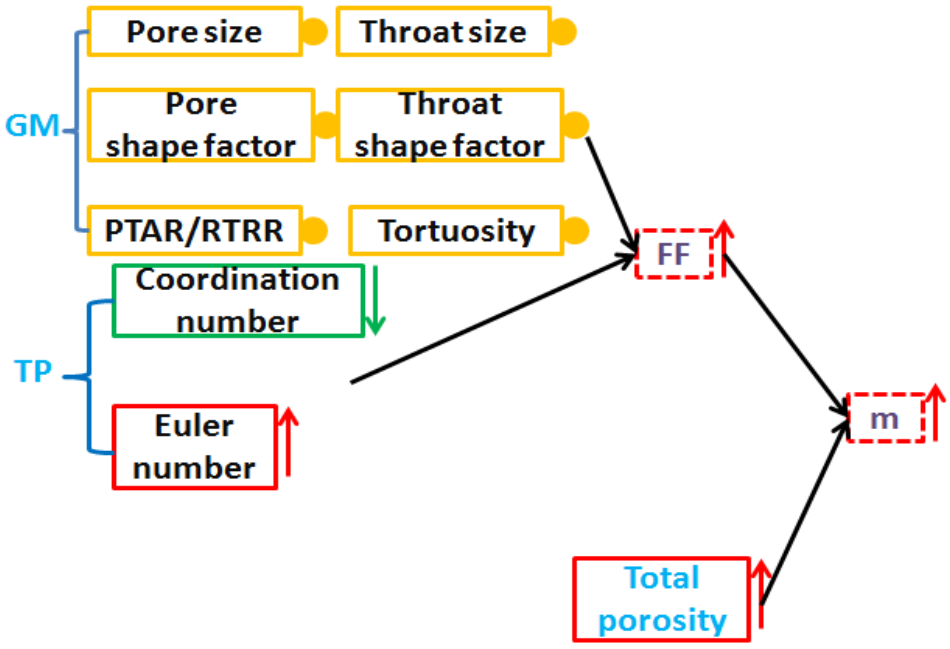

Figure 4.63: The effect of the IVG on the GM and TP and then on the FF and porosity exponent.

Based on the above analysis, it is clear that the pore type effect on the GM and TP predominantly is in pore body. This part just qualitatively analyses the effect of pore type on FF and porosity exponent, the quantitative relationship needs further work.

According to the effect of the pore type on the FF and porosity exponent, the distribution of the IG, IG+FT, IG+CVG as well as IG+IVG are shown in the schematic FF versus total porosity cross plot in order to show their contribution to the porosity exponent in Figure 4.64. The arrow is the boundary between the IG+CVG and IG+IVG indicating the condition that the VG just increase the porosity while do not contribute to the resistivity. Based on that, the distribution of the IG, IG+FT, IG+CVG as well as IG+IVG are shown in the schematic FF versus total porosity cross plot.

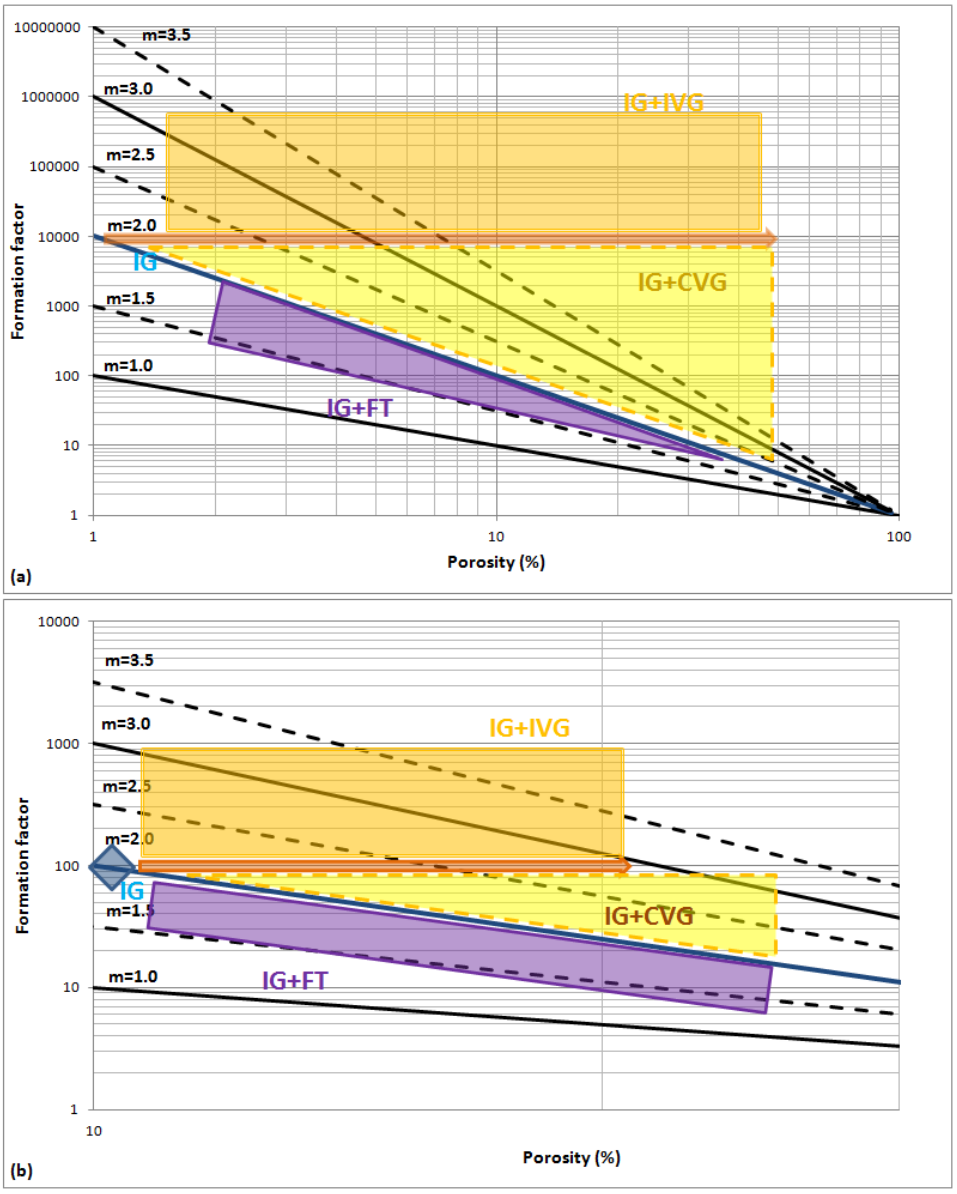

Figure 4.64: Schematic distribution of the IG, IG+FT, IG+CVG and IG+IVG in the Formation Factor versus porosity cross plot, (b) is the expanded image of (a).

4.7 Conclusion

Based on these studied, the main conclusions are given for this chapter.

- The porosity exponent is the mutual effect of the pore size, length and pore type (Figure 4.4, Figure 4.7, Figure 4.61, Figure 4.62 and Figure 4.63);
- FT causes the anisotropy of the porosity exponent while the effect of VG on the anisotropy is minimal with the possibility of decrease the anisotropy (Figure 4.31, Figure 4.32, Figure 4.33);
- Pore type can affect the GM and TP and then affect the Formation Factor and porosity exponent;

1) FT effect on GM and TP lies in the decrease of pore size, shape factor, Euler number and increase the coordination number and tortuosity generating an intricate pore system with well connectivity to decrease the FF and *m* (Figure 4.61).
2) CVG effect on GM and TP lies in the increase of the pore size, shape factor, PTAR and coordination number, tortuosity and slight decrease in Euler number to improve connectivity of a simple and large pore system to decrease FF and increase porosity. Its function mainly depends on the size of CVG (Figure 4.62).
3) IVG mainly reduces the connectivity of the pore system with a little effect on GM to increase FF and porosity exponent. Its effect mainly depends on the number of IVG (Figure 4.63).

- These effects are controlled by geological processes in carbonates and therefore to label the porosity exponent having to consider with all of these processes lead to average.

Additionally,

- FT, VG effect mainly on pore while less influence on the throat (Figure 4.35, Figure 4.36);
- The increase of the size and length (tortuosity) of the pore system causes the increase of the porosity exponent (Figure 4.4, Figure 4.7);
- The effect of the PTAR on the porosity exponent is related to the length of the pore and throat (Figure 4.7);
- The increase of the porosity exponent by IVG is obvious than the increase by CVG (Figure 4.24, Figure 4.25, Figure 4.32 and Figure 4.33).

Chapter 5

Discussion, Conclusion and Future Research

In this chapter, a discussion about the issues examined in this thesis is firstly presented, and then the conclusions are given. Finally, some further research issues are proposed. In brief, this thesis used several simulation methods to calculate porosity exponent based on the sub REV samples and extracted the topological and geometrical properties of the pore system for three carbonate samples. The relationship between these properties and porosity exponent and the effect of the pore types on the porosity exponent had been researched. According to these relationships and the simulation results, the accuracy of the numerical porosity exponent and a reasonable porosity exponent in each direction and different locations can be given. The original objectives of this thesis described in Chapter 1, have been achieved. Several computer models have been built and the simulated porosity exponent can match the theoretical data and can be used to explore porosity exponent anisotropy.

5.1 Discussion

In order to give an accurate porosity exponent by simulation methods and number of tasks is completed. Firstly the simulation results should compare with the experimental results to present the feasibility of these simulation methods and the effect of the external factors such as grey threshold, the size of the sub-sample on the simulation results. Secondly the appropriate simulation methods, proper threshold and representative elementary volume can be determined to avoid the external effects on the porosity exponent simulation as much as possible. Thirdly the internal factors affecting the porosity exponent of the three carbonate samples are searched and further to research their effects on the porosity exponent. Finally, based on these above works, the accuracy of the simulated porosity exponent and a reasonable porosity exponent based on simulation can be given.

1) The validation of the simulation methods including finite difference (FD), random walk (RW) and a renormalization was implemented by comparing the analytical and their numerical results for FD and RW as well as the experimental and simulated porosity exponent for FD, RW and a renormalization for the sandstones and carbonates.
2) The effect of the size of the samples (REV analysis) was studied firstly by the relationship between the porosity and the size of the sample. The representative elementary volume was determined by the size when the porosity was convergent. It could also be analysed by the two-point correlation and the

porosity exponent for the samples with different sizes. Based on both works, three kinds of representative elementary volume can be defined as Sub REV, REV and Sup REV. The effect of the REV on the porosity exponent was reflected by the comparison of the porosity exponent, calculated by RW, with the porosity exponent by FD in eight Sub REV samples of Pet6.

- The grey threshold effect on the porosity exponent during the binary segmentation was illustrated by the relationship between the grey thresholds and the porosity exponent of the samples based on these thresholds.
- Based on these work, the simulation porosity exponent should be mainly related to the pore system maximally removing the effect of the external influences.

3) The topology and geometry of the pore system was extracted and used to qualitatively relate to the porosity exponent.
    - The geometrical properties such as radius, shape factor, tortuosity as well as PTRR or PTAR and the topology including connection number and Euler number were extracted and used to explain the porosity exponent for each carbonate sample. The PTRR or PTAR reasonably explained the porosity exponent for each carbonate sample while the Euler number of these carbonate samples were abnormally large due to the existence of the isolated pore clusters. In order to obtain accurate Euler number and study the effect of different pore types with isolated pore clusters regarded as vug (VG) on the geometry and topology of the pore system as well as the porosity exponent, a component labelling algorithm was used to extract the predominant pore cluster for each carbonate sample.
    - By visual comparison the pore system of these three carbonate samples, the critical pore type for each carbonate sample was determined and the effect of the pore types on the topology and geometry were illustrated.
    - Based on the existence of the pore types in the pore system for each carbonate, their effect on the porosity exponent was researched by calculating the Formation Factor which was mainly determined by the predominant pore cluster contributing to the current flow and the porosity of this main pore cluster as well as the whole porosity to reflect the contribution of the pore types.

- The geometrical properties affecting the porosity exponent and the existence of pore types for these three carbonates were obtained.

4) The effect of this geometrical properties and pore types on the porosity exponent was modelled to give the criteria for further application and explanation of the accuracy and legitimacy of the simulated porosity exponent, that is, with these criteria, the relative geometrical properties, pore types, the accuracy of the simulated porosity exponent and an appropriately numerical porosity exponent could be given.
    - The effects of the length (tortuosity) and size reflected by the cross sectional radius or area, as well as PTRR or PTAR of the pore system on the porosity exponent were studied based on the pore-throat conjunction from the viewpoint of the electrical arrangement in series, parallel or both of them.
    - The effect of the vug and fracture on the porosity exponent was implemented by the simple pore network model and the models from random grain packs used to generate vug and fracture with the sandstone as intergranular pore system.
    - The effect of pore types on the geometry and topology and then on the Formation Factor and porosity exponent was investigated.

5.2 Conclusion

The main conclusions in this thesis from a modelling study of heterogeneous carbonates calibrated by laboratory data:

1) The experimental porosity exponents and permeability for three carbonates (Pet1, Pet4 and Pet6) as well as their relation to the GM and TP of the pore space is shown in a schematic in Figure 5.1 and Table 5.1.
   The pore and throat radius is: Pet6>Pet1>Pet4, the permeability Kpet6>Kpet1>Kpet4. The samples with larger pores and throats present larger permeability. The permeability is related to the pore and throat size.
2) The carbonate samples are much more heterogeneous and anisotropic than sandstones in porosity and porosity exponent. The porosity exponent for carbonates should be a vector (regional and directional) instead of scalar.
3) FT causes the anisotropy of the porosity exponent while the effect of VG on the anisotropy is minimal with the possibility of reducing the anisotropy.

4) The porosity exponent is the mutual effect of the pore size, length and pore types and not "cementation" alone. These effects are controlled by cementation and dissolution in carbonates and therefore to label the porosity exponent "cementation exponent" does not consider all of these processes.
5) Pore types affect the geometry and topology of the pore space and their effects result in the variation of the Formation Factor and porosity exponent.
   - Effect of FT on GM and TP lies in the decrease of pore size, shape factor, Euler number and increase of the coordination number and tortuosity generating an intricate pore system with well connectivity to decrease the FF and *m*.
   - Effect of CVG on GM and TP lies in the increase of the pore size, shape factor, PTAR, coordination number, tortuosity and slight decrease of Euler number to improve the connectivity of a simple and large pore system to decrease FF and increase porosity exponent.
   - IVG mainly reduces the connectivity of the pore system with a little effect on GM to increase FF and porosity exponent.

Additionally,

1) The porosity exponents for the larger Sub REV are much more robust than the smaller Sub REV. The voxel number of REV cube in each direction for coquinas is 600.
2) Simple, big pore system $\neq$ small porosity exponent; Complex pores in the pore system $\neq$ large porosity exponent.
3) The effect of FT, VG is mainly on pore while less influence on the throat.
4) The increase of the porosity exponent by IVG is much more obvious than the increase by CVG.

Based on that, the effect of the FT and VG on the porosity exponent can be shown diagrammatically to very systematically in Figure 5.3 or Figure 5.2 with consideration of the PTAR and Euler number.

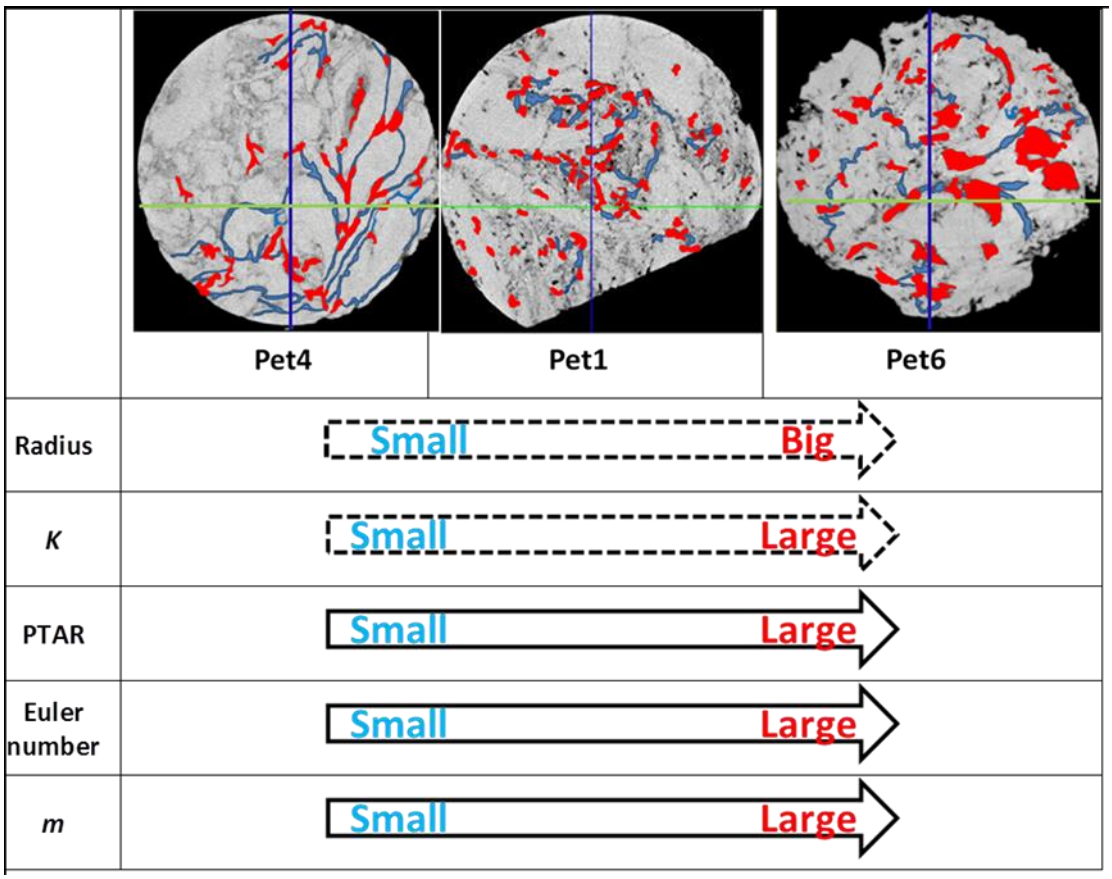

Figure 5.1: The porosity exponent and permeability for three carbonates increase from Pet4, Pet1 to Pet6. Porosity exponent is related to the PTAR and Euler number, the Permeability is related to the radius of the pore and throat. The first row shows the pore in red and throat in blue for them.

	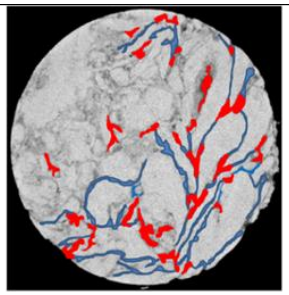 Pet4	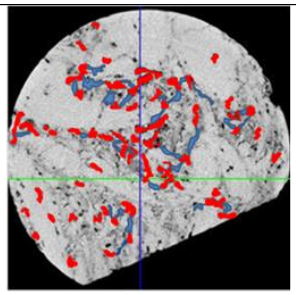 Pet1	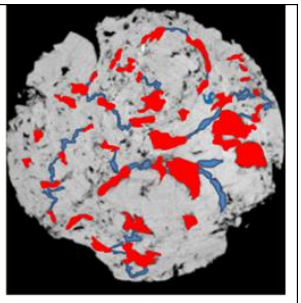 Pet6
Radius (μm)	**127**	**145**	**444**
K (mD)	**0.21**	**18.6**	**282**
PTAR	**104**	**170**	**1260**
Euler number (mm^{-3})	**-1.46**	**-0.298**	**-0.285**
m	**1.7**	**1.89**	**3.0**

Table 5.1: The porosity exponent and permeability for three carbonates increase from Pet4, Pet1 to Pet6. Porosity exponent is related to the PTAR and Euler number, the Permeability is related to the radius of the pore and throat. The first row shows the pore in red and throat in blue for them.

5.3 Future Research

In this field of research, some further work is needed.

1. The heterogeneity in porosity exponent is qualitatively analysed without introducing a parameter to quantitatively describe it. Further work is needed to find a parameter to quantify the heterogeneity.
2. The topological and geometrical properties based on MB can explain the porosity exponent for these three carbonate samples. However, there are several different pore network extraction methods such as MB, Medial axis, Voronoi and some improvements in the calculation of the topological (Euler number) and geometrical parameters (tortuosity for different methods). So these properties based on different pore network extraction methods for the sandstone Fb22 and these three carbonate samples Pet1, Pet4 and Pet6 can be compared to obtain the accurate topology and geometry, to show the differences of these extraction methods and their feasibility for further sandstone and carbonate studies.
3. The relationship between the geometrical properties and porosity exponent for the sandstone Fb22 and three carbonate samples Pet1, Pet4 and Pet6 is qualitative. The further research correlating these properties to the porosity exponent should be focused on building the formula between them and give their correlation coefficient on the porosity exponent. This work needs many more carbonate samples within the same system.
4. In the pore scale modelling, the geological processes effect on the porosity exponent is neglected just paying attention to the effect of the pore types on the porosity exponent. The contribution of the geological processes such as cementation, diagenesis, dissolution to the form of the pore types and then to the porosity exponent is out of the scope of this thesis. However, these processes critically affect the geometry and topology as well as the porosity exponent of the carbonates, this work should be done which would be helpful to understand the evolution of the porosity exponent of the carbonates.
5. The pores smaller than the resolution of the CT image ($\mu\phi$) is not considered in this work, which may very likely contribute to the resistivity. The consideration of these pores can reflect the contribution of the pore types in different scales to the porosity exponent. This work needs the CT images in different scales to study the pore in various scales.

6. Porosity exponent has a directional component. Therefore, it is a vector not a scalar. An "effective scalar porosity exponent" can be averagely obtained by careful upscaling in the heterogeneous media.
7. Application of directional porosity exponent, m, in carbonates need to be investigated in the log scale in interpretation of S_w in oilfields (vertical and horizontal wells).
8. The remaining saturation exponent, n, needs a similar procedure for drainage and imbibition, because the anisotropy of the porosity exponent may cause the Archie Law and saturation exponent becoming the vector instead of scalar.

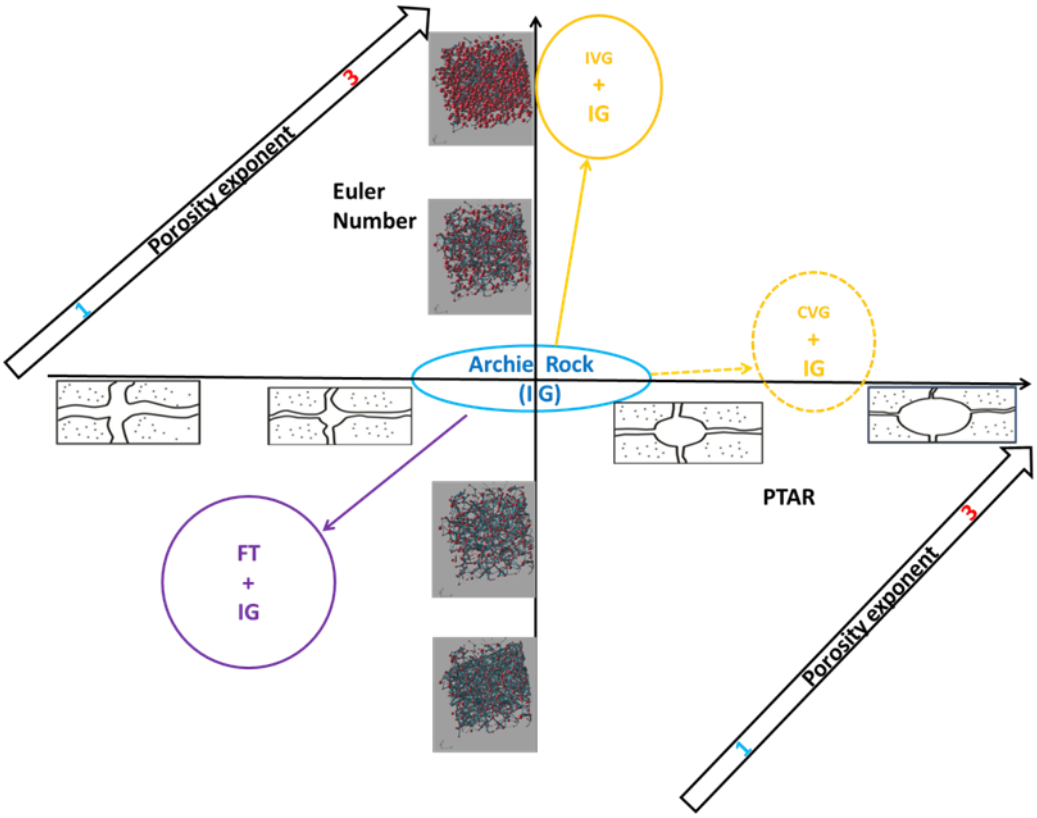

Figure 5.2: The porosity exponent is mainly affected by PTAR and Euler number as horizontal and vertical axis respectively. The porosity exponent increases along the diagonal direction. For FT+IG model, FT reduces the PTAR and Euler number reducing porosity exponent. For CVG+IG model, CVG mainly increases PTAR with less influence on Euler number resulting in the increase of the porosity exponent. For IVG+IG model, IVG increases the porosity exponent attributing to the increase of Euler number with less effect on PTAR. The increase of porosity exponent from IVG is larger than the increase from CVG.

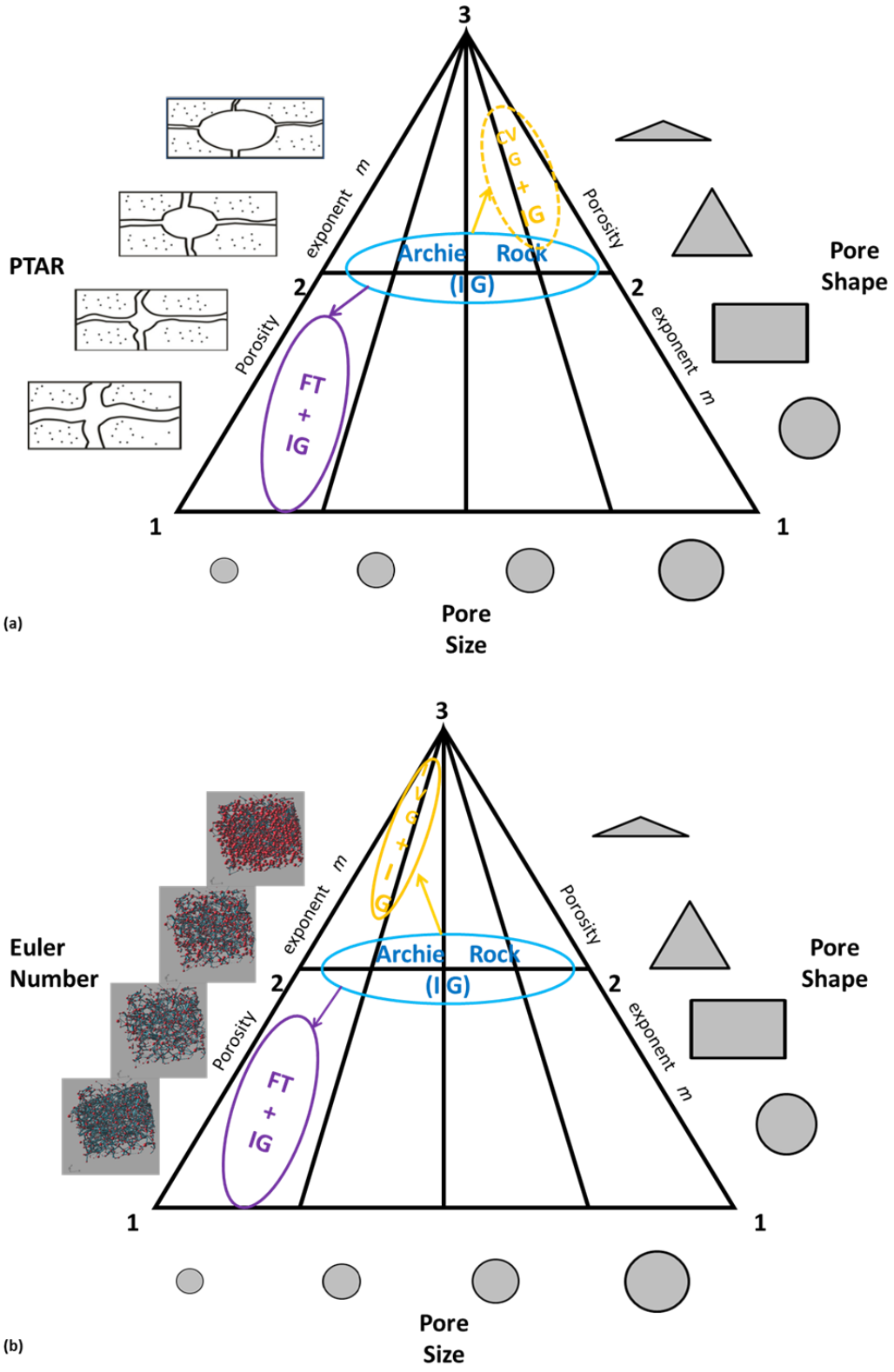

Figure 5.3: The porosity exponent is mainly affected by PTAR and Euler number with less influence from pore size. (a) for FT+IG and CVG+IG, FT decreases the PTAR reducing porosity exponent while CVG introduces larger PTAR increasing porosity exponent. (b) for FT+IG and IVG+IG, FT decreases the Euler number improving the connectivity of the pore space reducing porosity exponent while IVG increases Euler number undermining the connectivity of the pore space and increasing the porosity exponent.

Appendices

Appendix A A Random Walk Resolution for Direct Current Resistivity

A.1 Relationships between Tortuosity and Formation Factor and Resistivity Index

Mathematically, Formation Factor (FF) and Resistivity Index (RI) can be calculated by the diffusion tortuosity τ of the pore space completely saturated by brine (Rasmus, 1986[167]; Bassiouni, 1994[28]; Clennell, 1997[49]).

$$FF = \frac{\tau^2_{S_w=100\%}}{\phi} \approx \frac{1}{\phi^m} \qquad (A.1)$$

And

$$RI = \frac{1}{S_w}\left(\frac{\tau_{S_w<100\%}}{\tau_{S_w=100\%}}\right)^2 \approx \frac{1}{S_w^n} \qquad (A.2)$$

Archie law mathematically correlates the macroscopic properties to the electrical tortuosity $\tau_e = L_w/L$ defined as the ratio of the distance, L_w, along the path of the current flow between two points to the straight line distance, L, of the same two points. Although there are lots of definitions of the tortuosity (Bear, 1972 [29]; Dullien, 1992[66]; Clennell, 1997 [49]; Araújo *et al.*, 2006[14]), which are out of the scope of this study, the first definition is just used here.

Based on the definition of the formation factor, resistivity index, and tortuosity, the two above relationships can be derived from a simple electrical model just considered by Winsauer *et al.* (1952[219]) in Figure A.1.

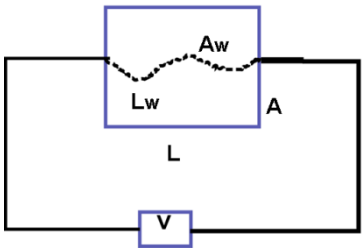

Figure A.1: Schematic of the electrical model. In the cylindrical rock sample model, its length is L and its cross section area is A with the voltage of the electrical circuit is V.

If the pore space of the model is filled with brine with the resistivity of R_w, the length and cross sectional area of the related pore space filled by brine are L_W and A_W respectively. According to Ohm law, the resistance of the brine, r_w, and sample fully saturated with brine, r_0, can be given in Equation A.3.

$$r = R\frac{L}{A} \qquad (A.3)$$

The Formation Factor is

$$FF = \frac{R_0}{R_w} \qquad (A.4)$$

Due to the porosity of the model and the tortuosity of the current,

$$\begin{aligned} \phi &= (A_w L_w)/(AL) \\ \tau_{S_w=100\%} &= L_w/L \end{aligned} \qquad (A.5)$$

The Formation Factor based on Equations (A.3), (A.4) and (A.5) above is equal to

$$FF = \frac{\tau^2_{S_w=100\%}}{\phi} \qquad (A.6)$$

This Equation (A.6) is the used to calculate FF from the estimation of the tortuosity in the random walk simulation.

Similarly, the resistivity index can be given by the resistances of the samples, r_0 and r_t with the saturation of the brine are 100% and s_w respectively.

$$\begin{aligned} r_0 &= R_w\frac{L_w}{A_w} = R_0\frac{L}{A} \\ r_t &= R_w\frac{L_w^{'}}{A_w^{'}} = R_t\frac{L}{A} \end{aligned} \qquad (A.7)$$

The saturation is $S_w = \frac{A_w^{'}L_w^{'}}{AL}$,

the resistivity index can be given as

$$RI = \frac{R_t}{R_0} \qquad (A.8)$$

According to the tortuosities $\tau_{Sw=100\%} = L_W/L$ and $\tau_{Sw<100\%} = L_W^{'}/L$

$\tau_{S_w<100\%} = L_w^{'}/L$ at different saturations of the brine, the resistivity index is

$$RI = \frac{1}{S_w}\left(\frac{\tau_{S_w<100\%}}{\tau_{S_w=100\%}}\right)^2 \qquad (A.9)$$

The definition of tortuosity is less practical due to the difficulty in direct measurement of the tortuosity in the complexity pore space. However, Toumelin and Torres-Verdín (2005[198]) made use of random walk simulation to represent the tortuosity of the pore scale geometry, which simulates Brownian motion diffusing in the

water-saturated pore space and providing the quantitative characterization of the tortuosity based on long time effective diffusivities.

A.2 Feasibility of Random Walk Simulation for DC Resistivity

The feasibility of the random walk simulation on predicting resistivity lies in the common Laplace equation at steady state for diffusion and conduction transport process.

For diffusion, D is the diffusivity and C is the concentration of a soluble species and

$$\nabla \cdot \left(D \nabla C \right) = 0 \tag{A.10}$$

At steady state, D and C are constant. The diffusive tortuosity is defined as:

$$\tau^2 = \frac{D_{bulk}}{D\left(t \to \infty\right)} \tag{A.11}$$

Where D_{bulk} is the diffusivity of the wet phase in pore space (brine). The long time asymptote $D\left(t \to \infty\right)$ can be estimated according to the Einstein's relation describing the relationship between the duration time δt and the displacement δr in the random walk simulation.

$$\begin{aligned} \delta r^2 &= 2 D_{bulk} \delta t \quad 1D \\ \delta r^2 &= 4 D_{bulk} \delta t \quad 2D \\ \delta r^2 &= 6 D_{bulk} \delta t \quad 3D \end{aligned} \tag{A.12}$$

For electrical transport, σ is the electrical conductivity and V is the electrical potential. Its Laplace equation in steady state is similar to the diffusion in fashion.

$$\nabla \cdot \left(\sigma \nabla V \right) = 0 \tag{A.13}$$

The electrical tortuosity is given by

$$\tau^2 = \frac{\sigma_{bulk}}{\sigma\left(t \to \infty\right)} \tag{A.14}$$

A correlation factor of $1/\phi$ linking the diffusive tortuosity to the electrical tortuosity is suggested by Clennell (1997[49]).

$$FF = \frac{R\left(t \to \infty\right)}{R_{bulk}} = \frac{\tau^2}{\phi} \tag{A.15}$$

If the conductive fluid in the pore space is brine, the formation factor can be written as

$$FF = \frac{1}{\phi}\left(\frac{Dbulk}{D(t\to\infty)}\right)_{S_w=100\%} \quad (A.16)$$

In this formula, the result can be simulated by the random walk reproducing the Brownian motion of the conductive fluid (water) molecules.

Similarly, the resistivity index as a function of tortuosity can be presented by the ratio of two diffusivities in different saturation of the conductive fluid (water).

$$RI = \frac{1}{S_w}\left(\frac{\tau_{S_w<100\%}}{\tau_{S_w=100\%}}\right)^2 = \frac{1}{S_w}\frac{\left(D(t\to\infty)\right)_{S_w=100\%}}{\left(D(t\to\infty)\right)_{S_w<100\%}} \quad (A.17)$$

A.3 Calculation of Tortuosity

The calculation of the FF depends on the diffusive tortuosity which can be estimated by the square mean displacement and its move time. In the random walk simulation, a pore voxel is chosen randomly as the starting point of one walker at $t=0$, where t is the dimensionless integer time. The walker can randomly jump to its nearest neighbour points and then the time increases by 1 and becomes $t+1$. If the random neighbour point is solid, this jump is cancelled while the addition of time is accepted. So in 3D, the output of the simulation is the relationship between square mean-displacement, $\langle r^2 \rangle$ and the jump time *t*.

$$\langle r^2(t)\rangle = \frac{1}{n}\sum_{i=1}^{n}\left[\left(x_i(t)-x_i(0)\right)^2+\left(y_i(t)-y_i(0)\right)^2+\left(z_i(t)-z_i(0)\right)^2\right] \quad (A.18)$$

Where n is the number of the walkers, $(x_i(0), y_i(0), z_i(0))$ is the coordination of the starting point for the *ith* walker and its destination coordination after t time is $(x_i(t), y_i(t), \boldsymbol{Z}_i(t))$. The asymptote D can expressed as

$$D(t) = \frac{1}{6}\frac{d\langle r^2\rangle}{dt} \quad (A.19)$$

In calculation, the unit of the time and displacement can be regarded as dimensionless variables. The diffusivity coefficient of the conductive fluid ($Dbulk$) is set as 1/6. In the free space (porosity is 100%),

$$\frac{d\langle r^2\rangle}{dt} = Dbulk = 1 \quad (A.20)$$

The slope of the relationship between mean square displacement and time (jump steps) for free space is one. The tortuosity of the pore space with porosity less than 100% can be only expressed by the slope of the mean square displacement and the step:

$$\tau^2 = 1 \Big/ \left[\lim_{t\to\infty} \frac{d\langle r^2 \rangle}{dt} \right] \qquad (A.21)$$

The directional diffusivity can also be calculated by the mean square displacements in each orthogonal direction (x-axis) such that

$$D_x = \frac{1}{6} \frac{d\langle x^2 \rangle}{dt} \qquad (A.22)$$

Where $\langle x^2(t) \rangle = \frac{1}{n} \sum_{i=1}^{n} \left[\left(x_i(t) - x_i(0) \right)^2 \right]$ and then the directional tortuosity is

$$\tau_x{}^2 = \frac{1}{3} \Big/ \left[\lim_{t\to\infty} \frac{d\langle x^2 \rangle}{dt} \right] \qquad (A.23)$$

Its accuracy can be validated by the simulation of tortuosity shown in Figure A.2.

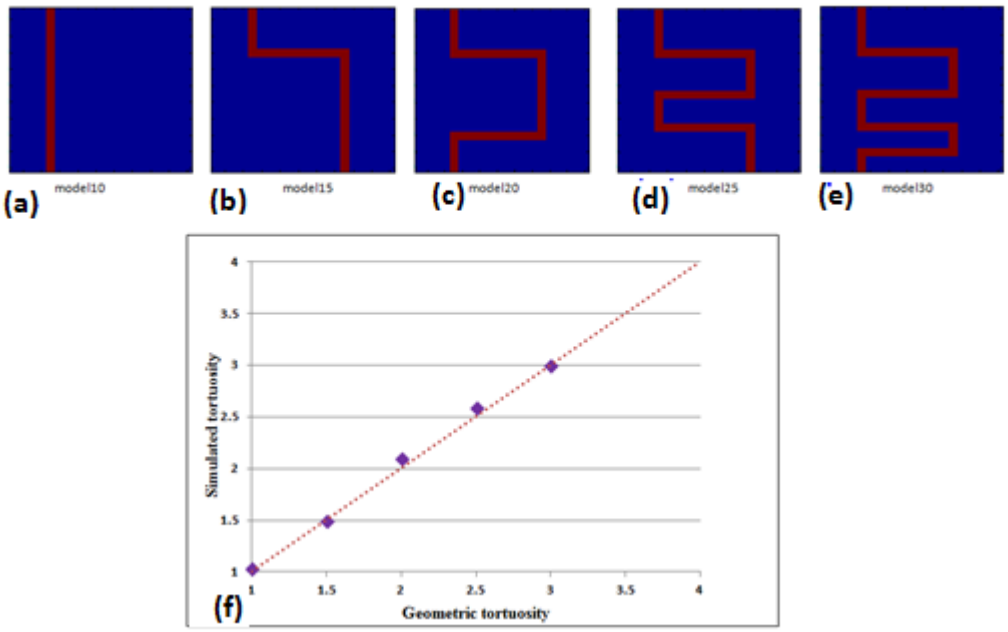

Figure A.2: Simple models (a), (b), (c), (d), (e) and the simulated tortuosity compared with the geometric results (f). In the top the red is pore and the dot line in the bottom images is 1:1.

Appendix B Micro-CT Image Processing and Visualization

The formats of the CT images from the CT scanners usually are a series of 2D cross-sections or a 3D array storing the volumetric data. In order to calculate the geometry and topology of the pore space and to simulate the physical properties, it is necessary to view CT images and then to choose an area or a space of CT images to do the simulation. These tasks can be solved by the free software ImageJ (http://imagej.nih.gov/ij/) which is a public domain, Java-based image processing program developed at the National Institutes of Health. It has open architecture that provides extensibility via Java plugins and recordable macros.

B.1 Importing and Saving Images

The format of one file is a 3D array including the grey scale of the whole image can be imported by "File->Import->Raw" and input the image type and the size of the images in three directions in this dialogue box.

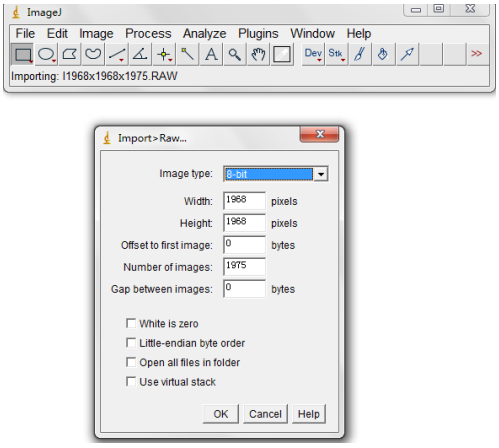

Figure B.1: Dialogue box for importing 3D volumetric data.

A series of the 2D cross –section can be filed by "File->Import->Image Sequence".

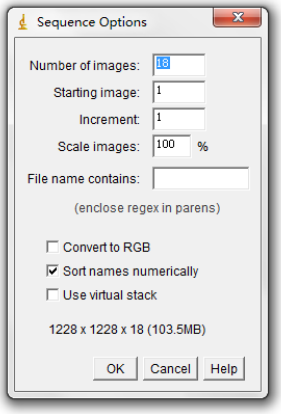

Figure B.2: Dialogue box for importing a series of 2D cross section images.

To save the images, go to "File->Save as->Raw Data". In order to keep the images saved in the same format, the size of each point in the images should be set in "I/O Options" dialogue in "Edit->Options->Input/Output".

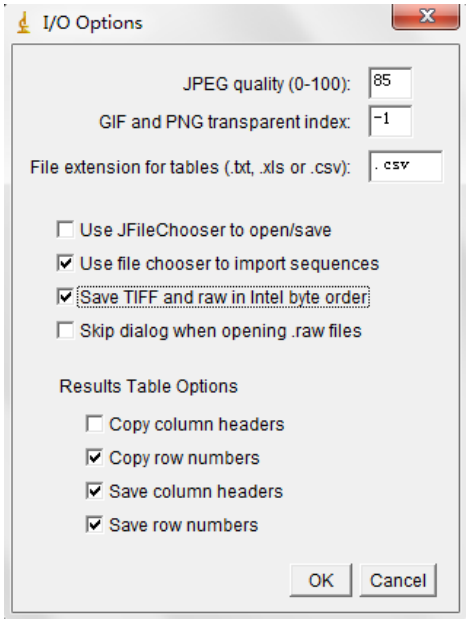

Figure B.3: Dialogue box for saving images in the same format.

B.2 Processing Images

B.2.1 Cropping

A sub samples can be extracted from the original images by choosing a cropping area by mouse and the order "Image->Crop" can be used to get the sub sample.

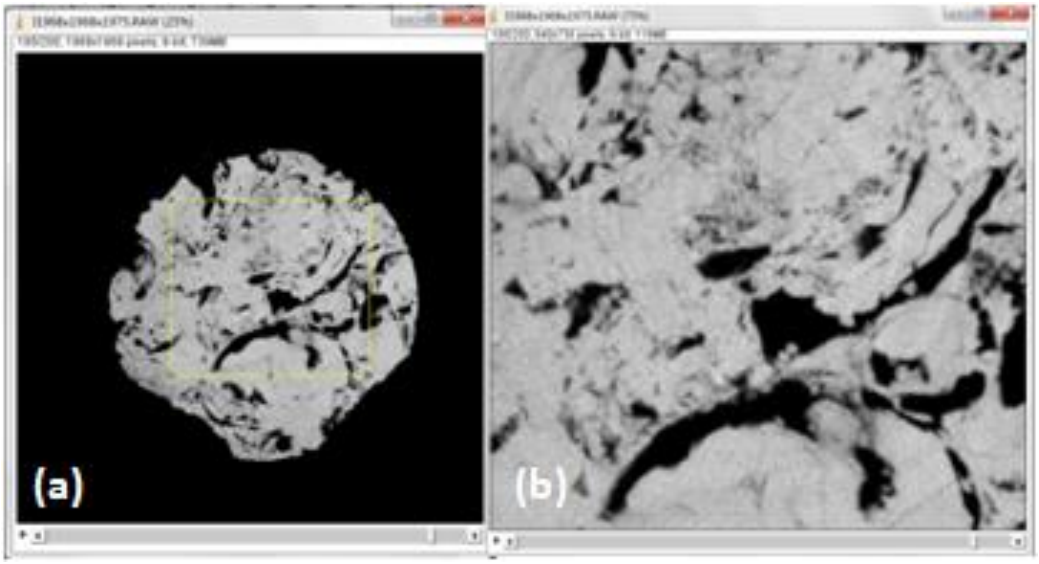

Figure B.4: The cropping area is set by the square with yellow boundary in (a) and (b) is the result after cropping.

B.2.2 Filtering

A median filter can be implemented by "Process->Filters->Median" showing the dialogue to set the radius of the region where the average of these grey scale data is used to replace the grey scale data of the point centred in this region. This median filter is 2D.

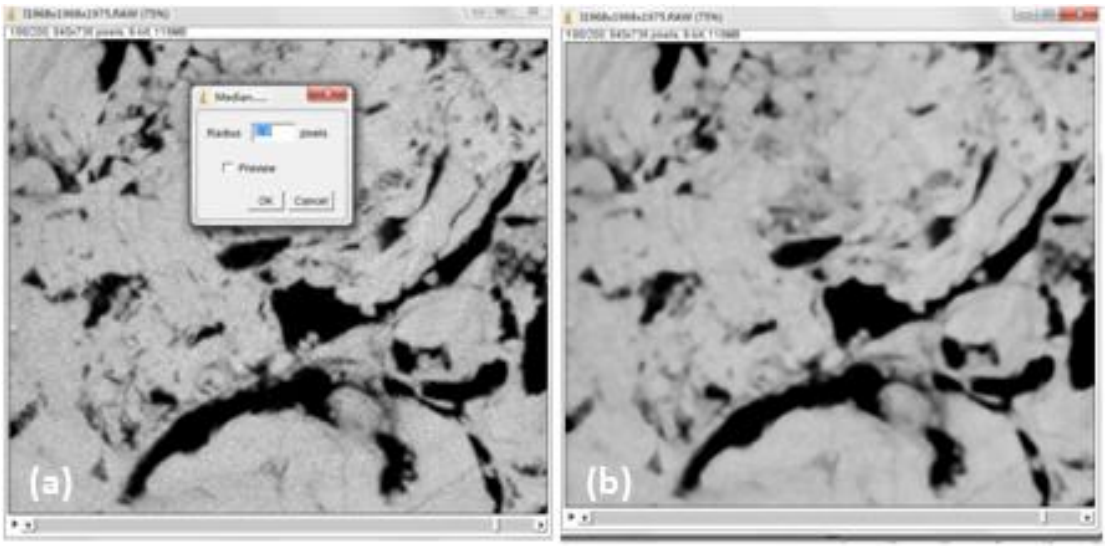

Figure B.5: The cropped images can be filtered by the median filter just set the radius of the filter. The effect of median filter can be shown in this figure. The noise which is the small points in (a) can be smoothed in (b).

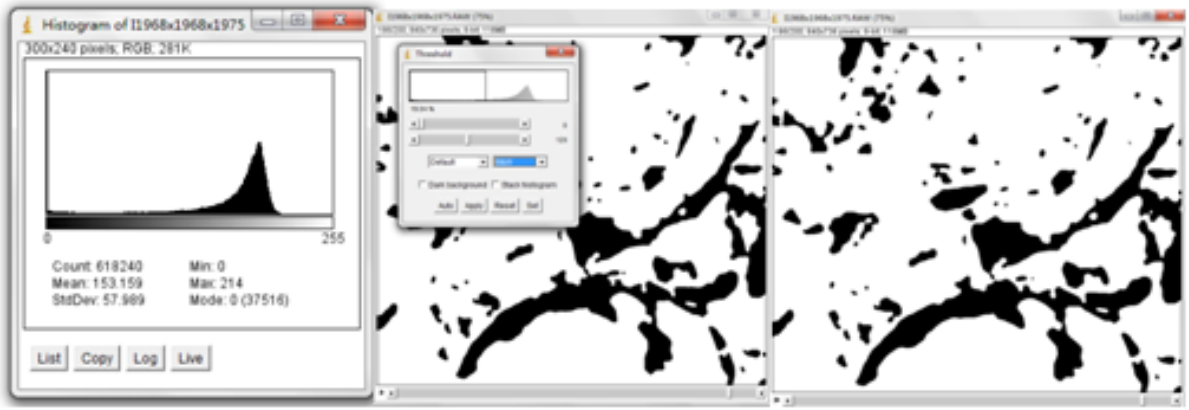

Figure B.6: The histogram of the images which can be used to offer threshold. If the threshold is difficult to extract from the histogram, the threshold can be chosen by comparing the difference of segmentation results with variable thresholds by the "Threshold" dialogue in (a) and (b). (c) is the binary image from auto threshold by the "Auto" function.

B.2.3 Segmentation

The segmentation is to divide the above grey scale data into binary data by setting threshold value.

This value can be determined from the histogram of these images shown from "Analyse->Histogram" in Figure B.6. There are two peaks in this histogram, the grey scale data of the one peak is in 0 and the grey scale data for the other one is about 191. The threshold data should be determined in the flat transition between the two peaks. Due to flat of the valley, it is not easy for user to determine the threshold while a auto threshold can be used in this software "Image->Adjust->Threshold". Visual inspection can be implemented by the dialogue box from this order to show the results of segmentation with different threshold by moving the tags in this box. The segmentation by auto threshold can be implemented by the "Auto" in this threshold dialogue box.

Appendix C Pore Network Extraction

Al-Khrausi and Blunt (2007[13]) proposed a series of criteria to define the maximal ball hierarchy. In the work of Silin *et al.* (2003[189]) and Silin and Patzek (2006[188]), only two kinds of relations are given, masters and slaves, respectively reflecting the bigger and smaller balls comparison to their neighbours. Another relationship was introduced by Al-Khrausi and Blunt (2007[13]), the cluster represents the adjacent maximal balls with the same size shown in Figure C.1. This solved the ambiguity from those identical balls which are not trivial in the pore space represented by maximal balls. However, their work needs tremendous memory usage and hence is useful for relatively small porous media with pores less than a thousand. Besides, pore network from their method tends to form high connection numbers.

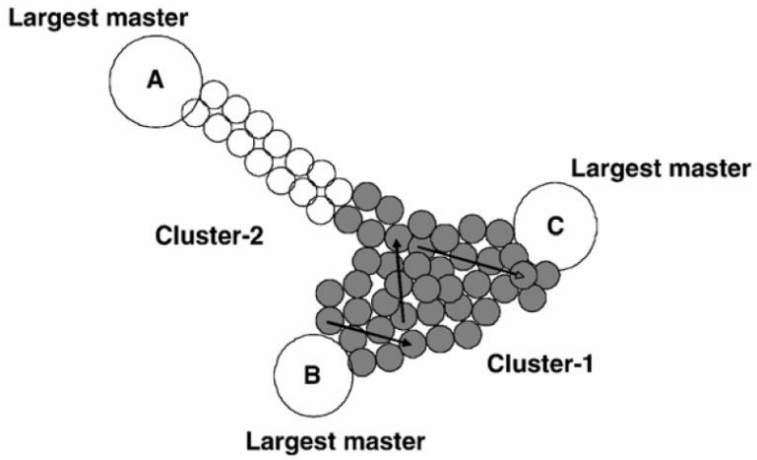

Figure C.1: Clusters are defined to merge the spheres with the same size in the pore space (Al-Khrausi and Blunt, 2007[13]).

In order to improve the maximal balls based method, Dong (2007[63]) used a new method to find maximal balls and proposed a cluster process to define pores and throats by ranking the maximal balls in a family tree by their size and their sequence being connected to existed branches on the family trees. The ancestor of each family tree is the pore and the common child is the throats. The cluster process begins with taking the largest maximal ball in the image as a pore and continues with the next biggest one. Thus the relationship between the ancestors and their children with a smaller size is the same as human intuition which is helpful for pore recognition.

In this section, the basic concepts used in the maximal ball based methods are introduced. These terms mainly are maximal balls, clusters and then the process of pore network extraction are given.

C.1 Basic concepts

C.1.1 Maximal Balls (MBs)

MBs are the basic element to represent the pore space and then to offer the geometrical and topological properties of the pore space. MB should touch the grain surface and cannot be totally overlapped by any other MB. The pore space of a porous medium can be quantified by the aggregate of all MBs without redundancy. In continuum scale, the sphere can be described by a centre *C* and radius *R*. However it is difficult to define a precise radius in the discrete image which is shown in Figure C.2.

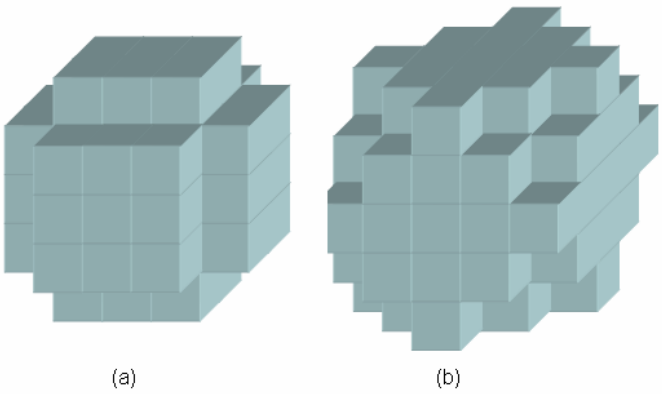

Figure C.2: Example of a digital sphere with $R_2=6$ (a) and $R_2=8$ (b) voxel units (Dong, 2007[63]).

So a range with lower and upper limits is used to define the size of a maximal ball, $R^2_{LEFT} <= R^2 <= R^2_{RIGHT}$.The R^2_{LEFT} and R^2_{RIGHT} are the squares of the lower and upper limits.

R^2_{RIGHT} is the squared Euler distance from the ball center $C(x_c, y_c, z_c)$ to the nearest solid voxel $V_g(x_g, y_g, z_g)$ calculated in Equation C.1.

$$R^2_{RIGHT} = dist^2\left(C, V_g\right) = \left(x_g - x_c\right)^2 + \left(y_g - y_c\right)^2 + \left(z_g - z_c\right)^2, C \in S, V_g \in S_g \qquad (C.1)$$

Where S and S_g mean the discrete void and solid space respectively.

R^2_{LEFT} is defined the maximum distance from the ball centres to the voxels in this ball.

$$R^2_{LEFT} = \max\left\{dist^2\left(C, V\right) \middle| dist^2\left(C, V\right) < R^2_{RIGHT}, V \in S, C \in S\right\} \qquad (C.2)$$

Figure C.3 give an example of digital spheres with squared radius are 6 and 8 which are the lower limit and upper limit for a maximal ball.

$R^2_{LEFT} \le R^2 \le R^2_{RIGHT}$

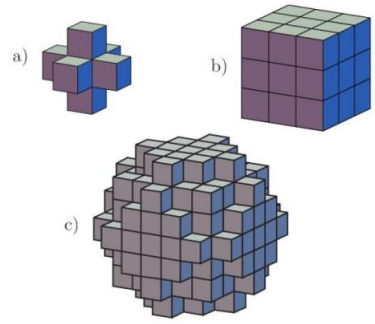

Figure C.3: The representation of digital balls with different radius by discrete voxels: (a) R=1;(b)R= $\sqrt{3}$;(c)R= $\sqrt{13}$ (Silin *et al.*, 2003[189]).

C.1.2 Cluster

MB exists not only in the central pore space but also in the irregular pore corners. In order to calculate the topology, the MBs should be classified as two kinds of clusters, single and multi clusters.

In a single cluster, a principal MB is determined by a largest maximal ball. Then this principal ball merges all its near smaller balls in its region. The process of merging these neighbours of an MB with a radius of R is shown in Figure C.4.

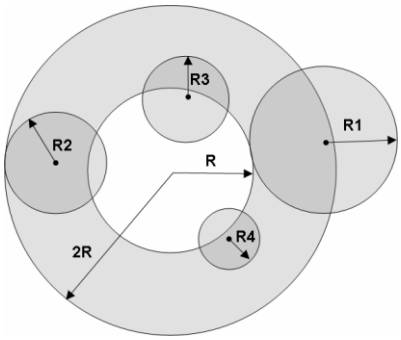

Figure C.4: This is a schematic figure of a single cluster. The white ball is the principal ball which is the parent and its children is the smaller balls surrounded in a range of *2R*, ($R>R_1>R_2>R_3>R_4$). The children are defined by the smaller pores overlapping or touching the parent ball and the generation number of the children will be 1 greater than their parent (Dong, 2007[63]).

The merging region of the principal MB is a spherical space with twice the radius of the ball sufficiently finding the smaller children. The squared Euler distance between the principal ball centre and the centre of a smaller ball can be used to determine whether this smaller ball in the merging region or not by Equation (C.3).

$$\mathrm{dist}\left(C_1,C_2\right) < R_{RIGHT,1} + R_{RIGHT,2}\ C_1\ C_2 \in S \qquad (C.3)$$

Where C_1, C_2 are the centres of balls.

The principal ball taken as parent and the smaller balls as children are arrangement by the concept of family tree. Each of them has a generation number. This generation number of direct children ranked as 1 is greater than the parent.

Multi-clusters can be built based on the concept of a single cluster. Any parent and its children can merge their related smaller balls as their related next generation with greater generation number in the family tree. By this way, the cluster becomes multi-clusters due to the generation of new children. Each node on this family tree uses the same rule to scan its *2R* spherical space and find its intersected offspring. The relationships between different generations in this family tree not only trace from parent to children but also reversely searching the parent for each node which is much more important for sub-level MBs to trace back until the common parent found.

So a number of family tree (pore clusters) with different common parent can be built in the pore space. In every pore cluster, the pore is defined by the common ancestor of its cluster while a MB connected to two clusters, which can trace two different common ancestors, can be regarded as throat. An MB chain can be determined from the throat to pore by tracing back to search parents which is shown in Figure C.5.

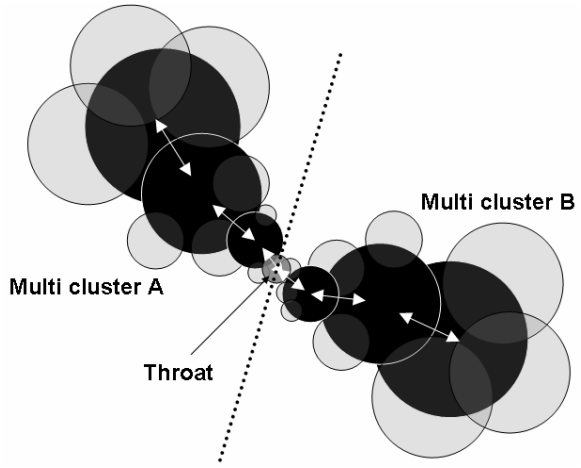

Figure C.5: Single clusters extend their family trees by absorbing their related new generations for the ancestor, and its offspring to generate multi-clusters. Generation number, family name and parent's name are recorded to keep the connection of the family tree from top to bottom and converse. When throat is distinguished as a common child of different families, MB chains are formed in white arrows and two pore-throat structures are built (Dong, 2007[63]).

The chains traced bilaterally from pore to throat are used to define the topology of the pore space. MBs are trivial for topology but are important to define the shape and size of the pores and throats. The individual pores and throats can be segmented based on the parenting hierarchy.

C.2 Pore Network Extraction

C.2.1 Maximal Balls Generation

In the binary image, the inscribed spheres at every pore voxels are firstly built by determination of the spheres centred in each pore voxel and just touching the grain surface. And then the spheres found inside an existing maximal ball will be removed as an inclusion.

The inscribed sphere at each voxel is determined by two steps. In the first expansion step is to find the solid or boundary in 26 directions including lateral, diagonal and diametrical lines which are shown in Figure C.6. In the second shrink step is to determine the real radius of R_{RIGHT} and R_{LEFT} by selecting the maximum of the distance from each pore voxel inside this sphere to the nearest solid voxel and choosing a distance less than maximum. The inscribed spheres on every pore voxels can be built before finding the maximal balls.

$$\text{B=B}\left(C_i, R_i, R_{RIGHTi}\right) B \subset S, C_i \in S, i = 1, 2, 3, ..., n \qquad (C.4)$$

Where n is the number of pore voxels in the 3D binary images.

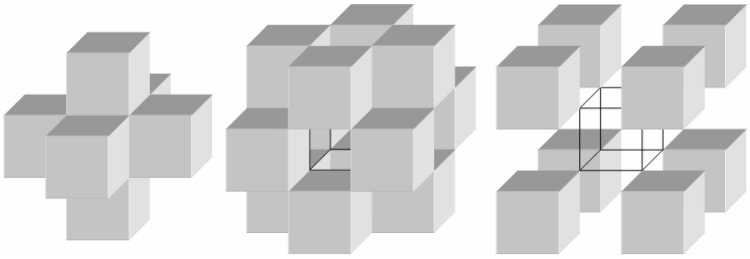

Figure C.6: Three kinds of directional lines based on central cell are used in inflating step to find the nearest solid surface. The left picture shows 6 lateral directions with 1 voxel length for each step. The middle figure is 12 diagonal lines and each step is $\sqrt{2}$ voxel length. The right one defines the 8 diametrical direction lines and the length of each step is $\sqrt{3}$ voxel (Dong, 2007[63]).

The inscribed spheres totally inside another sphere should be removed due to their redundancy without extra information for the determination of the void space. The remove can be implemented by comparing the distance from the two sphere centre with their related radius. Taking a ball A centred at C_A with the radius of $R_{RIGHT\ A}$ and $R_{LEFT\ A}$ and a ball B in C_B with radius $R_{LEFT\ B}<=R<R_{RIGHT\ B}$ for an example, Ball B is totally embedded in A if the Euclidean distance of centres is not more than the different of the radius expressed in Equation (C.5).

$$dist(C_A, C_B) \leq \left| R_{RIGHT,A} - R_{LEFT,B} \right| \qquad (C.5)$$

The difference of the radius is defined by the R_{RIGHT} radius of the outer ball and the R_{LEFT} radius of the embedded ball. After removing the inclusion, the overlapping maximal ball can fill the whole pore space without a redundancy. The discrete pore space is converted into an aggregate of maximal balls. Every void voxel in the image is occupied by one or more maximal balls and then the pores and throats of the pore space can be classified by clustering these maximal balls.

C.2.2 Identification of the Maximal Ball Clusters

To identify pores and throats, a clustering algorithm is described below:

Firstly, all maximal balls can be classified as different groups according to their size. These MBs with same size are in the same group. The largest MBs lie in the first group and the number of these balls in this group denoted by M with initially infinite rank.

Secondly, beginning with a first ball A with largest size, it is defined as a pore and ranked as first generation. All its smaller intersected maximal balls are merged by A and ranked as the second generation with remember their ancestor and parent to form a multi cluster.

Thirdly, a maximal ball B can be sorted from the rest of the balls in the first group. Starting from the first, ball B merges its smaller unranked maximal and ranks them the next younger generation in the family tree. This younger generation inherits the family name of ancestor and takes B as parent. If B is infinite before processing, B generates a new pore cluster as an ancestor of this cluster. If not, B is part of its ancestor's pore body and changes the name from family to children.

Fourthly, the next maximal ball with same size operates the same sorting and clustering processes until there is no processed maximal ball left in this group. And then these processes move to next group with smaller size.

Finally, the same sorting and clustering processed are used for all the groups. And the last group consists of maximal balls with the minimum size.

C.2.3 Pore Space Segmentation

The pore space segmentation is based on the pore-throat chains generated by maximal ball clustering. These chains form the skeleton of the pore space and the pore bodies are determined by the ancestor of each pore-throat chains. The main problem is

to determine the throat which is defined by the maximal ball where the two or more chains meet in Figure C.7.

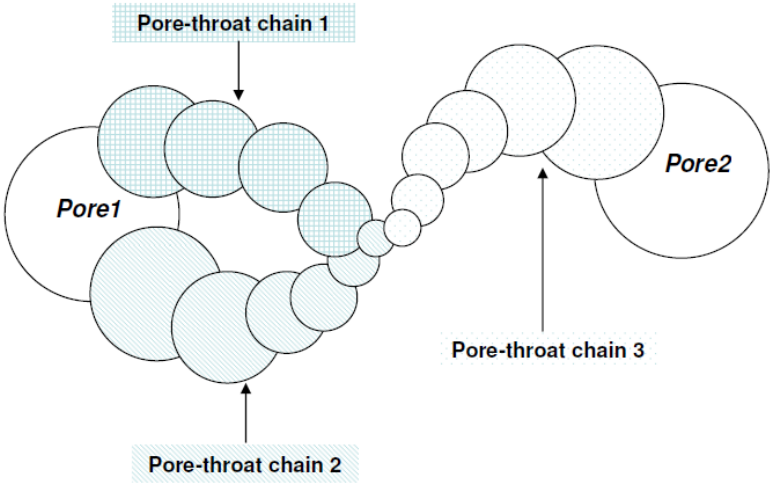

Figure C.7: Pore-throat chains merged in one channel (Dong, 2007[63]).

The benefit of this method is that it is easy for every maximal ball to connect to the pore-throat chains without tracing the ancestor. However it causes the underestimation of the throat length and overestimation of the pore length.

Appendix D Basic Definitions and Notations

Definition of Image

An n dimensional binary image P can be defined by a quadruple according to Kong and Rosenfeld (1989[107]).

$$P \equiv (V, \alpha, \beta, B) \tag{D.1}$$

where V is a finite subset of the rectilinear grid Z^n, called the image space of P, (α, β) is a pair of adjacencies and $B \subset V$ is the set of object points. In particular, an image P can be simplified as as $P = (V, B)$ without consideration of adjacencies.

Definition of a Point in the Image

A point p in $V \subset Z^n$ is uniquely defined by a set of n integers $(c_p^1, c_p^2, \cdots, c_p^n)$ simply representing the Cartesian coordinates of a point p in Z^n . In 2D discrete space, a point is called pixel denoted as (p_x, p_y) or (p_x, p_y, p_z) in 3D with the name of voxel.

For digital image processing, a finite rectangular lattice V with the range of $[0, L^j]$ in the *jth* direction is commonly expressed as

$$V = \left\{ (c_p^1, c_p^2, \cdots, c_p^n) : 0 \le c_p^j \le L^j \text{ and } L^j \in Z^+, j = 1, 2, \cdots, n \right\} \tag{D.2}$$

Definition of Interior and Border Points

For an image $P = (V, B)$, an interior point of p satisfies $0 < c_p^j < L^j, \forall\ j \in \{1, 2, \cdots, n\}$;

Otherwise p is a border point of image P.

Definition of Neighbourhood

For a rectangular lattice V, the direct neighbourhood of a point $p \in V$ in an image $P = (V, B)$ is defined as

$$N(p) = \left\{ q \in V : \max\left(\left| c_p^1 - c_q^1 \right|, \cdots, \left| c_p^n - c_q^n \right| \right) \le 1 \right\} \tag{D.3}$$

In Figure D.1, a direct neighbourhood of a point p in 2D and 3D is shown. The square in 2D or cube in 3D is used to represent a point of a discrete object consisting of a lattice of points.

The direct neighbourhood of the point p is $N(p)$ in expression. The set of points of $N(p)$ excluding the point p, $N(p)\setminus\{p\}$, is denoted as $N^*(p)$.

Each point in $N^*(p)$ is called an adjacent point of p.

Definition of Adjacency

Two points p and q are in $\alpha-$*adjacent*, if $q \in N_\alpha(p)$ or $p \in N_\alpha(q)$.

In 2D, there are two kinds of adjacencies, 4 and 8-adjaciency; In 3D, 6, 18 and 26-adjacency exist.

In Figure D.1 (a) and (b), for the points in $N^*(p)$, each pixel is 4- and 8-adjacent to p, each black pixel is 8-adjacent to p. In Figure D.1 (c), for the points in $N^*(p)$, each white is 6-, 18- and 26-adjacent to p, each grey point is 18- and 26-adjacent to p and each black is only 26-adjacent to p.

Definition of $\alpha-$Neighbourhood

The $\alpha-$neighbourhood of a point p is the set of all points in Z^n that are $\alpha-$adjacent to the point p including itself by the expression of $N_\alpha(p)$, $N_\alpha(q) = N_\alpha^*(p) \cup \{p\}$.

In Figure D.1 (a) and (b), the 4-neighbourhood of the central point p is in grey q_2, q_4, q_5, q_7 and the central point p. In Figure D.1 (c), the 26-neighbourhood $N_{26}(p)$ of the central point p includes 26 points respectively in white, grey and black as well as the central point.

According to the definition of adjacency, all points in $N^*(p)$ can be categorised as three different neighbours of p based on their adjacencies with p.

(I) A 6-neighbour is 6-adjacent to p;

(II) A 18-neighbour is 18-adjacent but not 6-adjacent to p;

(III) A26-neighbour is 26-adjacent but not 18-adjacent to p.

Similarly, in 2D two kinds of neighbours, 4- and 8-neighbours, can be identified according to the 4- and 8-adjacency.

Definition of $\alpha-$Neighbourhood-Set

The $\alpha-$neighbourhood-set of a point p, expressed by $\tilde{N}_\alpha(p)$, is the set of all $\alpha-$neighbour of the point p.

In Figure D.1 (c), each white point is 6-neighbourhood of p, $(q_5, q_{11}, q_{13}, q_{14}, q_{16}, q_{22})$; each grey point is 18-neighbourhood of p, $(q_2, q_4, q_6, q_8, q_{10}, q_{12}, q_{15}, q_{17}, q_{19}, q_{21}, q_{23}, q_{25})$; each black is 26-neighbourhood of p, $(q_1, q_3, q_7, q_9, q_{18}, q_{20}, q_{24}, q_{26})$. The 18-neighbourhood-set $\tilde{N}_{18}(p)$ consists of all grey points.

The relations between the direct neighbourhood $N(p)$, the $\alpha-$neighbourhood $N_\alpha(p)$ and the $\alpha-$neighbourhood-set $\tilde{N}_\alpha(p)$, $\alpha = 6, 18, 26$ of a point p is:

$$\begin{aligned} &N(p) = N_{26}(p); \\ &N_\alpha(p) = N^*_\alpha(p) \cup \{p\}, \alpha = 6, 18, 26; \\ &N^*_{26}(p) = \tilde{N}_{26}(p) \cup \tilde{N}_{18}(p) \cup \tilde{N}_6(p); \\ &N^*_{18}(p) = \tilde{N}_{18}(p) \cup \tilde{N}_6(p); \\ &N^*_6(p) = \tilde{N}_6(p). \end{aligned} \tag{D.4}$$

Definition of Connectedness

Two points of p and q are $\alpha-$connected is the existence of a sequence $\{p_1, p_2, \cdots, p_m\}$ between p and q satisfying

$$p_i = N_\alpha(p_{i+1}), \forall\, i = 1, 2, \cdots, m-1;\ p_1 = p, p_m = q. \tag{D.5}$$

Such a sequence is called a $\alpha-$path with end points of p and q. If the path with the case of $p_1 = p_m$, this path is a closed path containing no end points. A $\alpha-$path is called $\alpha-$curve if it does not intersect (Figure D.2a) or touch (Figure D.2b) itself except at end points.

Definition of $\alpha-$component

A subset of Z^n is said to be $\alpha-$component if any two points in this subset are $\alpha-$connected.

For instance, the set of grey in Figure D.2 (c) is an 8-component but not a 4-component. The set of grey in Figure D.2 (d) is a 26-component but it is neither an 18-component nor a 6-component.

For a binary image $P \equiv (V, \alpha, \beta, B)$, the object set B and background set V\B must satisfies different adjacencies (α, β) according to the requirement of the digital curve and surface theorem that a simple close curve or surface must separate the 2D or 3D space into two disconnected parts.

In 2D, the only two adjacent pairs are $(4,8)$ and $(8,4)$. In 3D, there are four adjacent pairs $(6,26)$, $(6,18)$, $(18,6)$ and $(26,6)$. For instance, points *s* and *t* both belonging to V\B are 8-adjacent so they cannot be separated by the 8-cruve. Hence, V\B must have 4-adjacency in order to separate by a black curve in B.

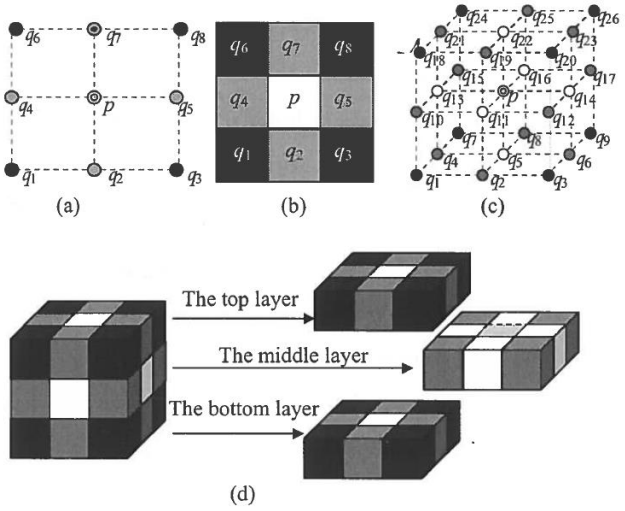

Figure D.1: The direct neighbourhoods $N(p)$ of a point p. (a) and (b) show different representations of the 2D direct (3×3) neighbourhoods, where $N(p) = \{q_1, q_2, q_3, q_4, p, q_5, q_6, q_7, q_8\}$; (c) and (d) show two different representation of the 3D direct $(3\times3\times3)$ neighbourhood, where $N(p) = \{q_1, q_2, \cdots, q_{13}, p, q_{14}, q_{15}, \cdots, q_{26},\}$ (Jiang, 2008[92]).

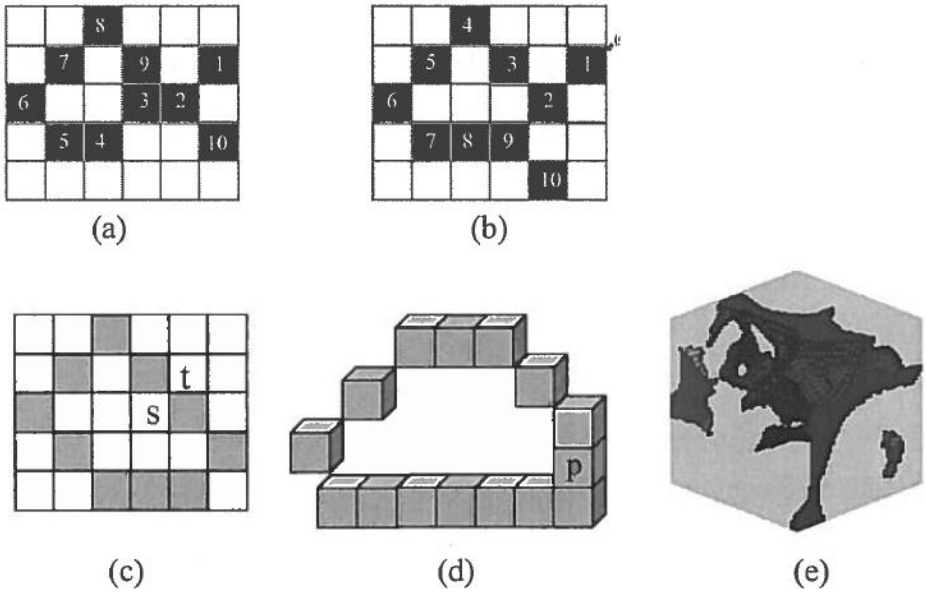

Figure D.2: Examples of paths, curves and components. (a) a path $\{1,2,\cdots,9,2,10\}$ intersect itself;(b) a path $\{1,2,\cdots,10\}$ touches itself; (c) the set of grey pixels can be organized as a closed 8-curve, but not as a 4-curve; (d) the set of grey voxels is a 26-path, but not a 26-curve because voxel p has three 26-adjacent grey voxels. The set of grey pixels in (c) is an 8-component but not 4-component, and the set of grey pixels in (d) is a 26-component but not a 18- or a 6-component. Note that in (a)~(d) all white (background) voxels are invisible for clarity. In (e) an example is shown of 4 26-components in 3D (Jiang, 2008[92]).

Appendix E Relationships between Pore (Throat) Radius, Shape Factor, Specific Surface and Cross Sectional Area

Appendix E: Relationships between Pore (Throat) Radius, Shape Factor, Specific Surface and Cross Sectional Area

From the point of network, the pore and throat in the pore network is presented as a series of capillary cylindrical tubes with a constant but arbitrary cross section and this section is described by a dimensionless shape factor G

$$G = \frac{VL}{A_s^2} \qquad (E.1)$$

Where A_s is the surface area of the pore or throat unit; V is the unit volume; L is the length of the pore or throat. It is equivalent to

$$G = \frac{A}{P^2} \qquad (E.2)$$

Where A is the cross-sectional area and P is perimeter (Mason and Morrow, 1991[130]).

In the pore network, the shapes of the cross section are usually presented by triangle, circle and square shown in Figure E.1.

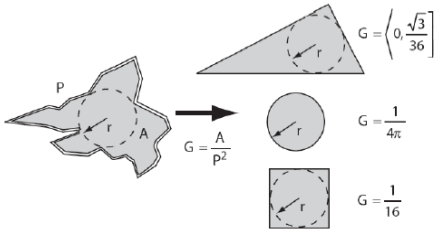

Figure E.1: The dimensionless shape factor for network pores and throats (Mason and Morrow, 1991[130]).

In the above figure, r is the radius of the pore and throat defined as the inscribed radius of the maximal ball (MB).

Another parameter used to describe the complexity of the pore system is specific area which is defined as

$$S = \frac{A_s}{V} \qquad (E.3)$$

Where A_s is the surface area of the pore or throat unit; V is the unit volume; It can be simplified as the ratio between the total perimeter P and the total pore space area A of the cross section.

$$S = \frac{P}{A} \qquad (E.4)$$

Generally, a small specific area presents a simple pore structure while a large number indicates an intricate pore system.

The relationship between shape factor, specific area, cross section area and pore unit radius can be derived according to the below formula.

For triangle in Figure E.2, the inscribed circle with radius r and the three angles for the triangle are 2α, 2β and 2γ respectively. The perimeter and area of the cross section can be expressed by the angles and radius.

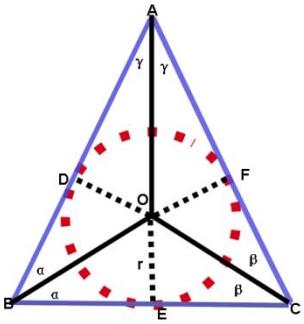

Figure E.2: The inscribed circle with radius r in an arbitrary triangle with three angles as 2α, 2β and 2γ.

The perimeter and area of the triangle can be expressed by the length of BD, FC and AD which are related to the inscribed circle radius r and the angles given in Equation E.5.

$$\begin{aligned} BD &= \frac{OD}{\tan\alpha} = \frac{r}{\tan\alpha} \\ FC &= \frac{OF}{\tan\beta} = \frac{r}{\tan\beta} \\ AD &= \frac{OD}{\tan\gamma} = \frac{r}{\tan\gamma} \end{aligned} \qquad (E.5)$$

And then the perimeter and area are expressed in Equation E.6 and E.7.

$$P = 2r\left(\frac{1}{\tan\alpha}+\frac{1}{\tan\beta}+\frac{1}{\tan\gamma}\right) \qquad (E.6)$$

$$A = r^2\left(\frac{1}{\tan\alpha}+\frac{1}{\tan\beta}+\frac{1}{\tan\gamma}\right) \qquad (E.7)$$

Setting $TAN = \left(\frac{1}{\tan\alpha}+\frac{1}{\tan\beta}+\frac{1}{\tan\gamma}\right)$, and then the relationship between shape factor and TAN is given by Equation E.8 and E.9.

$$G = \frac{1}{4TAN} \qquad (E.8)$$

$$TAN = \frac{1}{4G} \qquad (E.9)$$

The shape factor and the radius for each element (pore and throat) can be given in the pore network geometry, and then the area relating to the ratio of the cross section area between pore and throat (PTAR) and specific area reflecting the complexity of the pore system can be calculated by them in Equation E.10.

$$A = \frac{r^2}{4G}$$
$$S = \frac{2}{r} \qquad (E.10)$$

For the rectangle shape, the shape factor, area of the cross section and specific area can be expressed by the pore or throat radius r in Equation E.11.

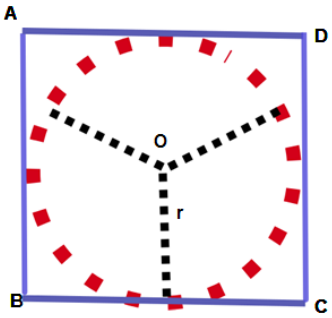

Figure E.3: The inscribed circle with radius r in a rectangular cross section.

$$G = \frac{1}{16}$$
$$A = 4r^2 \qquad (E.11)$$
$$S = \frac{2}{r}$$

For the circle shape, the shape factor, area of the cross section and specific area can be expressed by the pore or throat radius r in Equation E.12.

$$G = \frac{1}{4\pi}$$
$$A = \pi r^2 \qquad (E.12)$$
$$S = \frac{2}{r}$$

Appendix F Porosity Exponent for A Pore-Throat Conjunction in The Mix Electrical Combination

The effect of the length and size of the pore system including pore body and throat on the porosity exponent is theoretically analysed from the equivalent electrical model of the pore-throat conjunction. These results from the analysis of the theory can confirm the validity of the correlation between porosity exponents and the geometrical properties of the three carbonate samples. Considering the porosity in the sandstones and carbonates, the maximum of the porosity in each simple capillary electrical model is 40%.

The relationship between the formation factor and the porosity exponent is given in Equation known as Archie first law. It is expressed here as Equation F.1

$$F_R = \frac{R_0}{R_w} = \frac{1}{\phi^m} \quad (F.1)$$

Where R_0 and R_w are the resistivity of the porous media fully saturated by brine $S_w = 100\%$ and the resistivity of the brine respectively, ϕ is the porosity of the porous media.

In this section, the electrical resistance and conductance calculation are needed according to Ohm's Law.

$$r = R\frac{L}{A} \quad (F.2)$$

$$C = \sigma\frac{A}{L} \quad (F.3)$$

Where r and C are the resistance and conductance of the resistor respectively. Their resistivity and conductivity are R and σ respectively. A is the cross-section area and L is the length of the conductor.

According to the electrical resistor arrangement in series or parallel, the resistance for the n resistors in series is

$$r = \sum_{i=1}^{n} r_i \quad (F.4)$$

The conductance of the n resistors in parallel is

$$C = \sum_{i=1}^{n} Ci \quad (F.5)$$

In the next section, the relationship between the porosity exponent and the size or length of the pore system is in the form as

$$y = \frac{a}{b+x} \quad (F.6)$$

And its derivative reflecting the variation of the dependent variable y with the increase in argument x

$$\frac{dy}{dx} = -\frac{a}{(x+b)^2} \tag{F.7}$$

When the derivative $dy/dx > 0$, it is increasing function, that is, the dependent variable y increases with the increase of the argument; If the derivative $dy/dx < 0$, it is decreasing function, the dependent variable decreases with the increase of the argument . For the above derivative, the numerator $a < 0$ is for the increasing function.

F.1 Porosity Exponent for A Simple Channel

Started from a simple pore channel with a current flow path in the pore space is considered in Figure F.1.

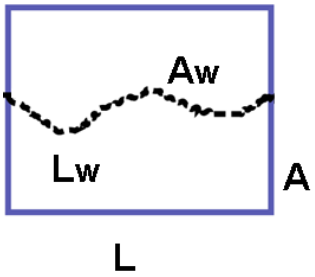

Figure F.1: Actual current flow path with its length L_w and cross sectional area A_w compared with the length L and the cross sectional area A of the pore-throat conjunction.

In the above Figure F.1, the tortuosity and the cross sectional area ratio can be defined as,

$$\begin{aligned} \tau &= L_w/L, \tau \geq 1 \\ \psi &= A_w/A, 0 < \psi < 1 \end{aligned} \tag{F.8}$$

The porosity of the channel can be given by

$$\phi = \frac{A_w L_w}{AL} = \psi\tau \tag{F.9}$$

Based on Equation F.1, F.2 and F.9, the porosity exponent is

$$m = -\frac{\log\tau - \log\psi}{\log\phi} = -\frac{\log\tau - \log\psi}{\log\tau + \log\psi} \tag{F.10}$$

F.1.1 Effect of The Tortuosity on The Porosity Exponent

The effect of the tortuosity on the porosity exponent is studied with the cross sectional area fixed, ψ constant. The new tortuosity is expressed by $\tau_{new} = x\tau, x \geq 0, \tau \geq 1$ and then the new porosity exponent based on Equation F.10 is

$$m_{new} = -1 + \frac{2\log\psi}{\log x + \log\tau + \log\psi} \tag{F.11}$$

According to Equation F.6, F.7 and F.8, its derivative is >0 indicates that with the increases of the tortuosity, the porosity exponent of this channel increases.

F.1.2 Effect of The Size of The Pore Channel on The Porosity Exponent

In this case, the tortuosity or the length of the pore channel is fixed, the cross section area changes from ψ to ψ_{new} , $\psi_{new} = x\psi, x \geq 0, 0 < \psi < 1$. The porosity exponent based on Equation F.10 is

$$m_{new} = 1 - \frac{2\log\tau}{\log x + \log\tau + \log\psi} \tag{F.12}$$

According to Equation F.6, F.7 and F.8, its derivative >0 indicates that with the increases of the cross sectional area, the porosity exponent of this channels increases.

F.2 Porosity Exponent for A Pore-Throat Conjunction

In this pore-throat conjunction, the n throats are in parallel and then they are connected to the pore in series according to the electrical arrangement in Figure F.2.

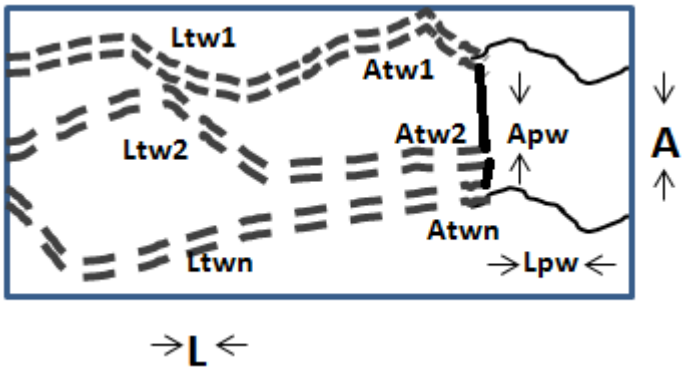

Figure F.2: The model for pore-throat conjunction with the throats in parallel and then connected to the pore in series. The size and the length of the throat are expressed by A_{twi} and L_{twi} and A_{pw}, L_{pw} are for pore with the length and the cross section area of this conjunction as L and A.

According to the Equation F.2, F.4 and F.5, the equivalent electrical resistance of the throats in parallel is

$$r_t = R_w \frac{1}{\sum_{i=1}^{n} \frac{A_{wti}}{L_{wti}}} \tag{F.13}$$

The resistance of this pore-throat junction is calculated based on Equation F.2, F.4 and F.13,

$$r_0 = r_p + r_t = R_w \left(\frac{L_{wp}}{A_{wp}} + \frac{1}{\sum_{i=1}^{n} \frac{A_{wti}}{L_{wti}}} \right) = R_0 \frac{L}{A} \tag{F.14}$$

The porosity is

$$\phi = A_{wp} L_{wp} + \sum_{i=1}^{n} A_{wti} L_{wti} \tag{F.15}$$

According to Equation F.8,

$$\begin{aligned} &\tau = \tau_p + \tau_t,\ \tau \geq 1 \\ &\tau_p = \mathrm{L_{Wp}}/\mathrm{L},\ \tau_p > 0 \\ &\tau_t = \mathrm{L_{Wt}}/\mathrm{L},\ \tau_t > 0 \end{aligned} \tag{F.16}$$

$$\psi = A_W / A, 0 < \psi < 1 \tag{F.17}$$

The porosity exponent of this conjunction can be given by Equation F.1, F.13, F.14, F.15, F.16 and F.17,

$$m = -\frac{\log\left(\frac{\tau_p}{\psi_p} + \frac{1}{\sum_{i=1}^{n} \frac{\psi_{ti}}{\tau_{ti}}} \right)}{\log\left(\psi_p \tau_p + \sum_{i=1}^{n} \psi_{ti} \tau_{ti} \right)} \tag{F.18}$$

F.2.1 Effect of The Tortuosity on The Porosity Exponent

The effect of the tortuosity on the porosity exponent is studied with the cross sectional area fixed, ψ constant. The new tortuosity is expressed by $\tau_{new} = x\tau, \tau_{pnew} = x\tau_p, \tau_{tnew} = x\tau_t, x \geq 0, \tau \geq 1$ and then the new porosity exponent based on Equation F.18 is

$$m_{new} = -\frac{\log\left(\frac{\tau_p}{\psi_p} + \frac{1}{\sum_{i=1}^{n} \frac{\psi_{ti}}{\tau_{ti}}} \right) + \log x}{\log\left(\psi_p \tau_p + \sum_{i=1}^{n} \psi_{ti} \tau_{ti} \right) + \log x} \tag{F.19}$$

Setting,

$$AN = -\log\left(\frac{\tau_p}{\psi_p} + \frac{1}{\sum_{i=1}^{n}\frac{\psi_{ti}}{\tau_{ti}}}\right) \quad (F.20)$$

$$BN = \log\left(\psi_p\tau_p + \sum_{i=1}^{n}\psi_{ti}\tau_{ti}\right) \quad (F.21)$$

According to F.15, $BN < 0$. The porosity exponent is

$$m_{new} = -1 + \frac{AN + BN}{BN + \log x} \quad (F.22)$$

According to F.17,

$$\frac{\tau_p}{\psi_p} + \frac{1}{\sum_{i=1}^{n}\frac{\psi_{ti}}{\tau_{ti}}} > \tau_p + \frac{1}{\sum_{i=1}^{n}\frac{\psi_{ti}}{\tau_{ti}}} \quad (F.23)$$

Based on F.16,

$$\min\{\tau_{ti}\} = 1 - \tau_p \quad (F.24)$$

According to Equation F.23 and F.24,

$$\sum_{i=1}^{n}\frac{\psi_{ti}}{\tau_{ti}} < \sum_{i=1}^{n}\frac{\psi_{ti}}{\tau_{\min}} = \frac{\sum_{i=1}^{n}\psi_{ti}}{1-\tau_p} \quad (F.25)$$

Due to the sum of the all throat cross sectional areal is less than the cross sectional area of the conjunction,

$$\sum_{i=1}^{n}\psi_{ti} < 1 \quad (F.26)$$

Based on Equation F.23, F.25 and F.26,

$$\frac{\tau_p}{\psi_p} + \frac{1}{\sum_{i=1}^{n}\frac{\psi_{ti}}{\tau_{ti}}} > \tau_p + \frac{1}{\sum_{i=1}^{n}\frac{\psi_{ti}}{\tau_{ti}}} > \tau_p + \frac{1-\tau_p}{\sum_{i=1}^{n}\psi_{ti}} > \tau_p + 1 - \tau_p = 1 \quad (F.27)$$

So $AN < 0$. According to F.20, F.21 and F.27,

$$(AN + BN) < 0 \quad (F.28)$$

According to Equation F.6, F.7 and F.28, its numerator is <0 so the derivative is >0 indicates that with the increases of the tortuosity, the porosity exponent of the pore-throat conjunction increases.

F.2.2 Effect of The Size of The Pore and Throat on The Porosity Exponent

In this case, the tortuosity or the lengths of the pore and throat in this conjunction are fixed, the cross section area changes from ψ to ψ_{new} , $\psi_{new} = x\psi, x \geq 0, 0 < \psi < 1$. The porosity exponent based on Equation F.18 is

$$m_{new} = -\frac{\log\left(\frac{\tau_p}{\psi_p} + \frac{1}{\sum_{i=1}^{n}\frac{\psi_{ti}}{\tau_{ti}}}\right) - \log x}{\log\left(\psi_p\tau_p + \sum_{i=1}^{n}\psi_{ti}\tau_{ti}\right) + \log x} \quad (F.29)$$

Based on Equation F.20 and F.21,

$$m_{new} = 1 + \frac{AN - BN}{BN + \log x} \quad (F.30)$$

$$AN - BN = -\log\left[\tau_p^2 + \tau_p\left(\frac{\psi_p}{\sum_{i=1}^{n}\frac{\psi_{ti}}{\tau_{ti}}} + \frac{\sum_{i=1}^{n}\psi_{ti}\tau_{ti}}{\psi_p}\right) + \frac{\sum_{i=1}^{n}\psi_{ti}\tau_{ti}}{\sum_{i=1}^{n}\frac{\psi_{ti}}{\tau_{ti}}}\right] \quad (F.31)$$

According to Equation F.24,

$$\sum_{i=1}^{n}\frac{\psi_{ti}}{\tau_{ti}} \leq \sum_{i=1}^{n}\frac{\psi_{ti}}{1-\tau_p} = \frac{\sum_{i=1}^{n}\psi_{ti}}{1-\tau_p} \quad (F.32)$$

$$\sum_{i=1}^{n}\psi_{ti}\tau_{ti} \geq \sum_{i=1}^{n}\psi_{ti}(1-\tau_p) \quad (F.33)$$

Based on Equation F.32 and F.33,

$$\frac{\psi_p}{\sum_{i=1}^{n}\frac{\psi_{ti}}{\tau_{ti}}} + \frac{\sum_{i=1}^{n}\psi_{ti}\tau_{ti}}{\psi_p} \geq \left(\frac{\psi_p}{\sum_{i=1}^{n}\psi_{ti}} + \frac{\sum_{i=1}^{n}\psi_{ti}}{\psi_p}\right)(1-\tau_p) \quad (F.34)$$

Due to

$$\frac{b}{a} + \frac{a}{b} \geq 2, \quad \forall ab > 0 \quad (F.35)$$

as well as the Equation F.31 and F.34,

$$\tau_p\left(\frac{\psi_p}{\sum_{i=1}^{n}\frac{\psi_{ti}}{\tau_{ti}}} + \frac{\sum_{i=1}^{n}\psi_{ti}\tau_{ti}}{\psi_p}\right) \geq 2\tau_p(1-\tau_p) \quad (F.36)$$

With the assumption that the porosity of each throat is the same,

$$\psi_{ti}\tau_{ti} = \psi_{ti}\tau_{ti}, \quad 1 \leq i \neq j \leq n \quad (F.37)$$

and Equation F.24,

$$\frac{1}{\sum_{i=1}^{n}\frac{\psi_{ti}}{\tau_{ti}}}\frac{1}{\frac{1}{\psi_{tj}\tau_{tj}}}=\frac{1}{\sum_{i=1}^{n}\frac{1}{\tau_{tj}^{2}}}\geq\frac{1}{\sum_{i=1}^{n}\frac{1}{\left(1-\tau_{p}\right)^{2}}}=\frac{\left(1-\tau_{p}\right)^{2}}{n} \qquad (F.38)$$

Based on this Equation,

$$\frac{\sum_{i=1}^{n}\psi_{ti}\tau_{ti}}{\sum_{i=1}^{n}\frac{\psi_{ti}}{\tau_{ti}}}=\frac{1}{\sum_{i=1}^{n}\frac{\psi_{ti}}{\tau_{ti}}}\frac{1}{\frac{1}{\psi_{t1}\tau_{t1}}}+\ldots+\frac{1}{\sum_{i=1}^{n}\frac{\psi_{ti}}{\tau_{ti}}}\frac{1}{\frac{1}{\psi_{tn}\tau_{tn}}}\geq\left(1-\tau_{p}\right)^{2} \qquad (F.39)$$

Based on Equation F.31, F.36 and F.39,

$$\tau_{p}^{2}+\tau_{p}\left(\frac{\psi_{p}}{\sum_{i=1}^{n}\frac{\psi_{ti}}{\tau_{ti}}}+\frac{\sum_{i=1}^{n}\psi_{ti}\tau_{ti}}{\psi_{p}}\right)+\frac{\sum_{i=1}^{n}\psi_{ti}\tau_{ti}}{\sum_{i=1}^{n}\frac{\psi_{ti}}{\tau_{ti}}}\geq\tau_{p}^{2}+2\tau_{p}\left(1-\tau_{p}\right)+\left(1-\tau_{p}\right)^{2}=1 \qquad (F.40)$$

According to Equation F.31and F.40,

$$(AN-BN)<0 \qquad (F.41)$$

According to Equation F.6, F.7 and F.41, its numerator is <0 so the derivative is >0 indicates that with the increases of the size of the pore and throat in the pore-throat conjunction, the porosity exponent of the pore-throat conjunction increases with the assumption that the porosity in each throat is the same.

References

[1]. Abousrafa, E., Somerville, J., Hamilton, S., Olden, P., Smart, B., and Ford, J., 2009: "*Pore geometrical model for the resistivity of brine saturated rocks"*. Journal of Petroleum Science and Engineering, 65(3-4): p. 113-122.

[2]. Adisoemarta, P., Anderson, G., Frailey, S., and Asquith, G., 2000: "*Historical use of m and a in well log interpretation: is conventional wisdom backwards?"*. SPE-59699 in the SPE Permian Basin Oil and Gas Recovery Conference, Midland, Texas, USA, 21-23 March. Society of Petroleum Engineers, p. 1-7.

[3]. Adler, P., Jacquin, C., and Quiblier, J., 1990: "*Flow in simulated porous media"*. International Journal of Multiphase Flow, 16(4): p. 691-712.

[4]. Adler, P.M., 1992: "*Porous media: geometry and transports"*, Boston, USA, Butterworth-Heinemann.540 p.

[5]. Aguilera, M.S. and Aguilera, R., 2003: "*Improved models for petrophysical analysis of dual porosity reservoirs"*. Petrophysics, 44(1): p. 21-35.

[6]. Aguilera, R., 1976: "*Analysis of Naturally Fractured Reservoirs From Conventional Well Logs (includes associated papers 6420 and 6421)"*. Journal of Petroleum Technology, 28(07): p. 764-772.

[7]. Aguilera, R., 1995: "*Naturally Fractured Reservoirs "*, 2nd Edition, Tulsa, Oklahoma, PennWell Books.521 p.

[8]. Aguilera, R., 2010: "*Effect of Fracture Dip and Fracture Tortuosity on Petrophysical Evaluation of Naturally Fractured Reservoirs"*. Journal of Canadian Petroleum Technology, 49(9): p. 69-76.

[9]. Aguilera, R.F. and Aguilera, R., 2004: "*A triple porosity model for petrophysical analysis of naturally fractured reservoirs"*. Petrophysics, 45(2): p. 157-166.

[10]. AL-Awad, M., 2001: "*Evaluating Uncertainty in Archie's Water Saturation Equation Parameters Determination Methods"*. SPE-68083 presented at SPE Middle East Oil Show, Bahrain, 17-20 March. Society of Petroleum Engineers. p. 1-10.

[11]. Al-Ghamdi, A., Aguilera, R., and Clarkson, C.R., 2011: "*Cementation Exponent Estimation for Complex Carbonate Reservoirs Using a Triple Porosity Model"*. SPE 149104 in the SPE/DGS Saudi Arabia Section Technical Symposium and Exhibition, Al-Khobar, Saudi Arabia, 15-18 May. Society of Petroleum Engineers, p. 1-12.

[12]. Al-Ghamdi, A., Chen, B., Behmanesh, H., Qanbari, F., and Aguilera, R., 2011: "*An Improved Triple-Porosity Model for Evaluation of Naturally Fractured Reservoirs"*. SPE Reservoir Evaluation & Engineering, 14(4): p. 377-384.

[13]. Al-Kharusi, A.S. and Blunt, M.J., 2007: "*Network extraction from sandstone and carbonate pore space images"*. Journal of Petroleum Science and Engineering, 56(4): p. 219-231.

[14]. Araújo, A.D., Bastos, W.B., Andrade Jr, J.S., and Herrmann, H.J., 2006: "*Distribution of local fluxes in diluted porous media"*. Physical Review E, 74(1): p. (010401)1-4.

[15]. Archie, G.E., 1942: "*The electrical resistivity log as an aid in determining some reservoir characteristics"*. Transactions of the AIME, 146(54): p. 54-62.

[16]. Archie, G.E., 1947: "*Electrical resistivity an aid in core-analysis interpretation"*. AAPG Bulletin, 31(2): p. 350-366.

[17]. Archie, G.E., 1952: "*Classification of carbonate reservoir rocks and petrophysical considerations"*. AAPG Bulletin, 36(2): p. 278-298.

[18]. Arns, C., Bauget, F., Ghous, A., Sakellariou, A., Senden, T., Sheppard, A., Sok, R., Pinczewski, W., Kelly, J., and Knackstedt, M., 2005a: "*Digital core*

laboratory: Petrophysical analysis from 3D imaging of reservoir core fragments". Petrophysics, 46(4): p. 260-277.

[19]. Arns, C.H., 2002: "*The influence of morphology on physical properties of reservoir rocks "*. PhD thesis, School of Petroleum Engineering, The University of New South Wales, Sydeny, Australia.244 p.

[20]. Arns, C.H., Bauget, F., Limaye, A., Sakellariou, A., Senden, T., Sheppard, A., Sok, R.M., Pinczewski, W., Bakke, S., and Berge, L.I., 2005b: "*Pore-scale characterization of carbonates using X-ray microtomography"*. SPE Journal, 10(4): p. 475-484.

[21]. Arns, C.H., Knackstedt, M.A., Pinczewski, W.V., and Garboczi, E.J., 2002: "*Computation of linear elastic properties from microtomographic images: Methodology and agreement between theory and experiment"*. Geophysics, 67(5): p. 1396-1405.

[22]. Arns, J., Sheppard, A., Arns, C., Knackstedt, M., Yelkhovsky, A., and Pinczewski, W., 2007: "*Pore-level validation of representative pore networks obtained from micro-CT images"*. SCA2007-15 in the Proceedings of the International Symposium of the Society of Core Analysts, Calgary, Canada, 10-12 September. p. 1-12.

[23]. Asquith, G.B., 1985: "*Handbook of log evaluation techniques for carbonate reservoirs"*, Tulsa, USA, American Association of Petroleum Geologists.47 p.

[24]. Auzerais, F., Dunsmuir, J., Ferreol, B., Martys, N., Olson, J., Ramakrishnan, T., Rothman, D., and Schwartz, L., 1996: "*Transport in sandstone: a study based on three dimensional microtomography"*. Geophysical Research Letters, 23(7): p. 705-708.

[25]. Bakke, S. and Øren, P.-E., 1997: "*3-D pore-scale modelling of sandstones and flow simulations in the pore networks"*. SPE Journal, 2: p. 136-149.

[26]. Bakke , S., Roth, S., Held, R.J., and Rueslåtten, H.G., 2007: "*Pore Scale Modelling of Carbonate Reservoir Rocks"*. SCA2007-18 in the International Symposium of the Society of Core Analysts, Calgary, Canada, 10-12 September. Society of Core Analysts, p. 1-12.

[27]. Ballay, R.E., 2012: *The "m" Exponent in Carbonate Petrophysics* [Online]. GeoNeurale.February, 2012, Available: http://www.geoneurale.com/ [Accessed 15 April 2012].

[28]. Bassiouni, Z., 1994: "*Chapter 1–electrical resistivity of rocks"*. In: (eds.) Theory, Measurement and Interpretation of Well Logs, SPE Textbook Series Richardson, Texas: Henry L. Doherty Memorial Fund of AIME, Society of Petroleum Engineers. p. 1-24.

[29]. Bear, J., 1972: "*Dynamics of fluids in porous media"*, New York, USA, American Elsevier Publishing Company.757 p.

[30]. Berg, C.R., 2004: *Dual and triple porosity models from effective medium theory* [Online].2004, Available: http://www.resdip.com/docs/new%20dual%20porosity2.doc. [Accessed 11 September 2014].

[31]. Berg, C.R., 2006: "*Dual-porosity equations from effective medium theory"*. SPE-101698 presented at SPE Annual Technical Conference and Exhibition, San Antonio, Texas, USA 24-27 September. Society of Petroleum Engineers. p. 1-10.

[32]. Blunt, M., Zhou, D., and Fenwick, D., 1995: "*Three-phase flow and gravity drainage in porous media"*. Transport in Porous Media, 20(1-2): p. 77-103.

[33]. Blunt, M.J., 2001: "*Flow in porous media—pore-network models and multiphase flow*". Current Opinion in Colloid & Interface Science, 6(3): p. 197-207.

[34]. Blunt, M.J., Bijeljic, B., Dong, H., Gharbi, O., Iglauer, S., Mostaghimi, P., Paluszny, A., and Pentland, C., 2013: "*Pore-scale imaging and modelling*". Advances in Water Resources, 51: p. 197-216.

[35]. Bohn, R.B. and Garboczi, E.J., 2003: "*User mannual for finite element and finite difference programs: a parellel version of NISTIR-6269*", Internal Report 6997, National Institute of Standards and Technology, Gaithersburg, Maryland, United States.

[36]. Borai, A., 1987: "*A new correlation for the cementation factor in low-porosity carbonates*". SPE Formation Evaluation, 2(04): p. 495-499.

[37]. Borai, A.M., 1985: "*A new correlation for cementation factor in low-porosity carbonates*". SPE 14401 presented at SPE Convention Proceeding for the 60 th Annual Technical Conferece and Exhibition, Los Vegas, USA, 22-25 September. p. 1-18.

[38]. Brannan, G.O. and Von Gonten, W., 1973: "*The effect of temperature on the formation resistivity factor of porous media*". paper U presented at SPWLA 14th Annual Logging Symposium, Lafayette, Louisiana, USA, 6-9 May. Society of Petrophysicists and Well-Log Analysts. p. 1-17.

[39]. Brown Jr, W.F., 1955: "*Solid mixture permittivities*". The Journal of Chemical Physics, 23(8): p. 1514-1517.

[40]. Bryant, S. and Blunt, M., 1992: "*Prediction of relative permeability in simple porous media*". Physical Review A, 46(4): p. 2004--2011.

[41]. Bryant, S.L., King, P.R., and Mellor, D.W., 1993: "*Network model evaluation of permeability and spatial correlation in a real random sphere packing*". Transport in Porous Media, 11(1): p. 53-70.

[42]. Câmara, R., Corbett, P., Tavares, C., Machado, A., Jesus, E., and Borghi, L., 2014: "*Carbonate Coquina Reservoirs-New Insights for Petrophysical Reservoir Characterisation*". in the 76th EAGE Conference and Exhibition 2014, Amsterdam, Netherlands. p.

[43]. Câmara, R.N., 2013: "*Petrophysical characterization of coquinas in Morro do Chaves Formation (Barremian-Aptian), pre-salt Sergipe-Alagoas Basin (in Portuguese)*". MS thesis, Institute of Geoscience, University Federal do Rio de Janeiro (UFRJ). Rio de Janeiro, Brazil.112 p.

[44]. Câmara, R.N., Corbett, P., Tavares, A.C., Borghi , L., Perosi, F., Machado, A., and Bagueira, R., 2015 (in review): "*Porosity Exponent Variation in Petrophysical Facies in Coquina Limestones, Barremian-Aptian, Morro do Chaves Formation, Sergipe-Alagoas Basin, Onshore NE Brazil*". Petrophysics: p.

[45]. Carothers, J.E., 1968: "*A statistical study of the formation factor relation*". The Log Analyst, 9(5): p. 13-20.

[46]. Chen, F. and Zhang, W., 1987: "*Application of the pore-throat conjunction in esimtaion of the residual oil saturation (in Chinese)*". Well Logging Technology, 03: p. 18-21.

[47]. Choquette, P.W. and Pray, L.C., 1970: "*Geologic nomenclature and classification of porosity in sedimentary carbonates*". AAPG Bulletin, 54(2): p. 207-250.

[48]. Clavier, C., Coates, G., and Dumanoir, J., 1977: "*The theoretical and experimental bases for the'dual water'model for the interpretation of shaly sands*". paper SPE 6859 presented at 52nd Annual Fall Technical Conference

and Exhibition of the SPE of AIME, Denver, Colorado, USA, 9 – 12 October. Society of Petroleum Engineers of AIME. p. 153-168.

[49]. Clennell, M.B., 1997: "*Tortuosity: a guide through the maze"*. Geological Society, London, Special Publications, 122(1): p. 299-344.

[50]. Cnudde, V. and Boone, M., 2013: "*High-resolution X-ray computed tomography in geosciences: A review of the current technology and applications"*. Earth-Science Reviews, 123: p. 1-17.

[51]. Coker, D.A., Torquato, S., and Dunsmuir, J.H., 1996: "*Morphology and physical properties of Fontainebleau sandstone via a tomographic analysis"*. Journal of Geophysical Research: Solid Earth (1978–2012), 101(B8): p. 17497-17506.

[52]. Coles, M., Hazlett, R., Muegge, E., Jones, K., Andrews, B., Dowd, B., Siddons, P., Peskin, A., Spanne, P., and Soll, W., 1996: "*Developments in synchrotron X-ray microtomography with applications to flow in porous media"*. SPE 36531 in the SPE Annual Technical Conference and Exhibition, Denver, Colorado, USA, 6–9 October. Society of Petroleum Engineers, p. 288-296.

[53]. Coles, M., Spanne, P., Muegge, E., and Jones, K., 1994: "*Computed microtomography of reservoir core samples"*. SCA-9401 in the Proceedings of the 1994 Annual SCA Meeting, Stavanger, Norway, 12-14 September. p. 9-20.

[54]. Corbett, P., Anggraeni, S., and Bowen, D., 1999: "*The use of the probe permeameter in carbonates-addressing the problems of permeability support and stationarity"*. The Log Analyst, 40(05): p. 316-326.

[55]. Corbett, P. and Borghi, L., 2013: "*Lacustrine Carbonates – for the purpose of reservoir characterisation are they different?"*. OTC-24482 presented at Offshore Technology Conference, Rio de Janeiro, Brazil, 29-31 October. Offshore Technology Conference. p. 1-9.

[56]. Corbett, P., Borghi, L., and Hagashi, Y., 2014: "*Evaluation of Representative Elementary Volume (REV) in Stromatolites of Lagoa Salgada"*. paper 016140 presented at 47th Geological Congress, Salvador, Brazil, 22-26 September. p.

[57]. Corbett, P., Borghi, L., Jiang, Z., Wang, H., Demyanov, V., Yuji Hayshi, F., Saad, M., Machado, A., and Srivastava, N., 2013a: "*Microbial Carbonates-A Sampling and Measurement Challenge for Petrophysics Addressed by Captruing the Bioarchitectrual Components"*. In: D.W.J. Bosence, K.A. Gibbons, D.P. le Heron, W.A. Morgan, T. Pritchard, and B.A. Vining (eds.) Microbial Carbonates in Space and Time: Implications for Global Exploration and Production. Geological Society, London: Special Publications. p. 1-18.

[58]. Corbett, P., Câmara, R., Monteiro, R., Tavares, A.C., Teixiera, B., and Borghi, L., 2013b: "*Framework for Modelling of Wireline Log Responses from Carbonate Outcrops"*. presented at 13th International Congress of the Brazillian Geophysical Society, Rio de Janeiro, Brazil, 26-29,August SBGf - Sociedade Brasileira de Geofísica. p. 1-3.

[59]. Daïan, J.-F., Fernandes, C., Philippi, P., and Bellini da Cunha Neto, J., 2004: "*3D reconstitution of porous media from image processing data using a multiscale percolation system"*. Journal of Petroleum Science and Engineering, 42(1): p. 15-28.

[60]. Delerue, J.-F. and Perrier, E., 2002: "*DXSoil, a library for 3D image analysis in soil science"*. Computers & Geosciences, 28(9): p. 1041-1050.

[61]. Dixon, J. and Marek, B., 1990: "*The Effect of Bimodal-Pore Size Distribution on Electrical Properties of Some Middle Eastern Limestones"*. SPE 20601 in the 65th Annual Technical Conference and Exhibition of the Society of

Petroleum Engineers, New Orleans, Louisiana, USA, 23-26 September Society of Petroleum Engineers, p. 743-750.

[62]. Dolka, M.E.-A., 1981: "*Effect of Temperature on Formation Resistivity of Some Saudi Reservoir Rocks"*. paper SPE-9617 presented at Middle East Technical Conference and Exhibition, Manama, Bahrain, 9-12 March. Society of Petroleum Engineers. p. 387-389.

[63]. Dong, H., 2007: "*Micro-CT imaging and pore network extraction"*. PhD thesis, the Department of Earth Science and Engineering, Imperial College, London, UK.217 p.

[64]. Doyen, P.M., 1988: "*Permeability, conductivity, and pore geometry of sandstone"*. Journal of Geophysical Research: Solid Earth (1978–2012), 93(B7): p. 7729-7740.

[65]. Draxler, J. and Edwards, D., 1986: "*Evaluation procedures in the Carboniferous of Northern Europe"*. Geological Society, London, Special Publications, 23(1): p. 151-167.

[66]. Dullien, F.A., 1992: "*Porous media: fluid transport and pore structure"*, 2nd, San Diego, California, Academic Press.574 p.

[67]. Dunsmuir, J.H., Ferguson, S., D'Amico, K., and Stokes, J., 1991: "*X-ray microtomography: A new tool for the characterization of porous media"*. SPE 22860 presented at SPE Annual Technical Conference and Exhibition, Dallas, Texas, USA, 6–9 October. Society of Petroleum Engineers. p. 41-48.

[68]. Ehrlich, R., Etris, E.L., Brumfield, D., Yuan, L., and Crabtree, S.J., 1991: "*Petrography and Reservoir Physics III: Physical Models for Permeability and Formation Factor (1)"*. AAPG Bulletin, 75(10): p. 1579-1592.

[69]. Elias, V.L.G. and Steagall, D.E., 1996: "*The Impact Of the Values of Cementation Factor and Saturation Exponent in The Calculation Of Water Saturation For Macaé Formation, Campos Basin"*. paper 9611 presented at International Symposium of the Society of Core Analysts, Montpelier, France, 8-10 September. Society of Core Analyst. p. 1-9.

[70]. Etris, E., Brumfield, D., Ehrlich, R., and Crabtree, S., 1989: "*Petrographic Insights Into The Relevance Of Archie's Equation: Formation Factor Without " M" and " A" "*. paper F presented at SPWLA 30th Annual Logging Symposium, Denver, Colorado, USA, 11-14 June. Society of Petrophysicists and Well-Log Analysts. p. 1-18.

[71]. Fatt, I., 1956: "*The network model of porous media, I. Capillary Pressure Characteristics"*. Petroleum Transactions, AIME, 207: p. 144-159.

[72]. Fatt, I., 1957: "*Effect of overburden and reservoir pressure on electric logging formation factor"*. AAPG Bulletin, 41(11): p. 2456-2466.

[73]. Flannery, B.P., Deckman, H.W., Roberge, W.G., and D'AMICO, K.L., 1987: "*Three-dimensional X-ray microtomography"*. Science, 237(4821): p. 1439-1444.

[74]. Focke, J. and Munn, D., 1987: "*Cementation exponents in Middle Eastern carbonate reservoirs"*. SPE Formation Evaluation, 2(02): p. 155-167.

[75]. Fredrich, J., Greaves, K., and Martin, J., 1993: "*Pore geometry and transport properties of Fontainebleau sandstone"*. International Journal of Rock Mechanics Minieral Sciences & Geomechanics Abstracts, 30(7): p. 691-697.

[76]. Garboczi, E. and Day, A.R., 1995: "*An algorithm for computing the effective linear elastic properties of heterogeneous materials: three-dimensional results for composites with equal phase Poisson ratios"*. Journal of the Mechanics and Physics of Solids, 43(9): p. 1349-1362.

[77]. Garboczi, E.J., 1998: *Finite element and finite difference programs for computing the linear electric and elastic properties of digital images of random materials* [Online]. Building and Fire Research Laboratory, National Institute of Standards and Technology.December, 1998, Available: http://fire.nist.gov/bfrlpubs/build98/art147.html [Accessed January 2011].

[78]. Glover, P., 2009: "*What is the cementation exponent? A new interpretation*". The Leading Edge, 28(1): p. 82-85.

[79]. Gomez-Rivero, O., 1976: "*A practical method for determining cementation exponents and some other parameters as an aid in well log analysis*". The Log Analyst, 17(05): p. 8-24.

[80]. Green, C.P. and Paterson, L., 2007: "*Analytical three-dimensional renormalization for calculating effective permeabilities*". Transport in Porous Media, 68(2): p. 237-248.

[81]. Guyod, H., 1944: "*Fundamental data for the interpretation of electric logs*". Oil Weekly, 115(38): p. 21-27.

[82]. Haghighi, M., Bagheri, A.M., and Namani, M., 2008: "*Investigation of Cementation Factor in Iranian Carbonate Reservoirs*". presented at 14th Formation Evaluation Symposium of Japan Chiba, Japan, 29-30 September. Australian School of Petroleum publications. p. 1-9.

[83]. Han, M., Youssef, S., Rosenberg, E., Fleury, M., and Levitz, P., 2009: "*Deviation from Archie's law in partially saturated porous media: wetting film versus disconnectedness of the conducting phase*". Physical Review E, 79(3): p. (031127) 1- 11.

[84]. Hartmann, D.J. and Beaumont, E.A., 1999: "*Predicting reservoir system quality and performance*". In: E.A. Beaumont and N.H. Foster (eds.) Exploring for oil and gas traps-Treatise of Petroleum geology. . Tulsa, Oklahoma: AAPG Treatise of Petroleum Geology. p. (9) 1-(9) 54.

[85]. Hazlett, R., 1995: "*Simulation of capillary-dominated displacements in microtomographic images of reservoir rocks*". Transport in Porous Media, 20(1-2): p. 21-35.

[86]. Hazlett, R., 1997: "*Statistical characterization and stochastic modeling of pore networks in relation to fluid flow*". Mathematical Geology, 29(6): p. 801-822.

[87]. Hilchie, D.W., 1982: "*Advanced well log interpretation*", Golden, Colorado, Douglas W. Hilchie Inc.300 p.

[88]. Hoshen, J. and Kopelman, R., 1976: "*Percolation and cluster distribution. I. Cluster multiple labeling technique and critical concentration algorithm*". Physical Review B, 14(8): p. 3438-3445.

[89]. Ioannidis, M. and Chatzis, I., 2000: "*On the geometry and topology of 3D stochastic porous media*". Journal of Colloid and Interface Science, 229(2): p. 323-334.

[90]. Jackson, P., Smith, D.T., and Stanford, P., 1978: "*Resistivity-porosity-particle shape relationships for marine sands*". Geophysics, 43(6): p. 1250-1268.

[91]. Jacquin, C., 1964: "*Corrélation entre la perméabilité et les caractéristiques géométriques du grès de Fontainebleau (in French)*". Revue Institut Francais du P étrole, 19: p. 921-937.

[92]. Jiang, Z., 2008: "*Quantitative characterisation of the geometry and topology of pore space in 3D rock images*". PhD thesis, Institute of Petroleum Engineering, Heriot-Watt University, Edinburgh, Scotland, UK.245 p.

[93]. Jiang, Z., Wu, K., Couples, G.D., and Ma, J., 2011: "*The Impact of Pore Size and Pore Connectivity on Single-Phase Fluid Flow in Porous Media*". Advanced Engineering Materials, 13(3): p. 208-215.

[94]. Jing, X.D. and Archer, J., 1991: "*Improved hydrocarbon-in-place determinations of shaly rocks from laboratory electrical resistivity measurements at reservoir conditions"*. SPE-23103 presented at Offshore Europe, Aberdeen, United Kingdom 3-6 September. Society of Petroleum Engineers. p. 67-78.

[95]. Johnson, D.L., Koplik, J., and Schwartz, L.M., 1986: "*New pore-size parameter characterizing transport in porous media"*. Physical Review Letters, 57(20): p. 2564-2567.

[96]. Joshi, M.Y., 1974: "*A class of stochastic models for porous media"*. PhD thesis, Chemical and Petroleum Engineering, University of Kansas, Lawrence, Kansas, USA.302 p.

[97]. Kadhim, F.S., Samsuri, A., and Kamal, A., 2013: "*A Review in Correlations between Cementation Factor and Carbonate Rocks Properties"*. Life Science Journal, 10(4): p. 2451-2458.

[98]. Kantzas, A., Chatzis, I., and Dullien, F., 1988: "*Enhanced oil recovery by inert gas injection"*. paper SPE/DOE 17379 in the SPE/DOE Enhanced Oil Recovery Symposium, Tulsa, Oklahoma 17-20 April. Society of Petroleum Engineers, p. 653-662.

[99]. Karim, M. and Krabbenhoft, K., 2010: "*New renormalization schemes for conductivity upscaling in heterogeneous media"*. Transport in Porous Media, 85(3): p. 677-690.

[100]. Kazatchenko, E. and Mousatov, A., 2002: "*Primary and secondary porosity estimation of carbonate formations using total porosity and the formation factor"*. paper SPE-77787 presented at SPE Annual Technical Conference and Exhibition, San Antonio, Texas, USA, 29 September-2 October. Society of Petroleum Engineers. p. 1-6.

[101]. Keller, G., 1953: "*Effect of wettability on the electrical resistivity of sand"*. Oil and Gas Journal, 51(1): p. 62-65.

[102]. Ketcham, R.A. and Carlson, W.D., 2001: "*Acquisition, optimization and interpretation of X-ray computed tomographic imagery: applications to the geosciences"*. Computers & Geosciences, 27(4): p. 381-400.

[103]. Khalili, A.D., Yanici, S., Cinar, Y., and Arns, C.H., 2012: "*Formation factor for heterogeneous carbonate rocks using multi-scale Xray-CT images"*. paper SPE-163389 presented at SPE Kuwait International Petroleum Conference and Exhibition, Kuwait City, Kuwait 10-12 December. Society of Petroleum Engineers. p. 5-28.

[104]. King, P., 1989: "*The use of renormalization for calculating effective permeability"*. Transport in Porous Media, 4(1): p. 37-58.

[105]. Knackstedt, M., Arns, C., Sheppard, A., Senden, T., Sok, R., Cinar, Y., Pinczewski, W., Ioannidis, M., and Padhy, G., 2007: "*Archie's exponents in complex lithologies derived from 3D digital core analysis"*. paper UU in the SPWLA 48th Annual Logging Symposium Transactions, Austin, Texas, USA, 3-6 June. p. 1-16.

[106]. Knackstedt, M.A., Jaime, P., Butcher, A., Botha, P., Middleton, J., and Sok, R., 2010: "*Integrating Reservoir Characterization: 3D Dynamic Petrophysical and Geological Description of Reservoir Facies"*. paper SPE-133981 presented at SPE Asia Pacific Oil and Gas Conference and Exhibition, Brisbane, Queensland, Australia 18-20 October. Society of Petroleum Engineers. p. 1-9.

[107]. Kong, T.Y. and Rosenfeld, A., 1989: "*Digital topology: Introduction and survey"*. Computer Vision, Graphics, and Image Processing, 48(3): p. 357-393.

[108]. Kostek, S., Schwartz, L.M., and Johnson, D.L., 1992: "*Fluid permeability in porous media: Comparison of electrical estimates with hydrodynamical calculations"*. Physical Review B, 45(1): p. 186-195.
[109]. Kunetz, G., 1966: "*principles of direct current resistivity prospecting. Geoexploration monograph series 1"*, Berlin, Germany, Geopublication Associates.103 p.
[110]. Kurniawan, B. and Bassiouni, Z., 2007: "*Use of Cec-Dependent Cementation and Saturation Exponents in Shaly Sand Resistivity Models"*. paper FFF in the 48th Annual Logging Symposium, Austin, Texas, USA, 3-6 June. Society of Petrophysicists and Well-Log Analysts, p. 1-9.
[111]. Lang, C., Ohser, J., and Hilfer, R., 2001: "*On the analysis of spatial binary images"*. Journal of Microscopy, 203(3): p. 303-313.
[112]. Levitz, P.E., 2007: "*Toolbox for 3D imaging and modelling of porous media :Relationship with transport properties"*. Cement and Concrete Research, 37(3): p. 351-359.
[113]. Li, X., Qin, R., Liu, C., and Mao, Z., 2013: "*The effect of rock electrical parameters on the calculation of reservoir saturation"*. Journal of Geophysics and Engineering, 10(5): p. (055007) 1- 8.
[114]. Liang, Z., Ioannidis, M., and Chatzis, I., 2000: "*Geometric and topological analysis of three-dimensional porous media: pore space partitioning based on morphological skeletonization"*. Journal of Colloid and Interface Science, 221(1): p. 13-24.
[115]. Lindquist, W. and Venkatarangan, A., 1999: "*Investigating 3D geometry of porous media from high resolution images"*. Physics and Chemistry of the Earth, Part A: Solid Earth and Geodesy, 24(7): p. 593-599.
[116]. Lindquist, W.B., 2006: "*The geometry of primary drainage"*. Journal of Colloid and Interface Science, 296(2): p. 655-668.
[117]. Lindquist, W.B., Lee, S.M., Coker, D.A., Jones, K.W., and Spanne, P., 1996: "*Medial axis analysis of void structure in three-dimensional tomographic images of porous media"*. Journal of Geophysical Research: Solid Earth (1978–2012), 101(B4): p. 8297-8310.
[118]. Lindquist, W.B., Venkatarangan, A., Dunsmuir, J., and Wong, T.f., 2000: "*Pore and throat size distributions measured from synchrotron X-ray tomographic images of Fontainebleau sandstones"*. Journal of Geophysical Research: Solid Earth (1978–2012), 105(B9): p. 21509-21527.
[119]. Lønøy, A., 2006: "*Making sense of carbonate pore systems"*. AAPG Bulletin, 90(9): p. 1381-1405.
[120]. Lu, C. and Mai, Y.-W., 2007: "*Permeability modelling of polymer-layered silicate nanocomposites"*. Composites Science and Technology, 67(14): p. 2895-2902.
[121]. Lucia, F., 1983: "*Petrophysical parameters estimated from visual descriptions of carbonate rocks: a field classification of carbonate pore space"*. Journal of Petroleum Technology, 35(03): p. 629-637.
[122]. Lucia, F.J., 1995: "*Rock-fabric/petrophysical classification of carbonate pore space for reservoir characterization"*. AAPG Bulletin, 79(9): p. 1275-1300.
[123]. Lucia, F.J., 1999: "*Carbonate Reservoir Characterization"*, Berlin, Germany, Springer.226 p.
[124]. Lucia, F.J., 2007: "*Carbonate Reservoir Characterization : An Integrated Approach"*, 2nd, Verlag Berlin Heidelberg, Springer.354 p.
[125]. Lunati, I., Bernard, D., Giudici, M., Parravicini, G., and Ponzini, G., 2001: "*A numerical comparison between two upscaling techniques: non-local inverse*

based scaling and simplified renormalization". Advances in Water Resources, 24(8): p. 913-929.

[126]. Mabrouk, W.M. and Soliman, K.S., 2014: "*A numerical technique for an accurate determination of formation resistivity factor using FR-RO overlays method"*. Arabian Journal of Geosciences: p. 1-7.

[127]. Mahmood, S., Maerefat, N., and Chang, M., 1991: "*Laboratory measurements of electrical resistivity at reservoir conditions"*. SPE Formation Evaluation, 6(03): p. 291-300.

[128]. Manwart, C. and Hilfer, R., 1999: "*Reconstruction of random media using Monte Carlo methods"*. Physical Review E, 59(5): p. 5596-5599.

[129]. Manwart, C., Torquato, S., and Hilfer, R., 2000: "*Stochastic reconstruction of sandstones"*. Physical Review E, 62(1): p. 893-899.

[130]. Mason, G. and Morrow, N.R., 1991: "*Capillary behavior of a perfectly wetting liquid in irregular triangular tubes"*. Journal of Colloid and Interface Science, 141(1): p. 262-274.

[131]. Maute, R., Lyle, W., and Sprunt, E.S., 1992: "*Improved Data-Analysis Method Determines Archie Parameters From Core Data (includes associated paper 24964)"*. Journal of Petroleum Technology, 44(01): p. 103-107.

[132]. McDougall, S. and Sorbie, K., 1995: "*The impact of wettability on waterflooding: pore-scale simulation"*. SPE Reservoir Engineering, 10(03): p. 208-213.

[133]. Mecke, K.R., 2000: "*Additivity, convexity, and beyond: applications of Minkowski Functionals in statistical physics"*. In: K.R. Mecke and D. Stoyan (eds.) Statistical Physics and Spatial Statistics. Berlin Heidelberg Germany: Springer. p. 111-184.

[134]. Mendelson, K.S. and Cohen, M.H., 1982: "*The effect of grain anisotropy on the electrical properties of sedimentary rocks"*. Geophysics, 47(2): p. 257-263.

[135]. Mousavi, M.A., 2010: "*Pore-scale characterization and modeling of two-phase flow in tight gas sandstones"*. PhD thesis, Petroleum and Geosystems Engineering, University of Texas at Austin, Austin, Texas, USA.152 p.

[136]. Mousavi, M.A. and Bryant, S.L., 2007: "*Geometric models of porosity reduction mechanisms in tight gas sands"*. paper SPE-107963 presented at Rocky Mountain Oil & Gas Technology Symposium, Denver, Colorado, USA, 16-18 April. Society of Petroleum Engineers. p. 1-13.

[137]. Mousavi, M.A. and Bryant, S.L., 2012: "*Connectivity of pore space as a control on two-phase flow properties of tight-gas sandstones"*. Transport in Porous Media, 94(2): p. 537-554.

[138]. Mousavi, M.A. and Bryant, S.L., 2013: "*Geometric models of porosity reduction by ductile grain compaction and cementation"*. AAPG Bulletin, 97(12): p. 2129-2148.

[139]. Mousavi, M.A., Prodanovic, M., and Jacobi, D., 2012: "*New classification of carbonate rocks for process-based pore-scale modeling"*. SPE Journal, 18(02): p. 243-263.

[140]. Nakashima, Y. and Kamiya, S., 2007: "*Mathematica programs for the analysis of three dimensional pore connectivity and anisotropic tortuosity of porous rocks using X-ray computed tomography image data"*. Journal of Nuclear Science and Technology, 44(9): p. 1233-1247.

[141]. Nakashima, Y. and Nakano, T., 2011: "*Accuracy of formation factors for three-dimensional pore-scale images of geo-materials estimated by renormalization technique"*. Journal of Applied Geophysics, 75(1): p. 31-41.

[142]. Ohser, J. and Mücklich, F., 2000: "*Statistical analysis of microstructures in materials science*", Chichester, England, Wiley 381 p.

[143]. Ohser, J., Nagel, W., and Schladitz, K., 2002: "*The Euler number of discretized sets—on the choice of adjacency in homogeneous lattices*". In: K.R. Mecke and D. Stoyan (eds.) Morphology of Condensed Matter Berlin Heidelberg Germany: Springer. p. 275-298.

[144]. Okabe, H. and Blunt, M.J., 2004: "*Prediction of permeability for porous media reconstructed using multiple-point statistics*". Physical Review E, 70(6): p. (066135) 1- 10.

[145]. Øren, P.-E. and Bakke, S., 2002: "*Process based reconstruction of sandstones and prediction of transport properties*". Transport in Porous Media, 46(2-3): p. 311-343.

[146]. Øren, P.-E. and Bakke, S., 2003: "*Reconstruction of Berea sandstone and pore-scale modelling of wettability effects*". Journal of Petroleum Science and Engineering, 39(3-4): p. 177-199.

[147]. Øren, P.-E., Bakke, S., and Arntzen, O.J., 1998: "*Extending predictive capabilities to network models*". SPE Journal, 3(4): p. 324-336.

[148]. Øren, P.-E., Bakke, S., and Held, R., 2007: "*Direct pore-scale computation of material and transport properties for North Sea reservoir rocks*". Water Resources Research, 43(12): p. 1-11.

[149]. Øren, P.-E., Billiotte, J., and Pinczewski, W., 1992: "*Mobilization of waterflood residual oil by gas injection for water-wet conditions*". SPE Formation Evaluation, 7(01): p. 70-78.

[150]. Øren, P.-E., Billiotte, J., and Pinczewski, W., 1994: "*Pore-Scale Network Modelling of Waterflood Residual Oil Recovery by Immiscible Gas Flooding*". paper SPE 27814 in the SPE/DOE 9th Sympoium on Improved Oil Recovery, Tulsa, Oklahoma, USA, 17-20 April. Society of Petroleum Engineers, p. 345-359.

[151]. Pancaldi, V., Christensen, K., and King, P.R., 2007: "*Permeability up-scaling using Haar wavelets*". Transport in Porous Media, 67(3): p. 395-412.

[152]. Park, C. and Rosenfeld, A., 1971: "*Connectivity and genus in three dimensions*", Technical Report TR-156-05/71, Computer Science Center, Maryland University, College Park USA.

[153]. Perez-Rosales, C., 1982: "*On the relationship between formation resistivity factor and porosity*". Society of Petroleum Engineers Journal, 22(04): p. 531-536.

[154]. Petrovic, A., Siebert, J., and Rieke, P., 1982: "*Soil bulk density analysis in three dimensions by computed tomographic scanning*". Soil Science Society of America Journal, 46(3): p. 445-450.

[155]. Pirson, S., 1947: "*Factors which affect true formation resistivity*". Oil and Gas Journal, 46(18): p. 76-84.

[156]. Porter, C.R. and Carothers, J.E., 1970: "*Formation factor-porosity relation derived from well log data*". paper D in the SPWLA 11th Annual Logging Symposium, Los Angeles, USA, 3-6 May. Society of Petrophysicists and Well-Log Analysts, p. 16-26.

[157]. Prodanović, M., Lindquist, W., and Seright, R., 2006: "*Porous structure and fluid partitioning in polyethylene cores from 3D X-ray microtomographic imaging*". Journal of Colloid and Interface Science, 298(1): p. 282-297.

[158]. Prodanović, M., Lindquist, W., and Seright, R., 2007: "*3D image-based characterization of fluid displacement in a Berea core*". Advances in Water Resources, 30(2): p. 214-226.

[159]. Pulido, H., Samaniego, F., Galicia-Muñoz, G., Rivera, J., and Vélez, C., 2007: "*Petrophysical Characterization of Carbonate Naturally Fractured Reservoirs for use in dual porosity simulators"*. in the Proceedings Thirty-Second Workshop on Geothermal Reservoir Engineering, Stanford University, Stanford, California, 22-24 January p. 1-12.

[160]. Quiblier, J.A., 1984: "*A new three-dimensional modeling technique for studying porous media"*. Journal of Colloid and Interface Science, 98(1): p. 84-102.

[161]. Ragland, D.A., 2002: "*Trends in cementation exponents (m) for carbonate pore systems"*. Petrophysics, 43(05): p. 434-446.

[162]. Rajan, R. and Delaney, P., 1991: "*Reconciliation of Log and Capillary Pressure Based Water Saturation in The Fateh Thamama Reservoir Dubai"*. paper UU in the SPWLA 32nd Annual Logging Symposium, Midland, Texas, USA, 16-19 June. Society of Petrophysicists and Well-Log Analysts, p. 1-24.

[163]. Ramakrishnan, T., Schwartz, L., Fordham, E., Kenyon, W., and Wilkinson, D., 1998: "*Forward models for nuclear magnetic resonance in carbonate rocks"*. paper SS in the SPWLA 39th Annual Logging Symposium, Keystone, Colorado, USA, 26-28 May. Society of Petrophysicists and Well-Log Analysts, p. 1-12.

[164]. Ransom, P., 1984: "*A contribution toward a better understanding of the modified Archie formation resistivity factor relationship"*. The Log Analyst, 25(02): p. 7-12.

[165]. Ransom, R.C., 1974: "*The bulk volume water concept of resistivity well-log interpretation: a theory based on a new reservoir rock resistivity model"*. The Log Analyst, 14(1): p. 3-16.

[166]. Rasmus, J., 1983: "*A variable cementation exponent, M, for fractured carbonates"*. The Log Analyst, 24(06): p. 13-23.

[167]. Rasmus.J.C., 1986: "*A summary of the effects of various pore geometries and their wettabilities on measured and in-situ values of cementation and saturation exponents"*. paper PP in the SPWLA 27th Annual Logging Symposium, Houston, Texas, USA, 9-13 June. Society of Petrophysicists and Well-Log Analysts., p. 1-25.

[168]. Renard, P. and De Marsily, G., 1997: "*Calculating equivalent permeability: a review"*. Advances in Water Resources, 20(5-6): p. 253-278.

[169]. Roberts, A.P., 1997: "*Statistical reconstruction of three-dimensional porous media from two-dimensional images"*. Physical Review E, 56(3): p. 3203-3212.

[170]. Salem, H.S., 1990: "*A theoretical and practical study of petrophysical, electric, and elastic parameters of sediments"*. PhD thesis, Mathematics and Natural Sciences Faculty, Kiel University Kiel, Germany.200 p.

[171]. Salem, H.S., 1993: "*Derivation of the Cementation Factor (Archie's Exponent) and the Kozeny-Carman Constant from Well Log Data and Their Dependence on Lithology and Other Physical Parameters"*. paper SPE-26309, Unsolicited manuscript: p. 2-26.

[172]. Salem, H.S., 1994: "*The electric and hydraulic anisotropic behavior of the Jeanne d'Arc basin reservoirs"*. Journal of Petroleum Science and Engineering, 12(1): p. 49-66.

[173]. Salem, H.S. and Chilingarian, G.V., 1999: "*The cementation factor of Archie's equation for shaly sandstone reservoirs"*. Journal of Petroleum Science and Engineering, 23(2): p. 83-93.

[174]. Sanyal, S.K., Marsden Jr, S., and Ramey Jr, H., 1972: "*The Effect of Temperature on Electrical Resistivity of Porous Media"*. paper I presented at

SPWLA 13th Annual Logging Symposium, Tulsa, Oklahoma, USA, 7-10 May. Society of Petrophysicists and Well-Log Analysts. p. 1-35.

[175]. Schlumberger, 1979: "*Log Interpretation charts"*, Houston,Texas, USA, Schlumberger Well Surveying Corp.97 p.

[176]. Schlumberger, 1987: "*Log Interpretation Principles /Applications"*, Houston Texas, USA, Schlumberger Educational Services.198 p.

[177]. Schwartz, L.M. and Banavar, J.R., 1989: "*Transport properties of disordered continuum systems"*. Physical Review B, 39(16): p. 11965-11970.

[178]. Schwartz, L.M., Banavar, J.R., and Halperin, B.I., 1989: "*Biased-diffusion calculations of electrical transport in inhomogeneous continuum systems"*. Physical Review B, 40(13): p. 9155-9161.

[179]. Sen, P., Scala, C., and Cohen, M., 1981: "*A self-similar model for sedimentary rocks with application to the dielectric constant of fused glass beads"*. Geophysics, 46(5): p. 781-795.

[180]. Sen, P.N., Kenyon, W.E., Takezaki, H., and Petricola, M., 1997: "*Formation factor of carbonate rocks with microporosity: model calculations"*. Journal of Petroleum Science and Engineering, 17(3): p. 345-352.

[181]. Serra, J., 1982: "*Image analysis and mathematical morphology, v. 1"*, New York, USA, Academic Press.610 p.

[182]. Serra, O., 1989: "*Formation microscanner image interpretation"*, Houston, Texas, USA, Schlumberger Educational Services.117 p.

[183]. Sethi, D.K., 1979: "*Some considerations about the formation resistivity factor-porosity relations"*. paper L in the SPWLA 20th Annual Logging Symposium, Tulsa, Oklahoma, USA, 3-6 June. Society of Petrophysicists and Well-Log Analysts, p. 1-12.

[184]. Sheppard, A., Sok, R., and Averdunk, H., 2005: "*Improved pore network extraction methods"*. paper SCA2005-20 in the International Symposium of the Society of Core Analysts, Toronto, Canada, 21-25 August. Society of Core Analysts, p. 1-11.

[185]. Sheppard, A.P., Knackstedt, M.A., Pinczewski, W., and Sahimi, M., 1999: "*Invasion percolation: new algorithms and universality classes"*. Journal of Physics A: Mathematical and General, 32(49): p. L521-L529.

[186]. Sherman, M.M., 1983: "*The determination of cementation exponents using high frequency dielectric measurements"*. paper D in the SPWLA 24th Annual Logging Symposium, Calgary, Alberta, 27-30 June. Society of Petrophysicists and Well-Log Analysts, p. 1-15.

[187]. Shin, H., Lindquist, W., Sahagian, D., and Song, S.-R., 2005: "*Analysis of the vesicular structure of basalts"*. Computers & Geosciences, 31(4): p. 473-487.

[188]. Silin, D. and Patzek, T., 2006: "*Pore space morphology analysis using maximal inscribed spheres"*. Physica A: Statistical Mechanics and its Applications, 371(2): p. 336-360.

[189]. Silin, D.B., Jin, G., and Patzek, T.W., 2003: "*Robust determination of the pore space morphology in sedimentary rocks"*. paper SPE 84296 presented at SPE Annual Technical Conference and Exhibition, Denver, Colorado, USA, 5-8 October Society of Petroleum Engineers. p. 1-15.

[190]. Sok, R.M., Knackstedt, M.A., Sheppard, A.P., Pinczewski, W., Lindquist, W., Venkatarangan, A., and Paterson, L., 2002: "*Direct and stochastic generation of network models from tomographic images; effect of topology on residual saturations"*. Transport in Porous Media, 46(2-3): p. 345-371.

[191]. Sok, R.M., Varslot, T., Ghous, A., Latham, S., Sheppard, A.P., and Knackstedt, M.A., 2010: "*Pore Scale Characterization of Carbonates at Multiple Scales:*

Integration of Micro-CT, BSEM, FIBSEM". paper SCA2009-18 presented at International Symposium of the Society of Core Analysts, Noordwijk, The Netherlands, 27-30 September. Society of Core Analysts. p. 1-12.

[192]. Spanne, P., Thovert, J., Jacquin, C., Lindquist, W., Jones, K., and Adler, P., 1994: "*Synchrotron computed microtomography of porous media: topology and transports"*. Physical Review Letters, 73(14): p. 2001-2004.

[193]. Tabibi, M. and Emadi, M., 2003: "*Variable cementation factor determination (empirical methods)"*. paper SPE-81485 presented at SPE 13th Middle East Oil Show & Conference, Bahrain, 9-12 June. Society of Petroleum Engineers. p. 1-9.

[194]. Thane, C.G., 2006: "*Geometry and topology of model sediments and their influence on sediment properties"*. MS thesis, Petroleum and Geosystems Engineering, University of Texas at Austin, Austin Texas USA.376 p.

[195]. Tiab, D. and Donaldson, E.C., 1996: "*Petrophysics: theory and practice of measuring reservoir rock and fluid transport properties"*, Oxford, UK, Gulf Professional Publishing.706 p.

[196]. Timur, A., Hempkins, W., and Worthington, A., 1972: "*Porosity and pressure dependence of formation resistivity factor for sandstones"*. paper D in the Proceedings of Canadian Well Logging Society, the 4th Formation Evaluation symposium, Calgary, Alberta, 9-10 May. Canadian Well Logging Society, p.

[197]. Torquato, S., 1991: "*Random heterogeneous media: microstructure and improved bounds on effective properties"*. Applied Mechanics Reviews, 44(2): p. 37-76.

[198]. Toumelin, E. and Torres-Verdín, C., 2005: "*Influence of oil saturation and wettability on rock resistivity measurements: a uniform pore-scale approach"*. paper PPP in the SPWLA 46th Annual Logging Symposium, New Orleans, Louisiana, USA, 26-29 June. Society of Petrophysicists and Well-Log Analysts, p. 1-14.

[199]. Toumelin, E. and Torres-Verdín, C., 2008: "*Object-oriented approach for the pore-scale simulation of DC electrical conductivity of two-phase saturated porous media"*. Geophysics, 73(2): p. E67-E79.

[200]. Toumelin, E., Torres-Verdín, C., Chen, S., and Fischer, D., 2002: "*Analysis of NMR diffusion coupling effects in two-phase carbonate rocks: Comparison of measurements with Monte Carlo simulations"*. paper JJJ presented at SPWLA 43rd Annual Logging SymposiumTransactions, Oiso, Japan, 2-5 June. Society of Petrophysicists and Well-Log Analysts. p. 1-13.

[201]. Towle, G., 1962: "*An analysis of the formation resistivity factor-porosity relationship of some assumed pore geometries"*. paper C presented at SPWLA 3rd Annual Logging Symposium, Houston, Texas, USA, 17-18 May. Society of Petrophysicists and Well-Log Analysts. p. 1-13.

[202]. Turner, M., Knüfing, L., Arns, C., Sakellariou, A., Senden, T., Sheppard, A., Sok, R., Limaye, A., Pinczewski, W., and Knackstedt, M., 2004: "*Three-dimensional imaging of multiphase flow in porous media"*. Physica A: Statistical Mechanics and its Applications, 339(1): p. 166-172.

[203]. Unalmiser, S. and Bova, J., 1993: "*A new correlation developed between Archie's parameters and continuous phase change saturation interval"*. paper SPE 25514 in the Production Operations Symposium, Oklahoma City, Oklahoma, USA, 21-23 March Society of Petroleum Engineers, p. 977-990.

[204]. Van Dijke, M. and Sorbie, K., 2002: "*Pore-scale network model for three-phase flow in mixed-wet porous media"*. Physical Review E, 66: p. (046302) 1-14.

[205]. Verwer, K., Eberli, G.P., and Weger, R.J., 2011: "*Effect of pore structure on electrical resistivity in carbonates"*. AAPG Bulletin, 95(2): p. 175-190.

[206]. Vik, B., Bastesen, E., and Skauge, A., 2013: "*Evaluation of representative elementary volume for a vuggy carbonate rock—Part: Porosity, permeability, and dispersivity"*. Journal of Petroleum Science and Engineering, 112: p. 36-47.

[207]. Vinegar, H.J. and Wellington, S.L., 1987: "*Tomographic imaging of three-phase flow experiments"*. Review of Scientific Instruments, 58(1): p. 96-107.

[208]. Vogel, H.-J., 1997: "*Morphological determination of pore connectivity as a function of pore size using serial sections"*. European Journal of Soil Science, 48(3): p. 365-377.

[209]. Vogel, H.-J., 2000: "*A numerical experiment on pore size, pore connectivity, water retention, permeability, and solute transport using network models"*. European Journal of Soil Science, 51(1): p. 99-105.

[210]. Vogel, H.-J., 2002: "*Topological characterization of porous media"*. In: K.R. Mecke and D. Stoyan (eds.) Morphology of Condensed Matter. Berlin Heidelberg Germany: Springer Berlin Heidelberg. p. 75-92.

[211]. Vogel, H.-J. and Roth, K., 2001: "*Quantitative morphology and network representation of soil pore structure"*. Advances in Water Resources, 24(3): p. 233-242.

[212]. Vogel, H.-J., Weller, U., and Schlüter, S., 2010: "*Quantification of soil structure based on Minkowski functions"*. Computers & Geosciences, 36(10): p. 1236-1245.

[213]. Walsh, J., Brown, S., and Asquith, G., 1994: "*Analyzing well logs from the Montoya lime using a new carbonate well log interpretation procedure"*. paper SPE-27645 presented at Permian Basin Oil and Gas Recovery Conference, Midland, Texas, USA, 16-18 March. Society of Petroleum Engineers. p. 291-299.

[214]. Wang, F.P. and Lucia, F.J., 1993: "*Comparison of empirical models for calculating the vuggy porosity and cementation exponent of carbonates from log responses"*, Austin, Texas, USA, Bureau of Economic Geology, University of Texas at Austin.27 p.

[215]. Wardlaw, N.C., 1980: "*The effects of pore structure on displacement efficiency in reservoir rocks and in glass micromodels"*. paper SPE-8843 presented at SPE/DOE Enhanced Oil Recovery Symposium, Tulsa, Oklahoma, USA, 20-23 April. Society of Petroleum Engineers. p. 345-352.

[216]. Watfa, M. and Nurmi, R., 1987: "*Calculation Of Saturation Secondary Porosity And Producibility In Complex Middle East Carbonate Reservoirs"*. paper CC in the SPWLA 28th Annual Logging Symposium, London, England, June 29-July 2. Society of Petrophysicists and Well-Log Analysts, p. 1-24.

[217]. Waxman, M.H. and Thomas, E., 1974: "*Electrical conductivities in Shaly Sands-I. The relation between hydrocarbon saturation and resistivity index; II. The temperature coefficient of electrical conductivity"*. Journal of Petroleum Technology, 26(02): p. 213-225.

[218]. Weibel, E.R., 1979: "*Stereological Methods: Vol.: 1.: Practical Methods for Biological Morphometry"*, London Academic Press.350 p.

[219]. Winsauer, W.O., Shearin Jr, H., Masson, P., and Williams, M., 1952: "*Resistivity of brine-saturated sands in relation to pore geometry"*. AAPG Bulletin, 36(2): p. 253-277.

[220]. Worthington, P.F., 1985: "*The evolution of shaly-sand concepts in reservoir evaluation"*. The Log Analyst, 26(01): p. 23-40.

[221]. Wu, K., Van Dijke, M.I., Couples, G.D., Jiang, Z., Ma, J., Sorbie, K.S., Crawford, J., Young, I., and Zhang, X., 2006: "*3D stochastic modelling of heterogeneous porous media–applications to reservoir rocks"*. Transport in Porous Media, 65(3): p. 443-467.

[222]. Wyble, D., 1958: "*Effect of Applied Pressure on the Conductivity Porosity and Permeability of Sandstones"*. Journal of Petroleum Technology, 10(11): p. 57-59.

[223]. Wyllie, M. and Gregory, A., 1953: "*Formation factors of unconsolidated porous medium: Influence of practical shale and effect of cementation"*. Journal of Petroleum Technology, 5(04): p. 103-110.

[224]. Wyllie, M. and Rose, W.D., 1950: "*Some theoretical considerations related to the quantitative evaluation of the physical characteristics of reservoir rock from electrical log data"*. Journal of Petroleum Technology, 2(04): p. 105-118.

[225]. Yeong, C. and Torquato, S., 1998: "*Reconstructing random media"*. Physical Review E, 57(1): p. 495-506.

[226]. Yeong, C. and Torquato, S., 1998: "*Reconstructing random media. II. Three-dimensional media from two-dimensional cuts"*. Physical Review E, 58(1): p. 224-233.

[227]. Yuan, H., 1991: "*Advances in apex technology: determination of cementation exponent and absolute permeability"*. The Log Analyst, 32(05): p. 557-570.

[228]. Zhao, H.Q., Macdonald, I.F., and Kwiecien, M.J., 1994: "*Multi-orientation scanning: a necessity in the identification of pore necks in porous media by 3-D computer reconstruction from serial section data"*. Journal of Colloid and Interface Science, 162(2): p. 390-401.